

Ligand Field Considerations for the Reactivity of High Valent Metal-Oxo Complexes and of Bimetallic HX Splitting Photocatalysts

by

Matthew Burke Chambers
B.A Chemistry, Cornell University, 2007

Submitted to the Department of Chemistry
in partial fulfillment of the requirements for the degree of

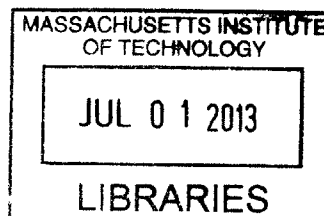
DOCTOR OF PHILOSOPHY IN INORGANIC CHEMISTRY

at the

MASSACHUSETTS INSTITUTE OF TECHNOLOGY

June 2013

ARCHIVES



© 2013 Massachusetts Institute of Technology. All rights reserved

Signature of Author: _____

Department of Chemistry
April 23, 2013


Certified by: _____

Daniel G. Nocera
Patterson Rockwood Professor of Energy
Thesis Supervisor

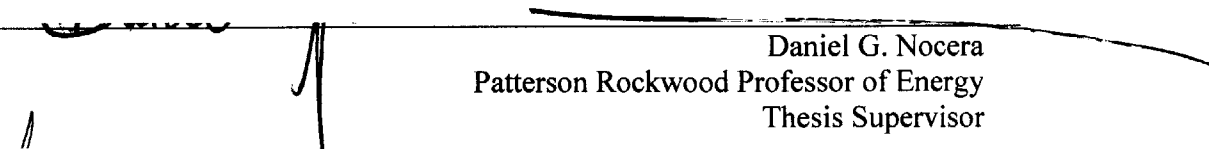
Accepted by: _____

Robert W. Field
Haslam and Dewey Professor of Chemistry
Chairman, Departmental Committee of Graduate Students

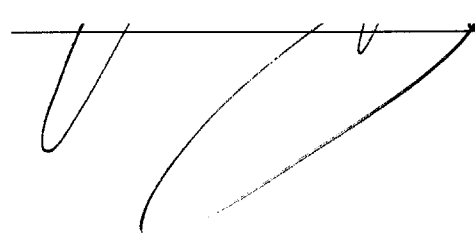
This doctoral thesis has been examined by a committee of the Department of Chemistry as follows:



Christopher C. Cummins
Professor of Chemistry
Committee Chairman



Daniel G. Nocera
Patterson Rockwood Professor of Energy
Thesis Supervisor



Mircea Dincă
Assistant Professor of Chemistry

To my entire family for their unconditional love and support.

In loving memory of my grandfather, Raymond J. Jacobi Sr.

Ligand Field Considerations for the Reactivity of High Valent Metal-Oxo Complexes and of Bimetallic HX Splitting Photocatalysts

by

Matthew Burke Chambers

Submitted to the Department of Chemistry on April 23, 2013, in partial fulfillment of the requirements for the degree of Doctor of Philosophy.

Abstract

Inorganic molecular complexes are used to probe mechanistic steps in two reaction reactions related to energy storage. The first reaction considered is the O–O bond formation step required for water oxidation to oxygen. The second reaction considered is the photocatalytic generation of hydrogen and halogen from hydrohalic acid.

Regarding the O–O bond formation process, terminal metal oxo complexes of pseudotetrahedral geometry were synthesized and studies focused on determining the electronic structure of these complexes as well as reactivity patterns. A novel series of low coordinate tris(alkoxide) complexes of divalent and trivalent metals were synthesized and characterized as single metal site models of oxidic metal clusters. Via oxygen atom transfer reactions, d^0 , d^1 , and d^2 early transition metal-oxo complexes were stabilized. Analysis of structural parameters, infrared spectroscopy and DFT calculations establish that the first two d electrons fill degenerate π^* orbitals with respect to the M–O bond. An electronic structure was determined wherein there is a low lying degenerate d_{xz} , d_{yz} set of orbitals, a more destabilized degenerate set of d_{xy} , $d_{x^2-y^2}$ orbital, with d_{z^2} as the most destabilized d orbital. Upon addition of oxygen atom transfer reagents to tris(alkoxide) divalent iron complexes, rapid C–H bond abstraction is observed to afford an Fe(III)–OH moiety. This rapid and indiscriminate nature in which this reaction proceeds is calculated to arise from the production of a terminal Fe(IV) oxo intermediate complex with a quintet spin state. The exceptionally weak ligand field orthogonal to the ferryl is proposed to stabilize a high spin state and promote the reactivity.

Regarding HX splitting, a new dirhodium diphosphazane structure is evaluated for photocatalytic HX splitting behavior. The complex photoreduces protons but degrades quickly. Rational ligand modifications afford an indefinitely stable proton reduction photocatalyst. Upon proton reduction from hydrohalic acid, valence isomers of a tetrachloride product were isolated. The efficiencies of halide elimination from the valence symmetric and mixed valent complexes were determined to be similar. Calculations suggest that halogen elimination proceeds through a bridging halide structure and access to this structure is the determining factor for the efficiency of halogen elimination.

Thesis Supervisor: Daniel G. Nocera
Title: Patterson Rockwood Professor of Energy

Table of Contents

Title Page	1
Thesis Committee	3
Dedication	5
Abstract	7
Table of Contents	9
List of Figures	13
List of Tables	19
List of Schemes	23
Chapter 1:	25
Homogeneous Systems Toward Renewable Energy Storage	
1.1 The Need for Renewable Energy Storage	26
1.1.1 Global Energy Demands	26
1.1.2 Energy Storage in Chemical Bonds	28
1.2 Water as a Substrate: The Problem of the O–O Bond	31
1.2.1 Water Oxidation and the Oxygen Evolving Reaction	31
1.2.2 O–O Bond Formation Mechanisms	34
1.2.3 OER Catalysts	35
1.2.4 Ancillary Ligand Effects of Metal–Oxos	37
1.3 HX as a Substrate: Catalyst Development	42
1.3.1 Motivation for Molecular Photocatalysts	42
1.3.2 Multicomponent Systems for Photochemical Hydrogen Production	44
1.3.3 Photochemistry of HX Solutions and M–X Bond Activation	47
1.3.4 Mixed Valency and Rhodium-Phosphazane Systems	49
1.4 Scope of Thesis	52
1.5 Concluding Remarks	53
1.6 References	54
Chapter 2:	59
Synthesis and Characterization of Tris(Alkoxide) Divalent and Trivalent 3d Transition Metal Complexes as Homogeneous Metal-Oxide Mimics	
2.1 Introduction	60
2.2 The $t\text{Bu}_2\text{MeCO}^-$ (Ditox) Ligand	61
2.3 Synthesis of Divalent and Trivalent Tris(ditox) Complexes	65
2.4 X-ray Crystallography and Jahn-Teller Distortions	67
2.5 Magnetism	74
2.6 Infrared Spectroscopy	75
2.7 UV-vis Spectroscopy	79

2.8 Concluding Remarks	81
2.9 Experimental Methods and Computational Details	83
2.9.1 General Considerations	83
2.9.2 Preparation of Kditox	83
2.9.3 Preparation of [Cr(ditox) ₃][K(15C5) ₂] (2.1)	84
2.9.4 Preparation of [Mn(ditox) ₃][K(15C5) ₂] (2.2)	84
2.9.5 Preparation of [Fe(ditox) ₃][K(15C5) ₂] (2.3)	85
2.9.6 Preparation of [Co(ditox) ₃][K(15C5) ₂] (2.4)	85
2.9.7 Preparation of [Ni(ditox) ₃][K(15C5) ₂] (2.5)	86
2.9.8 Preparation of V(ditox) ₃ THF (2.6-THF)	86
2.9.9 Preparation of Cr(ditox) ₃ (2.7)	87
2.9.10 Preparation of Fe(ditox) ₃ THF (2.8-THF)	87
2.9.11 Preparation of Co(ditox) ₃ (2.9)	87
2.9.12 Crystallographic Details	88
2.9.13 Computational Details	89
2.10 Crystallographic Tables	90
2.11 References	99
Chapter 3:	105
Electronic Structure and Reactivity of Chromium and Vanadium Tris(alkoxide) Complexes with Terminal Chalcogen Ligands	
3.1 Introduction	106
3.2 Pseudo-Tetrahedral d^0 , d^1 and d^2 Terminal Metal Oxo Complexes	108
3.2.1 Preparation	108
3.2.2 Crystallography	109
3.2.3 Infrared Spectroscopy	114
3.2.4 Computational Analysis	118
3.3 Reactivity Assay	120
3.4 Pseudotetrahedral Metal Sulfido	125
3.4.1 Motivation for Sulfido Complexes	125
3.4.2 Synthetic Methods	126
3.4.3 Electrochemical Analysis	128
3.4.4 Computational Analysis	131
3.5 Concluding Remarks	133
3.6 Experimental Methods and Computational Details	135
3.6.1 General Considerations	135
3.6.2 Preparation of V(ditox) ₃ (O) (3.4)	135
3.6.3 Preparation of Cr(ditox) ₃ (O) (3.5)	135
3.6.4 Preparation of [Cr(ditox) ₃ (O)][CoCp ₂] (3.6)	136
3.6.5 Preparation of Cr(ditox) ₃ (O)K(Et ₂ O) ₃ (3.7)	136

3.6.6 Preparation of Cr(ditox) ₃ (OSnBu ₃) (3.8)	137
3.6.7 Preparation of Cr(ditox) ₃ (O ^t Bu) (3.9)	137
3.6.8 Preparation of Cr(ditox) ₃ (OSiMe ₃) (3.10)	137
3.6.9 Preparation of [Cr(ditox) ₂ O] ₂ (3.11)	137
3.6.10 [Cr(ditox) ₃ (S)][K(15C5) ₂] (3.12)	138
3.6.11 Preparation of [Cr(ditox) ₃ (S)Ag] ₃ (3.13)	138
3.6.12 Crystallographic Details	139
3.6.13 Computational Details	139
3.7 Crystallographic Tables and Computational Model Coordinate Tables	141
3.8 References	154
Chapter 4:	159
Oxidation of Iron in the Tris(ditox) Ancillary Ligand Platform	
4.1 Introduction	160
4.2 O–O bond Formation versus C–H Bond Activation	161
4.3 Synthesis and Characterization of Fe-Ditox Compounds	162
4.4 Oxidation Chemistry	165
4.5 Computation of Fe(IV) Oxo Intermediate	173
4.6 Discussion	176
4.7 Concluding Remarks	180
4.8 Experimental Details and Computational Methods	181
4.8.1 General Considerations	181
4.8.2 Preparation of Fe(ditox) ₃ Li(OEt ₂) (4.2)	181
4.8.3 Preparation of Fe(ditox) ₃ Li(THF) (4.3)	182
4.8.4 Preparation of Fe(ditox) ₃ K(THF) ₂ (4.4)	182
4.8.5 Preparation of Fe(ditox) ₃ (ONMe ₃) (4.6)	182
4.8.6 Preparation of Fe(ditox) ₃ (OH)Li(THF) _n , n = 3 (4.7), n = 2 (4.7a), n = 0 (4.7b) and Fe(ditox) ₃ (OH)Li(di-THF) (4.8)	183
4.8.7 Preparation of [Fe(ditox) ₃ (OH)][K(15C5) ₂] (4.9)	184
4.8.8 X-ray crystallographic details	184
4.8.9 Computational Details	185
4.9 Crystallographic Tables and Computational Cartesian Coordinate Tables	186
4.10 References	197
Chapter 5:	201
HX Splitting Mediated by Rh–Rh Bimetallic Complexes	
5.1 Introduction	202
5.2 Photocatalytic Hydrogen Evolution from Rh ₂ (tfepma) ₂ (CN ^t Bu) ₂ Cl ₂	203
5.3 Photocatalytic Hydrogen Evolution from Rh ₂ (tfepma) ₂ (CNAd) ₂ Cl ₂	206
5.4 X ₂ Photoelimination from Rh ₂ (tfepma) ₂ (CNAd) ₂ Cl ₄ Isomers	210

5.5 Cl ₂ Photoelimination from Rh ₂ (tfepma) ₂ (CNAr)(μ-Cl)Cl ₃ Complexes	216
5.6 Concluding Remarks	218
5.7 Experimental Details and Computational Methods	220
5.7.1 General Considerations	220
5.7.2 Preparation of Rh ₂ ^{0,II} (tfepma) ₂ (CNAd) ₂ Cl ₂ (5.4)	220
5.7.3 Preparation of Rh ₂ ^{II,II} (tfepma) ₂ (CNAd) ₂ Cl ₃ H (5.5)	221
5.7.4 Preparation of Rh ₂ ^{II,II} (tfepma) ₂ (CNAd) ₂ Cl ₄ (5.6)	221
5.7.5 Preparation of Rh ₂ ^{I,III} (tfepma) ₂ (CNAd) ₂ Cl ₄ (5.7)	222
5.7.6 Preparation of Rh ₂ (tfepma) ₂ (μ- <i>p</i> -F-C ₆ H ₄ NC)Cl ₂ (5.10)	222
5.7.7 Preparation of Rh ₂ (tfepma) ₂ (μ- <i>p</i> -MeO-C ₆ H ₄ NC)Cl ₂ (5.11)	222
5.7.8 Preparation of Rh ₂ (tfepma) ₂ (μ- <i>p</i> -F-C ₆ H ₄ NC)Cl ₄ (5.12)	223
5.7.9 Preparation of Rh ₂ (tfepma) ₂ (μ- <i>p</i> -MeO-C ₆ H ₄ NC)Cl ₄ (5.13)	223
5.7.10 Crystallographic Details	223
5.7.11 Toepler pump measurements	224
5.7.12 Photolysis of 5.7 and 5.6	224
5.7.13 Spectral Fitting to Obtain Concentration Plots for Photolysis of 5.6 and 5.7	224
5.7.14 Determination of Quantum Yields	225
5.7.15 Time Resolved Photochemical Experiments General Considerations	226
5.7.16 Computational Details	227
5.8 Crystallographic Tables and Calculated Cartesian Coordinate Tables	229
5.9 References	236
Biographical Note	239
Acknowledgements	241

List of Figures

Chapter 1:

- Figure 1.1.** Total worldwide CO₂ emissions attributed to energy consumption between 1980 and 2010 showing approximately a 67% increase over the 30 year period. 27
- Figure 1.2.** Latimer diagram (adapted from reference 25) for water oxidation, illustrating the thermodynamic potentials for electrochemical steps in 1-electron, 2-electron and 4-electron steps at pH=7. Potentials exceeding the thermodynamic value for overall water oxidation are shown in red. 32
- Figure 1.3** Molecular orbital splitting diagram for O₂²⁻. (Left) without s-p mixing. (Right) with s-p mixing. The primary orbitals contributing to the O–O bond are shown in red. 33
- Figure 1.4.** General classes of mechanisms resulting in O–O bond formation. 34
- Figure 1.5.** Experimentally determined metal-oxidic cluster responsible for water oxidation within photosystem II (adapted from reference 28). 35
- Figure 1.6. (A)** Depiction and orientation of an isolated metal–oxo moiety. **(B)** Depiction of d-orbital splitting diagram resulting from an isolated metal oxo fragment. **(C)** Orbital interactions resulting in the three bonding interactions between a transition metal and a terminal oxo ligand. 38
- Figure 1.7. (A)** Example of a pseudo-tetrahedral Fe(IV) terminal nitride complex (adapted from reference 59) **(B)** Experimentally determined *d* orbital splitting diagram and ground state electronic structure for pseudo-tetrahedral Fe(IV) nitrido complexes. 39
- Figure 1.8.** Correlation diagram for *d* orbital splitting diagrams for terminal metal oxo complexes in tetragonal, trigonal bipyramidal and pseudo-tetrahedral geometries. The orbital ordering for the tetragonal and trigonal bipyramidal metal oxo complexes are experimentally determined. The orbital ordering for the pseud-tetrahedral metal oxo complex is a reproduction of the experimentally determined ordering found for pseudo-tetrahedral high valent iron nitrido complexes 40
- Figure 1.9.** General scheme for a multicomponent system for photocatalytic proton reduction. D = sacrificial electron donor; PS = photosensitizer; M= electron transfer mediator; cat = proton reduction catalyst. 45
- Figure 1.10.** Generalized scheme for multicomponent system for photocatalytic HX splitting created by replacing the sacrificial donor in a multicomponent photocatalytic proton reduction system with a multicomponent photocatalytic halide oxidation system utilizing a common photosensitizer. PS = photosensitizer; M = electron transfer mediator for proton reduction; cat = proton reduction catalyst; M' = electron transfer mediator for halide oxidation; cat' = halide oxidation catalyst. 46
- Figure 1.11.** Simplified system for light absorption, proton reduction, and halide oxidation occurring at a single catalyst complex. 46
- Figure 1.12.** The complex [Rh₂(bridge)₄]¹²⁺ reacts thermally with excess HCl to generate one equivalent of H₂ along with the dimeric species [Rh₂(bridge)₄Cl]₂⁺⁴. Photolysis of [Rh₂(bridge)₄Cl]₂⁺⁴ with visible light results in photoreduction of an additional equivalent of H₂ along with formation of the inert complex [Rh₂(bridge)₄Cl₂]⁺². 48

Figure 1.13. Photolysis of $\text{Mo}_2\text{Cl}_6(\text{dtbppm})_2$, dtbppm = bis(di-4-*tert*-butylphenyl)phosphinomethane, with UV light in THF in the presence of excess lutidine results in formal homolysis of a Mo–Cl bond and generation of two equivalents of Cl^\bullet radical. The Cl^\bullet radicals abstract hydrogen atoms from THF to form HCl which is trapped by the excess lutidine. 48

Figure 1.14. (Left) General depiction of the asymmetric distribution of π electron density promoted by phosphazane ligands which has been shown to stabilize mixed valent electronic structures in bimetallic complexes. (Right) Proposed catalytic cycle for the photocatalytic HX splitting initiated by photolysis of $\text{Rh}_2(\text{dfpma})_3(\text{CO})$, dfpma = *bis*-(difluorophosphino)methane, determined by the thermal and photochemical studies of model compounds. 50

Figure 1.15 Generalized structure for second generation HX splitting photocatalyst. R= $\text{CF}_3\text{CH}_2\text{O}-$, L = adamantly isocyanide or *tert*-butyl isocyanide. 51

Chapter 2:

Figure 2.1. Generalized depiction of the synthetic strategy for interrogation of homogeneous low coordinate metal oxo complexes. 61

Figure 2.2. Relationship between steric bulk of alkoxide and structure of metal–alkoxide complexes. Sterically crowded alkoxides (left) are unable to form tris(alkoxide) complexes. Smaller alkoxides (right) promote multimetallic species via a bridging bonding motif. Structure of metal alkoxide complexes supported by alkoxides of intermediate steric bulk (center) have been under explored. 63

Figure 2.3. Crystal structure of Kditox. 50% thermal ellipsoid probability density. Hydrogen atoms are omitted for clarity. 64

Figure 2.4. Single crystal x-ray diffraction structures for the series of divalent metal compound $[\text{M}(\text{ditox})_3][\text{K}(\text{15C5})_2]$ for (A) Cr, (B) Mn, (C) Fe, (D) Co and (E) Ni. Thermal ellipsoids presented at 50% probability density. Hydrogen atoms and $[\text{K}(\text{15C5})_2]$ cation omitted from all structures for clarity. 69

Figure 2.5. Qualitative d-orbital splitting for divalent metal-tris(alkoxide) complexes. (Center) Idealized D_{3h} geometries found for compounds **5.2** and **5.3**. (Left) Red lines indicate bond lengths shortening. Geometry based on structure of compound **5.1**. (Right) Blue line indicates a bond length elongating. Geometry based on structure of **5.4**. 70

Figure 2.6. Single crystal x-ray diffraction structures for the series of trivalent metal compounds $\text{M}(\text{ditox})_3$ for (A) V, (B) Cr, and (C) Fe. $\text{V}(\text{ditox})_3$ and $\text{Fe}(\text{ditox})_3$ are found to crystallize with a bound apical THF molecule. Thermal ellipsoids presented at 50% probability density. Hydrogen atoms are omitted from all structures for clarity 73

Figure 2.7. Infrared spectrum of $[\text{Ni}(\text{ditox})_3][\text{K}(\text{15C5})_2]$ depicted this common bands of vibrational stretching frequencies in the $[\text{M}(\text{ditox})_3][\text{K}(\text{15C5})_2]$ series of complexes. Regions A–D are assigned to $\nu(\text{MO}-\text{R})$ vibrational frequencies which couple with internal ligand $\nu(\text{C}-\text{C})$ vibrational frequencies. Region E is assigned to the $\nu(\text{M}-\text{O}_{alk})$ vibrational frequencies. As summary of the observed peaks within the 1200 cm^{-1} to 500 cm^{-1} range for compounds **2.1–2.5** can be found in Table 2.4. 76

Figure 2.8. Overlay of the normalized transmittance infrared spectra of divalent compounds **2.1–2.5** showing the similarity of the vibrational frequencies throughout the series of complexes, suggesting isomorphous structures and similar bonding interactions. (red) $[\text{Cr}(\text{ditox})_3][\text{K}(\text{15C5})_2]$, (orange) $[\text{Mn}(\text{ditox})_3][\text{K}(\text{15C5})_2]$, (green) $[\text{Fe}(\text{ditox})_3][\text{K}(\text{15C5})_2]$, (blue) $[\text{Co}(\text{ditox})_3][\text{K}(\text{15C5})_2]$, (purple) $[\text{Ni}(\text{ditox})_3][\text{K}(\text{15C5})_2]$. 78

- Figure 2.9.** Overlay of the normalized transmittance infrared spectra of trivalent compounds **2.6–2.9** showing the similarity of the vibrational frequencies throughout the series of complexes, suggesting isomorphous structures and similar bonding interactions. (red) V(ditox)₃THF, (green) Cr(ditox)₃, (blue) Fe(ditox)₃THF, (purple) Co(ditox)₃ 79
- Figure 2.10.** Electronic absorption spectrum of a tetrahydrofuran solution of [Fe(ditox)₃][K(15C5)₂] (**2.3**) depicting the two major features in the electronic absorption spectra of tris(ditox) compounds **2.1–2.9**: an intense ligand to metal charge transfer (LMCT) feature in the ultra-violet range and a broad and weakly absorbing *d-d* transition in the visible range. 80
- Chapter 3:**
- Figure 3.1.** Generalized *d* orbital splitting diagram for *d*² metal oxo complexes stabilized by tetragonal ancillary ligand fields. The low spin configuration (Left) formally features a triple bond between the metal and oxygen atom, thus rendering the metal oxo moiety electrophilic. The high spin configuration (Right) features a metal oxo bond order of 2.5 with radical character on the metal–oxo moiety. 106
- Figure 3.2.** Single crystal x-ray diffraction structures for V(ditox)₃(O), **3.4.** Thermal ellipsoids presented at 50% probability density. Hydrogen atoms omitted for clarity. 110
- Figure 3.3.** Single crystal x-ray diffraction structures for Cr(ditox)₃(O), **3.5.** Thermal ellipsoids presented at 50% probability density. Hydrogen atoms omitted for clarity. 112
- Figure 3.4.** Single crystal x-ray diffraction structures for [Cr(ditox)₃(O)][CoCp₂], **3.5.** Thermal ellipsoids presented at 50% probability density. Hydrogen atoms and [CoCp₂]⁺ omitted for clarity. 113
- Figure 3.5.** Single crystal x-ray diffraction structures for Cr(ditox)₃(O)K(Et₂O)₃, **3.6.** Thermal ellipsoids presented at 50% probability density. Hydrogen atoms omitted for clarity. 114
- Figure 3.6.** IR spectrum for **3.4**, V(ditox)₃(O), from 1200 cm⁻¹ to 500 cm⁻¹. The ν(V–O_{oxo}) vibration is labeled and is assigned to a peak at 981 cm⁻¹. Vibrations corresponding to ν(V–O_{alk}) are assigned at 735 cm⁻¹, 601 cm⁻¹, and 548 cm⁻¹. 115
- Figure 3.7.** IR spectra for ¹⁶O (red, natural abundance), ¹⁷O (green, 50% labeled) and ¹⁸O (blue, 70% labeled) isotopically labeled variant of **3.5**, Cr(ditox)₃(O). The ν(Cr–O_{oxo}) vibration is assigned to 946 cm⁻¹ for ¹⁶O-**3.5**, 925 cm⁻¹ for ¹⁷O-**3.5**, and 905 cm⁻¹ for ¹⁸O-**3.5**. 116
- Figure 3.8.** IR spectra for ¹⁶O (red, natural abundance), ¹⁷O (green, 50% labeled) and ¹⁸O (blue, 70% labeled) isotopically labeled variant of **3.6**, [Cr(ditox)₃(O)][CoCp₂]. The ν(Cr–O_{oxo}) vibration is assigned to 870 cm⁻¹ for ¹⁶O-**3.6**, ~850 cm⁻¹ for ¹⁷O-**3.6**, and 825 cm⁻¹ for ¹⁸O-**3.6**. 117
- Figure 3.9.** Generalized *d* orbital splitting diagram for pseudo-tetrahedral metal-oxo derived from experimental observations. 118
- Figure 3.10.** The computed d-orbital manifold for **3.A**, Cr(O^tBu)₃(O), derived from DFT calculations. Depictions of molecular orbitals presented with an isovalue of 0.04. 119
- Figure 3.11.** Single crystal x-ray diffraction structures for Cr(ditox)₃(OSnBu₃), **3.8.** Thermal ellipsoids presented at 50% probability density. Hydrogen atoms omitted for clarity. 122
- Figure 3.12.** Single crystal x-ray diffraction structures for Cr(ditox)₃(O^tBu), **3.9.** Thermal ellipsoids presented at 50% probability density. Hydrogen atoms omitted for clarity. 123

- Figure 3.13.** Single crystal x-ray diffraction structures for $\text{Cr}(\text{ditox})_3(\text{OTMS})$, **3.10**. Thermal ellipsoids presented at 50% probability density. Hydrogen atoms omitted for clarity. 123
- Figure 3.14.** Single crystal x-ray diffraction structures for $[\text{Cr}(\text{ditox})_2(\text{O})]_2$, **3.11**. Thermal ellipsoids presented at 50% probability density. Hydrogen atoms omitted for clarity. 124
- Figure 3.15.** Cycle for metal catalyzed oxidation of S^{-2} and reduction of S_8 showing the possible requirement for the metal to access a range of 4 oxidation states. 126
- Figure 3.16. (A)** Crystal structure of **3.12**, $[\text{Cr}(\text{ditox})_3(\text{S})][\text{K}(\text{15C5})_2]$. Thermal ellipsoids are presented at 50% probability density. Hydrogen atoms and $[\text{K}(\text{15C5})_2]^+$ cation omitted for clarity.. Structure is incompletely refined, but shows a terminal Cr–S bond distance of 2.09 Å. **(B)** Crystal structure of **3.13**, $[\text{Cr}(\text{ditox})_3(\text{S})\text{Ag}]_3$. Thermal ellipsoids presented at 50% probability density. Hydrogen atoms omitted for clarity. 128
- Figure 3.17.** Peak potential versus log (Scan Rate) plot for the electrochemical oxidation feature observed for **3.12**, $[\text{Cr}(\text{ditox})_3(\text{S})][\text{K}(\text{15C5})_2]$. The data is fit to a slope of 61 mV/dec which is indicative of rate limiting electron transfer from the electrode. 129
- Figure 3.18.** UV-vis spectra for the titration of $[\text{Cr}(\text{ditox})_3(\text{S})][\text{K}(\text{15C5})_2]$ with FcOTf: (red) 1.0 eq. FcOTf; (orange) 1.5 eq. FcOTf; (green) 2.0 eq. FcOTf; (blue) 2.2 eq. Fc OTf; (purple) 3.0 eq FcOTf. 130
- Figure 3.19** Computed frontier orbital diagram for calculated compound **3.D**, $\text{Cr}(\text{O}^t\text{Bu})_3(\text{O})$, derived from DFT calculations. Molecular orbital surfaces presented at an isovalue of 0.04. 132
- ## Chapter 4:
- Figure 4.1.** Preparative methods for trivalent and divalent iron tris(ditox) complexes. 163
- Figure 4.2 (A)** Crystal Structure of $\text{Fe}(\text{ditox})_3\text{Li}(\text{THF})$ (**4.3**), 50% probability ellipsoids. Hydrogen atoms omitted for clarity. **(B)** Crystal structure of $\text{Fe}(\text{ditox})_3\text{K}(\text{THF})_2$ (**4.4**), 50% probability ellipsoids. H atoms are omitted for clarity. 164
- Figure 4.3.** Reactivity of trigonal Fe(III) ditox compounds with oxo transfer reagents. 166
- Figure 4.4.** Crystal structure of $\text{Fe}(\text{ditox})_3(\text{ONMe}_3)$ (**4.6**), 50% probability ellipsoids. Hydrogen atoms omitted for clarity. 167
- Figure 4.5.** Crystal structure of $\text{Fe}(\text{ditox})_3(\text{OH})\text{Li}(\text{C}_8\text{O}_2\text{H}_{14})$, (**8**), 50% probability. H atoms and alternative conformations of ^tBu groups are omitted for clarity. 167
- Figure 4.6. (A)** Crystal structure of $\text{Fe}(\text{ditox})_3(\text{OH})\text{Li}(\text{THF})_3$, (**4.7**), 30% probability ellipsoids. H atoms, co-crystallized solvent molecules, and alternative conformations of ^tBu groups are omitted for clarity. **(B)** Crystal structure of $\text{Fe}(\text{ditox})_3(\text{OH})\text{Li}(\text{THF})_2$, (**4.7a**), 50% probability ellipsoids. H atoms, co-crystallized solvent molecules, and alternative conformations of ^tBu groups are omitted for clarity. **(C)** Structure $[\text{Fe}(\text{ditox})_3(\text{OH})\text{Li}]_2$, (**4.7b**), 30% probability ellipsoids. H atoms are omitted for clarity. 168
- Figure 4.7.** Structure $[\text{Fe}(\text{ditox})_3(\text{OH})][\text{K}(\text{15C5})_2]$, (**4.9**), 50% probability ellipsoids. H atoms are omitted for clarity. 170
- Figure 4.8.** Structure $[\text{Fe}(\text{ditox})_3(\text{CH}_2\text{CN})][\text{K}(\text{15C5})_2]$ (**4.10**), 50% probability ellipsoids. H atoms and $\text{K}(\text{15C5})_2$ are omitted for clarity. 172

- Figure 4.9.** Molecular orbital diagram the quintet ground state of $[\text{Fe}(\text{O}^t\text{Bu})_3(\text{O})]$ for the α orbitals shown with an isovalue of 0.4. 174
- Figure 4.10.** Optimized structures for the ground state geometry of $\text{Fe}(\text{O}^t\text{Bu})_3(\text{O})\text{Li}(\text{THF})$ and the corresponding transition state for hydrogen atom abstraction from α carbon of the coordinated THF. 176
- Figure 4.11.** Space filling models of **4.9** depicting the accessibility of an apical oxygen atom (red) in a pseudo-tetrahedral geometry. 178
- Chapter 5:**
- Figure 5.1.** UV-vis traces of a photolysis experiment monitoring the progression of the absorption feature of a solution of **5.1** with excess HCl under photolytic conditions. **(Left)** The early time points (0, 0.5, 1, 2, and 4 min) show the apparent buildup of product with isosbestic points at 323, 401 and 451 nm. **(Right)** The longer time points (4, 6, 8, 10, 88, 200 min) show an initial steady state regime between 6-10 min followed by degradation. 205
- Figure 5.2.** Turnover numbers (TON) of H_2 produced by 1 mM THF solution of $\text{Rh}_2^{0,\text{II}}(\text{tfepma})_2(\text{CN}^t\text{Bu})_2\text{Cl}_2$. Decomposition is observed with minimal additional hydrogen formation beyond 24 h. 206
- Figure 5.3. (A)** X-ray structure of $\text{Rh}_2^{\text{III,II}}(\text{tfepma})_2(\text{CNad})\text{Cl}_4$, **5.6.** Thermal ellipsoids presented at 50% probability. Hydrogen atoms, the $-\text{CH}_2\text{CF}_3$, and the adamantyl groups are omitted for clarity. **(B)** X-ray structure of $\text{Rh}_2^{\text{I,III}}(\text{tfepma})_2(\text{CNad})\text{Cl}_4$, **5.7.** Thermal ellipsoids presented at 50% probability. Hydrogen atoms, the $-\text{CH}_2\text{CF}_3$, and the adamantyl groups are omitted for clarity. 207
- Figure 5.4.** Spectral evolution of the photolysis of **5.6** (43 μM) in THF, using broad band light with $\lambda_{\text{exc}} > 305$ nm. Spectra were recorded every minute for a total of 20 min showing the conversion to **5.4**. 208
- Figure 5.5.** Spectral evolution for the photolysis of **5.5** in THF obtained after the addition of excess HCl to **5.4** (31 μM), using broad-band light with $\lambda_{\text{exc}} > 305$. (Left) Early time points 0, 40, 60, 90 sec and 2, 5, 10 and 15 min showing the buildup of **5.6**. (Right) Late time points 15, 20, 30, 60 and 120 min showing minimal degradation of reaction mixture. 208
- Figure 5.6.** Turnover numbers (TON) for H_2 production by a 1 mM THF solution of $\text{Rh}_2^{0,\text{II}}(\text{tfepma})_2(\text{CNad})_2\text{Cl}_2$, **5.4**, in photocatalytic conditions in the presence of excess HCl over time. 209
- Figure 5.7. (A)** Spectral evolution during photolysis of valence asymmetric $\text{Rh}_2^{\text{I,III}}\text{Cl}_4$ complex **5.7** in THF. Inset: Expanded spectrum to show that isosbestic points are not observed, consistent with evolution of a steady-state intermediate during the photolysis of **5.7**. **(B)** Concentration profiles of **5.7** (red circle), **5.6** (gray square) and **5.4** (blue triangle) during the photolysis of **5.7**. 211
- Figure 5.8. (A)** Spectral evolution during photolysis of valence symmetric $\text{Rh}_2^{\text{II,II}}\text{Cl}_4$ complex **5.6** in THF. Inset: Expanded spectrum to show that isosbestic points are observed, precluding a steady-state intermediate. **(B)** Concentration profiles of **5.7** (red circle), **5.6** (gray square) and **5.4** (blue triangle) during the photolysis of **5.6**. 212
- Figure 5.9 (A)** Transient absorption spectra obtained by laser flash photolysis ($\lambda_{\text{exc}} = 355$ nm) of complexes **5.7** (solid red) and **5.6** (solid black), respectively. Spectra are normalized to the absorbance at ~ 440 nm. Normalized absorption spectra of **5.7** (dashed red) and **5.6** (dashed black) are also shown. **(B)** Relevant oscillators (solid blue bars) from TD-DFT calculations for **5.6**, $\text{Rh}_2(\text{dfpma})_2(\text{CNMe})\text{Cl}_3$ with simulated absorption spectrum overlaid (solid red line) showing absorption feature at low energy (500 nm). 213

- Figure 5.10.** (A) Relevant oscillators (solid blue bars) from TD-DFT calculations for **5.A** with simulated absorption spectrum overlaid (solid red line). (B) Relevant oscillators (solid blue bars) from TD-DFT calculations for **5.B** with simulated absorption spectrum overlaid (solid red line). 214
- Figure 5.11.** TD-DFT calculations of model structures **5.A** (A) and **5.B** (B) indicate LMCT excited state in both complexes. Contributions of Rh-based and Cl-based orbitals are given for each individual MO. Contributions of each MO to the overall electronic transformation are given within parentheses 215
- Figure 5.12. (Top)** Synthesis of isocyanide-bridged (**5.10** and **5.11**) and chloride-bridged (**5.12** and **5.13**) dirhodium complexes, P-N-P = *bis*(trifluoroethoxy)phosphinyl)- methylamine (tfepma). (A) X-ray structure of $\text{Rh}_2^{\text{II}}(\text{tfepma})_2\text{-}\mu_2\text{-(CN-}p\text{-F-C}_6\text{H}_4\text{)Cl}_2$, **5.10**. Thermal ellipsoids presented at 50% probability. Hydrogen atoms, and the $\text{-CH}_2\text{CF}_3$ groups are omitted for clarity. (B) X-ray structure of $\text{Rh}_2^{\text{III}}(\text{tfepma})_2(\text{CN-}p\text{-F-C}_6\text{H}_4)(\mu_2\text{-Cl)Cl}_3$, **5.12**. Thermal ellipsoids presented at 50% probability. Hydrogen atoms, the $\text{-CH}_2\text{CF}_3$, and the aryl groups are omitted for clarity. 217
- Figure 5.13.** (A) Chloride-bridged dirhodium complex **5.12** undergoes photochemical, but not thermal, chlorine elimination to afford $\text{Rh}_2^{\text{II}}\text{Cl}_2$ complex **5.10**. (B) Spectral evolution during photolysis of chloride-bridged complex **5.12**. 218

List of Tables

Chapter 1:

Table 1.1. Gibbs Free Energy values for direct reduction of CO ₂ by H ₂ to yield single-carbon containing products.	29
Table 1.2. Gibbs Free Energy values for H ₂ generating transformations.	30
Table 1.3. Predicted Behavior for Metal–Oxo Complexes with d ⁰ -d ⁶ in different geometries and spin states based on electronic structure shown in Figure 1.8.	40

Chapter 2:

Table 2.1. Selected empirical bond distances for compounds 2.1-2.5 presented in angstroms with standard uncertainties in parenthesis.	68
Table 2.2. Selected empirical bond angles for compounds 2.1-2.5 with standard uncertainties in parenthesis.	68
Table 2.3. Magnetic susceptibilities determined via Evans method for compounds divalent and trivalent tris(ditox) complexes 2.1-2.9 in THF solution at room temperature.	75
Table 2.4. Summary of observed IR Frequencies (cm ⁻¹) for the series of divalent meta complexes [M(ditox) ₃][K(15C5) ₂].	77
Table 2.5. Summary of observed IR Stretches for the series of divalent meta complexes M(ditox) ₃ .	79
Table 2.6. Summary of UV-Vis Spectra Features for compounds 2.1-2.9 .	80
Table 2.7. Crystallographic data and structural refinement parameters for KOC ^t Bu ₂ Me (Kditox).	90
Table 2.8. Crystallographic data and structural refinement parameters for [Cr(ditox) ₃][K(15C5) ₂] (2.1).	91
Table 2.9. Crystallographic data and structural refinement parameters for [Mn(ditox) ₃][K(15C5) ₂] (2.2).	92
Table 2.10. Crystallographic data and structural refinement parameters for [Fe(ditox) ₃][K(15C5) ₂] (2.3).	93
Table 2.11. Crystallographic data and structural refinement parameters for [Co(ditox) ₃][K(15C5) ₂] (2.4).	94
Table 2.12. Crystallographic data and structural refinement parameters for [Ni(ditox) ₃][K(15C5) ₂] (2.5).	95
Table 2.13. Crystallographic data and structural refinement parameters for V(ditox) ₃ THF (2.6).	96
Table 2.14. Crystallographic data and structural refinement parameters for Cr(ditox) ₃ (2.7) and Cr(ditox) ₃ Cl.	97
Table 2.15. Crystallographic data and structural refinement parameters for Fe(ditox) ₃ THF (2.8).	98

Chapter 3:

Table 3.1. Crystallographic data and structural refinement parameters for $V(\text{ditox})_3(\text{O})$ (3.4).	141
Table 3.2. Crystallographic data and structural refinement parameters for $\text{Cr}(\text{ditox})_3(\text{O})$ (3.5).	142
Table 3.3. Crystallographic data and structural refinement parameters for $[\text{Cr}(\text{ditox})_3(\text{O})][\text{CoCp}_2]$ (3.6).	143
Table 3.4. Crystallographic data and structural refinement parameters for $\text{Cr}(\text{ditox})_3(\text{O})\text{K}(\text{Et}_2\text{O})_3$ (3.7).	144
Table 3.5. Crystallographic data and structural refinement parameters for $\text{Cr}(\text{ditox})_3(\text{OSnBu}_3)$ (3.8).	145
Table 3.6. Crystallographic data and structural refinement parameters for $\text{Cr}(\text{ditox})_3(\text{O}^t\text{Bu})$ (3.9).	146
Table 3.7. Crystallographic data and structural refinement parameters for $\text{Cr}(\text{ditox})_3(\text{OTMS})$ (3.10).	147
Table 3.8. Crystallographic data and structural refinement parameters for $[\text{Cr}(\text{ditox})_2(\text{O})]_2$ (3.11).	148
Table 3.9. Crystallographic data and structural refinement parameters for $[\text{Cr}(\text{ditox})_3(\text{S})\text{Ag}]_3$ (3.13).	149
Table 3.10. Cartesian coordinates for the DFT optimized geometry for the model of 3.A , $\text{Cr}(\text{O}^t\text{Bu})_3(\text{O})$.	150
Table 3.11. Cartesian coordinates for the DFT optimized geometry for the $S = 1$ model of 3.B , $[\text{Cr}(\text{O}^t\text{Bu})_3(\text{O})]^-$.	151
Table 3.12. Cartesian coordinates for the DFT optimized geometry for the $S=1$ model of 3.C , $[\text{Cr}(\text{O}^t\text{Bu})_3(\text{S})]^-$.	152
Table 3.13. Cartesian coordinates for the DFT optimized geometry for the model of 3.D , $\text{Cr}(\text{O}^t\text{Bu})_3(\text{S})$.	153

Chapter 4:

Table 4.1. Calculated multiplicities, selected parameters and relative energies referenced to quintet state respectively for $[\text{Fe}(\text{O}^t\text{Bu})_3(\text{O})]^-$ (4.A) and $[\text{Fe}(\text{O}^t\text{Bu})_3(\text{O})\text{Li}]$ (4.B).	173
Table 4.2 Calculated atomic orbital composition of frontier molecule orbitals for 4.A , $[\text{Fe}(\text{O}^t\text{Bu})_3(\text{O})]^-$	174
Table 4.3. Calculated atomic orbital composition of frontier molecule orbitals for 4.B , $\text{Fe}(\text{O}^t\text{Bu})_3(\text{O})\text{Li}$.	175
Table 4.4. Crystallographic data and structural refinement parameters for $\text{Fe}(\text{ditox})_3\text{Li}(\text{THF})$ (4.3).	186
Table 4.5. Crystallographic data and structural refinement parameters for $\text{Fe}(\text{ditox})_3\text{K}(\text{THF})_2$ (4.4).	187
Table 4.6. Crystallographic data and structural refinement parameters for $\text{Fe}(\text{ditox})_3(\text{ONMe}_3)$ (4.6).	188
Table 4.7. Crystallographic data and structural refinement parameters for $\text{Fe}(\text{ditox})_3(\text{OH})\text{Li}(\text{THF})_3$ (4.7).	189
Table 4.8. Crystallographic data and structural refinement parameters for $\text{Fe}(\text{ditox})_3(\text{OH})\text{Li}(\text{THF})_2$ (4.7a).	190
Table 4.9. Crystallographic data and structural refinement parameters for $[\text{Fe}(\text{ditox})_3(\text{OH})\text{Li}]_2$ (4.7b).	191
Table 4.10. Crystallographic data and structural refinement parameters for $\text{Fe}(\text{ditox})_3(\text{OH})\text{Li}(\text{THF})_2$ (4.8).	192

Table 4.11. Crystallographic data and structural refinement parameters for [Fe(ditox) ₃ (OH)][K(15C5) ₂] (4.9).	193
Table 4.12. Crystallographic data and structural refinement parameters for [Fe(ditox) ₃ (CH ₂ CN)][K(15C5) ₂] (4.10).	194
Table 4.13. Cartesian coordinates for the DFT optimized geometry for the S = 2 model of [Fe(O ^t Bu) ₃ (O)] ⁻ (4.B).	195
Chapter 5:	
Table 5.1. Gibbs Free Energy for HX splitting reactions (X=F, OH, Cl, Br, I).	202
Table 5.2. Crystallographic data and structural refinement parameters for Rh ₂ ^{II,II} (tfepma) ₂ (CNAd) ₂ Cl ₄ (5.6).	229
Table 5.3. Crystallographic data and structural refinement parameters for Rh ₂ ^{I,III} (tfepma) ₂ (CNAd) ₂ Cl ₄ (5.7).	230
Table 5.4. Crystallographic data and structural refinement parameters for Rh ₂ ^{I,I} (tfepma) ₂ (μ- <i>p</i> -F-C ₆ H ₄ NC)Cl ₂ (5.10).	231
Table 5.5. Crystallographic data and structural refinement parameters for Rh ₂ ^{II,II} (tfepma) ₂ (μ- <i>p</i> -F-C ₆ H ₄ NC)Cl ₄ (5.12).	232
Table 5.6. Cartesian coordinates for the geometry optimized structure of Rh ₂ ^{I,III} (dfpma) ₂ (MeCN) ₂ Cl ₄ (5.A).	233
Table 5.7. Cartesian coordinates for the geometry optimized structure of Rh ₂ ^{II,II} (dfpma) ₂ (MeCN) ₂ Cl ₄ (5.B).	234
Table 5.8. Cartesian coordinates for the geometry optimized structure of Rh ₂ (dfpma) ₂ (MeCN)Cl ₄ (5.C).	235

List of Schemes

Chapter 2:

- Scheme 2.1.** Synthesis of ditox ligand. 63
- Scheme 2.2.** Synthesis of divalent metal-tris(ditox) complexes. 65
- Scheme 2.3.** Synthesis of trivalent metal-tris(ditox) complexes. 66

Chapter 3:

- Scheme 3.1.** Mechanism for (porphinato)Cr^V(O) olefin epoxidation. 107
- Scheme 3.2.** Synthesis of d^0 - d^2 tris(ditox) metal oxo complexes. 108
- Scheme 3.3.** Reactivity of d^1 and d^2 tris(ditox) chromium oxo complexes. 121
- Scheme 3.4.** Proposed mechanism for Cr(ditox)₃(OH) decomposition. 125
- Scheme 3.5.** Proposed behavior of [Cr(ditox)₃(S)]⁻ in oxidizing conditions. 133

Chapter 4:

- Scheme 4.1.** Electrochemical behavior of divalent and trivalent iron-tris(ditox) complexes 164

Chapter 5:

- Scheme 5.1.** General HX splitting photocycle 204
- Scheme 5.2.** Quantum efficiencies for Rh₂^{I,III}Cl₄ and Rh₂^{II,II}Cl₄ photoreduction to Rh₂^{0,II}Cl₂. 212
- Scheme 5.3.** Mechanism for Rh₂^{I,III}Cl₄ and Rh₂^{II,II}Cl₄ photoreduction to Rh₂^{0,II}Cl₂. 216

CHAPTER 1

Homogeneous Systems Toward Renewable Energy Storage

1.1 The Need for Renewable Energy Storage

1.1.1 Global Energy Demands. The pursuit of clean and sustainable energy supplies for the global society is one of the most critical scientific challenges of the new century. Rates of worldwide energy consumption are enormous and continually increasing.¹⁻⁴ In 1980 the global energy consumption was reported to be 283 Quad BTU (7.07×10^{16} kcal), which corresponds to an average energy consumption rate of 9.39 terawatts (TW, TW equals 10^{12} watts, or 2.39×10^8 kcal per second).¹ In 2009, this rate drastically increased as worldwide energy consumption was reported to be 483 Quad BTU (1.24×10^{17} kcal), which corresponds to an average energy consumption rate of 16.2 TW.¹ This drastic increase is expected to continue and energy usage is expected double by 2050 and triple by 2100.²⁻⁴

The enhanced energy consumption rate represents an increase of 72.5% in the time period of nearly 30 years. One of the factors that has contributed to the increased global energy demand is a growing world population, which has increased from 4.5 billion people to 6.2 billion people between 1980 and 2001, and is projected to increase to 9.4 billion people by 2050.⁵ An additional concern is the quickly increasing gross domestic product (GDP) (11.0 trillion US dollars in 1980 versus 63.1 trillion US dollars in 2010), which corresponds to a greater energy demand.⁶ As population and GDP are not expected to decrease, we as a global society are forced to face the prospect of a continually increasing global energy demand. Assuming a constant rate of increase in energy consumption, it is predicted that in the year 2050 the global society will consume energy at a rate of approximately 30 TW, which corresponds to an additional energy requirement of over 15 TW.²

In order to supply the additional future energy demand, it is possible to utilize current and future supplies of fossil fuels; petroleum and natural gas. The World Energy Assessment Report estimates 50-150 years' worth of oil available.⁷ Additionally, there could be between 207-590 years of natural gas reserves globally, including methane clathrates in continental shelves.⁷ Furthermore, 1,000-2,000 years of coal, shale and tar sands are estimated to be available.⁷ As a result, the ability to sustain energy consumption rates around 30 TW is not a primary concern due to the abundant global reserves of fossil fuel resources. However, there is a debate as to whether or not we *should* use fossil fuels to fulfill our increasing energy demands due to potential harmful effects on the environment.⁸⁻¹⁰

Burning fossil fuels result in the formation of carbon dioxide (CO₂), which is released into the atmosphere.^{11,12} While the current and future effects of releasing CO₂ into the atmosphere are unknown, it is unequivocal that rates of CO₂ emissions are increasing as atmospheric CO₂ levels have increased from 315 parts per million (ppm) in 1960 to 400 ppm in 2010.^{11,12} Figure 1.1 shows the direct impact of CO₂ emissions from energy consumption processes as 18,500 million metric tons of CO₂ were released in 1980 which increased to 30,000 million metric tons released in 2009.^{11,12} The increased levels of atmospheric CO₂ can be correlated to potentially deleterious global trends, such as increased worldwide temperature.¹³ Utilization of fossil fuel reserves to meet the growing energy demands would necessitate increased rates of CO₂ emissions. Estimates predict that continuing increases in fossil fuel usage could result in atmospheric CO₂ levels being as high as 650 ppm by 2050.¹³

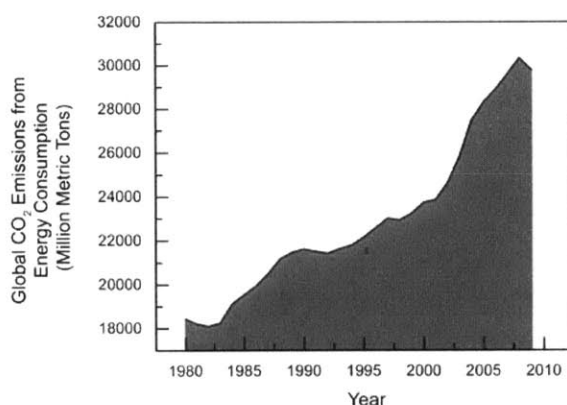


Figure 1.1. Total worldwide CO₂ emissions attributed to energy consumption between 1980 and 2010 showing approximately a 67% increase over the 30 year period.

In the absence of utilizing the vast reserves of fossil fuels or significant advances in atmospheric CO₂ sequestration, supplying the additional 15-20 TW needed globally by 2050 becomes a daunting proposition with limited possible solutions. Biomass represents a viable source of energy, however, the limited efficiency of photosynthesis along with the potentially diminishing availability of food resources for a growing population makes biomass limited in its practical utility.^{14,15} Nuclear fission is a possible source of energy, however, the intense energy cost of building nuclear power plants results in each facility running at an energy deficient for 35 years.^{2,16} Furthermore, modern technology allows for approximately 1 gigawatt of power to be

produced per nuclear power plant.² In order to meet the global energy demand exclusively via nuclear power, a new nuclear power plant would have to be built every 1.6 days for 45 years.²

Renewable energy sources such as solar, hydroelectric, and wind energy, theoretically represent an attractive source of energy in that they are abundant and carbon neutral. Solar energy alone has the capacity to meet the increased global energy demands.¹⁷⁻¹⁹ More solar energy contacts the surface of the earth in one hour (1.0×10^{17} kcal) than total energy is consumed by the global population in a year (9.8×10^{16} kcal in 2001).² Despite the overwhelming abundance of solar energy, less than 0.1% of electricity and less than 1.5% of fuels are derived from solar sources.^{2,20} The quantity of solar energy available makes renewable energy an ideal option to contribute greatly in fulfilling the global energy appetite.

There are several drawbacks to the pursuit of renewable energy sources as a major contributor to the global energy market. Economic drawbacks stem from current energy derived from renewable energy sources being quite expensive (approximately $\$0.35$ [kW hr]⁻¹) compared to energy derived from fossil fuels (approximately $\$0.05$ [kW hr]⁻¹).² It is difficult to expect widespread adoption of renewable energy sources in both impoverished areas of the world as well as regions that have a free market based economy.² There are practical concerns as well, primarily dealing with the availability of renewable energy sources. As an example, sunlight is diurnal and is subject to intermittency based on global positioning and atmospheric conditions.²⁰ Conversely, energy consumption worldwide is continuous throughout the day, if not higher during the night hours as more lights are powered. It seems unattractive to propose a scenario in which solar energy is directly converted to electrical energy for immediate consumption. Given the vast excess of renewable energy sources, one can envision capturing and storing renewable energy for later consumption. As such, new cost effect methods for renewable energy storage present a frontier in scientific and technological development.

1.1.2 Energy Storage in Chemical Bonds. There are many different strategies for energy storage ranging from the utilization of batteries (storing energy in chemical potential gradients), to mechanical methods (energy storage via pumping water uphill or by compressing air or in the rotational energy of flywheels), to magnetic methods (storing energy as unfavorable magnetic conformations within superconducting magnetic energy storage devices).²⁰ One drawback for all of these methods is that they possess poor energy density values (energy per mass or energy per volume) of between 10 and 100 Wh/kg.²⁰ Low energy density values typically correlate with

higher capex costs and energetic inputs to manufacture the devices, as well as large spatial footprints, making the energy sources unsuitable for transportation demands.²¹ A more appealing option for energy storage in terms of energy density is the usage of chemical fuels, which have energy densities between 1000 and 10,000 Wh/kg.²⁰

Chemical fuels can be an energy-dense and distributable solution for renewable energy storage. Fuels achieve high energy densities in comparison to other energy storage options through the storage of electrons in the small volume of a two-electron bond between light elements (i.e., C–H, N–H, and H–H bonds).²² In comparing the energy densities of fuels as a function of energy density by *mass* and energy density by *volume* for hydrocarbon fuels (C–H based), nitrogen-rich fuels (N–H based), and hydrogen (H₂), a few key points emerge: (1) hydrogen (H₂) has the largest energy density by mass (143 MJ kg) but suffers in volumetric energy density because it is as gas, (2) nitrogen-based fuels have modestly high energy content by mass and volume, and (3) hydrocarbon fuels provide the optimum energy supply in terms of volumetric energy density.²⁰ This latter point provides the basis for the choice of hydrocarbon fuels as the energy currency of modern society.²⁰ A shift in perspective must occur wherein our view of chemical fuels becomes one wherein they are thought of as a form of *energy storage* (derived from renewable energy sources) and thought of less as an *energy source* (derived from fossil fuel deposits).

Table 1.1 Gibbs Free Energy values for direct reduction of CO₂ by H₂ to yield single-carbon containing products.

Reaction	ΔG_f° (kcal/mol)
$\text{CO}_{2(g)} + \text{H}_{2(g)} \longrightarrow \text{CO}_{(g)} + \text{H}_2\text{O}_{(g)}$	6.8
$\text{CO}_{2(g)} + \text{H}_{2(g)} \longrightarrow \text{HCOOH}_{(l)}$	7.9
$\text{CO}_{2(g)} + 2\text{H}_{2(g)} \longrightarrow \text{HCHO}_{(g)} + \text{H}_2\text{O}_{(g)}$	15.1
$\text{CO}_{2(g)} + 3\text{H}_{2(g)} \longrightarrow \text{CH}_3\text{OH}_{(g)} + \text{H}_2\text{O}_{(g)}$	0.8
$\text{CO}_{2(g)} + 4\text{H}_{2(g)} \longrightarrow \text{CH}_4_{(g)} + 2\text{H}_2\text{O}_{(g)}$	-27.0

Because of the attractive energy density characteristics of hydrocarbon based fuels, methods of converting oxidized forms of carbon (CO₂) to reduced carbon products that can be used as fuels (methane, methanol, formaldehyde, or formic acid) have been targeted. The thermodynamic values for direct reduction of CO₂ by hydrogen to single-carbon containing products are outlined in Table 1.1.²³ The data in the table show that production of reduced carbon products from hydrogen and CO₂ does not afford viable energy storage pathways as the average

energy stored is approximately 10 kcal/mol for each 2-electron reduction.²³ In some cases, as in production of methane and methanol, the direct synthesis of reduced carbon products have been determined to be either a net energy lose or close to thermoneutral. Consequently, the direct production of reduced carbon products and other hydrocarbons themselves do not result in substantial *energy storage* options.

Production of H₂ through the splitting of H–X bonds, on the other hand, affords significant energy storage. Table 1.2 presents the thermodynamic values for various methods of synthesizing H₂.²² With the proper selection of the reactant, production of H₂ results in the storage of between 8 kcal/mol to over 130 kcal/mol for each 2-electron process. Thus, it is within the production of hydrogen where *energy is stored* and it is in the production of hydrocarbons where *hydrogen is stored*. As a result, efficient energy storage within chemical bond must begin with efficient reduction of protons (H⁺) to H₂ along with a corresponding oxidation half reaction. It should be noted that the in a thermodynamic sense, the oxidation half reaction is the primary source of energy storage, as the reduction potential of protons at pH=0 is set as 0 kcal/mol.²⁴

Table 1.2 Gibbs Free Energy values for H₂ generating transformations.

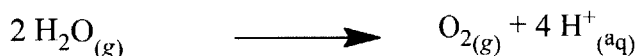
Reaction		ΔG_f° (kcal/mol)
2HF _(g)	→ H _{2(g)} + F _{2(g)}	130.5
H ₂ O _(g)	→ H _{2(g)} + 1/2O _{2(g)}	54.6
2HCl _(g)	→ H _{2(g)} + Cl _{2(g)}	45.5
2HBr _(g)	→ H _{2(g)} + Br _{2(l)}	25.5
H ₂ S _(g)	→ H _{2(g)} + 1/8S _{8(s)}	8.0
CO _(g) + H ₂ O _(g)	→ H _{2(g)} + CO _{2(g)}	6.8
2HI _(g)	→ H _{2(g)} + I _{2(s)}	-0.4

Production of H₂ can be separated into two half reactions. The cathodic half reaction involves the two electron reduction of protons to H₂ gas. At pH = 0, this half reaction has a Gibbs Free Energy value that is arbitrarily fixed to 0 kcal/mol. This presents the intriguing scenario wherein the amount of energy stored in production of hydrogen is primarily determined by the nature of the oxidation half reaction. Therefore, the choice of substrates as a precursor for H₂ production (water, hydrohalic acids, hydrogen sulfide, etc.) is vital. This evidenced by the wide range of values for energy storage found in Table 1.2. Challenges associated with the execution of the splitting of HX (H reduction and X oxidation) for each substrate must be

carefully considered and weighed against possible energy storage. As such, the anodic half reaction of two potential substrates for H₂ production (H₂O and hydrohalic acids) will be considered. Each substrate presents unique problems and questions that will be addressed through the use of homogeneous inorganic chemistry.

1.2 Water as a substrate: The Problem of the O–O Bond

1.2.1 Water Oxidation and the Oxygen Evolving Reaction. Water (H₂O) is considered the most ideal substrate for renewable energy storage by splitting it into H₂ and O₂ because H₂O is the product of aerobic H₂ fuel cell reactions. Thus, such fuel cells are generally considered to be environmentally benign. Using H₂O as a source of H₂ would afford a closed system for energy storage and energy release via an aerobic H₂ fuel cell. Additionally, the electrophilic nature of oxygen atoms afford a weak O–O bond in O₂ while simultaneously resulting in strong bonds to hydrogen.²⁴ Furthermore, the diradical nature of the ground state of O₂ provides a relatively inert molecule capable of storage and use as a fuel.²⁴ However, as simple and attractive as a closed cycle for energy storage and usage would be, it is not without complications arising from mediating the 4-electron/ 4-proton anodic half reaction of water oxidation:



Electrochemical analysis of the anodic half reaction provides thermodynamic parameters for the oxygen evolving reaction (OER) that highlight the poor efficiency of water oxidation. The Latimer diagram shown in Figure 1.2 summarizes the thermodynamic values for water oxidation at pH = 7 in steps that are primarily 1-electron/1-proton based, 2-electron/2-proton based, and a concerted 4-electron/4-proton step.²⁵ In Figure 1.2, transformations with an experimentally measured potential greater than that of overall water oxidation to O₂ are shown in red. As can be seen in Figure 1.2, conversion of H₂O to O₂ in 1-electron/1 proton steps or 2-electron/2 proton steps results in the generation of intermediate species of higher potential than O₂ itself.²⁵ Thus, in considering the energetics of possible intermediate compounds on a pathway toward water oxidation, even while ignoring the energetic penalties associated with transition states, intermediates are formed that have higher potential energies than O₂ causing unavoidable inefficiencies to the overall process. A purely 1-electron/1-proton mechanism results in about 1.5 V of excess thermodynamic driving force required for the formation of a HO• radical, whereas a 2-electron/2-proton mechanism to H₂O₂ results in about 0.5 V of additional thermodynamic

energy (versus the 0.815 V of stored energy) in order to generate an unstable hydrogen peroxide compound.²⁵

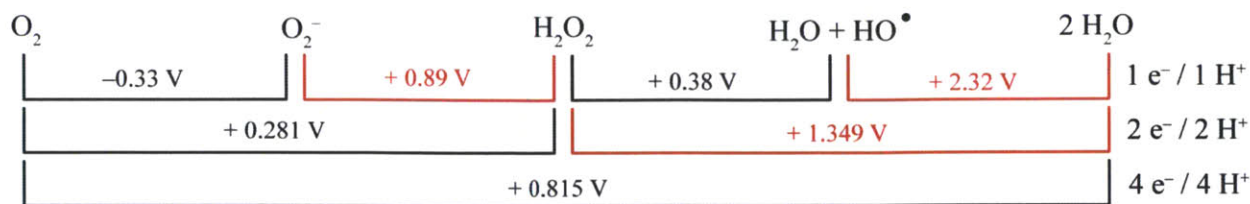


Figure 1.2. Latimer diagram (adapted from reference 25) for water oxidation, illustrating the thermodynamic potentials for electrochemical steps in 1-electron, 2-electron and 4-electron steps at pH = 7. Potentials exceeding the thermodynamic value for overall water oxidation are shown in red.

It should be noted that the formation of high energy intermediates are either within the initial O–O bond formation step itself or the energetic penalty is paid to generate a high energy species necessary for the formation of the first O–O bond.²⁵ In the 1-electron stepwise mechanism, it is the formation of the highly reactive HO• radical species, which is poised to further reaction with either H₂O or another equivalent of HO• to generate H₂O₂, which forms at 2.32 V.²⁵ In the 2-electron stepwise mechanism, it is the first 2-electron process in which 2 equivalents of H₂O are oxidized to H₂O₂ that requires over 1.0 V greater potential than the second 2-electron process to yield O₂.²⁵ Consequently, when considering a perfectly catalyzed water oxidation mechanism, where no additional activation energy is required, it is the inherent difficulty in generating the initial O–O bond that results in at least 0.5 V of additional energy. As such, efficient formation of O–O bonds along with stabilization of the resulting peroxy intermediate, or its avoidance, is essential to designing thermodynamically efficient water oxidation catalysts. Furthermore, water oxidation processes typically involve even greater overpotentials in order to generate O₂, which is due to additional parameters such as Coulombic repulsion, diffusion entropy, reorganization energy and local concentration effects. These challenges typically require a catalyst to mediate the overall transformation and mitigate the kinetic demands. These issues together create an imperative to develop efficient water oxidation catalysts.

The OER is particularly challenging as it must involve the transient formation of an unstable O–O single bond. Compounds with peroxy moieties typically have a bond dissociation energy around 50 kcal/mol, compared to 118 kcal/mol for the double bond of O₂, and for this reason they are difficult to stabilize. The extreme weak and reactive nature of the O–O σ bond is

commonly attributed to Pauli repulsion forces between the two oxygen atoms resulting in a bond distance that is too long for efficient orbital overlap between the two σ orbitals of the oxygen atoms.²⁶ The instability of the bond can also be explained via s-p molecular orbital mixing within the O_2^{2-} diatomic framework (Figure 1.3). A generalized molecular orbital diagram for the 14 electron diatomic O_2^{2-} molecule with s-p molecular orbital mixing and without s-p molecular orbital mixing are shown to the left and right of Figure 1.3 respectively. As O_2^{2-} is a 14 electron compound, only the $2\sigma^*(p)$ orbital remains unoccupied.

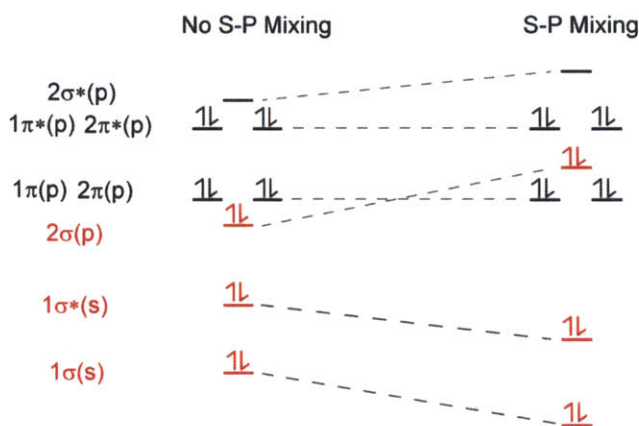


Figure 1.3 Molecular orbital splitting diagram for O_2^{2-} . (Left) without s-p mixing. (Right) with s-p mixing. The primary orbitals contributing to the O–O bond are shown in red.

The strength of the bond between the two oxygen atoms will not be affected greatly by the nature of the $1\pi(p)$ orbitals or the $2\pi(p)$ orbitals as both the bonding and antibonding orbital combinations are occupied. The orbitals with the most significant contribution to strength and stability of the bond are the $1\sigma(s)$, $1\sigma^*(s)$ and $2\sigma(p)$ orbitals, which is shown in red in Figure 1.3. Relative to carbon and nitrogen, the oxygen diatomic has a thermodynamically weaker single bond. One key difference between oxygen and lighter elements of the same row in the periodic table is that oxygen has significantly less s-p molecular orbital mixing which is a contributing factor to the weak O–O bond. In the extreme of significant s-p mixing (Figure 1.3, right) the $1\sigma(s)$ and $2\sigma(p)$ orbitals mix and the $1\sigma^*(s)$ and $2\sigma^*(p)$ mix greatly. As the $1\sigma(s)$ and $2\sigma(p)$ are fully occupied in a 14 electron diatomic molecule, the energetic effects of this mixing are negated. Alternatively, the mixing of the $1\sigma^*(s)$ and $2\sigma^*(p)$ does have an effect on the bonding as only the $1\sigma^*(s)$ is occupied. Since s-p mixing results in stabilization of the $1\sigma^*(s)$ orbital, the

resulting bonding interaction between the atoms is also stabilized. Thus, s-p mixing has an overall stabilizing effect on a diatomic molecule. Single bonds of atoms lighter than oxygen are thus further stabilized due to s-p mixing. However, the oxygen diatomic molecule is known to be a poor example of s-p molecular orbital mixing. The orbital ordering of O_2^{2-} is qualitatively similar to the left of Figure 1.3 and no stabilization occurs due to s-p mixing. Consequently, the weak nature of the O–O single bond relative to light atoms, such as carbon and nitrogen, can be further explained by the less significant s-p orbital mixing found for oxygen atoms. The analysis of the importance of s-p mixing correlating to a stronger single bond for diatomic molecules is an extension of the justification for the observed Be–Be bond of Be_2 found in the gas phase.^{27,28}

For oxygen, the result of electrostatic repulsion between oxygen atoms as well as the poor s-p mixing of the molecular orbitals of the O_2^{2-} diatomic cause the O–O single bond to be weak and reactive. For this reason, mechanisms by which O–O bonds form will be considered in more detail as understanding these transformations is of paramount importance to the transient generation and stabilization of O–O bonds necessary for water oxidation to O_2 .

1.2.2 O–O Bond Formation Mechanisms. As the initial O–O bond formation step is critical to the OER, it is important to introduce the two different general mechanisms of O–O bond formation to guide further discussions.^{29,30}

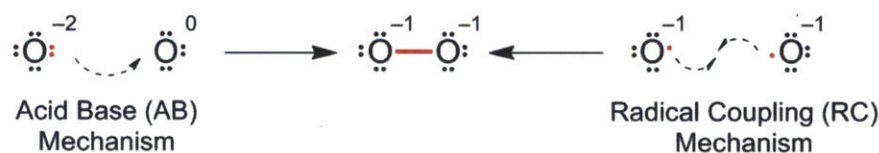


Figure 1.4 General classes of mechanisms resulting in O–O bond formation.

The left side of Figure 1.4 shows the Acid Base (AB) Mechanism. This mechanism involves both electrons that form the O–O bond originating from the same oxygen atom by performing a nucleophilic attack by one oxygen atom on a second electrophilic oxygen atom. Figure 1.4 depicts the AB mechanism in a limiting case in which one oxygen atom is formally reduced by two electrons, possessing a -2 charge, while the other oxygen atom is formally neutral. It is important to note that this limiting scenario need not be the case. More generally, the only requirement for an AB mechanism is that one oxygen atom is susceptible to a nucleophilic attack by another oxygen atom. An electrophilic oxygen atom only needs to have

unoccupied frontier orbitals that are thermodynamically accessible to the nucleophile. Thus, the important principle for the AB mechanism is that a *nucleophilic* oxygen atom is generated in proximity to an *electrophilic* oxygen atom that is susceptible to nucleophilic attack.^{29,30}

The right side of Figure 1.4 depicts the Radical Coupling (RC) Mechanism. The RC mechanism involves each oxygen atom contributing one electron to the two electron O–O bond. Again, Figure 1.4 shows a limiting case for the RC mechanism wherein both oxygen atoms are formally reduced by one electron, possessing a -1 charge, and the lone unpaired electron of each atom couple to one another to form the O–O bond. In general, the defining characteristic of the RC mechanism is that two oxygen atoms possess unpaired spin density that couple to form the two electron bond. The key criterion for the RC mechanism is that two oxygen atoms have unpaired spin density at the appropriate thermodynamic potentials.^{29,30}

1.2.3 OER Catalysts. Despite the many challenges to the OER, nature has developed a catalyst within photosystem II capable of catalyzing water oxidation for energy storage. The active site within the photosystem II is comprised of a $\text{Mn}_4\text{O}_5\text{Ca}$ cluster known as the oxygen evolving complex (OEC). Umena and coworkers have recently obtained crystallographic data supporting that the structure of the OEC within photosystem II is comprised of an open structure for the Mn_4O_5 redox active portion of the cluster with the Ca atom coordinating three of the bridging oxygen atoms.³¹ This structure is reproduced in Figure 1.5.

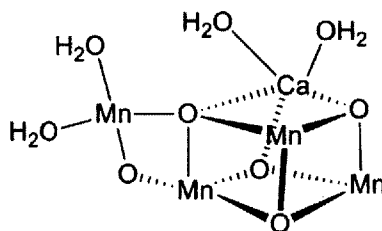


Figure 1.5 Experimentally determined metal oxidic cluster responsible for water oxidation within photosystem II (adapted from reference 28).

Extensive mechanistic studies have determined that the OEC operates through the five state Kok cycle with sequential oxidation events typically coupled to proton loss.³² However, the precise nature of oxidation events (metal based, localized, delocalized, etc.) and the proton loss events (from coordinated water molecules on Mn or Ca, or bridging hydroxyl ligands) remain unknown.^{33,34} As such, the mechanism of O–O bond formation is still debated and several

proposals exist.^{33,34} Two favored mechanisms involve a hydroxide attack on a high valent terminal Mn–oxo moiety that is templated by the Ca cation (AB mechanism) or the coupling of a high valent terminal Mn–oxo with a bridging oxo (RC mechanism).^{35–38} While chemically very different, both mechanisms for O–O bond formation identify a *high valent terminal metal oxo moiety* as the reactive intermediate, as it either is susceptible to nucleophilic attack or acts as one half of a radical coupling reactant.

Heterogeneous catalysts for water oxidation display many of the same general features as the OEC of photosystem II. Metal oxide materials, such as NiO₂,^{39,40} Co₃O₄,^{41,42} PtO₂,⁴³ RuO₂,⁴⁴ IrO₂,⁴⁵ and MnO₂³⁴ are found to electrochemically oxidize water with modest overpotentials (between 0.1 V and 0.4 V, current = 0.1 mA/cm). The most efficient of these materials, such as PtO₂, IrO₂, and RuO₂, require utilizing expensive and rare noble metals and thus are not practical candidates for large scale utility. Like the OEC of photosystem II, these materials are comprised of fundamental [M₂O₂] moieties supported in oxygen rich ligand environments. Due to intrinsic difficulties of studying discrete chemical steps on an extended heterogeneous surface, the precise nature of the O–O bond formation step of these heterogeneous catalyst are also unknown. Although, much like that which is proposed for the OEC, high valent terminal metal oxo species are thought to be active in the O–O bond formation.

Homogeneous systems afford the ability to probe the mechanistic questions associated with O–O bond formation, especially when the homogenous molecules are reminiscent of the catalytically relevant species of known water oxidation catalysts.^{46–48} The most thoroughly studied homogenous system for water oxidation is Meyer’s ruthenium “blue dimer”, [Ru(bpy)₂(H₂O)(μ-O)Ru(bpy)₂(H₂O)]⁴⁺ (bpy = 2,2-bipyridine), which has been postulated to form a Ru(V)–O prior to the O–O bond formation step.^{49,50} Whereas the electrochemical profile of this system has been mapped out, the high activity of the catalyst, in correlation with low stability (10 turnover numbers), have precluded definitive assignment of the mechanism of activity for [Ru(bpy)₂(H₂O)(μ-O)Ru(bpy)₂(H₂O)]⁴⁺ as well as similar ruthenium polypyridyl compounds.^{51–55} A separate class of homogeneous oxygen evolving catalysts that is more biologically inspired involves bimetallic manganese complexes and is hallmarked by the compound [Mn(trpy)(H₂O)(μ-O)₂Mn(trpy)(H₂O)]³⁺ (trpy = 2,2′6′,2′′-terpyridine).^{56,57} In a similar manner to other ruthenium polypyridal systems, the proposed mechanism for oxygen evolution from polypyridyl bimetallic manganese compounds includes a terminal Mn(V)–O

moiety that is necessary for O–O bond formation. Monometallic species have also been reported to generate O₂ from water, with these compounds invoking terminal metal oxo intermediates within proposed mechanisms.⁴¹

Despite a plethora of mechanistic studies towards homogenous catalysis for water oxidation, direct interrogation of the nature of the O–O bond formation process remains elusive. Drawbacks to these systems include that they are quite active, so isolation of intermediates is difficult, and they are not exceptionally stable with turnover numbers often below 10. However, throughout the interrogations of all water oxidation catalysts (the OEC of photosystem II, metal-oxide surfaces, and homogenous systems) the importance of high valent metal oxo moieties for the O–O bond formation process is unequivocal. Metal oxo bonds are highly variable and depending on the electronic structure of the entire compound, they can be either nucleophilic or electrophilic, and may or may not possess radical electron density. The subsequent section will discuss the nature of high valent metal oxo moieties, the importance of the ancillary ligand field supporting the metal oxo and reactivity patterns expected based on the bonding motif between the metal and the oxo ligand.

1.2.4 Ancillary Ligand Effects for Metal oxos. The synthesis of metal oxo complexes and the study of the metal oxo multiple bonds has been a long studied area of research. Metal oxo complexes were so abundant through the late 1800's that Koppel and Goldman suggested a nomenclature scheme in 1903 wherein the dianionic oxo ligand be referred to as the “-yl” ion.⁵⁸ The -yl ions studied initially were aqueous ions. A cohesive description of the metal oxo bonding structure was presented by Ballhausen and Gray via the experimental and theoretical study of the vanadyl ion (VO²⁺_(aq)).^{59,60}

One of the outcomes of the work by Ballhausen and Gray was the notion that a terminal oxo (O²⁻) ligand has the ability to form three bonds with a metal center. As depicted in Figure 1.6, taking the z-axis as the metal oxo bonding vector, the *d*_{z²} orbital participates in σ-bonding while the *d*_{xz} and *d*_{yz} orbitals participate in respective π-bonding. In order to form a stable metal oxo bond, a bond order of 2 must remain between the metal and the oxo ligand. Thus, no more than 2 electrons are allowed to populate the *d*_{xz} and *d*_{yz} orbitals (π* orbitals). Depending on the ancillary ligand field, this allows between 2 and 6 *d* electrons to be present in a stable metal oxo complex. In a local tetragonal (C₄) environment, preservation of the oxo moiety is typically found with *d* electron counts of 4 or fewer. The first two electrons populate an essentially

nonbonding orbital, d_{xy} , and the subsequent addition of electrons populates the degenerate M–O π^* orbitals, d_{xz} and d_{yz} . This electronic structure is supported in the M–O bond distance of the d^1 complex $[(\text{HMPA-B})\text{Mn}^{\text{V}}(\text{O})]^-$ (HMPA-B: 1,2-bis(2-hydroxy-2-methylpropanamido)benzene) which is in agreement of a M–O triple bond,⁶¹ whereas the M–O bond distance of the d^1 ground state ($S = 1$) $[(\text{TMC})\text{Fe}^{\text{IV}}(\text{O})]^{2+}$ is consistent with a M–O double bond.⁶² Consequently, a bond order of less than 2 would afford a reactive metal oxo moiety that should be thermodynamically unstable, resulting in the now ubiquitous “oxo wall”.⁵³ If no d electrons were populating the d_{xz} and d_{yz} orbitals, the bond order of the metal oxo moiety would be 3, furnishing an electrophilic metal oxo fragment.

The Ballhausen and Gray bonding scheme for metal oxo complexes has been instrumental in guiding the discussions of synthetic metal oxo complexes and explaining the stability of the over 10,000 terminal oxo complexes listed in the Cambridge Structural Database (CSD).⁶³ However, despite the abundance of synthetic metal oxo complexes, there is an overwhelming propensity to utilize nitrogen donor ligands and ancillary ligand fields in tetragonal or trigonal bipyramidal geometries. This is evidenced in that of the 10,000 terminal oxo complexes in the CSD, only 8% of those structures involve a metal center with three or fewer ancillary ligands. Of these compounds, over half of the lower coordinate structures are of Group IV or Group V transition metals. This is indicative of there being relatively few examples of low coordinate late transition metal oxo complexes.

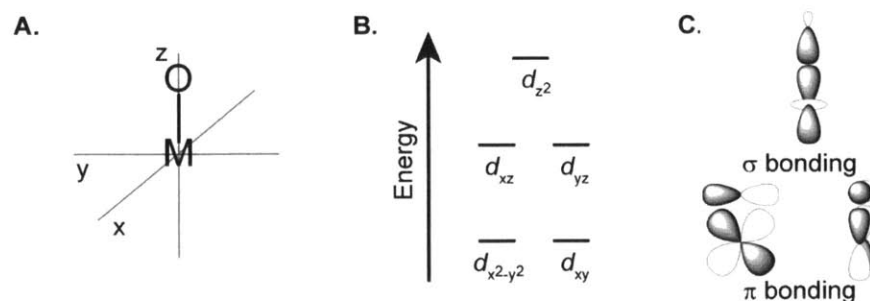


Figure 1.6. (A) Depiction and orientation of an isolated metal oxo moiety. (B) Depiction of d orbital splitting diagram resulting from an isolated metal oxo fragment. (C) Orbital interactions resulting in the three bonding interactions between a transition metal and a terminal oxo ligand.

In an attempt to understand the manner in which ancillary ligand types and geometries affect the bonding between transition metals and oxo ligands, and subsequent reactivity different

ligand archetypes should be explored. With metal–nitrogen multiple bonds, Peters and co-workers have explored the bonding structure between pseudo-tetrahedral (C_3) 3d transition metals and ligands such as nitriles and imidos.⁶⁴ They report an electronic structure for pseudo-tetrahedral metal-nitrogen multiply bonded species as shown in Figure 1.7. The first 4 electrons populate the non-bonding orbitals $d_{x^2-y^2}$ and d_{xy} with the σ^* (d_{z^2}) and π^* (d_{xz} and d_{yz}) orbitals lying close together in energy and destabilized to a much greater extent. Complexes with as many as 4 d electrons maintain a formal triple bond between the metal and the nitrido ligand. This is in contrast to tetragonal ancillary ligand fields where the bond order is observed to lower with the addition of the second or third electron.

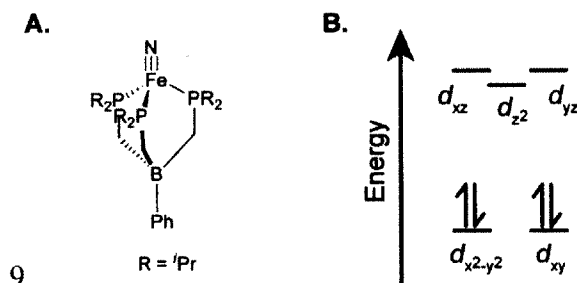


Figure 1.7 (A) Example of a pseudo-tetrahedral Fe(IV) terminal nitride complex (adapted from reference 58) (B) Experimentally determined d orbital splitting diagram and ground state electronic structure for pseudo-tetrahedral Fe(IV) nitrido complexes.

Taking the reported electronic structures of pseudo-tetrahedral metal-nitrido complexes as a benchmark, a correlation diagram for the electronic structure of metal oxo species in different geometries can be constructed as shown in Figure 1.8.^{29,30} The correlation diagram suggests significantly different criteria for stabilizing metal oxo complexes in different geometries and different reactivity is expected for metal oxo complexes of different d electron counts.^{29,30} For a tetragonal ancillary ligand field, stable metal oxo complexes are expected for d^0 - d^4 electron counts.^{29,30} Assuming low spin electronic structure, electrophilic behavior of the metal oxo complex is expected for d^0 - d^2 compounds.^{29,30} Radical reactivity can be expected for d^3 complexes.^{29,30} Nucleophilic reactivity is expected from d^4 species.^{29,30} Assuming low spin configurations, trigonal bipyramidal metal oxo complexes are expected to be stable with d electron counts between d^0 and d^2 .^{29,30} Electrophilic behavior is predicted for d^0 , radical behavior is predicted for d^1 , and nucleophilic behavior is predicted for d^2 .^{29,30}

The expectations are vastly different for low spin pseudo-tetrahedral metal oxo complexes. In this geometry, metal oxo compounds theoretically are stable with as many as 6 d electrons (d^0 - d^6).^{29,30} Electrophilic behavior of the metal oxo is expected for electron counts between d^0 - d^4 .^{29,30} Radical reactivity is expected for d^5 electron counts, whereas nucleophilic behavior is predicted for a d^6 electron count.^{29,30} Thus, the pseudo-tetrahedral geometry may afford the possibility to stabilize more electron rich metal centers (as high as d^6) and could support significantly more electrophilic metal oxo moieties than those found in other geometries.^{29,30} These predictions, however, assume a low spin electronic configuration and a d orbital manifold that is comparable to that which is found in pseudo-tetrahedral metal-nitrido complexes. These expectations would certainly change with high spin or intermediate spin configuration, which should be expected for 3d transition metal complexes. These scenarios are summarized in Table 1.3.

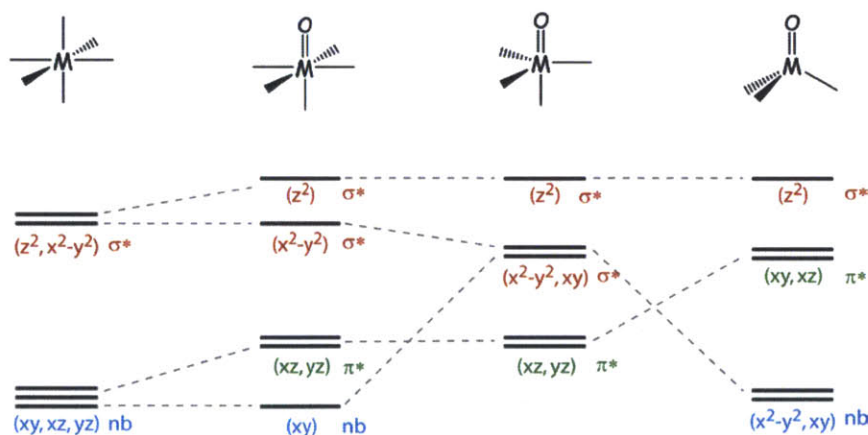


Figure 1.8 Correlation diagram for d orbital splitting diagrams for terminal metal oxo complexes in tetragonal, trigonal bipyramidal and pseudo-tetrahedral geometries. The orbital orderings for the tetragonal and trigonal bipyramidal metal oxo complexes are experimentally determined. The orbital ordering for the pseudo-tetrahedral metal oxo complex is a reproduction of the experimentally determined ordering found for pseudo-tetrahedral high valent iron nitrido complexes.

Table 1.3 Predicted behaviors for metal oxo complexes with d electron counts between d^0 - d^6 in different geometries and spin states based on electronic structure shown in Figure 1.8.

d electrons	Geometry	Spin State	M–O Bond Order	Predicted Behavior
0	Tetragonal	Low	3	Electrophilic
		Intermediate		
	High			
Trigonal Bipyramidal	Low	3	Electrophilic	
	Intermediate			
High				
Tetrahedral	Low	3	Electrophilic	
	Intermediate			
High				
1	Tetragonal	Low	3	Electrophilic

		Intermediate High		
	Trigonal Bipyramidal	Low Intermediate High	2.5	Radical
	Tetrahedral	Low Intermediate High	3	Electrophilic
2	Tetragonal	Low Intermediate High	3 2.5	Electrophilic Radical
	Trigonal Bipyramidal	Low Intermediate High	2	Nucleophilic
	Tetrahedral	Low Intermediate High	3	Electrophilic
3	Tetragonal	Low Intermediate High	2.5 2	Radical Nucleophilic
	Trigonal Bipyramidal	Low Intermediate High	1.5 2	Unstable Nucleophilic
	Tetrahedral	Low Intermediate High	3 2.5	Electrophilic Radical
4	Tetragonal	Low Intermediate High	2	Nucleophilic
	Trigonal Bipyramidal	Low Intermediate High	1 1.5 2	Unstable Nucleophilic
	Tetrahedral	Low Intermediate High	3 2.5 2	Electrophilic Radical Nucleophilic
5	Tetragonal	Low Intermediate High	1.5	Unstable
	Trigonal Bipyramidal	Low Intermediate High	1 1.5	Unstable
	Tetrahedral	Low Intermediate High	2.5 1.5	Radical Unstable
6	Tetragonal	Low Intermediate High	1 1.5	Unstable
	Trigonal Bipyramidal	Low Intermediate High	1	Unstable
	Tetrahedral	Low Intermediate High	2 1.5	Nucleophilic Unstable

Figure 1.8 and Table 1.3 show differences in predicted for the reactivity and stability of metal oxo complexes upon the utilization of a pseudo-tetrahedral coordination geometry around

the metal center. However, it should be noted that these predictions are based on an *assumed* electronic configuration and need not be the case for any or all ancillary ligand types. Nevertheless, Table 1.3 does present the fundamental differences that may exist due to novel coordination geometries. Currently there is a dearth of experimentally derived electronic structures for pseudo-tetrahedral metal oxo complexes across a range of *d* electron counts. Based on the desire to interrogate the relationship between coordination geometry and reactivity via the metal oxo moiety for the purposes of O–O bond formation, this dissertation will aim to experimentally investigate the fundamental electronic structure of metal oxo complexes in a pseudo-tetrahedral geometry and subsequent reactivity.

1.3 HX as a Substrate: Catalyst Development

1.3.1 Motivation for Molecular Photocatalysts Whereas water is often regarded as an ideal substrate for hydrogen generation and energy storage, motivation for hydrohalic acids (HX) as a substrate stems from the lack of understanding about multi-electron and multi-proton coupled processes. For water as a substrate, the fuel generating process is an overall 4-electron 4-proton coupled transformation of which many details remain poorly understood (i.e. the nature of the critical O–O bond forming step). Fuel generation from HX substrates is fundamentally simpler as the overall transformation is a 2-electron 2-proton coupled process. Managing the kinetic demands of such a transformation should in principle be more feasible resulting in overall higher efficiencies for fuel generation and utilization. With fewer variables to consider, molecular systems which exhibit HX splitting chemistry can possibly provide insight into the fundamental aspects of proton coupled electron processes which can help govern new theories to be applied to the generation fuels from any potential substrate.

Practically, motivation for HX as a fuel generation substrate is furthered in that H_2-X_2 fuel cells offer several advantages over H_2-O_2 fuel cells.⁶⁵ As the science behind HX splitting is simpler than water splitting, the subsequent energy releasing transformation back to HX is likewise less complicated than the analogous H_2O formation from H_2 and O_2 . This can be seen in that H_2-Cl_2 fuel cells are reported to have operating efficiencies as high as 70%⁶⁶ whereas the best H_2-O_2 fuel cells currently operated at around 50% efficiency.⁶⁷ Relative to oxygen reduction, the mechanistically simpler Cl_2 reduction process affords higher current densities for the cathode due to faster electrode kinetics and ultimately facilitates higher efficiencies and

power densities for $\text{H}_2\text{-Cl}_2$ fuel cells. A major drawback that is specific for $\text{H}_2\text{-O}_2$ fuel cells is the possible formation of parasitic side products (peroxides), which can contribute to electrode and membrane degradation within an operating system.⁶⁸ Deleterious side reactions are significantly less common for chlorine and bromine reduction leading to greater system stability for $\text{H}_2\text{-X}_2$ fuel cells. $\text{H}_2\text{-Br}_2$ fuel cells offer an additional benefit due to the liquid nature of Br_2 , which negates the need for high pressure storage tanks for O_2 or Cl_2 storage while still maintaining comparable thermodynamic properties. $\text{H}_2\text{-Br}_2$ fuel cells are additionally attractive in that a system using a PtRu alloy cathode was reporting to afford efficiencies as high as 90%, showing significant efficiency advantages over $\text{H}_2\text{-O}_2$ fuel cells.⁶⁹ Thus, $\text{H}_2\text{-X}_2$ fuel cells in general show higher efficiencies and greater stabilities to comparable $\text{H}_2\text{-O}_2$ fuel cells, and in the case of $\text{H}_2\text{-Br}_2$, additional benefits are found in the facile nature in which liquid bromine can be stored.

Despite the advantages of HX splitting and subsequent $\text{H}_2\text{-X}_2$ fuel cells, there are obstacles to widespread utilization. Of primary concern is the corrosive nature of hydrohalic acids as well as the resulting halogen (Cl_2 or Br_2). Because of this, $\text{H}_2\text{-X}_2$ fuel cells do require additional and costly system considerations that are not needed for $\text{H}_2\text{-O}_2$ fuel cells. Regardless, procedures exist for safe handling and storage for chlorine and in 2001 over 43 million tons of chlorine was produced industrially for plastics, pharmaceuticals and chemical industries.⁷⁰ However, it is acknowledged that the possible deleterious effects that could result from mass environmental exposure of chlorine or bromine remains a significant barrier to larger scale general acceptance and adoption of $\text{H}_2\text{-X}_2$ fuel cells.

With these considerations in mind, HX splitting affords the opportunity to explore the basic science behind the process of storing energy directly within chemical transformations and bonds. As HX splitting is kinetically simpler than water splitting, it also lends itself to evaluating the merit of potential system designs for fuel generation from renewable energy sources. There are two basic system designs for fuel generation. The first involves renewable energy being converted to electricity to subsequently power an electrolyzer that drives the fuel generation reaction. For solar energy, this model would involve the integration of a photovoltaic (for solar energy to electricity transformation) with an electrolyzer. A second system model involves the direct energy to chemical fuel generation. Again using solar energy as the example, this entails

the development of a photoanode and photocathode material that directly converts solar energy into the desired fuel.

Electrochemical pathways for H₂ and X₂ generation have historically dominated the area of HX splitting research.⁷¹⁻⁷³ Much has been reported on the different available mechanisms for electrochemical HX splitting as well as evaluating electrode materials.⁷⁴⁻⁷⁷ Conversely, this dissertation will focus on the direct renewable energy to HX splitting process via replacing the electrolyzer with photoactive materials capable of mediating the direct sunlight to fuel transformation.

For mechanistic studies, homogeneous systems offer several advantages over electrodes or photoelectrodes. Whereas electrodes and photoelectrodes can be characterized by their specific behavior, which affords the opportunity to build a model for the active species, homogeneous molecules are amenable to structural characterization so that the exact nature of important species can be known and evaluated. Furthermore, during catalysis, intermediates may be spectroscopically observed by transient methods. Homogeneous systems can also be synthetically tuned in order to better understand how steric accessibility and electronic structure affect the observed chemistry. These are among some of the reasons for focusing on molecular photocatalysts for HX splitting reactions.

1.3.2 Multicomponent Systems for Photochemical Hydrogen Production.

Photochemical hydrogen production has been previously reported for many molecular systems.⁷⁸ Whereas many of these systems utilize dehydration reactions of alcohols⁷⁹⁻⁸¹ and alkanes⁸²⁻⁸⁴, there are many examples wherein the conditions are more relevant to energy storage. The earliest reports of photoreduction of protons involved irradiation of metal ions, such as Eu²⁺,⁸⁵ Cr²⁺,⁸⁶ Fe²⁺,⁸⁷ Ce²⁺,⁸⁸ and Cu²⁺,⁸⁹ in the presence of acid to yield stoichiometric amount of H₂. With the appropriate complexation of the metal ions, photocatalysis can be observed. For example, both Pt(PEt)₂Cl₂⁹⁰ and [Ir^{III}Cl₆]³⁻⁹¹ have been shown to photocatalytically generate hydrogen. While mechanistic details were difficult to obtain, both systems are thought to react via excitation into a M-Cl σ* orbital, with subsequent bond homolysis. This highlights a fundamental aspect to transition metal photochemistry: electronically excited complexes customarily react according to a single electron mechanism. As H₂ generation is a 2-electron reaction, the efficiency of direct H₂ production from an excited state that reacts in a 1-electron mechanism is typically poor.

Chemical systems have thus been designed wherein the light harvesting event is separate from but coupled to a catalyst performing the proton reduction transformation.

The most common molecular motif for separating the generation of excited states from the proton reduction transformation for photochemical H₂ production is a multicomponent design (Figure 1.9). Within this strategy, a photochemically generated reduction potential at a photosensitizer is relayed through a mediator to a catalyst that performs proton reduction. The oxidized photosensitizer is then reduced back to its initial state via a reaction with a sacrificial electron donor. The components of this system required for H₂ production are the sacrificial electron donor (D), the photosensitizer (PS), the mediator (M), and the catalyst itself (cat). The simplest of these systems involves a [Ru(bpy)₃]²⁺ (bpy = 2,2-bipyridine) photosensitizer, methylviologen as a mediator, and Pt compound for H₂ production.^{92,93} Systems such as these have been amenable to systematic variation of the components (the donor, photosensitizer, mediator, catalyst, proton source) and many advances have been made to improve the operation of multicomponent system. In some scenarios, the mediator itself can be eliminated from the system. With [Ru(bpy)₂(phen)]²⁺ as a light harvesting component, the photochemically generated charge can be directly transferred to a covalently linked Pt(bpy)²⁺ catalyst.⁹⁴

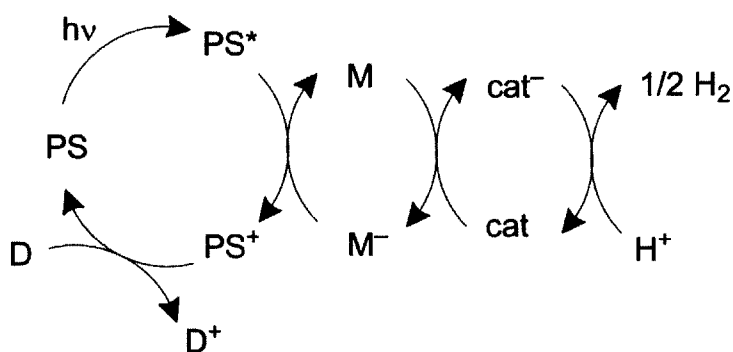


Figure 1.9. General scheme for a multicomponent system for photocatalytic proton reduction. D = sacrificial electron donor; PS = photosensitizer; M = electron transfer mediator; cat = proton reduction catalyst.

Whereas the electron mediator can theoretically be removed from a photochemical system for H₂ production, by direct association of the catalyst to the photosensitizer, the sacrificial donor cannot be circumvented. The multicomponent system described in Figure 1.9 involves the photosensitizer (PS), upon excitation (PS*), transferring an electron to the catalyst or a mediator to result in the formation of oxidized photosensitizer molecule (PS⁺). The need for the oxidized

photosensitizer PS^+ to be reduced to PS in order to continue catalysis cannot be bypassed, and thus a sacrificial electron donor is required. Neglected to this point, as is the case for most studies, has been the anodic $2X^-/X_2$ half reaction that needs to accompany proton reduction. Authentic HX splitting demands photooxidation of X^- , essentially doubling the potential costs associated with a multicomponent photochemical HX splitting system. If the oxidized photosensitizer can participate in the photooxidation of X^- , then the need for a sacrificial donor is eliminated as well as is the need for separate components for the photooxidation of X^- . A generalized hypothetical system where the photosensitizer participates in both photooxidation and photoreduction is shown in Figure 1.10.

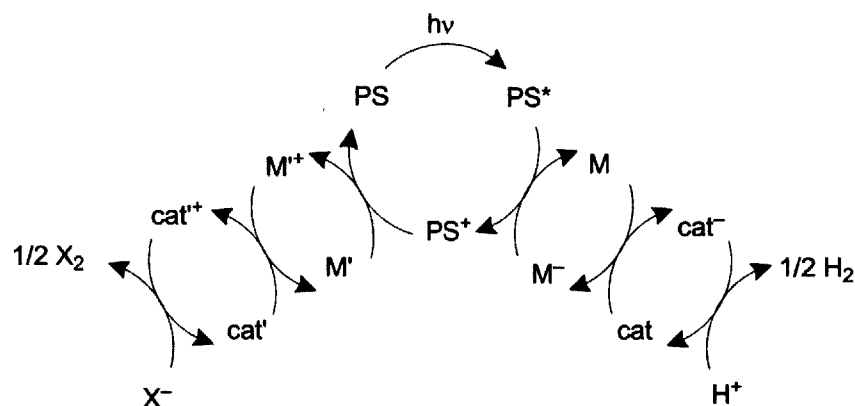


Figure 1.10. Generalized scheme for multicomponent system for photocatalytic HX splitting created by replacing the sacrificial donor in a multicomponent photocatalytic proton reduction system with a multicomponent photocatalytic halide oxidation system utilizing a common photosensitizer. PS = photosensitizer; M = electron transfer mediator for proton reduction; cat = proton reduction catalyst; M' = electron transfer mediator for halide oxidation; cat' = halide oxidation catalyst.

While simpler than two tandem multicomponent systems for proton photoreduction and halide photooxidation, the design in Figure 1.10 remains complicated with many components needing to be compatible and to react in concert. Noting that the electron mediator can be eliminated if the catalyst is closely associated with the photosensitizer, the system design can be further simplified if the catalysts are directly associated with the photosensitizer or combined in a single molecule. In this case, the catalyst performs the function of light harvesting and promoting the photoreduction/photooxidation transformation. In order to avoid the requirement for a sacrificial electron donor or acceptor, and ideal case is realized if the photocatalyst can perform both the anodic and cathodic reaction. Such a scheme is generalized in Figure 1.11.

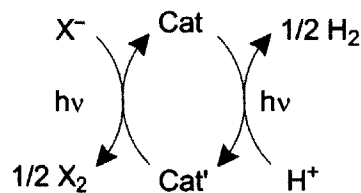


Figure 1.11. Simplified system for light absorption, proton reduction, and halide oxidation occurring at a single catalyst complex.

Figure 1.11 is significantly more simplified and desirable than the complexity of the multicomponent systems typically studied for photogeneration of H_2 . This simplicity comes with demands on the catalyst design. The ideal catalyst has to be capable of light harvesting, proton reduction, and halide oxidation, as well as being stable to the hydrohalic catalytic conditions utilized. Thus, the behavior of metal compounds under photolytic conditions in the presence of hydrohalic acids needs to be considered.

1.3.3 Photochemistry of HX Solutions and M–X Bond Activation. Authentic HX splitting catalysts are limited by the ability of metals to catalyze X^- oxidation. Reduced metals centers have been well established to be able to reduce protons, often times thermally. However, the thermodynamic stability of metal-halide bonds presents significant barriers to completing HX splitting catalysis. A previously mentioned, an early example of a competent HX splitting photocatalyst is $[IrCl_6]^{3-}$. Treatment of $[IrCl_6]^{3-}$ with HCl results in the thermal production of H_2 along with the formation of $[IrCl_6]^{2-}$. Photolysis of $[IrCl_6]^{2-}$ with UV light (254 nm) results in $Cl\cdot$ radicals which can couple to form Cl_2 . While fairly efficient at high energy wavelength (quantum yield = 0.28) the use of lower energy wavelengths showed a fast decline in efficiency. Thus, the combination of the one electron radical nature of the halide oxidation as well as the need for high energy photolysis set the stage for the further development of catalysts. The primary goals include efficient operation at lower energy wavelengths as well as operate in a more controlled manner, either via a two electron mechanism or a controlled radical mechanism wherein decomposition cause by high energy $Cl\cdot$ radicals is negated.

Organometallic transition metal complexes have also been shown to photochemically generate H_2 from HX solutions, but similarly suffer from thermodynamically stable M–X bond. One of the first example reported by Gray and coworkers used a bimetallic rhodium complex, $[Rh_2^{II}(\text{diisocyanopropane})_4]^{2+}$, (Figure 1.12),^{95–97} to generate H_2 from HCl, HBr and HI. Addition of excess HCl to $[Rh_2^{II}(\text{diisocyanopropane})_4]^{2+}$ results in thermal formation of H_2 and

the dichloro species $[\text{Rh}_2^{\text{II,II}}(\text{diisocyanopropane})_4\text{Cl}_2]^{2+}$. Photolysis of $[\text{Rh}_2^{\text{II,II}}(\text{diisocyanopropane})_4\text{Cl}_2]^{2+}$ with UV light in the presence of HCl releases a second equivalent of H_2 and affords $[\text{Rh}_2^{\text{III,III}}(\text{diisocyanopropane})_4\text{Cl}_4]^{2+}$, which is inert to further photolysis.^{98,99} This chemistry further highlights the continuing challenge of activating the M–X bonds upon generation of H_2 from HX.

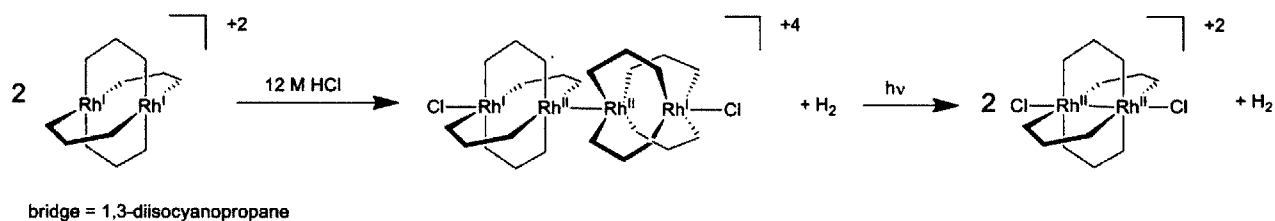


Figure 1.12 The complex $[\text{Rh}_2(\text{bridge})_4]^{2+}$ reacts thermally with excess HCl to generate one equivalent of H_2 along with the dimeric species $[\text{Rh}_2(\text{bridge})_4\text{Cl}]_2^{4+}$. Photolysis of $[\text{Rh}_2(\text{bridge})_4\text{Cl}]_2^{4+}$ with visible light results in photoreduction of an additional equivalent of H_2 along with formation of the inert complex $[\text{Rh}_2(\text{bridge})_4\text{Cl}_2]^{2+}$.

One potential problem with X_2 photoelimination from $[\text{Rh}_2^{\text{II,II}}(\text{diisocyanopropane})_4\text{Cl}_2]^{2+}$ is one of geometry, as the two chloride ligands bind in axial positions on opposite sides of the molecule. Therefore, a concerted 2-electron reductive elimination pathway for M–X bond activation is impossible without significant ligand rearrangement, which is unlikely due to the chelating nature of the diisocyanopropane to the dirhodium core. This geometric concern does not rule out possible M–X bond homolysis via excitation into a σ^* M–X bond. However, based on the lack of reported product formation associated with the generation of halogen radicals, this is deemed unlikely.

The activation of M–X bonds via a possible 2 electron mechanism from structurally similar bimetallic cores is observed for the complex $\text{Mo}_2^{\text{III,III}}(\text{dtbppm})_2\text{Cl}_6$ (dtbppm = bis(di-4-*tert*-butylphenyl)phosphinomethane).¹⁰⁰ The structure of $\text{Mo}_2^{\text{III,III}}(\text{dtbppm})_2\text{Cl}_6$ include two bridging chloride ligand along with two terminal chloride ligands on each molybdenum atom (Figure 1.13). Photolysis of with UV light in THF in the presence of lutidine results in the isolation of $\text{Mo}_2^{\text{II,II}}(\text{dtbppm})_2\text{Cl}_4$ and two equivalents of lutidinium hydrochloride. The lutidinium hydrochloride is the product of M–X bond homolysis from $\text{Mo}_2^{\text{III,III}}(\text{dtbppm})_2\text{Cl}_6$ followed by hydrogen atom abstraction of the alpha C–H bond of THF by the $\text{Cl}\cdot$ radical. The HCl produced is then trapped as an adduct with lutidine.

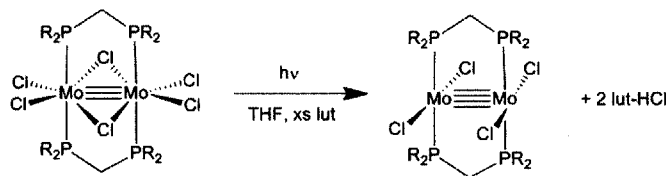


Figure 1.13 Photolysis of $\text{Mo}_2\text{Cl}_6(\text{dtbppm})_2$, dtbppm = bis(di-4-*tert*-butylphenyl)phosphinomethane, with UV light in THF in the presence of excess lutidine results in formal homolysis of a Mo–Cl bond and generation of two equivalents of $\text{Cl}\cdot$ radical. The $\text{Cl}\cdot$ radicals abstract hydrogen atoms from THF to form HCl which is trapped by the excess lutidine.

While efficiencies for the M–X bond activation are low, the ability to activate M–X bonds from this molecular motif along with the ability of later metal complexes, such as rhodium, to photogenerate H_2 , presents a framework for developing HX splitting photocatalysts. Bimetallic rhodium complexes with open coordination sites in equatorial positions could possibly present a “best of both worlds scenario” in that the nature of the electron rich dirhodium core could facilitate H_2 formation, and the ability to access coordination modes of M–X bonds besides terminal halogen ligands which could be amenable to bond homolysis or a 2-electron elimination mechanisms.

1.3.4 Mixed Valency and Bimetallic Rhodium-Phosphazane Systems. The previously mentioned examples of photogeneration of H_2 , HX or X_2 proceed through metal-ligand bond homolysis mechanisms. However, the generation of reactive radical species can potentially lead to decomposition pathways. This is observed in the chemistry of $\text{Mo}_2\text{Cl}_6(\text{dtbppm})_2$ as the $\text{Cl}\cdot$ radicals released abstract hydrogen atoms from solvent. Despite formally reducing the bimetallic core twice, the reduction events can be thought of as two uncoupled $\text{Cl}\cdot$ eliminations. A more appealing mechanistic pathway would be a direct concerted 2-electron reductive elimination. It is hypothesized that a photochemically generated zwitterionic structure of a bimetallic core ($\text{M}^+ - \text{M}^-$) could promote two electron reductions at the anionic metal site and two electron oxidations at the cationic site as the oxidizing or reducing equivalents are coupled and localized on a single metal center.⁷³ In order to promote a zwitterionic excited state, phosphazane ligands (Figure 1.14, left) were utilized to stabilize mixed valent bimetallic complexes in the ground state. The phosphazane class of ligands has been shown to stabilize mixed valent bimetallic complexes via asymmetrically distributing π electron density, as depicted in Figure 1.14 (left). The ability of phosphines to both donate and accept π electron density allows for one phosphine of the phosphazane ligand to accept electron density from a reduced metal, while donating electron density to the bridging nitrogen atom. The other phosphine moiety consequently accepts electron

density from the bridging nitrogen atom and donates electron density to the oxidized metal center.

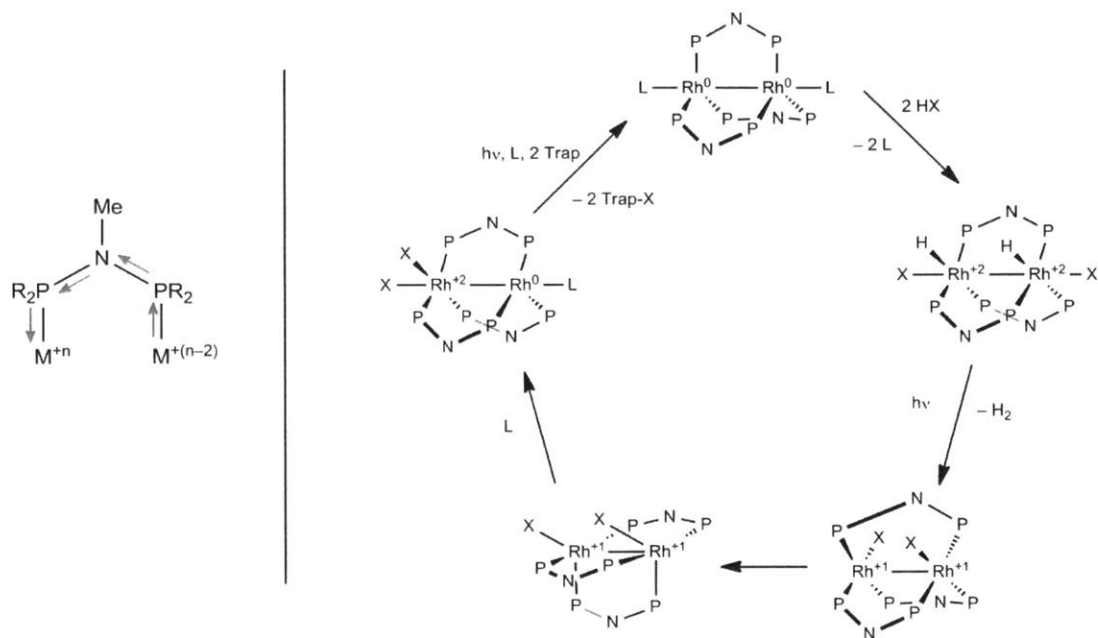


Figure 1.14 (Left) General depiction of the asymmetric distribution of π electron density promoted by phosphazane ligands which has been shown to stabilize mixed valent electronic structures in bimetallic complexes. (Right) Proposed catalytic cycle for the photocatalytic HX splitting initiated by photolysis of $\text{Rh}_2(\text{dfpma})_3(\text{CO})$, dfpma = *bis* (difluorophosphino)methane, determined by the thermal and photochemical studies of model compounds.

With the utilization of the phosphazane ligand *bis*(difluorophosphino)methylamine, dfpma = $((\text{PF}_2)_2\text{NMe})$, $\text{Rh}^{0,0}_2(\text{dfpma})_3(\text{CO})_2$ can be isolated and has been shown to be an HX splitting catalyst under photolytic conditions in the presence of HX ($\text{X} = \text{Cl}$ or Br) and a halogen trap.^{101,102} Thorough mechanistic studies determined a catalytic cycle as shown in Figure 1.14 right. The cycle involves the addition of HX, with subsequent photoelimination of H_2 and photoelimination of X_2 . This initial system was shown possess an overall quantum yield for the cycle of $\sim 1\%$ and stable as turnover numbers of 80 were reported. However, this first generation catalyst required a halogen trap in order to promote the Rh–Cl bond activation photoreaction. This need for a trap not only potentially alters the halogen elimination mechanism but also results in the overall reaction being exergonic. Mechanistic studies with model compounds along with supporting computational studies showed that the operative pathway for both H_2 and X_2 photoelimination was via a mixed valent bimetallic core.^{103–105} This supports the initial hypothesis that excitation of mixed valent bimetallic complex could engender preferential 2-

electron elimination chemistry. However, the $\text{Rh}^{0,0}(\text{phosphazane})_3(\text{L})_2$ was incapable of authentic X_2 elimination. Subsequent studies of exclusively X_2 elimination on similar bimetallic structure with more electronegative metals (Pt, Pd, Au) were able to surmise a key intermediate for X_2 elimination as a bridging halide, similar to that which is suggested for H_2 elimination.^{106–109} As such, access to such a bridging halogen bonding structure could potentially promote authentic X_2 elimination

With the goal of working towards a single photocatalyst capable of executing both proton reduction and halide oxidation, a second generation dirhodium-phosphazane compound for catalytic proton photoreduction chemistry as well as halogen photoelimination has been developed (Figure 1.15). Whereas previous iterations of dirhodium-phosphazane complexes have been chelated by three phosphazane ligands, the new archetype is stabilized by only two phosphazane ligands, rendering the bimetallic core less sterically crowded and in favor of bridging ligand coordination modes. Furthermore, the reduced state of the compound (Figure 1.15) includes a coordinatively unsaturated Rh center. This is in contrast to first generation catalysts, which required loss of a ligand prior to oxidative addition HX , and re-coordination of the ligand upon elimination of halogen. Eliminating the requirement for ligand loss and re-coordination within the second generation structure simplifies the overall catalytic cycle as well as increases the stability of the catalyst by maintaining a constant primary coordination sphere for the bimetallic core. Additionally, valence isomers of a tetrachloro form of the catalyst have been isolated: a mixed valent $\text{Rh}^{\text{I,III}}$ as well as a valence symmetric $\text{Rh}^{\text{II,II}}$ species. Halogen elimination from both valence isomers are independently evaluated in order to assess the benefit of mixed valency for Rh-X bond activation in the Rh -phosphazane class of compounds.

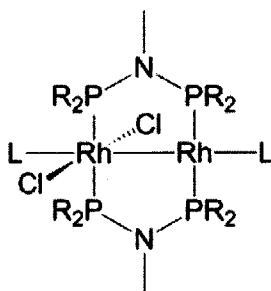


Figure 1.15 Generalized structure for second generation HX splitting photocatalyst. $\text{R} = \text{CF}_3\text{CH}_2\text{O}-$, $\text{L} =$ adamantly isocyanide or *tert*-butyl isocyanide.

1.4 Scope of Thesis

The storage of renewable energy within the rearrangements of chemical bonds creates an imperative to study the fundamental aspects relevant to performing the desired energy storage reactions. Any endergonic reaction can potentially be utilized as an energy storage mechanism. This thesis will use homogenous inorganic complexes to address fundamental aspects associated with two specific endergonic reactions: The splitting of water to hydrogen and oxygen, and the splitting of hydrohalic acids HX to hydrogen and halogen.

Regarding H₂O as a substrate for energy storage, the initial chapters will focus on evaluating terminal metal oxo complexes in a unique pseudo-tetrahedral ancillary ligand environment. Chapter 2 addresses the synthesis and characterization of a class reduced metal precursors to be used for the synthesis of pseudo-tetrahedral metal oxo complexes and establishes the monometallic complexes in oxygen rich ancillary ligand environments as single metal site models to the oxidic metal clusters and surfaces that act as water oxidation catalysts. Chapter 3 described the synthesis of early transition metal terminal metal oxo complexes to establish the electronic structure of the pseudo-tetrahedral metal oxo complexes and correlates the electronic structure to reactivity patterns of the terminal oxo moiety. Chapter 4 explores the reactivity of pseudo-tetrahedral high valent iron complexes. Using the electronic structure previously established in the early transition metal systems, the reactivity of high valent pseudo-tetrahedral iron is evaluated and compared to the reactivity reported for other high valent iron-oxo complexes in tetragonal and trigonal bipyramidal ligand environments in order to determine the beneficial and detrimental effects of a pseudo-tetrahedral ancillary ligand environment on the reactivity metal oxo complexes.

Regarding HX as a substrate, this thesis will focus on studying both H₂ and X₂ from HX sources on a bimetallic rhodium platform. Chapter 5 will evaluate the proton photoreduction and utilizes ligand modifications to enhance photocatalytic stability. Upon establishing a stable H₂ production catalyst, the nature of the X₂ photoelimination is interrogated. The importance of a mixed valence state for the bimetallic core versus a valence symmetric core is explored. Observed intermediates involved in X₂ elimination are independently synthesized and characterized.

1.5 Concluding Remarks

Within the landscape of *energy science* and *energy storage* research, the study of homogeneous solutions of inorganic complexes, relative to heterogeneous chemistry and materials development, has a unique ability to target very specific questions of great importance to energy science and glean insights that that would be otherwise unavailable. This is never more apparent than in the study of transformations relevant to energy storage within chemical bonds. Rational catalyst design requires insights into the precise manner in which substrates interact with catalytic sites, the manner in which electrons are transferred, mechanisms by which bonds are formed and products are released; all of these are specific areas in which homogenous molecular chemistry excels at interrogating. As the most important chemical transformations relevant to efficient and economical energy storage are still unknown, studies aimed towards all potentially useful transformation are sought. The subsequent chapters will deal with two different transformations: H₂O and HX splitting. Within the context of water splitting, the manners in which the electronic structure of the ancillary ligand field affect the reactivity of a terminal metal oxo moiety are investigated. Within the very different context of HX splitting, development of stable photocatalysts capable of both H₂ and X₂ photogeneration is continued, as well as insights into the manner in which the electronic structure of a bimetallic catalyst (mixed valence versus valence symmetric) affects the efficiency of X₂ elimination.

1.6 References

- (1) Energy Information Association; U.S. Department of Energy, www.eie.doe.gov (accessed January 2013).
- (2) Lewis, N. S.; Nocera, D. G. *Proc. Natl. Acad. Sci U.S.A.* **2006**, *103*, 15729.
- (3) Hoffert, M. I.; Caldeira, K.; Jain, A. K.; Haites, E. F.; Harvey, L. D. D.; Potter, S. D.; Schlesinger, M. E.; Schneider, S. H.; Watts, R. G.; Wigley, T. M. L.; Wuebbles, D. J. *Nature* **1998**, *395*, 88.
- (4) Smalley, R. E. *MRS Bull.* **2005**, *30*, 412.
- (5) *2009 World Population Data Sheet*; Population Reference Bureau: Washington, DC, 2009; www.prb.org.
- (6) Bureau of Economic Analysis; U. S. Department of Commerce, www.bea.gov (accessed January 2013).
- (7) Goldemberg, J. *World Energy Assessment: Energy and the Challenge of Sustainability*; United Nations, Dept. of Economic and Social Affairs, World Energy Council. United Nations Development Programme: New York City, 2000.
- (8) Houghton, J. T.; Filho, L. G. M.; Griggs, D. J.; Maskell, K. *Stabilization of Atmospheric Greenhouse Gases: Physical, Biological and Socio-Economical Implications*, IPCC Technical Paper III, **1997**.
- (9) Caldeira, K.; Jain, A.K.; Hoffert, M.I. *Science* **2003**, *299*, 2052.
- (10) O'Neill, B. C.; Oppenheimer, M. *Science* **2002**, *296*, 1971.
- (11) Canadell, J. G.; Le Quéré, C.; Raupach, M. R.; Field, C. B.; Buitenhuis, E. T.; Ciais, P.; Conway, T. J.; Gillett, N. P.; Houghton, R. A.; Marlan, G. *P.N.A.S.* **2007**, *104*, 18866.
- (12) Boden, T.A.; Marland, G.; Andres, R. J. *Global, Regional, and National Fossil-Fuel CO₂ Emissions*. Carbon Dioxide Information Analysis Center, Oak Ridge National Laboratory, U.S. Department of Energy, Oak Ridge, Tenn., U.S.A. **2010**.
- (13) Nakicenovic, N.; Swart, R. *Special Report on Emissions Scenarios*; Intergovernmental Panel on Climate Change. Washington, DC, 2000; pp 48.
- (14) Blankenship, R. E.; Tiede, D.M.; Barber, J.; Brudvig, G. W.; Flemming, G.; Ghirardi, M.; Gunner, M. R.; Junge, W.; Kramer, D. M.; Melis, A.; Moore, T. A.; Moser, C. C.; Nocera, D. G.; Nozik, A. J.; Ort, D. R.; Parson, W. W.; Prince, R. C.; Sayre, R. T. *Science* **2010**, *332*, 805.

- (15) Bolton, J. R.; Hall, D. O. *Annu. Rev. Energy* **1979**, *4*, 353.
- (16) Abbott, D. *Proc. IEEE* **2010**, *98*, 42.
- (17) Barber, J. *Chem. Soc. Rev.* **2009**, *38*, 15.
- (18) Eisenberg, R.; Nocera, D. G. *Inorg. Chem.* **2005**, *44*, 6799.
- (19) Nocera, D. G. *Daedalus* **2006**, *135*, 112.
- (20) Cook, T. R.; Dougtan, D. K.; Reece, S. Y.; Surendranath, Y.; Teets, T. S; Nocera, D. G. *Chem. Rev.* **2010**, *110*, 6474.
- (21) Nocera, D.G. *Energy Environ. Sci.* **2010**, *3*, 993.
- (22) Alternative Fuels and Advanced Vehicles Data Center: U.S. Department of Energy, http://www.afdc.energy.gov/fuels/fuel_properties.php (accessed January 2013).
- (23) Haynes, W. M. ed. *CRC Handbook of Chemistry and Physics*, 93rd Edition (Internet Version 2013), CRC Press/Taylor and Francis, Boca Raton, Florida.
- (24) Weiss, H. M. *J. Chem. Educ.* **2008**, *85*, 1218.
- (25) Wood, P. M. *Biochem. J.* **1988**, *253*, 287.
- (26) Pitzer, K. S. *J. Am. Chem. Soc.*, **1948**, *70*, 2140.
- (27) Dekock, R. L.; Gray, H. B. *Chemical Structure and Bonding*, University Science Books, Sausalito, California (1989); pp 229-230.
- (28) Whitesides, R. A.; Krishnan, R.; Pople, J. A.; Krogh-Jerpersion, M.-B.; von Rague Schleyer, P.; Wenke, G. *J. Comp. Chem.* **1980**, *1*, 307.
- (29) Betley, T. A.; Surendranath, Y.; Childress, M. V.; Alliger, G. E.; Fu, R.; Cummins, C. C.; Nocera, D. G. *Phil. Trans. R. Soc. B.* **2008**, *363*, 1293.
- (30) Betley, T. A.; Wu, Q.; Van Voorhis, T.; Nocera, D. G. *Inorg. Chem.* **2008**, *47*, 1849.
- (31) Umena, Y.; Kawakami, K.; Shen, J.-R.; Kamiya, N. *Nature* **2011**, *473*, 55.
- (32) Joliot, P.; Kok, B. *Bioenergetics of Photosynthesis*; Govindjee Ed.; Academic Press: New York, 1975; pp 387-412.
- (33) Brudvig, G. W. *Phil. Trans. R. Soc. B.* **2008**, *363*, 1211.
- (34) Siegbahn, P. E. M. *J. Photochem. Photobio. B. Bio.* **2011**, *104*, 94.
- (35) Siegbahn, P. E. M. *Chem. Eur. J.* **2008**, *14*, 8290.
- (36) Siegbahn, P. E. M. *Phil. Trans. R. Soc. B.* **2008**, *363*, 1221.

- (37) Barber, J.; Siegbahn, P. E. M.; Nocera, D.; Dau, H.; Armstrong, F.; Rich, P. *Phil. Trans. R. Soc. B.* **2008**, *363*, 1228.
- (38) Dau, H.; Limberg, C.; Reier, T.; Roggan, S.; Strasser, P. *ChemCatChem* **2010**, *2*, 724.
- (39) Bockris, J. O'M.; Otagawa, T. *J. Phys. Chem.* **1983**, *87*, 2960.
- (40) Bediako, D. K.; Lassalle-Kaiser, B.; Surendranath, Y.; Yano, J.; Yachandra, V. K.; Nocera, D. G. *J. Am. Chem. Soc.* **2012**, *134*, 6801.
- (41) Singh, R. N.; Koenig, J.-F.; Poillerat, G.; Chartier, P. *J. Electrochem. Soc.* **1990**, *137*, 1408.
- (42) Kanan, M. W.; Yano, J.; Surendranath, Y.; Dinca, M.; Yachandra, V. K.; Nocera, D. G. *J. Am. Chem. Soc.* **2010**, *132*, 13692.
- (43) Rasiyah, P.; Tseung, A. C. C. *J. Electrochem. Soc.* **1984**, *131*, 803.
- (44) Burke, L. D.; Murphy, O. J.; O'Neill, J. F.; Venkatesan, S.; Schuldiner, S. *J. Chem. Soc. Faraday Trans.* **1977**, *73*, 1659.
- (45) Hu, J.-M.; Zhang, J.-Q.; Cao, C.-N. *Int. J. Hydrogen Energy* **2004**, *29*, 791.
- (46) Cao, R.; Lai, W.; Du, P. *Energy Environ. Sci.* **2012**, *5*, 8134.
- (47) Ruttinger, W.; Dismukes, G. C. *Chem. Rev.* **1997**, *97*, 1.
- (48) Yagi, M.; Kaneko, M. *Chem. Rev.* **2001**, *101*, 21.
- (49) Gersten, S. W.; Samuels, G. J.; Meyer, T. J. *J. Am. Chem. Soc.* **1982**, *104*, 4029.
- (50) Hurst, J. K.; Zhou, J.; Lei, Y. *Inorg. Chem.* **1992**, *31*, 1010.
- (51) Chronister, C. W.; Binstead, R. A.; Ni, J. F.; Meyer, T. J. *Inorg. Chem.* **1997**, *36*, 3814.
- (52) Rotzinger, F. P.; Munavalli, S.; Comte, P.; Hurst, J. K.; Gratzel, M.; Pern, F.-J.; Frank, A. J. *J. Am. Chem. Soc.* **1987**, *109*, 6619.
- (53) Nazeeruddin, M. K.; Rotzinger, F. P.; Comte, P.; Gratzel, M. *J. Chem. Soc., Chem Commun.* **1988**, *52*, 63.
- (54) Ramaeraj, R.; Risa, A.; Kaneko, M. *J. Chem. Soc., Chem Commun.* **1986**, 1707.
- (55) Britigan, B. E.; Rosen, G. M.; Chai, Y.; Chohen, M. S. *J. Biol. Chem.* **1986**, *261*, 4426.
- (56) Limburg, J.; Vrettos, J. S.; Liable-Sands, L. M.; Rheingold, A. L.; Crabtree, R. H.; Brudvig G. W. *Science* **1999**, *283*, 1524.
- (57) Collomb, M. N.; Deronzier, A.; Richardot, A.; Pecaut, J. *New. J. Chem.* **1999**, *23*, 351.
- (58) Koppel, J.; Goldmann, R. *Z. Anorg. Allg. Chem.* **1903**, *36*, 281.
- (59) Ballhausen, C. J.; Gray, H. B. *Inorg. Chem.* **1962**, *1*, 111.

- (60) Winkler, J. R.; Gray, H.B. *Struct. Bond*; **2012**, *142*, 17.
- (61) Collins, T. J.; Gordon-Wylie, S. W. *J. Am. Chem. Soc.* **1989**, *111*, 4511.
- (62) Rohde, J.-U.; In, J.-J.; Lim, M. H.; Brennessel, W. W.; Bukowski, M. R.; Stubna, A.; Munck, R.; Nam, W.; Que, L. Jr. *Science*, **2003**, *299*, 1037.
- (63) Allen, F. H. *Acta Crystallogr., Sect. B* **2002**, *58*, 380.
- (64) Saouma, C. T.; Peters, J. C. *Coord. Chem. Rev.* **2011**, *255*, 920.
- (65) Thomassen, M.; Sandnes, E.; Børresen, B.; Tunold, R. *J. Appl. Electrochem.* **2006**, *36*, 813.
- (66) Yeo, R. S.; McBreen, J.; Tseung, A. C. C.; Srinivasan, S. *J. Appl. Electrochem.* **1980**, *10*, 393.
- (67) Ledjeff, K.; Mahlendorf, F.; Peineche, V.; Heinzl, A. *Electochim. Acta* **1995**, *40*, 315.
- (68) Thomassen, M.; Børresen, B.; Hagen, G.; Tunold, R.; *J. Appl. Electrochem.* **2003**, *33*, 9.
- (69) Livshits, V.; Ulus, A.; Peled, E. *Electrochem. Commun.* **2006**, *8*, 1358.
- (70) Kiros, Y.; Bursell, M. *Int. J. Electrochem. Sci.* **2008**, *3*, 444.
- (71) Hansen, H. A.; Man, I. C.; Studt, F.; Abild-Pederson, F.; Bligaard, T.; Rossmeisl, J. *Phys. Chem. Chem. Phys.* **2010**, *12*, 283.
- (72) Faita, G.; Fiori, G. I. Augustynski, J. W.; *J. Electrochem. Soc.* **1969**, *116*, 928.
- (73) Krishtalki, L. I. *Electrochim. Acta* **1981**, *26*, 329.
- (74) Hepel, T.; Pollak, F. H.; O'Grady, W. E. *J. Electrochem. Soc.* **1986**, *133*, 69.
- (75) Janssen, L. J. J.; Starmans, L. M. C.; Visser, J. G.; Barendrecht, E. *Electrochim. Acta* **1977**, *22*, 1093.
- (76) Trasatti, S. *Electrochim. Acta* **1987**, *32*, 369.
- (77) Janseen, L. J. *J. Electrochim. Acta* **1974**, *19*, 257.
- (78) Esswein, A. J.; Nocera, D. G. *Chem. Rev.* **2007**, *107*, 4022.
- (79) Arakawa, H.; Sugi, Y. *Chem. Lett.* **1981**, 1323.
- (80) Griggs, C. G.; Smith, D. J. H. *J. Organomet. Chem.* **1984**, *273*, 105.
- (81) Simpson, M. C.; Cole-Hamilton, D. J. *Coord. Chem. Rev.* **1996**, *155*,
- (82) Geoffroy, G. L.; Wrighton, M. S. *Organometallic Photochemistry*; Academic Press: New York, 1979.
- (83) Bitterwolf, T. E. *J. Organomet. Chem.* **2004**, *689*, 3939,
- (84) Vlcek, A. Jr. *Coord. Chem. Rev.* **1998**, *177*, 219

- (85) Ryason, P. R. *Sol. Energy* **1977**, *19*, 445.
- (86) Collinson, E.; Dainton, F. S. I Malati, M. A. *Trans. Faraday Soc.* **1959**, *55*, 2096.
- (87) Heidt, L. J.; Mullin, M. G.; Martin, W. B. Jr.; Beatty, M. J. *J. Phys. Chem.* **1962**, *66*, 336.
- (88) Heidt, L. J.; McMillan, A. F. *J. Am. Chem. Soc.* **1954**, *76*, 2135.
- (89) Stevenson, K. L.; Kaehler, D. M.; Davis, D. D; Davis, C. R. *Inorg. Chem.* **1980**, *19* 781.
- (90) Jones, R. F.; Cole-Hamilton, D. J. *J. Chem. Soc., Chem. Commun.* **1981**, 1245.
- (91) Gray, H. B.; Maverick, A. W. *Science* **1981**, *214*, 1201.
- (92) Durham, B.; Dressick, W. J. I Meyer, T. J. *J. Chem Soc. Chem Commun.* **1979**, 381.
- (93) Miller, D.; McLendon, G. *Inorg. Chem.* **1981**, *20*, 950.
- (94) Ozawa, H. I Masa-aki, H.; Sakai, K. *J. Am. Chem. Soc.* **2006**, *128*, 4926.
- (95) Lewis, N. S. I Mann, K. R.; Gordon, J. G. II; Gray, H. B. *J. Am. Chem. Soc.* **1976**, *98*, 7461.
- (96) Mann, K. R.; Lewis, N. S.; Miskowski, V. M.; Erwin, D. K. I Hammond, G. S.; Gray, H. B. *J. Am. Chem. Soc.* **1977**, *99*, 5525.
- (97) Mann, K. R.; Bell, R. A.; Gray, H. B. *Inorg. Chem.* **1979**, *18*, 2671.
- (98) Miskowski, V. M.; Sigal, I. S.; Mann, K. R.; Gray, H. B.; Milder, S. J.; Hammond, G. S.; Ryason, P. R. *J. Am. Chem. Soc.* **1979**, *101*, 4383.
- (99) Sigal, I. S.; Mann, K. R.; Gray, H. B. *J. Am. Chem. Soc.* **1980**, *102*, 7252.
- (100) Pistorio, B. J.; Nocera, D. G. *Chem. Commun.* **1999**, 1831.
- (101) Heyduk, A. F.; Nocera, D. G. *Science*, **2001**, *293*, 1639,
- (102) Odom, A. L.; Heyduk, A. F.; Nocera, D. G. *Inorg. Chim. Acta* **2000**, *297*, 330
- (103) Esswein, A. J.; Veige, A. S.; Nocera, D. G. *J. Am. Chem. Soc.* **2005**, *127*, 16641.
- (104) Rosenthal, J.; Bachman, J.; Dempsey, J. L.; Esswein, A. J.; Gray, T. G.; Hodgkiss, J. M.; Manke, D. R.; Lockett, T. D.; Pistorio, B. J.; Veige, A. S.; Nocera, D. G. *Coord. Chem. Rev.* **2005**, *249*, 1316.
- (105) Gray, T. G.; Nocera, D. G. *Chem. Comm.* **2005**, *12*, 1540.
- (106) Cook, T. R; McCarthy, B. D.; Lutterman, D. A.; Nocera, D. G. *Inorg. Chem.* **2010**, *51*, 5152.
- (107) Cook, T. R.; Surendranath, Y.; Nocera, D. G. *J. Am. Chem. Soc.* **2009**, *131*, 28.
- (108) Cook, T. R.; Esswein, A. J.; Nocera, D. G. *J. Am. Chem. Soc.* **2007**, *129*, 10094.
- (109) Teets, T. S.; Nocera, D. G. *J. Am. Chem. Soc.* **2009**, *131*, 7411.

CHAPTER 2

Synthesis and Characterization of Tris(Alkoxide) Divalent and Trivalent 3d Transition Metal Complexes as Homogeneous Metal Oxide Mimics

2.1 Introduction

As presented in Chapter 1, the need to better understand the O–O bond forming processes creates an imperative to interrogate the fundamental bonding and reactivity patterns of 3d metal oxo complexes in geometries beyond tetragonal and trigonal bipyramidal. The pseudo-tetrahedral geometry provides synthetic targets that have been largely underexplored. Pseudo-tetrahedral metal oxo complexes could be considered ideal candidates for O–O bond formation reactions as the lower coordination number at the metal center should engender the complex more electrophilic. Additionally, depending on the spin state of the pseudo-tetrahedral complex, late 3d metals (Mn, Fe or Co) could either be susceptible to an Acid Base (AB) O–O formation mechanism (if low spin) or a Radical Coupling (RC) mechanism (if high spin).¹ As such, trigonal planar 3d transition metal complexes in reduced oxidation states are targeted in order to act as the trigonal platform for the oxygen of desired metal oxo complexes.

Besides geometric similarities, a commonality in the majority of reported high valent monomeric metal oxo complexes is the utilization of primary coordination spheres comprising of nitrogen donor ligands.²⁻¹¹ However, as described in Chapter 1, relevant water oxidation catalysts, such as metal oxide surfaces¹²⁻¹⁴ and the Mn₄CaO₅ cluster of photosystem II,^{15,16} have primary coordination spheres dominated by oxygen donor ligands. Thus, this dissertation aims to explore the primary coordination spheres of 3d transition metals with oxygen donor ligands as the ancillary ligand platform. Further motivation for targeting the synthesis of homogeneous models of oxidic metal surfaces is that these solid surfaces are important to many other catalytic processes such as water oxidation,¹⁷⁻¹⁹ hydrocarbon oxidation,²⁰⁻²² ammonia oxidation,²³ and other transformations²⁴⁻²⁹. Due to the heterogeneous nature of these catalytic reactions, mechanistic interrogations of proposed intermediate transformations within catalytic cycles have been challenging, furthering the desire for homogeneous systems that display comparable properties to metal oxidic surfaces.

Homogeneous metal alkoxide complexes have been suggested to model structures and reactivity patterns proposed for metal oxide surfaces.^{30,31} However, discrete reactivity studies at single metal centers in alkoxide-rich ligand environments are lacking due to the multimetallic and heterometallic nature of typical metal-alkoxide complexes.³²⁻³⁵ Therefore, we seek the synthesis of reduced trigonal planar homoleptic monometallic 3d transition metal complexes with open coordination sites to act as models for reactivity studies and for the formation of

pseudo-tetrahedral metal oxo complexes. Monodentate alkoxides were targeted owing to the propensity of chelating κ^3 ligands to coordinate the face of an octahedron instead of the base of a tetrahedron.³⁶⁻³⁸ Monodentate ligands afford the flexibility to stabilize reduced metal complexes in a trigonal planar geometry, while being able to accommodate the desired tetrahedral geometry of an oxidized metal oxo complex. The general desired strategy is outlined in Figure 2.1. This chapter will describe the design and synthesis of the alkoxide ligand as well as the synthesis and characterization of the trigonal planar 3d metal complexes supported by monodentate alkoxide ligands. Chapters 3 and 4 will then describe the synthesis and study of pseudo-tetrahedral metal oxo complexes.

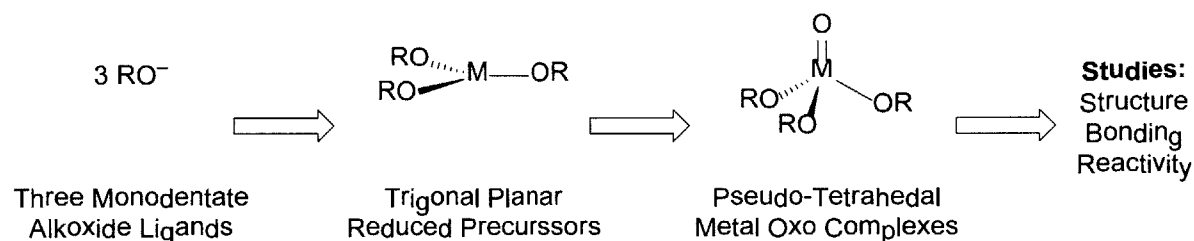


Figure 2.1. Generalized depiction of the synthetic strategy for interrogation of homogeneous low coordinate metal oxo complexes.

2.2 The $t\text{Bu}_2\text{MeCO}^-$ (Ditox) Ligand

Alkoxide compounds have a rich chemistry dating back to initial reports by Ebelman and Bouquet in 1846 of alkoxides bound to main group elements such as Si and B.³⁹ Attention was subsequently turned to alkoxides as ligands for d block elements as Demarcay reported the synthesis of titanium alkoxide compounds in 1875 via the treatment of TiCl_4 with various alcohols.⁴⁰ With these beginnings, the chemistries of metal alkoxide compounds have gone through several phases, all of which were dominated by the synthesis of compounds that were multimetallic with one or more alkoxide ligand bridging two or more metal center to furnish oligomers.³¹ The prevalence of oligomers has stifled the ability to interrogate the chemistry at a single metal site supported by a homoleptic alkoxide ancillary ligand field.

Homoleptic monometallic alkoxide complexes are difficult to stabilize owing to the facile manner in which p orbital electrons associated with the oxygen donor atom of the alkoxide ligands participate in bonding to two or three metal centers, resulting in a majority of metal-alkoxide complexes containing a pseudo-diamond core $[\text{M}_2\text{OR}_2]$ unit.⁴¹ The nature of alkoxides

bridging multiple metal centers has also resulted in higher coordination numbers around the metal to which they are bound resulting in coordinatively saturated complexes.^{42,43} Alkoxide ligands supporting monometallic complexes are not uncommon, however the alkoxide ligand typically represents one component of a heteroleptic ancillary ligand field.⁴⁴ It has been shown that by increasing the steric bulk of an alkoxide ligand, more alkoxide rich monometallic complexes can be stabilized.^{45,46} These species, however, typically possess at least one ligand of a different type bound to the metal or they are stabilized via chelation.⁴⁷⁻⁵¹

Consequently, well defined and characterized classes of monometallic homoleptic alkoxide complexes are not easily found in the literature. One example from Doerrer and coworkers utilizes electron deficient fluorinated alkoxide ligands to stabilize homoleptic alkoxide complexes with potentially open coordination sites.⁵² These complexes are often found to either be coordinatively saturated or in equilibrium with coordinatively saturated structural isomers.⁵³

The difficulty in stabilizing tris(alkoxide) metal complexes is illustrated by comparing the different structures furnished from $t\text{Bu}_2\text{HCO}^-$ versus $t\text{Bu}_3\text{CO}^-$ to stabilize metal complexes, as shown in Figure 2.2. Using divalent manganese as an example, the sterically smaller $t\text{Bu}_2\text{HCO}^-$ ligand stabilizes a tri-manganese complex $(t\text{Bu}_2\text{HCO})_6\text{Mn}_3$, depicted in Figure 2 (right).⁵⁴ The structure shows two characteristics of complexes possessing the smaller alkoxide. First, there is a propensity to bridge transition metals and form multimetallic complexes. Second, the cone angle of approximately 85° allows for the possibility of four alkoxides coordinating to one metal center. For different reasons, the bulkier $t\text{Bu}_3\text{CO}^-$ ligand is unable to form tris(alkoxide) manganese complexes, owing to a cone angle of 125° , which is too large to spatially arrange three ligands around a single metal center.⁵⁵ For the case of divalent manganese, in order to maintain an appropriate coordination sphere around the Mn(II) cation, halogen ligands remain within the primary coordination sphere, as shown in Figure 2 (left).

The structurally and electronically similar ligands $t\text{Bu}_2\text{HCO}^-$ and $t\text{Bu}_3\text{CO}^-$ define opposing limits of steric congestion (Figure 2.2). $t\text{Bu}_3\text{CO}^-$ has enough steric bulk enough to discourage bridging between transition metal centers and favors monometallic complexes, but it is too large to afford tris(alkoxide) homoleptic complexes. Conversely, $t\text{Bu}_2\text{HCO}^-$ is small enough to allow for tris(alkoxide) homoleptic complexes, but is too small to discourage multi-metallic species as well as higher coordination number homoleptic complexes.⁵⁶⁻⁵⁸ We surmised that an alkoxide ligand of intermediate steric bulk could favor monometallic complexes while also spatially

affording tris(alkoxide) ancillary ligand fields. For these reasons, ${}^t\text{Bu}_2\text{MeCO}^-$ (ditox) was targeted as a potential ligand for 3d transition metal complexes. Of note, there is precedent for the name *ditox* to refer to the ${}^t\text{Bu}_2\text{HCO}^-$ ligand.⁵⁷ However, throughout this dissertation *ditox* will be in reference to the ${}^t\text{Bu}_2\text{MeCO}^-$ ligand.

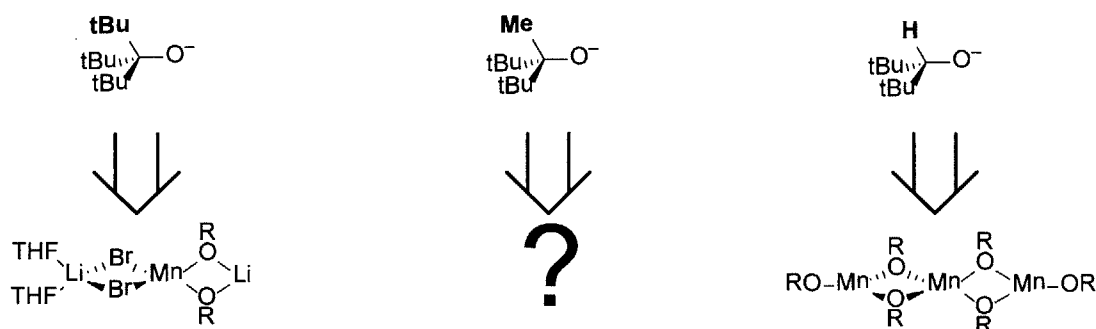
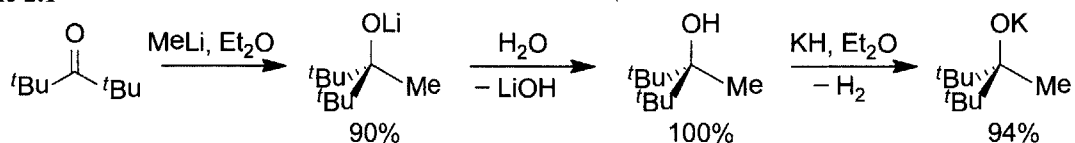


Figure 2.2. Relationship between steric bulk of alkoxide and structure of metal alkoxide complexes. Sterically crowded alkoxides (left) are unable to form tris(alkoxide) complexes. Smaller alkoxides (right) promote multimetallic species via a bridging bonding motif. Structure of metal alkoxide complexes supported by alkoxides of intermediate steric bulk (center) have been under explored.

The protonated ditox ligand, ${}^t\text{Bu}_2\text{MeCOH}$, was first synthesized by Napolitano and coworkers in 1996 as a tertiary alcohol with an earthy odor as a potential candidate for a perfume additive.⁵⁹ The chemistry of ${}^t\text{Bu}_2\text{MeCO}^-$ as a transition metal ligand has since been unexplored. The synthesis of the ditox ligand is outlined in Scheme 2.1. Liditox can be synthesized in one step by the addition of commercially available MeLi (1.6 M diethyl ether solution) to a diethyl solution of the commercially available ketone ${}^t\text{Bu}_2\text{CO}$ under an inert atmosphere at room temperature. Recrystallization from a concentrated solution diethyl ether at $-40\text{ }^\circ\text{C}$ affords analytically pure Liditox in 90% yield.

Scheme 2.1



Liditox can be hydrolyzed by the addition of water to give the tertiary alcohol Hditox in quantitative yield. Hditox can be extracted from water with diethyl ether. Removal of diethyl ether in vacuo results in pure Hditox, which can subsequently be deprotonated with a base of

choice. Of particular synthetic utility has been Kditox, which is synthesized by the addition of KH to a diethyl ether solution of Hditox at room temperature under an inert atmosphere. The reaction is complete within 60 min. Subsequent filtration through Celite and concentration afford a diethyl ether solution of Kditox, which can be crystallized at $-40\text{ }^{\circ}\text{C}$ to give pure Kditox in 94% yield. Liditox, Hditox and Kditox can all be synthesized on multi-gram scales (10-12 grams).

The crystal structure of Kditox is shown in Figure 2.3. Kditox crystallizes in the tetragonal space group $I\bar{4}$ as a tetramer in a pseudo-cubane geometry. There are three unique potassium-oxygen bond distances: $\text{K}(1)\text{-O}(1) = 2.613(1)\text{ \AA}$, $\text{K}(1\text{A})\text{-O}(1) = 2.665(1)\text{ \AA}$ and $\text{K}(1\text{B})\text{-O}(1) = 2.697(1)\text{ \AA}$. This corresponds to three unique bond angles as well: $\text{K}(1)\text{-O}(1)\text{-K}(1\text{A}) = 92.93(4)^{\circ}$, $\text{K}(1)\text{-O}(1)\text{-K}(1\text{B}) = 94.12(4)^{\circ}$, and $\text{K}(1)\text{-O}(1)\text{-K}(1\text{A}) = 97.42(4)^{\circ}$. The pseudo-cubane geometry for the tetramer of Kditox is in agreement with that which is typically observed for the solid state structures of alkali metal alkoxide complexes.⁶⁰⁻⁶⁴ The facility in which Kditox crystallizes is generally attributed to the formation of the stable alkoxide tetramer.

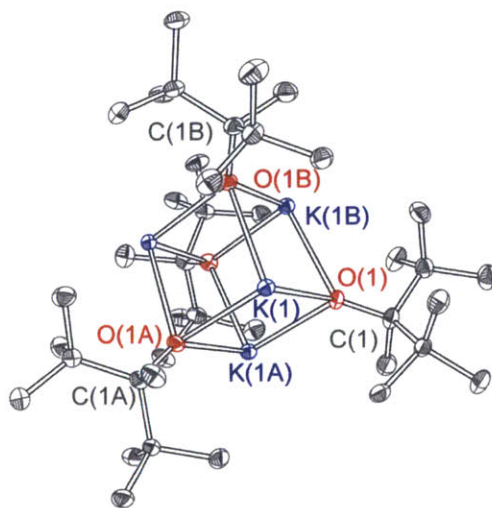


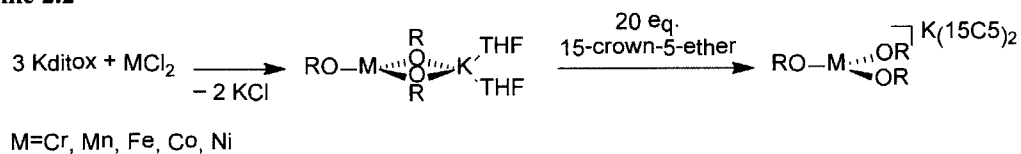
Figure 2.3. Crystal structure of Kditox. 50% thermal ellipsoid probability density. Hydrogen atoms are omitted for clarity. Selected bond distances: $d(\text{K-O1}) = 2.613(1)\text{ \AA}$, $d(\text{K-O1A}) = 2.665(1)\text{ \AA}$, $d(\text{K-O1B}) = 2.697(1)\text{ \AA}$, $d(\text{O1-C1}) = 1.385(2)\text{ \AA}$. Selected bond angles: $\angle(\text{K1-O1-K1A}) = 92.93(4)^{\circ}$, $\angle(\text{K1-O1-K1B}) = 94.12(4)^{\circ}$, $\angle(\text{KA-O1-K1B}) = 97.42(4)^{\circ}$.

With the synthesis and characterization of Liditox and Kditox completed, the remainder of this chapter explores the capacity of ditox to support 3d transition metal complexes. Specifically, trigonal planar geometries of divalent and trivalent 3d transition metals will be targeted.

2.3 Synthesis of Tris(ditox) Complexes of Divalent and Trivalent Metals

The synthesis of tris(ditox) complexes of divalent metals, as outlined in Scheme 2.2, utilizes a salt metathesis strategy for M–OR bond formation as pioneered by Demarcay.³⁹ Treatment of MCl₂ precursors (M = Cr, Mn, Fe, Co, Ni) with 3 equiv of Kditox in THF results in loss of 2 equiv KCl and formation of M(ditox)₃K(THF)₂, which can be independently identified crystallographically. Upon removal of THF in vacuo the residue can be dissolved in pentane and filtered through Celite. To the resulting pentane solution, excess (~20 equiv) of 15-crown-5-ether (15C5) is added. A precipitate forms immediately. The precipitate is allowed to settle to the bottom of the reaction vessel and the remaining pentane is removed via pipette. A THF/diethyl ether solvent mixture (1:9) is then added to the residue. The solution is filtered through Celite, and concentrated and cooled to –40 °C for crystallization to yield compounds of the formula [M(ditox)₃][K(15C5)₂]. (M = Cr, Mn, Fe, Co, and Ni for compounds **2.1**, **2.2**, **2.3**, **2.4** and **2.5** respectively). Compounds **2.1**, **2.2**, **2.3**, **2.4**, and **2.5** are light blue, pale yellow, yellow green, blue and orange, respectively. Yields are ~60% and are consistent throughout the series of divalent metal compounds.

Scheme 2.2

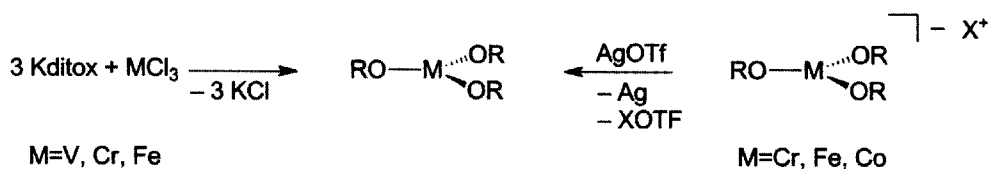


Of note, Kditox is favored over Liditox for synthesis of tris(ditox) complexes of divalent metals as the sequestration of the potassium cation was found to be more reproducible. Attempts to synthesize the V(II) analog from VCl₂ was unsuccessful as intractable mixtures of products are obtained. Compounds **2.1–2.5** are extremely air and moisture sensitive and must be kept under inert atmosphere. At room temperature, the isolated solids are observed to slowly decompose over the time period of weeks, likely via a reaction with trace chemical vapors and O₂. Compounds **2.1–2.5** are also generally unstable in common halogenated solvents (methylene chloride and chloroform) as halide abstractions are observed to occur. Whereas these reactions are nonspecific, in the case of [Cr(ditox)₃][K(15C5)₂] **2.1**, exposure to methylene chloride results in the formation of [Cr(ditox)₃Cl][K(15C5)₂]. Despite the sensitivity, compounds **2.1–2.5** can all be synthesized on gram quantity scales.

Exposure of additional equivalents of ditox ligand to **2.1-2.5** did not yield divalent tetrakis(ditox) metal complexes. This suggests that the steric bulk of the ditox ligand is large enough to discourage the formation of homoleptic complexes with a coordination number higher than 3. Furthermore, multimetallic complexes comprised of metal tris(ditox) units with bridging ditox ligands have not been observed. However, when MnCl_2 is treated with 2 equiv of Kditox, crystals can be grown from the reaction mixture of $[(\text{ditox})_2\text{Mn}_2(\mu\text{-ditox})_2(\mu\text{-THF})]$. The presence of bridging ditox ligands establishes the ability of ditox to bridge transition metal centers, although the lack of any observation of such bridged species during the synthesis of the tris(ditox) complexes indicates preferential formation of monometallic tris(ditox) species over multimetallic species.

The strategies for the synthesis of tris(ditox) complexes of trivalent metals are outlined in Scheme 2.3. Treatment of MCl_3 ($\text{M} = \text{V}, \text{Cr}, \text{Fe}$) with 3 equiv of $\text{K}(\text{ditox})$ or $\text{Li}(\text{ditox})$ in THF results in the loss of 3 equiv of KCl or LiCl and formation of $\text{M}(\text{ditox})_3$ complexes ($\text{M} = \text{V}$ **2.6**, $\text{M} = \text{Cr}$ **2.7**, $\text{M} = \text{Fe}$ **2.8**). Products can be isolated by removal of THF in vacuo followed by dissolving the remaining residue in pentane. Subsequent filtration of the pentane soluble products followed by concentration and cooling to $-40\text{ }^\circ\text{C}$ overnight for crystallization yields compounds **2.6**, **2.7**, and **2.8** in respective yields of 50%, 54% and 60%. The cobalt analog, $\text{Co}(\text{ditox})_3$ (**2.9**), can be synthesized by oxidation of $[\text{Co}(\text{ditox})_3][\text{K}(\text{15C5})_2]$, **2.4**, with AgOTf in 23% yield. Similarly, divalent compounds $[\text{Cr}(\text{ditox})_3][\text{K}(\text{15C5})_2]$, **2.1**, and $[\text{Fe}(\text{ditox})_3][\text{K}(\text{15C5})_2]$, **2.3**, can be oxidized to their corresponding trivalent analogs $\text{Cr}(\text{ditox})_3$, **2.7**, and $\text{Fe}(\text{ditox})_3$, **2.8**, via silver ion. The trivalent tris(ditox) metal complexes are comparably sensitive as the previously discussed divalent complexes excepting the trivalent tris(ditox) iron **2.8** and trivalent tris(ditox) cobalt **2.9** complexes, which are more stable in the presence of common halogenated solvents.

Scheme 2.3



The ability to chemically cycle between the divalent and trivalent states of tris(alkoxide) metal complexes was unsuccessful for V, Mn and Ni. As previously reported, V(ditox)₃ shows no cathodic behavior electrochemically and is inert towards chemical reductants, as evidenced by the lack of reactivity with KC₈.⁶⁵ Thus it appears as if [V(ditox)₃]⁻ is thermodynamically inaccessible within a tris(alkoxide) platform. Oxidation of [Mn(ditox)₃]⁻ yields an immediate color change from colorless to red, however, the red material has not been isolable. Oxidation of [Ni(ditox)₃]⁻ results in nonspecific reactivity and the only isolable product being K(ditox) ligand, which was characterized crystallographically and via ¹H NMR; no detectable Ni(III) species were obtained. As such, [V(ditox)₃]⁻, Mn(ditox)₃, and Ni(ditox)₃ are the missing compounds for the series of tris(ditox) complexes of divalent and trivalent 3d metals of Group V to Group X.

2.4 X-ray Crystallography and Jahn-Teller Distortions

With a [K(15C5)₂] counter cation, single crystals can readily be obtained for the divalent tris(ditox) metal complex series (Cr, Mn, Fe, Co, Ni) via preparation of a concentrated solution of the desired complex in diethyl ether and cooling to -40 °C over a duration of 24 to 48 h. The single crystals typically exhibit a block morphology with preferential crystal formation along one axis to give a rectangular prismatic crystal shape. Crystal dimensions vary from 0.1 mm to 0.7 mm. Diffraction patterns were seen to be fairly weak, partially due to the high degree of rotational disorder of the ^tBu groups with the ditox ligand, and thus larger crystals were sought for acceptable diffraction data. With the exception of [Cr(ditox)₃][K(15C5)₂], all divalent compounds crystallize in the monoclinic space group *P2₁/c*. The chromium variant crystallized in the triclinic space group *P $\bar{1}$* . Refinement of the divalent complexes involved modeling the rotational disorder of the ^tBu groups as well as the positional disorder of both the 15-crown-5-ether molecules.

The structures of the series of divalent metal-tris(alkoxide) complexes **2.1-2.5** are presented in Figure 2.4. Selected bond lengths and selected bond angles are summarized in Table 2.1 and Table 2.2, respectively. The observed average M-O_{alk} bond distances follows a periodic trend as that decreases with decreasing ionic radii of the metal. Notably the correlation with ionic radii is stronger than a correlation with covalent radii, including the increased M-O_{alk} bond distance of Mn relative to Cr, suggesting the ionic bonding nature of the alkoxides. This is supported by no significant changes in the internal ligand metrics of the ditox ligands. The inert

nature of the ligand is exemplified by the constant O–C_{alk} bond distance, remaining at approximately 1.40 Å, throughout the series of divalent complexes. In a conceptually similar manner to the trans-influence, the O–C_{alk} bond distance need not be constant as it could elongate in the presence of a strong bonding interaction between the metal and the oxygen atom of the alkoxide. In the structure of Kditox, the O–C_{alk} distance is observed to contract (1.38 Å). Thus, in comparing ditox in a traditional ionic bond (Kditox) to the more covalent bonds found in compounds **2.1-2.5**, the O–C_{alk} bond distance increases by 0.02 Å. This suggests that an increased covalency in the metal-ditox bond causes an elongation of the O–C_{alk} bond distance of ditox. However, the structural constancy of the entire ditox ligand throughout the divalent series of complexes additionally suggests that, while more covalent than the correspond K–O_{alk} bond, the divalent M–O_{alk} bond remains primarily ionic in nature

Table 2.1 Selected empirical bond distances for compounds **2.1-2.5** presented in angstroms with standard uncertainties in parenthesis.

	d(M–O1)	d(M–O2)	d(M–O3)	Avg d(O–C)
Tris(ditox) Divalent Metal Compound				
Cr	1.905(1)	1.929(1)	1.918(1)	1.400
Mn	1.935(2)	1.930(2)	1.927(3)	1.391
Fe	1.864(2)	1.870(2)	1.865(2)	1.400
Co	1.881(3)	1.856(3)	1.854(3)	1.392
Ni	1.832(3)	1.847(2)	1.870(2)	1.401
Tris(ditox) Trivalent Metal Compounds				
V	1.853(2)	1.820(2)	1.854(2)	1.430
Cr	1.760(4)	1.772(3)	1.789(4)	1.451
Fe	1.823(1)	1.823(1)	1.826(1)	1.424

^aBond distances in the tris(ditox) divalent metal complex series attributed to Jahn-Teller distortions are bold

Table 2.2 Selected empirical bond angles for compounds **2.1-2.5** with standard uncertainties in parenthesis.^b

	∠(O1–M–O2)	∠(O1–M–O3)	∠(O2–M–O3)	Sum of angles
Tris(ditox) Divalent Metal Compounds				
Cr	105.2(1)	120.7(1)	133.9(1)	359.8
Mn	120.1(1)	119.6(1)	120.1(1)	359.8
Fe	120.2(1)	120.1(1)	119.6(1)	359.9
Co	124.7(2)	115.3(2)	119.9(2)	359.9
Ni	130.1(1)	112.7(2)	115.8(1)	358.6
Tris(ditox) Trivalent Metal Compounds				
V	119.6(1)	121.5(1)	116.0(1)	356.1
Cr	119.1(2)	124.9(2)	116.0(2)	360.0
Fe	113.4(1)	119.9(1)	118.9(1)	352.2

^bBond angles in the tris(ditox) divalent metal complex series attributed to Jahn-Teller distortions are bold

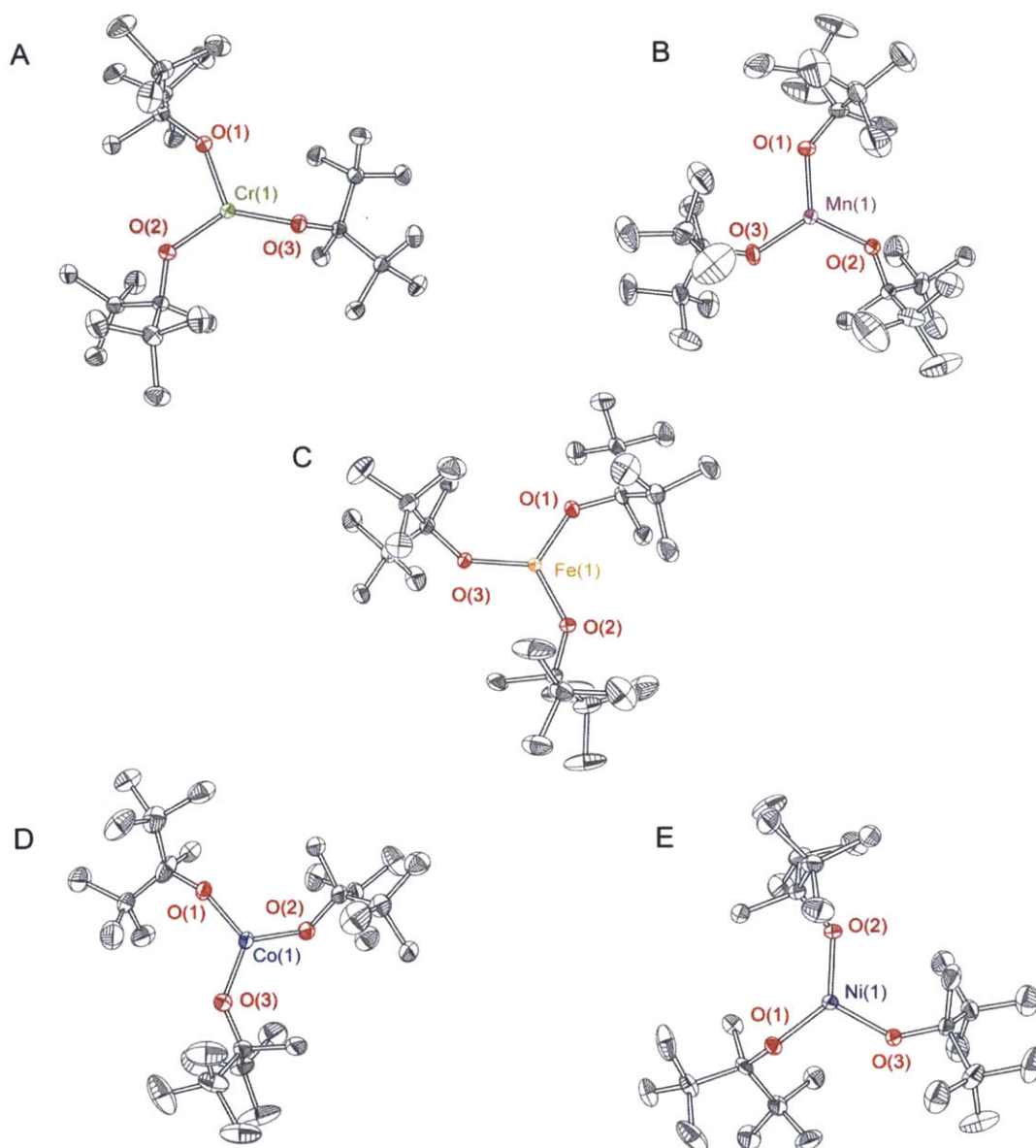


Figure 2.4. Single crystal x-ray diffraction structures for the series of divalent metal compounds $[M(\text{ditox})_3][\text{K}(15\text{C}5)_2]$ for (A) Cr, (B) Mn, (C) Fe, (D) Co and (E) Ni. Thermal ellipsoids presented at 50% probability density. Hydrogen atoms and $[\text{K}(15\text{C}5)_2]$ cation omitted from all structures for clarity.

The geometry around the metal of complexes **2.1-2.5** can be described as trigonal planar with pseudo- D_{3h} symmetry. Insight into the electronic structure of the complexes can be gleaned from analysis of distortions from an idealized geometry. Compounds **2.2**, $[\text{Mn}(\text{ditox})_3][\text{K}(15\text{C}5)_2]$, and **2.3**, $[\text{Fe}(\text{ditox})_3][\text{K}(15\text{C}5)_2]$, display a nearly unperturbed pseudo- D_{3h} geometry. All three $\text{M}-\text{O}_{\text{alk}}$ bond lengths for **2.2** and **2.3** are the same, 1.93 Å and 1.87 Å respectively, and all $\text{O}_{\text{alk}}-\text{M}-\text{O}_{\text{alk}}$ bond angles are an expected 120° . Consequently, a d orbital

manifold will not reflect Jahn-Teller distortions for these d^5 and d^6 electron counts. However, distortions are observed for **2.1**, $[\text{Cr}(\text{ditox})_3][\text{K}(\text{15C5})_2]$, and **2.4**, $[\text{Co}(\text{ditox})_3][\text{K}(\text{15C5})_2]$ as bond distances are no longer internally consistent. Two of the three bond angles deviate from the idealized 120° geometry. As such, the d orbital splitting manifold is described by a D_{3h} d orbital ligand field as shown in Figure 2.5 (center) with a lowest energy nonbonding a_1' (d_{z^2}) orbital, followed by $\pi^* e''$ (d_{xz}, d_{yz}) degenerate orbitals, and highest energy $\sigma^* e'$ ($d_{x^2-y^2}, d_{xy}$) degenerate orbitals. Single point DFT calculations performed on the observed geometries substituting ditox for the smaller $t\text{-BuO}^-$ ligand confirm the d orbital splitting diagram.

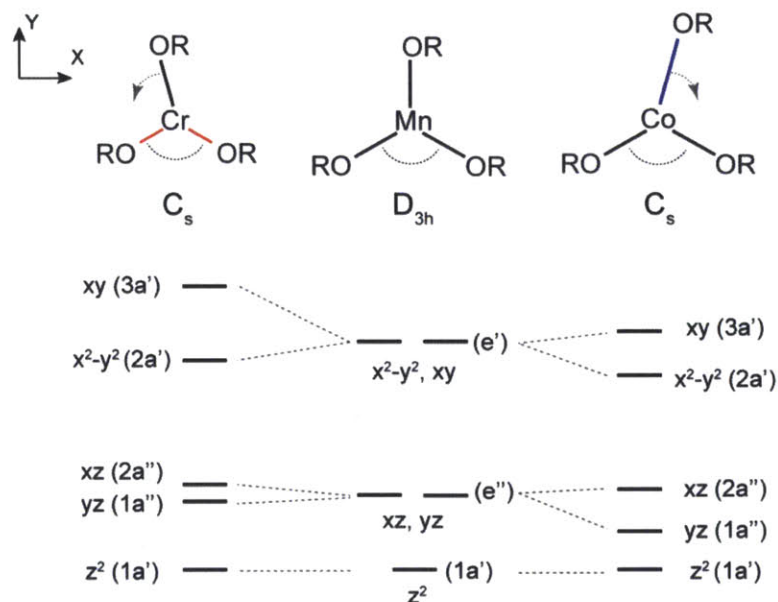


Figure 2.5. Qualitative d orbital splitting for divalent metal tris(alkoxide) complexes. (Center) Idealized D_{3h} geometries found for compounds **5.2** and **5.3**. (Left) Red lines indicates bond lengths shortening. Geometry based on structure of compound **5.1**. (Right) Blue line indicates a bond length elongating. Geometry based on structure of **5.4**.

As shown in Table 2.1 and Table 2.2, the nature of the observed Jahn-Teller distortions for compound **2.1**, $[\text{Cr}(\text{ditox})_3][\text{K}(\text{15C5})_2]$ and **2.4**, $[\text{Co}(\text{ditox})_3][\text{K}(\text{15C5})_2]$ are fundamentally different. The different distortions affect the d orbitals manifold of these respective complexes uniquely, as outlined in Figure 2.5. In a D_{3h} geometry, compound **2.1** would have an asymmetrically filled $\sigma^* e'$ orbital (σ -based Jahn Teller distortion) whereas compound **2.4** would have an asymmetrically filled $\pi^* e''$ orbital (π -based Jahn Teller distortion). The manner in which the geometry distorts for a σ -based distortion is significantly different from that for a π -based distortion.

For compound **2.1** there is an observed contraction of two bond lengths: M–O(1) and M–O(3) (Table 2.1), which are on average 0.015 Å shorter than the unperturbed bond lengths found for the d^5 compound **2.2**, [Mn(ditox)₃][K(15C5)₂]. These bonds are highlighted in red in Figure 2.5. Additionally, the third M–O(2) bond that rotates away from the idealized 120° bond angle geometry. Thus, the bond angle contraction does not originate from a distortion of the metal alkoxide bond. This is pictorially represented in Figure 2.5 (left). In considering the effects of these two perturbations, the bond length contractions should destabilize the d_{xy} orbital due to superior orbital overlap while the bond angle perturbation should result in poorer overlap with $d_{x^2-y^2}$ and consequently stabilize the orbital. The destabilization of d_{xy} is tolerated for the d^4 compound **2.1**, [Cr(ditox)₃][K(15C5)₂], as the orbital is unoccupied. This qualitative d orbital splitting diagram is supported by a single point calculation on truncated molecule [Cr(O^tBu)₃][−]. No geometry optimization was performed in order to more accurately assess the specific effects of the experimentally observed distortions.

For compound **2.4**, [Co(ditox)₃][K(15C5)₂], which presents a π -based distortion, only one bond length is observed to perturb, M–O(1) in Table 2.2. This bond, which is highlighted in blue in Figure 2.5 is 0.01 Å longer than the average bond length found for compound **2.3**, [Fe(ditox)₃][K(15C5)₂], which is unperturbed. Unlike in compound **2.1**, the M–O(1) bond vector of **2.4** is observed to be further perturbed by a rotation away from an ideal 120° bond angle as depicted in Figure 2.5 (right). In considering the effects of these two perturbations, both can be thought to stabilize the $d_{x^2-y^2}$ orbital by minimizing orbital overlap while having minimal effect on the destabilization of d_{xy} . Additionally, both perturbations should result in worse orbital overlap with the π^* orbital d_{yz} while having minimal effect on d_{xz} . Single point DFT calculations on the truncated molecules [Co(O^tBu)₃][−] confirm the proposed d orbital ordering and relative orbital energies with respect to undistorted [Mn(O^tBu)₃][−]. As a result, it is seen that the more electron rich **2.4**, with all d orbitals at least partially occupied, distorts in a manner that is fundamentally *stabilizing*. In contrast, the more electron deficient **2.1**, with an unoccupied d_{xy} distorts in a manner that is fundamentally *destabilizing*.

Unmentioned to this point is the structure of compound **2.5**, [Ni(ditox)₃][K(15C5)₂]. The coordination geometry can be described as Y-shaped, with one bond angle much larger than 120°, O(1)–M–O(2) = 130°, and two bond angles much smaller than 120°, O(1)–M–O(3) = 113° and O(2)–M–O(3) = 116°. While not common, this distortion is in agreement with that which is

reported for other three coordinate Ni(II) complexes, stabilized by mesityl⁶⁶ and amides.⁶⁷ Thus, while d^8 three-coordinate Ni(II) is not expected to distort *a priori*, tris(alkoxide), tris(mesityl) and tris(amide) ancillary ligand fields all support distorted Y-shaped trigonal Ni(II) geometries.

The crystal structures for the trivalent metal tris(ditox) complexes V(ditox)₃THF (**2.6-THF**), Cr(ditox)₃ (**2.7**) and Fe(ditox)₃THF (**2.8-THF**) are presented in Figure 2.6. Selected bond distances can be found in Table 2.1 and selected bond angles are reported in Table 2.2. Crystals of **2.6-THF** and **2.8-THF** were grown by cooling a concentrated solution of the respective complexes in a 10:1 mixture of pentane/THF to -40°C for 24 to 48 h. Compounds **2.6** and **2.8** crystallize in a distorted trigonal pyramidal geometry with a molecule of tetrahydrofuran coordinated in the apical position and the metal center slightly out of the plane of the supporting ditox ligands. Single crystals of compounds **2.7**, Cr(ditox)₃, and **2.9**, Co(ditox)₃, were unable to be prepared in a similar method. In general, single crystal X-ray diffraction data suitable for refinement has been difficult to obtain for the trivalent metal tris(alkoxide) series. The three coordinate nature and three fold geometry of the species with no supporting cation typically affords hexagonal space groups. In concert with rotational disorder about the metal center, properly refined crystal structures of trigonal species are either elusive or difficult to obtain. In the absence apically of coordinating ligands, compounds **2.7** and **2.9** can be crystallized from pure pentane solutions, but structures cannot be refined. The reported structure of compound **2.7**, Cr(ditox)₃, in Figure 2.6 was obtained due to a serendipitous co-crystallization with Cr(ditox)₃Cl. The packing effects from the co-crystallization could be the cause of the large distortion away from an idealized trigonal planar geometry observed for Cr(ditox)₃. The average Cr–O_{alk} bond distances are found to be on average 0.05 Å shorter than that of the M–O_{alk} bond distances found in trivalent compounds **2.6-THF** and **2.8-THF**. This is attributed to a lower coordination number for compound **2.7** resulting in a stronger electrostatic interaction between the metal and ligand, and thus a shorter metal–ligand bond distance.

Comparison of the trivalent metal series with the divalent series reveals a noticeable difference in the manner to which the alkoxides bind trivalent metal cations. As previously described, the structural parameters for the divalent series suggest that the structure reflects a more ionic bonding motif as the M–O_{alk} bond distance vary with the ionic radii (and minimal ligand variation is therefore seen). Comparing trivalent compounds **2.6-THF** and **2.8-THF** to the divalent metal series of tris(ditox) complexes, the M–O_{alk} bond distances are observed to contract

uniformly by 0.05 Å. The contraction of the $M-O_{alk}$ bond in the trivalent complexes is more striking when considering a trivalent metal compound with the same coordination number as the divalent complexes, as the three coordinate **2.7** is found to have $M-O_{alk}$ bond distances that are contracted on average 0.10 Å relative to the three coordinate divalent metal complexes. This is attributed to the more oxidized metal cation of the trivalent metal series having a smaller radius.

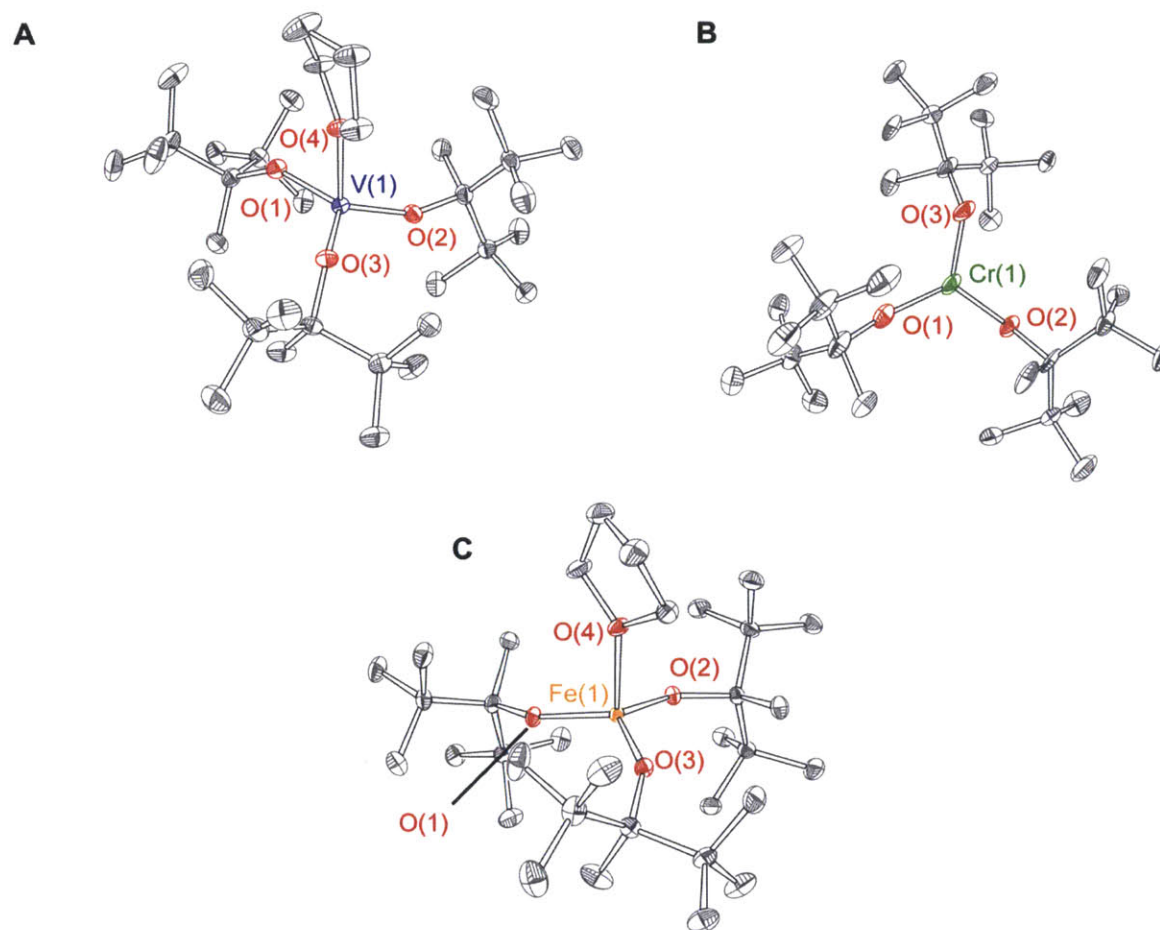


Figure 2.6. Single crystal x-ray diffraction structures for the series of trivalent metal compounds $M(\text{ditox})_3$ for (A) V, (B) Cr, and (C) Fe. $V(\text{ditox})_3$ and $Fe(\text{ditox})_3$ are found to crystallize with a bound apical THF molecule. Thermal ellipsoids presented at 50% probability density. Hydrogen atoms are omitted from all structures for clarity. Selected bond distances and selected bond angles can be found in Table 2.1 and Table 2.2, respectively.

Unlike the invariant $O-C_{alk}$ bond distance with respect to the $M-O_{alk}$ bond distance of the divalent metal tris(ditox) series, the trivalent series shows an elongation of the $O-C_{alk}$ distance correlated to a contraction in $M-O_{alk}$ distance. The $O-C_{alk}$ distance within the trivalent metal series is found to increase between 0.25 Å and 0.50 Å. This empirical evidence suggests a

significantly stronger metal alkoxide bond within trivalent compounds and the variability in response to the population of the d orbital manifolds reflects a significantly higher degree of covalency in the trivalent metal alkoxide bond.

These observed structural characteristics of the trivalent series of metal tris(ditox) complexes support a bonding model wherein the metal alkoxide bond is significantly more covalent in nature compared to the divalent series. This can be rationalized by the more oxidized metal centers being more electronegative and thus more energetically proximate to mix with the oxygen based p orbitals. This effect is commonly observed in metal oxide surfaces. As a metal-oxide surface is oxidized, the metal based d orbitals become more energetically equivalent to oxygen based p orbitals.⁶⁸ For example, valence band photoelectron spectroscopy shows that the energetic difference between the $O(2p)$ orbitals and the $Cr(3d)$ orbitals decreases from nearly 2 eV in a Cr_2O_3 surface to about 1 eV in CrO_2 .⁶⁹ Additionally, whereas the $Fe(3d)$ and $O(2p)$ orbitals have distinct energetic populations in an FeO surface, the $Fe(3d)$ and $O(2p)$ orbitals contribute equally to all valence orbital energy levels in Fe_2O_3 .⁶⁸ This results in a higher degree of covalency and delocalization of electron density upon oxidation. Thus, the manner in which divalent metals to bind to ditox in an ionic nature and trivalent metals appear to bind to ditox in a more covalent nature approximately mimic the behavior found in metal-oxide surfaces. Further oxidations would be predicted to be delocalized to a greater extent across the metal and the alkoxides analogously to a metal-oxyl radical formation in a metal oxide surface.

2.5 Magnetism

Magnetic susceptibilities were measured via room temperature Evans methods procedure, as ^{19}F NMR analyses were performed on THF/ C_6F_6 solutions of compounds **2.1-2.9**. The summary of calculated magnetic moments is presented in Table 2.3. Unsurprisingly the low coordination numbers of compounds **2.1-2.9** in solution afford high spin states at room temperature. Observed magnetic moments correlate very closely to predicted spin only values even in cases where larger angular orbital contributions would be expected, such as d^2 $V(ditox)_3(THF)$, d^4 $[Cr(ditox)_3][K(15C5)_2]$, and d^7 $[Co(ditox)_3][K(15C5)_2]$. In these cases, magnetic moments more similar to spin only values can be rationalized upon considering the significance of the aforementioned structural distortions observed in the solid state. If it is assumed that these distortions persist in the solution phase, then asymmetrically occupied

degenerate orbitals would lose degeneracy. Thus, the low coordinate tris(alkoxide) platform affords high spin states with magnetic susceptibilities near those of spin only values for both the divalent and trivalent metal tris(ditox) complexes, which suggests solid state distortions persist in the solution.

Table 2.3 Magnetic susceptibilities determined via Evans method for compounds divalent metal and trivalent metal tris(ditox) complexes **2.1-2.9** in THF solution at room temperature.

Metal	Oxidation State	Magnetic Moment (BM)	Spin State
V	II	N/A	N/A
	III	2.7	S=3
Cr	II	4.3	S=5
	III	3.6	S=4
Mn	II	6.0	S=6
	III	N/A	N/A
Fe	II	4.9	S=5
	III	5.9	S=6
Co	II	4.5	S=4
	III	5.1	S=5
Ni	II	2.6	S=3
	III	N/A	N/A

2.6 Infrared Spectroscopy

Due to the paramagnetic nature of the divalent and trivalent metal tris(ditox) complexes, NMR spectroscopies provides little interpretable information with regard to composition and purity of materials. The ability to characterize these divalent and trivalent metal complexes structurally has afforded the opportunity to correlate structure and purity confidently to infrared spectra. As such, IR spectroscopy has become an efficient and practical method to analyze and characterize samples of metal tris(ditox) complexes. Historically, IR spectroscopy has been useful for characterization of metal alkoxide complexes due to the complex geometry and low molecular symmetry of the initially synthesized metal alkoxide complexes.⁷⁰⁻⁷² Seminal work by Barraclough and coworkers was instrumental in parsing the often complicated spectra and identifying the signature $\nu(\text{M-O}_{alk})$ and $\nu(\text{MO}_{alk}\text{-R})$ frequencies for a series of metal alkoxide compounds.⁷⁰ This has afforded an abundance of data with which to guide the interpretation of the spectra of monometallic tris(ditox) complexes.^{71,72}

Vibrational spectra of metal alkoxide complexes are typically analyzed by assessing the $\nu(\text{M}-\text{O}_{alk})$ region, approximately 800 cm^{-1} to 450 cm^{-1} , and the $\nu(\text{MO}_{alk}-\text{R})$ region, approximately 1200 cm^{-1} to 800 cm^{-1} . The IR spectrum of compound **2.5**, $[\text{Ni}(\text{ditox})_3][\text{K}(\text{15C5})_2]$, is presented in Figure 2.7 as a sample spectrum that highlights the primary features observed in the spectra of the divalent metal tris(ditox) complexes.

There are five main regions within each spectra and they are identified A-E in Figure 2.7. The $\nu(\text{MO}_{alk}-\text{R})$ region is divided into four bands of stretches labeled A, B, C and D. The $\nu(\text{MO}_{alk}-\text{R})$ vibrational frequencies of metal alkoxide complexes couple strongly with $\nu(\text{C}-\text{C})$ vibrations of the alkoxide. The complicated patterns observed for metal alkoxides becomes more complex with a larger number of C-C bonds within the alkoxide. For example, methoxide is observed to display two IR vibrations whereas *iso*-propoxide displays six IR vibrations.⁷¹ As ditox has a large number of C-C bonds (9 unique bonds) the assignment of the $\nu(\text{MO}_{alk}-\text{R})$ region of the divalent metal tris(ditox) complexes becomes difficult. The $\nu(\text{M}-\text{O}_{alk}\text{R})$ labeled region is identified as between 700 cm^{-1} and 500 cm^{-1} as E in Figure 2.7.

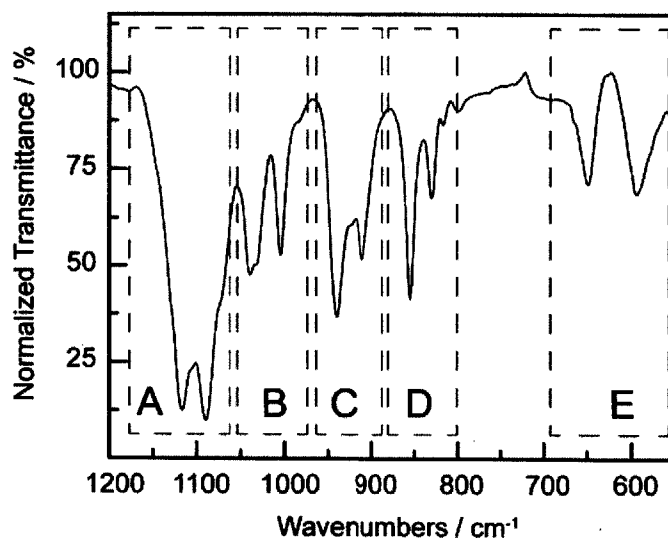


Figure 2.7. Infrared spectrum of $[\text{Ni}(\text{ditox})_3][\text{K}(\text{15C5})_2]$ depicted this common bands of vibrational stretching frequencies in the $[\text{M}(\text{ditox})_3][\text{K}(\text{15C5})_2]$ series of complexes. Regions A-D are assigned to $\nu(\text{MO}_{alk}-\text{R})$ vibrational frequencies which couple with internal ligand $\nu(\text{C}-\text{C})$ vibrational frequencies. Region E is assigned to the $\nu(\text{M}-\text{O}_{alk}\text{R})$ vibrational frequencies. A summary of the observed peaks within the 1200 cm^{-1} to 500 cm^{-1} range for compounds **2.1-2.5** can be found in Table 2.4.

The IR spectra for divalent metal compounds **2.1-2.5** are overlaid in Figure 2.8 and summarized in Table 2.4. Compounds **2.1-2.5** exhibit virtually identical stretches in the $\nu(\text{MO}_{\text{alk}}-\text{R})$ region. Four distinct and conserved bands of $\nu(\text{MO}_{\text{alk}}-\text{R})$ stretches of the divalent metal series are difficult to assign due to the previously discussed complex splitting patterns and broadening associated with strong coupling to internal C–C vibrations from the ligands. Additionally, the counter cation, $[\text{K}(\text{15C5})_2]^+$ exhibits $\nu(\text{C}-\text{O})$ and $\nu(\text{C}-\text{C})$ stretching frequencies in a similar region, thus making assignments additionally challenging. The structural distortions of the divalent compounds are not manifested in the observed stretching frequency pattern. The number of distinct peaks and the energy of the peaks are remarkably conserved across the series, varying by 5 cm^{-1} at most. As a result, we conclude that the changes in electronic structure by varying the metal center do not significantly affect the bonding internally within the ligand. This is again consistent with significant ionic bonding of ditox to the divalent metal centers. There are two clearly identifiable stretches assigned to a higher energy conventional $\nu(\text{M}-\text{O}_{\text{alk}}\text{R})$ stretching mode, observed between 660 cm^{-1} and 645 cm^{-1} , and a lower energy $\nu[(\text{RO}_{\text{alk}})-\text{M}-(\text{O}_{\text{alk}}\text{R})]$ bending mode, observed between 595 cm^{-1} and 580 cm^{-1} . The similarity of these stretching frequencies suggest uniformity in the coordination environment across the divalent tris(ditox) metal complexes.

Table 2.4 Summary of observed IR Frequencies (cm^{-1}) for the series of divalent metal complexes $[\text{M}(\text{ditox})_3][\text{K}(\text{15C5})_2]$.

Metal	$\nu(\text{M}-\text{O}_{\text{alk}}\text{R})$	$\nu(\text{MO}_{\text{alk}}-\text{R})$ Band (D)	$\nu(\text{MO}_{\text{alk}}-\text{R})$ Band (C)	$\nu(\text{MO}_{\text{alk}}-\text{R})$ Band (B)	$\nu(\text{MO}_{\text{alk}}-\text{R})$ Band (A)
Cr	658, 588	856, 830, 817	940, 923, 909	1041, 1032 1006, 985	1118, 1105, 1090
Mn	646, 581	855, 830, 818	940, 915, 890	1040, 1030 1008, 982	1118, 1107, 1090
Fe	662, 592	855, 830, 817	939, 919, 905	1039, 1031, 1010, 981	1117, 1102, 1090,
Co	652, 587	855, 829, 816	939, 914, 900	1039, 1031, 1006, 978	1117, 1102, 1090
Ni	649, 595	830, 817	940, 911, 890	1039, 1032, 1005, 983	1117, 1103, 1090

The IR spectra of the trivalent metal tris(ditox) complexes **2.6-2.9** are overlaid in Figure 2.9 and summarized in Table 2.5. In a similar manner to the divalent series, the $\nu(\text{MO}_{\text{alk}}-\text{R})$ stretching frequencies observed to have three distinct bands whose splitting and patterns are complicated due to internal C–C vibrational coupling. Of note, fewer total number of $\nu(\text{M}-\text{O}_{\text{alk}})$ features are observed for the trivalent metal series owing to the lack of crown-ether stretches present for the trivalent series. Additional strong features observed in compound **2.6-THF**,

$V(\text{ditox})_3\text{THF}$, and compound **2.8**, $\text{Fe}(\text{ditox})_3\text{THF}$, at 944 cm^{-1} and 938 cm^{-1} are assigned to $\nu(\text{C-O})$ vibrations of the apically bound THF molecule.

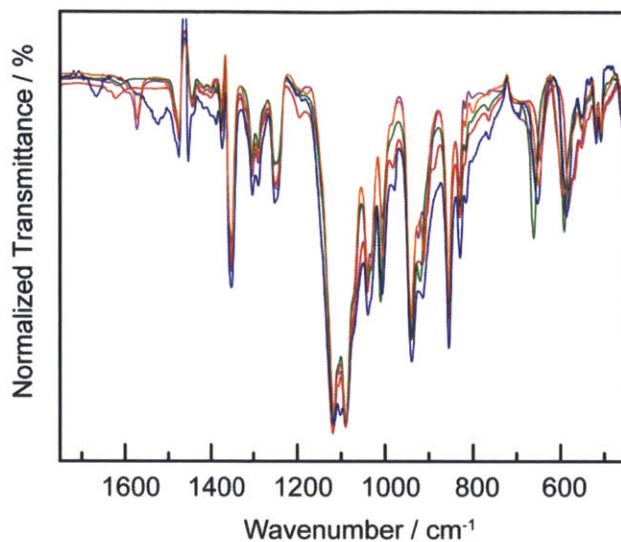


Figure 2.8. Overlay of the normalized transmittance infrared spectra of divalent metal compounds **2.1–2.5** showing the similarity of the vibrational frequencies throughout the series of complexes, suggesting isomorphous structures and similar bonding interactions. (red) $[\text{Cr}(\text{ditox})_3][\text{K}(\text{15C5})_2]$, (orange) $[\text{Mn}(\text{ditox})_3][\text{K}(\text{15C5})_2]$, (green) $[\text{Fe}(\text{ditox})_3][\text{K}(\text{15C5})_2]$, (blue) $[\text{Co}(\text{ditox})_3][\text{K}(\text{15C5})_2]$, (purple) $[\text{Ni}(\text{ditox})_3][\text{K}(\text{15C5})_2]$.

Analysis of the internal alkoxide $\nu(\text{M}\text{O}_{\text{alk}}\text{R})$ vibrations of the trivalent metal tris(ditox) series of complexes is in accord with more covalent bonding of the alkoxide ligand. Because of better mixing of metal and ligand orbitals, a greater variance in frequency is expected, and indeed observed. The ligand vibrations vary upwards of 20 cm^{-1} for the trivalent metal series whereas no more than a 5 cm^{-1} variance is observed for the divalent metal series (Table 2.5).

Table 2.4 shows that there are two $\nu(\text{M}\text{O}_{\text{alk}}\text{R})$ features in the IR spectra for the trivalent series. As in the case of the divalent metal complexes, these are similarly assigned to be a high energy $\nu(\text{M}\text{O}_{\text{alk}}\text{R})$ stretching mode and a low energy $\nu[(\text{RO}_{\text{alk}})\text{M}(\text{O}_{\text{alk}}\text{R})]$ bending mode. These features are shifted to higher energy relative to the divalent series. The $\nu(\text{M}\text{O}_{\text{alk}}\text{R})$ stretching feature shifts to $725\text{--}685\text{ cm}^{-1}$ from $660\text{--}645\text{ cm}^{-1}$ and the $\nu[(\text{RO}_{\text{alk}})\text{M}(\text{O}_{\text{alk}}\text{R})]$ feature shifts to $605\text{--}590\text{ cm}^{-1}$ from $595\text{--}580\text{ cm}^{-1}$. This observed shift to higher energy is ascribed to the increased oxidation state of the metal in the trivalent series resulting in a stronger electrostatic interaction between the metal and alkoxide. This is also in agreement with an

interpretation of a higher degree of covalency between the metal and alkoxide ligand in the trivalent series.

Table 2.5 Summary of observed IR Stretches for the series of trivalent metal complexes $M(\text{ditox})_3$.

Metal	$\nu(\text{M}-\text{O}_{\text{alk}}\text{R})$	$\nu(\text{MO}_{\text{alk}}-\text{R})$ Band (D)	$\nu(\text{MO}_{\text{alk}}-\text{R})$ Band (C)	$\nu(\text{MO}_{\text{alk}}-\text{R})$ Band (B)	$\nu(\text{MO}_{\text{alk}}-\text{R})$ Band (A)
V	718, 603	864, 834	961, 944, 933, 928, 921, 909	1039, 1016 1005, 997	1101, 1080
Cr	723, 599	876, 835	938, 923	1021, 998	1100, 1076
Fe	688, 592	870, 832	938, 923, 919	1030, 1002	1097, 1082
Co	714, 602	874, 832	962, 940, 924, 894	1025, 1002	1099, 1079

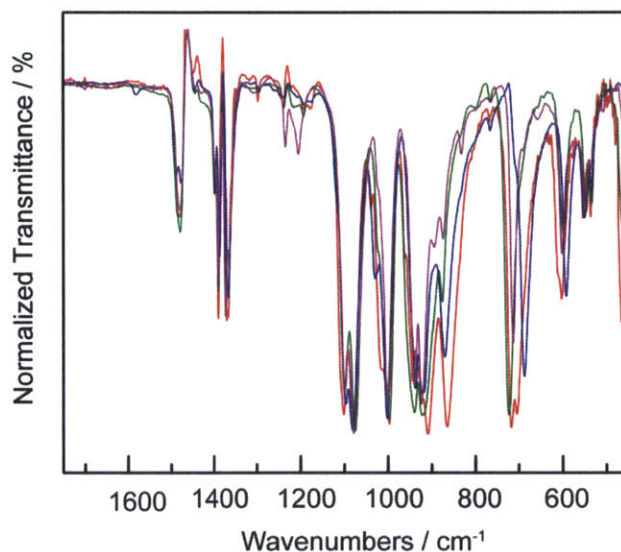


Figure 2.9. Overlay of the normalized transmittance infrared spectra of trivalent metal compounds **2.6–2.9** showing the similarity of the vibrational frequencies throughout the series of complexes, suggesting isomorphous structures and similar bonding interactions. (red) $\text{V}(\text{ditox})_3\text{THF}$, (green) $\text{Cr}(\text{ditox})_3$, (blue) $\text{Fe}(\text{ditox})_3\text{THF}$, (purple) $\text{Co}(\text{ditox})_3$.

2.7 UV-vis Spectroscopy

Electronic absorption spectra were acquired in solutions of THF at room temperature. A summary of the absorption data collected is presented in Table 7. The absorption spectrum of compound **2.6**, $[\text{Fe}(\text{ditox})_3][\text{K}(\text{15C5})_2]$, presented in Figure 2.10, is exemplar of the metal-tris(ditox) complexes. The absorption profile is dominated by an intense feature in the UV and a weak feature in the visible spectral region.

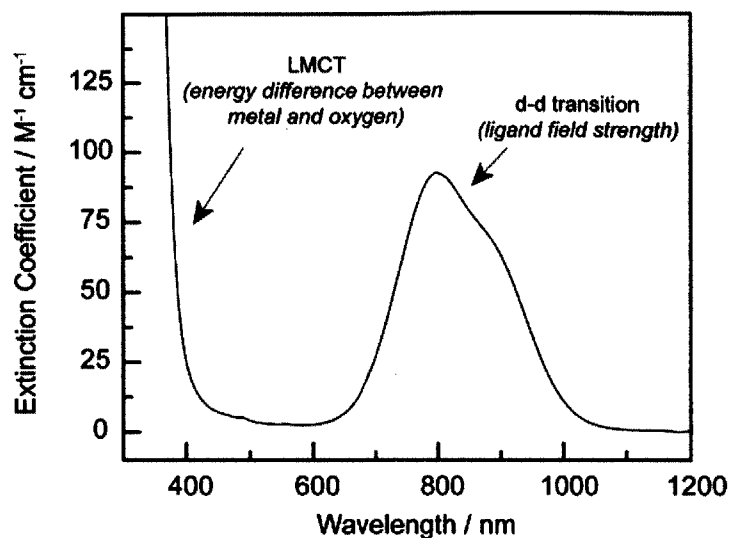


Figure 2.10. Electronic absorption spectrum of a tetrahydrofuran solution of $[\text{Fe}(\text{ditox})_3][\text{K}(15\text{C}5)_2]$ (**2.3**) depicting the two major features in the electronic absorption spectra of tris(ditox) compounds **2.1–2.9**: an intense ligand to metal charge transfer (LMCT) feature in the ultra-violet range and two overlapping and weakly absorbing d–d transition in the visible range. Assuming a D_{3h} geometry the transitions at 798 and 890 have been assigned to ${}^5A'_1 \rightarrow {}^5E'$ and ${}^5A'_1 \rightarrow {}^5E''$ transitions respectively.

Table 2.6 Summary of UV-Vis Spectra Features for compounds **2.1–2.9**.

	λ max (nm)	ϵ at 400 nm ($\text{M}^{-1} \text{cm}^{-1}$)
Divalent Series		
Cr	675, 880 (sh)	44
Mn	none	7
Fe	798, 890 (sh)	91
Co	672, 1235	130
Ni	488, 788	25
Trivalent Series		
V	626, 775 (sh), 972	65
Cr	680, 790 (sh), 1030	88
Fe	none	1830
Co	387 (sh), 677, 720 (sh)	664

The UV absorption band, based on other metal alkoxide complexes,⁷³ is assigned as a ligand to-metal-charge transfer (LMCT) absorption ($\text{O}(p) \rightarrow \text{Metal}(d)$). The LMCT feature is qualitatively related to the energetic difference between the alkoxide based oxygen orbitals and the metal based orbitals. As the metal is oxidized, this energy gap should decrease due to the metal becoming more electrophilic and closer in energy to the oxygen p orbitals of the alkoxide. Consequently the LMCT feature should blue shift upon metal oxidation. This trend is observed using the extinction coefficient at 400 nm as a benchmark as to the extent to which the LMCT feature absorbs into the visible region (Table 2.6), it is observed that there is significantly greater

absorption at 400 nm in the trivalent series relative to the divalent series. This difference is most striking in the isoelectronic d^5 $[\text{Mn}(\text{ditox})_3][\text{K}(\text{15C5})_2]$ (**2.2**) and $\text{Fe}(\text{ditox})_3$ (**2.7**) complexes. The absorption spectra of these two high spin d^5 compounds display no absorptions attributable to a $d-d$ transition, and as such all absorption can confidently be assigned to the LMCT transitions. In the divalent state, the d^5 tris(ditox) complex has an extinction coefficient of $7 \text{ M}^{-1} \text{ cm}^{-1}$ whereas the trivalent d^5 tris(ditox) complex has an extinction coefficient of 1830 cm^{-1} , indicating a significantly smaller energy gap between frontier metal based orbitals and occupied ligand orbitals for trivalent metals.

The absorption feature at higher wavelength has very low extinction coefficients, $\sim 100 \text{ M}^{-1} \text{ cm}^{-1}$, and it is assigned to metal based $d-d$ electronic transitions. The assignment is in agreement with the absence of a feature in the high spin d^5 complexes. There is no clear trend observed in the energy of absorption feature across the divalent and trivalent series when the two series of considered independent of one another. This could be explained by ligand distortions present observed in the solid state structures persisting in the solution phase and altering the energetics of the d orbital manifolds in a manner that is not purely periodic. However, there is a trend observed when comparing the divalent and trivalent series to one another as the $d-d$ transition of isoelectronic complexes shifts to higher energy in the trivalent series. An example of this observation is found in comparing λ_{max} of the isoelectronic d^6 **2.3**, $[\text{Fe}(\text{ditox})_3][\text{K}(\text{15C5})_2]$, and **2.8**, $\text{Co}(\text{ditox})_3$ complexes. The primary $d-d$ transition for **2.3** is observed at 798 nm whereas the analogous transition for **2.8** is observed at 677 nm, representing a 110 nm shift to higher energy. This shift to higher energy in the trivalent series is in agreement with the metal alkoxide bond being stronger in the trivalent series due to stronger electrostatic interactions and higher degree of covalency.

Analysis of the electronic absorption features provides further evidence towards the increased covalency in the metal alkoxide bonds in the trivalent series, based on the shift of the LMCT absorption to lower energy and the shift of the $d-d$ transitions to higher energy.

In order to assess the relative ligand field strength afforded by a tris(alkoxide) platform, the $d-d$ transitions observed in $\text{Cr}(\text{ditox})_3$ can be compared to the $d-d$ transitions of trivalent chromium in other ligand fields. The $d-d$ transitions for $\text{Cr}(\text{ditox})_3$, 680 nm with a shoulder at 790 nm, are energetically lower than those reported for trigonal fields comprised on anionic sulfur and nitrogen ligands; $\text{Cr}(\text{SCH}_2\text{Ph})_3$ ⁷⁴, $\text{Cr}(\text{N}(\text{CHMePh})_2)_3$ ⁷⁵, $\text{Cr}(\text{N}(\text{SiMe}_3)_2)_3$ ⁷⁶ have $d-d$

transitions reported to occur around 600 nm, 467 nm, and 675 nm respectively. The $d-d$ transitions of $\text{Cr}(\text{ditox})_3$ are comparable to that which is reported for another three coordinate trivalent chromium compound with an oxygen rich ligand field; $\text{Cr}(\text{OSi}^t\text{Bu}_3)_3$ ⁷⁷ has a reported transition of 751 nm. The weaker $d-d$ transitions observed for $\text{Cr}(\text{ditox})_3$ and $\text{Cr}(\text{OSi}^t\text{Bu}_3)_3$ suggests that a primary coordination sphere that is oxygen rich affords a significantly weaker ligand field relative to nitrogen and sulfur analogs.

2.8 Concluding Remarks

Through tuning the steric bulk of the alkoxide ligand, $t\text{BuMeCO}^-$ (ditox) has been shown to stabilize monometallic tris(alkoxide) complexes of 3d transition metals via the initial synthetic strategy of Demarcay in 1875. A series of tris(ditox) divalent and trivalent transition metal complexes have been synthesized and characterized (**2.1-2.9**), representing one of the first series of three coordinate transition metal complexes supported by a homoleptic alkoxide ligand platform. Compound **2.1-2.9** extends this homoleptic alkoxide platforms to the growing class of three-coordinate metal complexes that have been instrumental to study of small molecule activation processes.^{78,79}

An understanding of the origins of structural distortions, electronic structure, as well as the nature of the ditox–metal bond has been gained through a comparison of the structural, magnetic, vibrational spectroscopic and electronic absorption data of compounds **2.1-2.9**. Upon oxidation from the divalent state to the trivalent state, the metal alkoxide bonding interaction appears to become more covalent relative to the ionic bond in the divalent state. The increasing covalency in a M–O bond with oxidation is found in metal-oxide surfaces which are relevant to O–O bond forming processes, suggesting that compound **2.1-2.9** can be viewed as homogeneous models of a single metal site of a metal-oxide. Chapters 3 and 4 will address the formation of high valent oxygen-rich species derived from the reduced complexes **2.1-2.9** and the subsequent reactivity.

2.9 Experimental Details and Computational Methods

2.9.1 General Considerations All reactions involving air-sensitive materials were performed in a nitrogen-filled glovebox. Solvents were purified using SG Water Glass Contour Solvent System and stored over 4-Å molecular sieves. Compounds were routinely characterized by IR, elemental analyses, and the X-ray analysis; selected compounds were characterized by NMR. IR spectra of powdered samples were recorded on a PerkinElmer Spectrum 400 FT-IR/FT-FIR Spectrometer outfitted with a Pike Technologies GladiATR attenuated total reflectance accessory with a monolithic diamond crystal stage and pressure clamp. All NMR spectra were recorded at the MIT Department of Chemistry Instrumentation Facility on a Varian Mercury 300 NMR spectrometer in C₆D₆ at room temperature. Magnetic moments were determined in C₆H₆ at room temperature on a Varian Mercury 300 NMR Spectrometer using Evans method.⁸⁰ Pascal constants were used to estimate diamagnetic correction. UV-vis measurements were recorded on a Varian Cary 5000 spectrometer and references to appropriate solvent. All UV-vis measurements were performed on sample in solutions of THF. Elemental analyses were performed by Midwest Microlab LLC. Methyl lithium (1.6 M in ether), 2,2,4,4-tetramethyl-3-pentanone, 15-crown-5-ether, VCl₃(THF)₃, CrCl₂, CrCl₃, MnCl₂, FeCl₂, Fe Br₂, FeCl₃, CoCl₂, NiCl₂ were purchased from Aldrich. ^tBu₂MeCOLi and ^tBu₂MeCOH (Liditox and Hditox, respectively, hereafter) were prepared according to literature procedures.⁸¹

2.9.2 Preparation of Kditox. 3.000 g (18.95 mmol) of Hditox was added as a solid in small portions over the course of 15 min to a solution of ether (50 mL) that contained 0.836 g (20.9 mmol) of KH. The solution was stirred for 15 min. The resulting white slurry was stirred at room temperature for 6 h or longer until gas evolution subsided. Diethyl ether solution was filtered through Celite and volatiles were removed in vacuo. Resulting white solid was extracted with pentane/diethyl ether mixture (5:1, ca 20 mL) and was filtered through Celite. The colorless solution was concentrated to ca. 4 mL and left to stand at -40 °C for 12 h. Colorless crystals were obtained, collected, and dried in vacuo (94.99% yield, 3.530 g, 18.00 mmol). Anal. Calcd. (Found) for C₁₀H₂₁KO: C, 60.25 (59.82); H, 12.11 (11.33). ¹H NMR (C₆D₆, 300 MHz) δ 1.10 (s, ^tBu), 0.96 (s, Me). IR (cm⁻¹): 1478 (m), 1389 (m), 1381 (m), 1360 (m), 1115 (s), 1084 (s), 1013 (sh), 996 (m), 945 (m), 926 (m), 897 (m), 877 (sh), 831 (sh), 675 (m), 649 (m), 583 (s), 560 (m), 537 (w), 495 (s).

2.9.3 Preparation of [Cr(ditox)₃][K(15C5)₂] (2.1). A 1.00 g (5.09 mmol) portion of Kditox in 3 mL of THF was added to the stirred turquoise tetrahydrofuran suspension (2 mL) of CrCl₂ (202 mg, 1.64 mmol). The ensuing homogeneous solution assumed a blue color. After 1 h, volatiles were removed in vacuo, and the residue was extracted with pentane (12 mL) and filtered through Celite. The blue pentane solution was collected and concentrated to 7 mL. To the solution an excess of 15-crown-5-ether was added (ca. 2 mL, 10.1 mmol) at room temperature and immediately a light blue precipitate formed. The reaction mixture was stirred as a light blue suspension for 30 min. The stirring was ceased and a light blue solid was allowed to settle to the bottom of the reaction vessel. The pale blue supernatant was removed via pipette. Remaining solid was washed 3 × 5 mL of pentane. The light blue solid was dissolved in diethyl ether (8 mL) and filtered through Celite. Diethyl ether solution was collected and concentrated to approximately 1 mL and the solution was left to stand at -40 °C for 24 h to give **2.1** in 62.7% yield (1.033 g, 1.026 mmol). Anal. Calcd. (Found) for C₅₀H₁₀₃CrKO₁₃: C, 59.85 (59.97); H, 10.35 (10.27). IR (cm⁻¹): 1485 (m), 1415 (m), 1392 (w), 1360 (m), 1118 (s), 1105 (sh), 1090 (s), 1041 (sh), 1032 (m), 1006 (sh), 985 (m), 940 (s), 923 (s), 909(m), 856 (s), 830 (m), 817 (w), 658 (m), 588 (m), 532 (w). UV-vis: 675 nm [94 M⁻¹cm⁻¹], 880 nm (sh) [21 M⁻¹ cm⁻¹]. $\mu_{\text{eff}} = 4.75 \mu\text{B}$

2.9.4 Preparation of [Mn(ditox)₃][K(15C5)₂] (2.2) A 1.00 g (5.09 mmol) portion of Kditox in 3 mL of THF was added to the stirred pale pink tetrahydrofuran suspension (2 mL) of MnCl₂ (207 mg, 1.64 mmol). The solution became cloudy and colorless. After 1 h, volatiles were removed in vacuo, and the residue was extracted with pentane (12 mL) and filtered through Celite. The colorless pentane solution was collected and concentrated to 7 mL. To the solution, an excess of 15-crown-5-ether was added (ca. 2 mL, 10.1 mmol) at room temperature and immediately a pale yellow precipitate formed. The reaction mixture was stirred as a pale yellow suspension for 30 min. The stirring was ceased and a pale yellow solid was allowed to settle to the bottom of the reaction vessel. The colorless supernatant removed via pipette. Remaining solid was washed 3 × 5 mL of pentane. The pale yellow solid was dissolved in diethyl ether (8 mL) and filtered through Celite. Diethyl ether solution was collected and concentrated to approximately 1 mL and the solution was left to stand at -40 °C for 24 h to give **2.2** in 55.6% yield (0.919 g, 0.913 mmol). Anal. Calcd. (Found) for C₅₀H₁₀₃O₁₃MnK: C, 59.67 (59.42); H, 10.32 (10.28). IR (cm⁻¹): 1475 (m), 1399 (w), 1390 (s), 1323 (m), 1303 (m), 1289 (m), 1250 (m), 1211 (w), 1118 (s), 1107 (sh), 1090 (s), 1040 (sh), 1030 (m), 1008 (m), 982 (m), 940 (w), 915

(s), 890 (m), 855 (w), 830 (s), 818(m), 646 (m), 581 (m), 532 (w). UV-vis: No detectable features observed. $\mu_{\text{eff}} = 6.00 \mu\text{B}$.

2.9.5 Preparation of [Fe(ditox)₃][K(15C5)₂] (2.3) A 1.00 g (5.09 mmol) portion of Kditox in 3 mL of THF was added to the stirred pale yellow tetrahydrofuran suspension (2 mL) of FeBr₂ (366 mg, 1.70 mmol). The ensuing homogeneous solution assumed a green color. After 2 h, volatiles were removed in vacuo, and the residue was extracted with pentane (12 mL) and filtered through Celite. Pentane solution was collected and concentrated to 7 mL. To the solution an excess of 15-crown-5-ether was added (ca. 2 mL, 10.1 mmol) at room temperature and immediately a light green precipitate formed. The reaction mixture was stirred as a light green suspension for 30 min. The stirring was ceased and a light green solid was allowed to settle to the bottom of the reaction vessel. Colorless supernatant was removed via pipette. Remaining solid was washed 3 × 5 mL of pentane. The light green solid was dissolved in diethyl ether (8 mL) and filtered through Celite. Diethyl ether solution was collected and concentrated to approximately. 1 mL the solution was left to stand at -40 °C for 24 h to give **2.3** in 54.8% yield (907 mg, 0.89 mmol). Anal. Calcd. (Found) for C₅₀H₁₀₃ O₁₃FeK: C, 59.62 (59.96); H, 10.02 (10.31). IR (cm⁻¹): 1475 (m), 1401 (m), 1378 (sh), 1352 (m), 1303 (m), 1289 (s), 1250 (br, m), 1201 (w), 1118 (vs), 1090 (vs), 1052 (sh), 1040 (s), 1016 (s), 976 (s), 940 (s), 855 (s), 830 (m), 806 (s), 691 (w), 667 (w), 632 (m), 576 (m), 547 (m), 519 (m), 508 (m). UV-Vis: 798 nm [98 M⁻¹ cm⁻¹]. $\mu_{\text{eff}} = 4.75 \mu\text{B}$.

2.9.6 Preparation of [Co(ditox)₃][K(15C5)₂] (2.4). A 1.00 g (5.09 mmol) portion of Kditox in 3 mL of THF was added to the stirred blue tetrahydrofuran suspension (2 mL) of CoCl₂ (213 mg, 1.64 mmol). The ensuing homogeneous solution assumed a blue color. After 1 h, volatiles were removed in vacuo, and the residue was extracted with pentane (12 mL) and filtered through Celite. The blue pentane solution was collected and concentrated to 7 mL. To the solution an excess of 15-crown-5-ether was added (ca. 2 mL, 10.1 mmol) at room temperature and immediately a dark blue precipitate formed. The reaction mixture was stirred as a blue suspension for 30 min. The stirring was ceased and a dark blue solid was allowed to settle to the bottom of the reaction vessel. The pale blue supernatant removed via pipette. Remaining solid was washed 3 × 5 mL of pentane. The light blue solid was dissolved in diethyl ether (8 mL) and filtered through Celite. Diethyl ether solution was collected and concentrated to approximately. 1 mL and the solution was left to stand at -40 °C for 24 h to give **2.1** in 74.2% yield (1.321 g,

1.223 mmol). Anal. Calcd. (Found) for $C_{50}H_{103}O_{13}CoK$: C, 59.44 (59.31); H, 10.28 (10.17). IR (cm^{-1}): 1475 (w), 1401 (w), 1378 (sh), 1352 (m), 1303 (m), 1282 (m), 1232 (m), 1201 (w), 1117 (s), 1102 (sh), 1090 (s), 1039 (sh), 1031 (m), 1006(sh), 978 (m), 939 (w), 914 (s), 900 (m), 855 (s), 829 (s), 816 (m), 652 (m), 587 (m), 532 (w). UV-Vis: 672 nm [$212 M^{-1} cm^{-1}$], 1235 nm [$27 M^{-1} cm^{-1}$]. $\mu_{eff} = 4.51 \mu B$.

2.9.7 Preparation of $[Ni(ditox)_3][K(15C5)_2]$ (2.5). A 1.00 g (5.09 mmol) portion of Kditox in 3 mL of THF was added to the stirred yellow tetrahydrofuran suspension (2 mL) of $NiCl_2$ (213 mg, 1.64 mmol). The ensuing homogeneous solution assumed an orange color. After 1 h, volatiles were removed in vacuo, and the residue was extracted with pentane (12 mL) and filtered through Celite. The orange pentane solution was collected and concentrated to 7 mL. To the solution an excess of 15-crown-5-ether was added (ca. 2 mL, 10.1 mmol) at room temperature and immediately a dark orange precipitate formed. The reaction mixture was stirred as an orange suspension for 30 min. The stirring was ceased and an orange solid was allowed to settle to the bottom of the reaction vessel. The yellow supernatant was removed via pipette. Remaining solid was washed 3×5 mL of pentane. The orange solid was dissolved in diethyl ether (8 mL) and filtered through Celite. Diethyl ether solution was collected and concentrated to approximately 1 mL and the solution was left to stand at -40 °C for 24 h to give **2.5** in 68.7% yield (1.140 g, 1.131 mmol). Anal. Calcd. (Found) for $C_{50}H_{103} O_{13}NiK$: C, 59.45 (59.61); H, 10.28 (10.20). IR (cm^{-1}): 1475 (w), 1401 (w), 1378 (sh), 1352 (m), 1300 (m), 1282 (m), 1222 (m), 1117 (s), 1103 (sh), 1090 (s), 1039 (sh), 1032 (m), 1005 (sh), 983 (m), 940 (s), 911(sh), 890 (m), 830 (s), 817 (m), 649 (m), 595 (m), 532 (w). UV-vis: 488 nm [$145 M^{-1} cm^{-1}$], 788 nm [$40 M^{-1} cm^{-1}$]. $\mu_{eff} = 2.65 \mu B$.

2.9.8 Preparation of $V(ditox)_3THF$ (2.6-THF). A 134 (0.817 mmol, 3 equiv) portion of Liditox in 2 mL of diethyl ether was added to a stirred pink THF/diethyl ether suspension (1:2 mL) of $[VCl_3(THF)_3]$ (102 mg, 0.273 mmol) in one portion. The color changed to blue and a white precipitate formed. After 1 h, the solution was filtered, the solvent was removed, and the resulting blue solid was recrystallized from pentane/THF mixture (10:1 ratio), giving $[V(ditox)_3(THF)]$ as blue crystals in two crops (80 mg, 0.135 mmol, 50% yield). Anal. Calcd. (Found) for $C_{34}H_{71}O_4V$: C, 68.7 (68.4); H, 12.0 (11.8). IR (cm^{-1}): 1477(m), 1388 (m), 1364 (s), 1100 (vs), 1078 (s), 1030 (sh), 996 (s), 942 (sh), 906 (vs), 863 (s), 716 (s), 702 (sh), 599 (m), 548 (w), 535 (w). UV-vis: 375 nm (sh) [$103 M^{-1} cm^{-1}$], 626 nm [$280 M^{-1} cm^{-1}$], 775 nm (sh) [$98 M^{-1} cm^{-1}$].

$^1 \text{ cm}^{-1}$], 972 nm [$83 \text{ M}^{-1} \text{ cm}^{-1}$]. $\mu_{\text{eff}} = 2.71 \text{ } \mu\text{B}$. Kditox can be substituted for Liditox at the equivalent molar concentrations.

2.9.9 Preparation of Cr(ditox)₃ (2.7). A 134 mg (0.817 mmol, 3 equiv) portion of Liditox in 2 mL of tetrahydrofuran was added to the stirred violet THF suspension (2 mL) of [CrCl₃THF₃] (103 mg, 0.273 mmol) in one portion. The color changed to turquoise and a white precipitate formed. After 1 h, the solution was filtered, the solvent was removed, and the resulting solid was recrystallized from pentane (1 mL), giving [Cr(ditox)₃] as turquoise crystals in two crops (79 mg, 0.147 mmol, 54% yield). Anal. Calcd. (Found) for C₃₀H₆₃O₃Cr: C, 68.79 (68.49); H 12.12 (12.11), Cl 0.0 (0.0). IR (cm⁻¹): 1477 (m), 1388 (m), 1364 (m), 1098 (s), 1074 (vs), 996 (s), 937 (s), 915 (vs), 721 (s), 594 (w), 531 (w). UV-vis: 680 nm [$215 \text{ M}^{-1} \text{ cm}^{-1}$], 790 nm (sh) [$205 \text{ M}^{-1} \text{ cm}^{-1}$], 1030 nm) [$118 \text{ M}^{-1} \text{ cm}^{-1}$]. $\mu_{\text{eff}} = 3.65 \text{ } \mu\text{B}$. Kditox can be substituted for Liditox at the equivalent molar concentrations.

2.9.10 Preparation of Fe(ditox)₃THF (2.8-THF). A 271 mg (1.65 mmol) portion of Liditox was dissolved in ether (2 mL) and was added to the orange solution of 89 mg (0.55 mmol) of FeCl₃ in THF (2 mL). White solid formed immediately. The solution was stirred for 30 min, filtered, and the solvents were removed. The residue was extracted with pentane (1 mL), filtered, and the solution was stored at -40 °C. The product was obtained as yellow crystals in two crops (64% yield, 210 mg, 0.35 mmol). Anal. Calcd (Found) for C₃₄H₇₁O₄Fe: C, 68.09 (68.01); H, 11.93 (11.52). IR (cm⁻¹): 1474 (m), 1390 (sh), 1385 (m), 1364 (m), 1095 (sh), 1081 (vs), 1017 (sh), 1001 (s), 936 (s), 916 (vs), 868 (s), 686 (s), 590 (m), 546 (w), 532 (w). UV-vis : no notable features. $\mu_{\text{eff}} = 5.09 \text{ } \mu\text{B}$. Alternatively, **2.8** could be prepared from **2.3**. AgPF₆ (41 mg) was dissolved in 2 mL of THF and added to the stirred pale blue-green solution of [Fe(ditox)₃][K(15C5)] (98.0 mg, 0.161 mmol) in ether (1 mL). The solution turned dark brown and it was stirred for 1 h, filtered, and the solvent was removed in vacuo. The brown residue was extracted with pentane (1 mL, yellow-brown solution), and left to stand at -40 °C. The product was obtained as yellow crystals in two crops (60% yield, 58 mg, 0.097 mmol).

2.9.11 Preparation of Co(ditox)₃ (2.9). A 0.500 (1.13 mmol) gram portion of compound **2.4**, [Co(ditox)₃][K(15C5)₂], is weighed into a 12 dram vial with a magnetic stir bar. A 0.319 gram (1.24 mmol) portion of AgOTf is weighed into a separate vial. To each vial, 5 mL of THF is added to result in a blue solution of compound **2.4** in THF and a colorless solution of AgOTf. At room temperature, the solution of AgOTf is pipetted into the stirring solution of **2.4**. The

reaction mixture immediate becomes dark as the solution changes to green with a dark grey precipitate forms. The THF solvent is removed in vacuo as the reaction mixture is taken to dryness. To the crude mixture, hexanes is added to afford a green solution. The green hexanes solution is filtered through Celite twice and collected. The solvent can either be removed in vacuo to afford **2.9** as a dark green powder (0.329 g, 0.621 mmol, 55.0% yield) or the solution can be concentrated to 1 mL and stored at $-40\text{ }^{\circ}\text{C}$ for 48 h to obtain green crystals of **2.9** in 22.6% yield (0.135 g, 0.255 mmol). Anal. Calcd. (Found) for $\text{C}_{30}\text{H}_{63}\text{O}_3\text{Co}$: C, 67.89 (67.57); H 11.96 (11.54). IR (cm^{-1}): 1475 (m), 1398 (m), 1373 (m), 1099 (s), 1079 (s), 1025 (sh), 1002 (s), 962 (sh), 940 (s), 924 (s), 894 (sh), 874 (m), 832 (m), 714 (s), 602 (m), 532 (w). UV-vis: 387 nm [$678\text{ M}^{-1}\text{ cm}^{-1}$], 677 nm [$240\text{ M}^{-1}\text{ cm}^{-1}$], 720 nm (sh) [$186\text{ M}^{-1}\text{ cm}^{-1}$]. $\mu_{\text{eff}} = 5.12\text{ }\mu\text{B}$.

2.9.12 Crystallographic Details Crystals were mounted on a Bruker three circle goniometer platform equipped with an APEX detector. A graphite monochromator was employed for wavelength selection of the Mo $\text{K}\alpha$ radiation ($\lambda = 0.71073\text{ }\text{\AA}$). Data were processed and refined using the program SAINT supplied by Siemens Industrial Automation. Structures were solved by direct methods in SHELXS and refined by standard difference Fourier techniques in the SHELXTL program suite (6.10 v., Sheldrick G. M., and Siemens Industrial Automation, 2000). Hydrogen atoms were placed in calculated positions using the standard riding model and refined isotropically; all other atoms were refined anisotropically. Rigid bond restraints were used in all refinement models. X-ray quality crystals of Kditox were grown by cooling a concentrated solution of the compound in diethyl ether to $-40\text{ }^{\circ}\text{C}$ overnight. The refinement was found to have no disorder in need of refinement and no major alerts detected by CheckCIF/Platon.

X-ray quality crystals of the divalent tris(alkoxide) compounds, **2.1-2.5**, were grown by cooling a concentrated solution of the respective compound in diethyl ether to $-40\text{ }^{\circ}\text{C}$ for 24 to 48 h. The refinement of **2.1** involved modeling of a rotational disorder of one molecule of 15-crown-5-ether which is coordinated to a K cation. The disorder was modeled as two parts, with each part representing a different position, and with the occupancy of each part treated as a freely refined variable. Two level A alerts were detected by CheckCIF/Platon⁸² both of which identify a high parameter shift for the anisotropic value of one carbon atom in the disordered 15-crown-5-ether molecule coordinated to the countercation. Attempts to utilize further constraints and restraints to alleviate this alert were unsuccessful. The structure is presented since there are no

alerts corresponding to the anionic portion of the compound, $[\text{Cr}(\text{ditox})_3]^-$, of which structural metrics are analyzed. The refinement of **2.4** involved modeling positional disorder of one ditox ligand. The positional disorder was modeled as two parts, with each part representing a different position, and with the occupancy of each part treated as a freely refined variable. Bond length constraints were used within the refinement of the minor contributor to the disordered ligand. No major alerts were detected by CheckCIF/Platon. The refinement of **2.5** involved modeling positional disorder of one ditox ligand, which was modeled as two parts, with each part representing a different position, and with the occupancy of each part treated as a freely refined variable. Bond length and anisotropic constraints were implemented the disordered ligand. No major alerts were detected by CheckCIF/Platon

X-ray quality crystals for the trivalent compounds **2.6** and **2.8** were grown by cooling a concentrated solution of the respective compound in a pentane/THF mixture (10:1) to -40°C for 24 h. An X-ray quality crystal of **2.7** could not be obtained, however the structure of **2.7** was obtained as a co-crystal with $[\text{Cr}(\text{ditox})_3\text{Cl}]$, obtained by the oxidation of $\text{Cr}(\text{ditox})_3$ with halogenated solvents). The refinement of **2.7** involved modeling the positional disorder of one ditox ligand which was treated as two parts. Each part represented a different position and the occupancy of each part was treated as a freely refined variable. Bond length constraints were used within the refinement of the minor contributor to the disordered ligand. Compounds **2.6-2.8** had significant $t\text{Bu}$ rotational disorder that was modeled as two parts, with each part representing a different orientation of the $t\text{Bu}$ group. The occupancies of the orientations were freely refined.

2.9.13 Computational Details. Density functional theory (DFT) calculations were performed with the hybrid functional Becke-3 parameter exchange functional⁸³ and the Lee-Yang-Parr nonlocal correlation functional (B3LYP)⁸⁴ as implemented in the Gaussian 03, Revision B.05 software package.⁸⁵ An effective core potential (ECP) representing the 1s2s2p core was used for iron (LANL2DZ).⁸⁶ The double- ζ quality correlation-consistent polarized ccc-pvdz basis set by Dunning and coworkers was used on all oxygen atoms, while double- ζ quality basis sets (D95) were used on carbon and hydrogen.⁸⁷ Single point calculations were performed on simplified models of the experimentally determined structures of compounds **1-5** in which all $t\text{Bu}$ groups were truncated to Me groups within the ditox ligand and counter cations were not included. Computations were used to confirm the relative d orbital ordering depicted in Figure 2.5.

2.10 Crystallographic Tables

Table 2.7 Crystallographic data and structural refinement parameters for KOC^tBu₂Me (Kditox).

Identification code	Kditox	
Empirical formula	C ₁₀ H ₂₁ O ₁ K	
Formula weight	196.37 g/mol	
Temperature	-173(2) °C	
Wavelength	1.54178 Å	
Crystal system	Tetragonal	
Space group	<i>I</i> -4	
Unit cell dimensions	<i>a</i> = 11.7035(1) Å	$\alpha = 90.00^\circ$
	<i>b</i> = 11.7035(1) Å	$\beta = 90.00^\circ$
	<i>c</i> = 16.5681(1) Å	$\gamma = 90.00^\circ$
Volume	2269.36(3) Å ³	
Z	8	
Density (calculated)	1.148 Mg/m ³	
Absorption coefficient	3.743 mm ⁻¹	
F(000)	864	
Crystal size	0.37 × 0.24 × 0.20 mm ³	
θ range for data collection	1.81 to 28.24°	
Index ranges	-13 ≤ <i>h</i> ≤ 14, -14 ≤ <i>k</i> ≤ 14, -20 ≤ <i>l</i> ≤ 20	
Reflections collected	23234	
Independent reflections	2142 [<i>R</i> _{int} = 0.0138]	
Completeness to $\theta = 28.28^\circ$	99.7%	
Absorption correction	Empirical SADABS	
Max. and min. transmission	0.6037 and 0.5212	
Refinement method	Full-matrix least-squared on <i>F</i> ²	
Data / restraints/ parameters	2142 / 21 / 193	
^a Goodness-of-fit on <i>F</i> ²	0.997	
^{b,c} Final R indices [<i>I</i> > 2σ(<i>I</i>)]	<i>R</i> ₁ = 0.0267, <i>wR</i> ₂ = 0.0692	
^{b,c} R indices (all data)	<i>R</i> ₁ = 0.0269, <i>wR</i> ₂ = 0.0695	
Largest diff. peak and hole	0.272 and -0.194 e/Å ⁻³	

^a GOF = $(\sum w(F_o^2 - F_c^2)^2 / (n - p))^{1/2}$ where *n* is the number of data and *p* is the number of parameters refined.

^b $R_1 = \sum ||F_o - |F_c|| / \sum |F_o|$

$${}^c wR_2 = \left(\frac{\sum (w(F_o^2 - F_c^2)^2)}{\sum (w(F_o^2)^2)} \right)^{1/2}$$

Table 2.8 Crystallographic data and structural refinement parameters for [Cr(ditox)₃][K(15C5)₂] (2.1).

Identification code	Cr(ditox) ₃ _K(15C5) ₂	
Empirical formula	C ₅₀ H ₁₀₃ O ₁₃ KCr	
Formula weight	1003.50 g/mol	
Temperature	-173(2) °C	
Wavelength	0.70173 Å	
Crystal system	Triclinic	
Space group	<i>P</i> -1	
Unit cell dimensions	<i>a</i> = 11.358(2) Å	<i>α</i> = 89.037(2)°
	<i>b</i> = 15.438(2) Å	<i>β</i> = 88.706(2)°
	<i>c</i> = 16.947(2) Å	<i>γ</i> = 71.300(2)°
Volume	2814.0(5) Å ³	
Z	2	
Density (calculated)	1.196 Mg/m ³	
Absorption coefficient	0.334 mm ⁻¹	
F(000)	1120	
Crystal size	0.20 × 0.13 × 0.08 mm ³	
Θ range for data collection	1.83 to 28.28°	
Index ranges	-15 ≤ <i>h</i> ≤ 15, -20 ≤ <i>k</i> ≤ 20, -22 ≤ <i>l</i> ≤ 22	
Reflections collected	66864	
Independent reflections	13936 [<i>R</i> _{int} = 0.0202]	
Completeness to Θ = 28.28°	99.8%	
Absorption correction	Empirical SADABS	
Max. and min. transmission	0.7312 and 0.6462	
Refinement method	Full-matrix least-squared on <i>F</i> ²	
Data / restraints/ parameters	13936 / 838 / 854	
^a Goodness-of-fit on <i>F</i> ²	1.039	
^{b,c} Final R indices [<i>I</i> > 2σ(<i>I</i>)]	<i>R</i> _{<i>I</i>} = 0.0309, <i>wR</i> ₂ = 0.0757	
^{b,c} R indices (all data)	<i>R</i> _{<i>I</i>} = 0.0393, <i>wR</i> ₂ = 0.0821	
Largest diff. peak and hole	0.501 and -0.362 e/Å ⁻³	

^a GOF = $(\sum w(F_o^2 - F_c^2)^2 / (n - p))^{1/2}$ where *n* is the number of data and *p* is the number of parameters refined.

^b $R_I = \sum ||F_o - |F_c|| / \sum |F_o|$

$${}^c wR_2 = \left(\frac{\sum (w(F_o^2 - F_c^2)^2)}{\sum (w(F_o^2)^2)} \right)^{\frac{1}{2}}$$

Table 2.9 Crystallographic data and structural refinement parameters for [Mn(ditox)₃][K(15C5)₂] (**2.2**).

Identification code	Mn(ditox) ₃ _K(15C5) ₂	
Empirical formula	C ₅₀ H ₁₀₃ O ₁₃ KMn	
Formula weight	1006.36 g/mol	
Temperature	-173(2) °C	
Wavelength	0.70173 Å	
Crystal system	Monoclinic	
Space group	P2 ₁ /n	
Unit cell dimensions	$a = 11.399(1) \text{ \AA}$	$\alpha = 90.00^\circ$
	$b = 17.271(1) \text{ \AA}$	$\beta = 91.466(1)$
	$c = 29.134(2) \text{ \AA}$	$\gamma = 90.00^\circ$
Volume	5733.9(5) Å ³	
Z	4	
Density (calculated)	1.166 Mg/m ³	
Absorption coefficient	0.358 mm ⁻¹	
F(000)	2201	
Crystal size	0.32 × 0.11 × 0.09 mm ³	
θ range for data collection	1.37 to 25.00°	
Index ranges	-13 ≤ <i>h</i> ≤ 13, -22 ≤ <i>k</i> ≤ 22, -34 ≤ <i>l</i> ≤ 34	
Reflections collected	77183	
Independent reflections	10101 [R _{int} = 0.0235]	
Completeness to $\theta = 28.28^\circ$	99.9%	
Absorption correction	Empirical SADABS	
Max. and min. transmission	0.6823 and 0.5043	
Refinement method	Full-matrix least-squared on F^2	
Data / restraints/ parameters	10101 / 601 / 607	
^a Goodness-of-fit on F^2	1.061	
^{b,c} Final R indices [$I > 2\sigma(I)$]	$R_1 = 0.0753$, $wR_2 = 0.2042$	
^{b,c} R indices (all data)	$R_1 = 0.0895$, $wR_2 = 0.2200$	
Largest diff. peak and hole	1.027 and -0.658 e/Å ⁻³	

^a GOF = $(\sum w(F_o^2 - F_c^2)^2 / (n - p))^{1/2}$ where *n* is the number of data and *p* is the number of parameters refined.

^b $R_1 = \sum ||F_o - |F_c|| / \sum |F_o|$

$${}^c wR_2 = \left(\frac{\sum (w(F_o^2 - F_c^2)^2)}{\sum (w(F_o^2)^2)} \right)^{1/2}$$

Table 2.10 Crystallographic data and structural refinement parameters for [Fe(ditox)₃][K(15C5)₂] (**2.3**).

Identification code	cmpd_5_Fe(Ditox)3K(15C5)2	
Empirical formula	C ₅₀ H ₁₀₃ O ₁₃ KFe	
Formula weight	1007.27 g/mol	
Temperature	-173(2) °C	
Wavelength	0.70173 Å	
Crystal system	Monoclinic	
Space group	<i>P2₁/n</i>	
Unit cell dimensions	<i>a</i> = 11.381(3) Å	<i>α</i> = 90.00°
	<i>b</i> = 17.218(5) Å	<i>β</i> = 91.295(5)°
	<i>c</i> = 29.190(9) Å	<i>γ</i> = 90.00°
Volume	5719(3) Å ³	
Z	4	
Density (calculated)	1.170 Mg/m ³	
Absorption coefficient	0.392 mm ⁻¹	
F(000)	2208	
Crystal size	0.20 × 0.20 × 0.20 mm ³	
θ range for data collection	1.37 to 25.35°	
Index ranges	-13 ≤ <i>h</i> ≤ 13, -20 ≤ <i>k</i> ≤ 20, -35 ≤ <i>l</i> ≤ 35	
Reflections collected	95450	
Independent reflections	10479 [R _{int} = 0.0384]	
Completeness to θ = 28.28°	100.0%	
Absorption correction	Empirical SADABS	
Max. and min. transmission	0.9257 and 0.9257	
Refinement method	Full-matrix least-squared on <i>F</i> ²	
Data / restraints/ parameters	10479 / 601 / 607	
^a Goodness-of-fit on <i>F</i> ²	1.013	
^{b,c} Final R indices [I > 2σ(I)]	<i>R</i> ₁ = 0.0422, <i>wR</i> ₂ = 0.0958	
^{b,c} R indices (all data)	<i>R</i> ₁ = 0.0644, <i>wR</i> ₂ = 0.1088	
Largest diff. peak and hole	0.744 and -0.326 e/Å ⁻³	

^a GOF = $(\sum w(F_o^2 - F_c^2)^2 / (n - p))^{1/2}$ where *n* is the number of data and *p* is the number of parameters refined.

^b $R_1 = \sum ||F_o - |F_c|| / \sum |F_o|$

^c $wR_2 = \left(\frac{\sum (w(F_o^2 - F_c^2)^2)}{\sum (w(F_o^2)^2)} \right)^{1/2}$

Table 2.11 Crystallographic data and structural refinement parameters for [Co(ditox)₃][K(15C5)₂] (2.4).

Identification code	Co(Ditox)3K(15C5)2	
Empirical formula	C ₅₀ H ₁₀₃ O ₁₃ KCo	
Formula weight	1002.29 g/mol	
Temperature	-173(2) °C	
Wavelength	0.70173 Å	
Crystal system	Monoclinic	
Space group	P2 ₁ /n	
Unit cell dimensions	$a = 11.242(1) \text{ \AA}$	$\alpha = 90.00^\circ$
	$b = 16.957(1) \text{ \AA}$	$\beta = 91.194(1)^\circ$
	$c = 29.521(2) \text{ \AA}$	$\gamma = 90.00^\circ$
Volume	5626.2(5) Å ³	
Z	4	
Density (calculated)	1.183 Mg/m ³	
Absorption coefficient	0.435 mm ⁻¹	
F(000)	2180	
Crystal size	0.30 × 0.20 × 0.10 mm ³	
θ range for data collection	1.38 to 24.10°	
Index ranges	-12 ≤ <i>h</i> ≤ 12, -19 ≤ <i>k</i> ≤ 19, -33 ≤ <i>l</i> ≤ 33	
Reflections collected	83760	
Independent reflections	8925 [R _{int} = 0.0373]	
Completeness to $\theta = 28.28^\circ$	99.9%	
Absorption correction	Empirical SADABS	
Max. and min. transmission	0.9257 and 0.9257	
Refinement method	Full-matrix least-squared on F^2	
Data / restraints/ parameters	8925 / 768 / 696	
^a Goodness-of-fit on F^2	1.018	
^{b,c} Final R indices [$I > 2\sigma(I)$]	$R_1 = 0.0693$, $wR_2 = 0.1575$	
^{b,c} R indices (all data)	$R_1 = 0.0999$, $wR_2 = 0.1798$	
Largest diff. peak and hole	1.457 and -0.840 e/Å ⁻³	

^a GOF = $(\sum w(F_o^2 - F_c^2)^2 / (n - p))^{1/2}$ where *n* is the number of data and *p* is the number of parameters refined.

^b $R_1 = \sum ||F_o - |F_c|| / \sum |F_o|$

^c $wR_2 = \left(\frac{\sum (w(F_o^2 - F_c^2)^2)}{\sum (w(F_o^2)^2)} \right)^{1/2}$

Table 2.12 Crystallographic data and structural refinement parameters for [Ni(ditox)₃][K(15C5)₂] (2.5).

Identification code	Ni(Ditox)3K(15C5)2	
Empirical formula	C ₅₀ H ₁₀₃ O ₁₃ KNi	
Formula weight	1010.13 g/mol	
Temperature	-173(2) °C	
Wavelength	0.70173 Å	
Crystal system	Monoclinic	
Space group	P2 ₁ /n	
Unit cell dimensions	$a = 11.213(1) \text{ \AA}$	$\alpha = 90.00^\circ$
	$b = 16.917(1) \text{ \AA}$	$\beta = 91.248(1)^\circ$
	$c = 29.659(2) \text{ \AA}$	$\gamma = 90.00^\circ$
Volume	5624.7(5) Å ³	
Z	4	
Density (calculated)	1.193 Mg/m ³	
Absorption coefficient	0.475 mm ⁻¹	
F(000)	2216	
Crystal size	0.20 × 0.20 × 0.08 mm ³	
θ range for data collection	1.37 to 26.37°	
Index ranges	-14 ≤ h ≤ 14, -21 ≤ k ≤ 21, -37 ≤ l ≤ 37	
Reflections collected	100279	
Independent reflections	11488 [R _{int} = 0.0260]	
Completeness to $\theta = 28.28^\circ$	99.9%	
Absorption correction	Empirical SADABS	
Max. and min. transmission	0.7312 and 0.6462	
Refinement method	Full-matrix least-squared on F ²	
Data / restraints/ parameters	11488 / 852 / 672	
^a Goodness-of-fit on F ²	1.002	
^{b,c} Final R indices [I > 2σ(I)]	R _I = 0.0677, wR ₂ = 0.1659	
^{b,c} R indices (all data)	R _I = 0.0806, wR ₂ = 0.1756	
Largest diff. peak and hole	1.545 and -0.620 e/Å ⁻³	

^a GOF = $(\sum w(F_o^2 - F_c^2)^2 / (n - p))^{1/2}$ where n is the number of data and p is the number of parameters refined.

^b R_I = $\sum ||F_o - |F_c|| / \sum |F_o|$

$${}^c wR_2 = \left(\frac{\sum (w(F_o^2 - F_c^2)^2)}{\sum (w(F_o^2)^2)} \right)^{1/2}$$

Table 2.13 Crystallographic data and structural refinement parameters for V(ditox)₃THF (2.6).

Identification code	V(ditox) ₃ THF	
Empirical formula	C ₃₄ H ₇₁ O ₄ V	
Formula weight	59.84 g/mol	
Temperature	-173(2) °C	
Wavelength	0.70173 Å	
Crystal system	Triclinic	
Space group	<i>P</i> -1	
Unit cell dimensions	<i>a</i> = 10.901(2) Å	<i>α</i> = 98.796(2)°
	<i>b</i> = 11.550(2) Å	<i>β</i> = 95.313(2)°
	<i>c</i> = 15.686(2) Å	<i>γ</i> = 113.907(2)°
Volume	1758.0(5) Å ³	
Z	2	
Density (calculated)	1.124 Mg/m ³	
Absorption coefficient	0.315 mm ⁻¹	
F(000)	660	
Crystal size	0.30 × 0.25 × 0.10 mm ³	
<i>θ</i> range for data collection	1.86 to 29.45°	
Index ranges	-14 ≤ <i>h</i> ≤ 14, -14 ≤ <i>k</i> ≤ 15, -20 ≤ <i>l</i> ≤ 20	
Reflections collected	34288	
Independent reflections	8078 [R _{int} = 0.0610]	
Completeness to <i>θ</i> = 28.28°	99.3%	
Absorption correction	Empirical SADABS	
Max. and min. transmission	0.9692 and 0.9115	
Refinement method	Full-matrix least-squared on <i>F</i> ²	
Data / restraints/ parameters	8078 / 0 / 373	
^a Goodness-of-fit on <i>F</i> ²	1.025	
^{b,c} Final R indices [I > 2σ(I)]	<i>R</i> ₁ = 0.0603, <i>wR</i> ₂ = 0.1551	
^{b,c} R indices (all data)	<i>R</i> ₁ = 0.0816, <i>wR</i> ₂ = 0.1652	
Largest diff. peak and hole	1.545 and -0.620 e/Å ⁻³	

^a GOF = $(\sum w(F_o^2 - F_c^2)^2 / (n - p))^{1/2}$ where *n* is the number of data and *p* is the number of parameters refined.

^b $R_1 = \sum ||F_o - |F_c|| / \sum |F_o|$

^c $wR_2 = \left(\frac{\sum (w(F_o^2 - F_c^2)^2)}{\sum (w(F_o^2)^2)} \right)^{1/2}$

Table 2.14 Crystallographic data and structural refinement parameters for Cr(ditox)₃ (2.7) and Cr(ditox)₃Cl.

Identification code	C63H126O6Cr2Cl	
Empirical formula	C ₆₃ H ₁₂₆ O ₆ Cr ₂ Cl	
Formula weight	1083.06 g/mol	
Temperature	-173(2) °C	
Wavelength	0.70173 Å	
Crystal system	Triclinic	
Space group	<i>P</i> -1	
Unit cell dimensions	<i>a</i> = 11.708(2) Å	<i>α</i> = 82.740(3)°
	<i>b</i> = 11.717(2) Å	<i>β</i> = 82.557(2)°
	<i>c</i> = 27.118(4) Å	<i>γ</i> = 60.937(2)°
Volume	5624.7(5) Å ³	
Z	2	
Density (calculated)	1.119 Mg/m ³	
Absorption coefficient	0.423 mm ⁻¹	
F(000)	1198	
Crystal size	0.25 × 0.25 × 0.20 mm ³	
θ range for data collection	1.52 to 25.00°	
Index ranges	-13 ≤ <i>h</i> ≤ 13, -13 ≤ <i>k</i> ≤ 13, -32 ≤ <i>l</i> ≤ 32	
Reflections collected	46380	
Independent reflections	11295 [R _{int} = 0.0682]	
Completeness to θ = 28.28°	99.8%	
Absorption correction	Empirical SADABS	
Max. and min. transmission	0.9202 and 0.9016	
Refinement method	Full-matrix least-squared on <i>F</i> ²	
Data / restraints/ parameters	11295 / 5 / 805	
^a Goodness-of-fit on <i>F</i> ²	1.099	
^{b,c} Final R indices [I > 2σ(I)]	<i>R</i> _{<i>i</i>} = 0.0700, <i>wR</i> ₂ = 0.1569	
^{b,c} R indices (all data)	<i>R</i> _{<i>i</i>} = 0.1054, <i>wR</i> ₂ = 0.1731	
Largest diff. peak and hole	0.468 and -0.511 e/Å ⁻³	

^a GOF = $(\sum w(F_o^2 - F_c^2)^2 / (n - p))^{1/2}$ where *n* is the number of data and *p* is the number of parameters refined.

^b $R_i = \sum ||F_o - |F_c|| / \sum |F_o|$

$${}^c wR_2 = \left(\frac{\sum (w(F_o^2 - F_c^2)^2)}{\sum (w(F_o^2)^2)} \right)^{\frac{1}{2}}$$

Table 2.15 Crystallographic data and structural refinement parameters for Fe(ditox)₃THF (**2.8**).

Identification code	compd_1_Fe(ditox) ₃ THF	
Empirical formula	C ₃₄ H ₁₇₁ O ₄ Fe	
Formula weight	599.76 g/mol	
Temperature	-173(2) °C	
Wavelength	0.70173 Å	
Crystal system	Triclinic	
Space group	<i>P</i> -1	
Unit cell dimensions	<i>a</i> = 11.526(1) Å	<i>α</i> = 65.010(1)°
	<i>b</i> = 17.383(2) Å	<i>β</i> = 84.451(1)°
	<i>c</i> = 19.912(2) Å	<i>γ</i> = 77.465(1)°
Volume	3529.8(4) Å ³	
<i>Z</i>	2	
Density (calculated)	1.129 Mg/m ³	
Absorption coefficient	0.460 mm ⁻¹	
<i>F</i> (000)	1332	
Crystal size	0.35 × 0.25 × 0.10 mm ³	
<i>θ</i> range for data collection	1.13 to 28.39°	
Index ranges	-15 ≤ <i>h</i> ≤ 15, -23 ≤ <i>k</i> ≤ 23, -26 ≤ <i>l</i> ≤ 26	
Reflections collected	68708	
Independent reflections	17553 [<i>R</i> _{int} = 0.0427]	
Completeness to <i>θ</i> = 28.28°	99.0%	
Absorption correction	Empirical SADABS	
Max. and min. transmission	0.9555 and 0.8557	
Refinement method	Full-matrix least-squared on <i>F</i> ²	
Data / restraints/ parameters	17553/ 0 / 745	
^a Goodness-of-fit on <i>F</i> ²	1.032	
^{b,c} Final <i>R</i> indices [<i>I</i> > 2σ(<i>I</i>)]	<i>R</i> _{<i>f</i>} = 0.0469, <i>wR</i> ₂ = 0.1173	
^{b,c} <i>R</i> indices (all data)	<i>R</i> _{<i>f</i>} = 0.0710, <i>wR</i> ₂ = 0.1328	
Largest diff. peak and hole	0.745 and -0.519 e/Å ⁻³	

^a GOF = (∑ *w*(*F*_o² - *F*_c²)² / (*n* - *p*))^{1/2} where *n* is the number of data and *p* is the number of parameters refined.

^b *R*_{*f*} = ∑ ||*F*_o - |*F*_c|| / ∑ |*F*_o|

^c *wR*₂ = (∑ (*w*(*F*_o² - *F*_c²)²) / ∑ (*w**F*_o²))^{1/2}

2.11 References

- (1) Betley, T. A.; Wu, Q.; Van Voorhis, T.; Nocera, D. G. *Inorg. Chem.* **2008**, *47*, 1849.
- (2) Meier-Callahan, A. E.; Gray, H. B.; Gross, Z. *Inorg. Chem.* **2000**, *39*, 3605.
- (3) Pestovsky, O.; Bakac, A. *J. Am. Chem. Soc.* **2003**, *125*, 14714.
- (4) Song, W. J.; Seo, M-S; DeBeer George, S.; Ohta, T.; Song, R.; Kang, M-J.; Tosha, T.; Kitagawa, T.; Solomon, E. I.; Nam, W. *J. Am. Chem. Soc.* **2007**, *129*, 1268.
- (5) Leeladee, P.; Baglia, R. A.; Prokop, K. A.; Latifi, R.; de Visser, S. P.; Goldberg, D. P. *J. Am. Chem. Soc.* **2012**, *134*, 10397.
- (6) Nam, W. *Acc. Chem. Res.* **2007**, *40*, 522.
- (7) Shan, X.; Que, L. Jr. *J. Inorg. Biochem.* **2006**, 421.
- (8) Fuji, H. *Coord. Chem. Rev.* **2002**, *226*, 51.
- (9) Harischandra, D. N.; Zhang, R.; Newcomb, M. *J. Am. Chem. Soc.* **2005**, *127*, 13776.
- (10) McDonald, A. R.; Que, L. Jr. *Coord. Chem. Rev.* **2013**, *257*, 414.
- (11) Nam, W.; Kim, I.; Kim, Y.; Kim, C. *Chem. Comm.* **2001**, 1262.
- (12) Dau, H.; Limberg, C.; Reier, T.; Risch, M.; Roggan, S.; Strasser, P. *Chem. Cat. Chem.* **2010**, *2*, 724.
- (13) Jiao, F.; Frei, H. *Energ. Environ. Sci.* **2010**, *3*, 1018.
- (14) Elizarova, G. L.; Zhidomirov, G. M.; Parmon, V. N. *Catalysis Today* **2000**, *58*, 71.
- (15) Yachandra, V. K.; Sauer, K.; Klein, M. P. *Chem. Rev.* **1996**, 2927.
- (16) Umena, Y.; Kawakami, K.; Shen, J-R.; Kamiya, N. *Nature* **2011**, *473*, 55.
- (17) Kanan, M. W.; Surendranath, Y.; Nocera, D. G. *Chem Soc. Rev.* **2009**, *38*, 109.
- (18) Bediako, D. K.; Lassalle-Kaiser, B.; Surendranath, Y.; Yano, J.; Yachandra, V. K.; Nocera, D. G. *J. Am. Chem. Soc.* **2012**, *134*, 6801.
- (19) Machida, M.; Miyazaki, Y.; Matsunaga, Y.; Ikeue K. *Chem, Commun.* **2011**, *47*, 9591.
- (20) Neri, G.; Bonaccorsi, L.; Donata, A.; Milone, C.; Musolino, M. G.; Visco, A. M. *Applied Catalysis B: Environmental* **1997**, *11*, 217.
- (21) Yao, Y-F. Y. *Journal of Catalysis* **1975**, *39m*, 104.
- (22) Luo, M-F.; Yan, Z-L.; Jin, L-Y. *Journal of Molecular Catalysis A: Chemical* **2006**, *260*, 157.
- (23) Il'chenko, N. I.; Gologets, G. I. *Journal of Catalysis* **1975**, *39*, 57.

- (24) Ng, C. F.; Selwood, P. W. *Journal of Catalysis* **1976**, *43*, 252.
- (25) Krupay, B. W.; Ross, R. A. *Can. J. Chem.* **1979**, *57*, 320.
- (26) Hattori, H. *Materials Chemistry and Physics*, **1988**, *18*, 533.
- (27) Kitajima, N.; Fukuzumi, S.-I.; Ono, Y. *The Journal of Physical Chemistry*, **1978**, *72*, 1505.
- (28) Cavani, F., Centi, G. and Marion, P. (2009) Catalytic Ammoxidation of Hydrocarbons on Mixed Oxides, in *Metal Oxide Catalysis* (eds S. D. Jackson and J. S. J. Hargreaves), Wiley-VCH Verlag GmbH & Co. KGaA, Weinheim, Germany.
- (29) Wachs, I. E. and Kim, T. (2009) Oxidation Reactions over Supported Metal Oxide Catalysts: Molecular/Electronic Structure – Activity/Selectivity Relationships, in *Metal Oxide Catalysis* (eds S. D. Jackson and J. S. J. Hargreaves), Wiley-VCH Verlag GmbH & Co. KGaA, Weinheim, Germany.
- (30) Chisholm, M. H.; Huffman, J. C.; Kirkpatrick, C. C.; Leonelli, J.; Folting, K. *J. Am. Chem. Soc.* **1981**, *103*, 6093.
- (31) Seisenbaeva, G. A.; Kessler, V. G.; Pazik R.; Strekm, W. *Dalton. Trans.* **2008**, 3412.
- (32) Mehrotra, R. C. and Singh, A. (2007) Recent Trends in Metal Alkoxide Chemistry, in *Progress in Inorganic Chemistry*, Volume 46 (ed K. D. Karlin), John Wiley & Sons, Inc., Hoboken, NJ, USA.
- (33) Hubert-Pfalzgraf, L. G. *Coord. Chem. Rev.* **1998**, *178-180(Pt. 2)*, 967.
- (34) Mehrotra, R. C.; Sing, A. *Chem. Soc. Rev.* **1996**, *25*, 1.
- (35) Schubert, U. *Acc. Chem. Res.* **2007**, *40*, 730.
- (36) Trofimenko, S. *Chem. Rev.* **1993**, *93*, 943.
- (37) Edelmann, F. T. *Angew. Chem. Int. Ed.* **2001**, *40*, 1656.
- (38) Gade, L. H. *Chem. Comm.* **2000**, *3*, 173.
- (39) Ebelman, J. J.; Bouquet, M. *Ann. Chim. Phys.* **1846**, *17*, 54.
- (40) Demarcay, E. *Compt. Rend.* **1875**, *80*, 51.
- (41) Turova, N. Y.; Turevskaya, E. P.; Kessler, V. G.; Yanovskaya, M. I. *Crystal and Molecular Structures of Metal Alkoxides. The Chemistry of Metal Alkoxides*; Kluwer Academic Publisher: Norwell, Massachusetts, 2002; p 41.
- (42) Bradley, D. C. *Chem. Rev.* **1989**, *89*, 1317.
- (43) Mehrotra, R. C. *Journal of Non-Crystalline Solids*, **1988**, *100*, 1.

- (44) Schrock, R.R. *Acc. Chem Res.* **1990**, *23*, 158.
- (45) Rothwell, I. P. *Acc. Chem. Res.* **1988**, *21*, 153.
- (46) Sigel, G. A.; Barlett, R. A.; Decker, D.; Olmstead, M. M.; Power, P. P. *Inorg. Chem* **1987**, *26*, 1773.
- (47) Ringel, C.; Boden, G. *Z. Anorg. Allg. Chem.* **1972**, *1*, 65.
- (48) Lynch, M. W.; Hendrickson, D. N.; Fitzgerald, B. J.; Pierpont C. G.; *J. Am. Chem. Soc.* **1968**, *356*, 132.
- (49) Roesky, H. W.; Scholz, M.; Noltemeyer, M. *Ber.* **1990**, *123*, 2303.
- (50) Stecher, H. A.; Sen, A.; Rheingold, A. L. *Inorg. Chem.* **1988**, *28*, 1130.
- (51) Eller, P. G.; Vergamini, P. J. *Inorg. Chem.* **1983**, *23*, 3184.
- (52) Cantalupo, S. A.; Lum, J. S.; Buzzeo, M. C.; Moore, C.; DiPasquale, A. G.; Rheingold A. L.; Doerrler, L. H. *Dalt. Trans.* **2010**, *39*, 374.
- (53) Zheng, BN.; Miranda, M. O.; DiPasquale, A. G.; Golen, J. A.; Rheingold, A. L.; Doerrler, L. H. *Inorg. Chem.* **2009**, *48*, 4274.
- (54) Bochmann, M.; Wilkinson, G.; Young, G. B.; Hursthouse, M. B.; Abdul Malik, K. M. *J. Chem. Soc. Dalt. Trans* **1980**, 1863.
- (55) Murray, B. D.; Power, P. P. *J. Am. Chem. Soc.* **1984**, *106*, 7011.
- (56) Kras, L. H.; Euvrard, A.; Grassel, Y. N.; Ronda, S. M.; Stewart, J. L. *Main Group Metal Chemistry* **1994**, *17*, 409.
- (57) Herrmann, W. A.; Anwander, R.; Kleine, M.; Scherer, W. *Chem. Ber.* **1992**, *125*, 1971.
- (58) Stecher, H. A.; Sen, A.; Rheingold, A. L. *Inorg. Chem.* **1989**, *28*, 3280.
- (59) Napolitano, E.; Giovani, E.; Ceccarelli, N.; Pelosi, P. *J. Agric. Food Chem.* **1996**, *44*, 2806
- (60) Weiss, E.; Alsdorf, H.; Kuhr, H.; Grutzmacher, H. *Ber.*, **1968**, *101*, 377.
- (61) Weiss, E.; Alsdorf, H.; Kuhr, H.; Grutzmacher, H. *Z. anorg. allg. Chem.* **1970**, *372*, 206.
- (62) Weiss, E.; Alsdorf, H.; Kuhr, H.; Grutzmacher, H. *Helv. Chim. Acta.* **1963**, *46*, 1121.
- (63) Weiss, E.; Alsdorf, H.; Kuhr, H.; Grutzmacher, H. *Angew. Chem.* **1967**, *79*, 816.
- (64) Weiss, E.; Büchner, W. *Z. anorg. allg. Chem.* **1964**, *330*, 251.
- (65) Groysman, S.; Villagrán, D.; Freedman, D. E.; Nocera, D. G. *Chem. Comm.* **2011**, *47*, 10242.

- (66) Hay-Motherwell, R.; Wilkinson, G.; Sweet, T. K. N.; Hurtshouse, M. B. *Polyhedron* **1996**, *15*, 3163.
- (67) Hope, H.; Olmstead, M. M.; Murray, B. D.; Power, P. P. *J. Am. Chem. Soc.* **1985**, *107*, 712.
- (68) Wertheim, G. K.; Hujner, S. *Phys. Rev. Lett.*, **1972**, *28*, 1028.
- (69) Zimmermann, R.; Steiner, P.; Claessen, R.; Reinart, F.; Hufner, S.; Blaha, P.; Dufek, P. *J. Phys.: Condens. Matter* **1999**, *11*, 1657.
- (70) Barraclough, C. G.; Bradley, D. C.; Lewis, J.; Thomas, L. M. *J. Chem. Soc.* **1961**, 2601.
- (71) Lynch, C. T.; Mazdiyasi, K. S.; Smith, J. S.; Crawford, W. J. *Anal. Chem.* **1964**, *36*, 2332.
- (72) Bradley, D. C.; Westlake, A. H. *Proc. Symp. Coord. Chem.* Beck, M. ed.; Publ. House Hung. Acad. Sci.:Budapest, Hungary, 1965; pp 309.
- (73) Alyea, E. C.; Bradley, D.C. *J. Chem. Soc. A* **1969**, 1255.
- (74) Brown, D. A.; Glass, W. K.; Kumar, B. *J. Chem. Soc. A* **1969**, 1510.
- (75) Samuel, R. S.; Patrick, B. O.; Smith, K. M. *Can. J. Chem.* **2004**, *82*, 1788.
- (76) Alyea, E. C.; Bradley, D. C.; Coperthwaite R. G.; Sales, K. D. *J. Chem. Soc. Dalton Trans.* **1973**, *2*, 185.
- (77) Sydora, O. L.; Wolczanski, P. T.; Lobkovsky, E. B.; Buda, C.; Cundari, T. R. *Inorg. Chem.* **2005**, *44*, 2606.
- (78) Eller, P. G.; Bradley, D. C.; Hurtshouse, M.B.; Meek, D. W. *Coord. Chem. Rev.* **1977**, *24*, 1.
- (79) Cummins, C. C. Three Coordinate Complexes of "Hard" Ligands: Advances in Synthesis, Structure and Reactivity. In *Progress in Inorganic Chemistry*. **1998**, *47*, 685.
- (80) Evans, D. F. *J. Chem. Soc.* **1959**, 2003.
- (81) Napolitano, E.; Giovani, E.; Ceccarelli, N.; Pelosi, P. *J. Agric. Food Chem.* **1996**, *44*, 2806.
- (82) Spek, A. L. *J. Appl. Cryst.* **2003**, *36*, 7.
- (83) (a) Becke, A. D. *Phys. Rev. A* **1988**, *38*, 3098. (b) Becke, A. D. *J. Chem. Phys.* **1993**, *98*, 1372. (c) Becke, A. D. *J. Chem Phys.* **1993**, *98*, 5648.
- (84) Lee, C.; Yang, W.; Parr, R. G. *Phys. Rev. B* **1988**, *37*, 785.
- (85) Gaussian 03, Revision C.02, Frisch, M. J.; Trucks, G. W.; Schlegel, H. B.; Scuseria, G. E.; Robb, M. A.; Cheeseman, J. R.; Montgomery, Jr., J. A.; Vreven, T.; Kudin, K. N.; Burant, J. C.; Millam, J. M.; Iyengar, S. S.; Tomasi, J.; Barone, V.; Mennucci, B.; Cossi, M.; Scalmani, G.; Rega, N.; Petersson, G. A.; Nakatsuji, H.; Hada, M.; Ehara, M.; Toyota, K.; Fukuda, R.;

Hasegawa, J.; Ishida, M.; Nakajima, T.; Honda, Y.; Kitao, O.; Nakai, H.; Klene, M.; Li, X.; Knox, J. E.; Hratchian, H. P.; Cross, J. B.; Bakken, V.; Adamo, C.; Jaramillo, J.; Gomperts, R.; Stratmann, R. E.; Yazyev, O.; Austin, A. J.; Cammi, R.; Pomelli, C.; Ochterski, J. W.; Ayala, P. Y.; Morokuma, K.; Voth, G. A.; Salvador, P.; Dannenberg, J. J.; Zakrzewski, V. G.; Dapprich, S.; Daniels, A. D.; Strain, M. C.; Farkas, O.; Malick, D. K.; Rabuck, A. D.; Raghavachari, K.; Foresman, J. B.; Ortiz, J. V.; Cui, Q.; Baboul, A. G.; Clifford, S.; Cioslowski, J.; Stefanov, B. B.; Liu, G.; Liashenko, A.; Piskorz, P.; Komaromi, I.; Martin, R. L.; Fox, D. J.; Keith, T.; Al-Laham, M. A.; Peng, C. Y.; Nanayakkara, A.; Challacombe, M.; Gill, P. M. W.; Johnson, B.; Chen, W.; Wong, M. W.; Gonzalez, C.; and Pople, J. A.; Gaussian, Inc., Wallingford CT, 2004.

(86) (a) Wadt, W. R.; Hay, P. J. *J. Chem Phys.* **1985**, *82*, 284. (b) Hay P. J.; Wadt, W. R. *J. Chem. Phys.* **1985**, *82*, 299.

(87) (a) Dunning, T. H., Jr. *J. Chem. Phys.* **1989**, *90*, 1007. (b) Dunning, T. H.; Hay, P. J. *In Modern Theoretical Chemistry. 3. Methods of Electronic Structure Theory*; Schaefer, H. F., III, Ed.; Plenum Press: New York, 1977. (c) Woon, D. E.; Dunning, T. H. *J. Chem. Phys.* **1993**, *98*, 1358.

CHAPTER 3

Electronic Structure and Reactivity of Chromium and Vanadium Tris(alkoxide) Complexes with Terminal Chalcogen Ligands

3.1 Introduction

The synthesis of transition metal oxo complexes of low electron counts (d^0 - d^2) provides an opportunity to stabilize metal oxo moieties in a specifically desired ancillary ligand platform. Complexes of low electron counts by their nature typically involve early transition metals (V and Cr) and thus they exhibit oxophilic behavior and form thermodynamically stable metal oxo bonds: $\Delta G^\circ_f(\text{V}_3\text{O}_5) = -431$ kcal/mol; $\Delta G^\circ_f(\text{Cr}_2\text{O}_3) = -253$ kcal/mol; $\Delta G^\circ_f(\text{Mn}_2\text{O}_3) = -221$; $\Delta G^\circ_f(\text{Fe}_2\text{O}_3) = -177$ kcal/mol.¹ The stability of the early transition metal oxo bonds afford isolable complexes that can be utilized to structurally and spectroscopically interrogate the electronic environment imparted to the metal oxo moiety by the particular ancillary ligand field. The ligand field of interest to the work described here is a tris(ditox) ancillary ligand environment to provide a pseudo-tetrahedral geometry of metal oxo complexes of low electron counts.

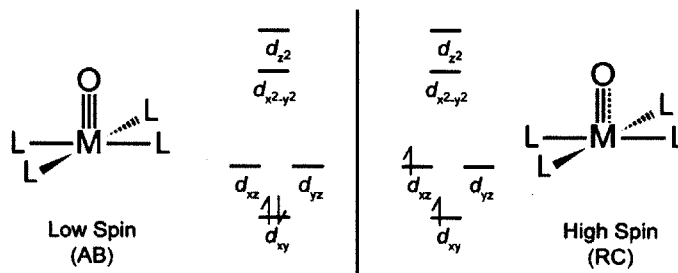


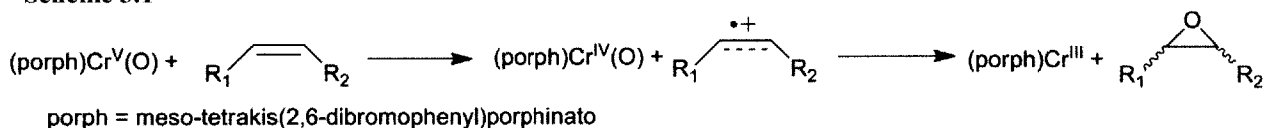
Figure 3.1. Generalized d orbital splitting diagram for d^2 metal oxo complexes stabilized by tetragonal ancillary ligand fields. The low spin configuration (left) formally features a triple bond between the metal and oxygen atom, thus rendering the metal oxo moiety electrophilic. The high spin configuration (right) features a metal oxo bond order of 2.5 with radical character on the metal oxo moiety.

Low spin metal oxo complexes of d^0 - d^2 electron counts in a tetragonal ligand field have been shown to formally feature a triple bond between the metal and the oxygen atom.² Figure 3.1 (left) depicts a d orbital splitting diagram for a low spin tetragonal d^2 metal oxo complex showing only population of the d_{xy} orbital, which is non-bonding with respect to the metal oxo bond. The triple bond engenders the metal oxo moiety electrophilic,³⁻¹⁰ resulting in facile reactivity with nucleophiles such as olefins, thio-ethers and phosphines, in a mechanism similar to that described in Chapter 1 for the Acid-Base (AB) mechanism for O–O bond formation processes. However, this electrophilic behavior of d^2 metal oxo complexes is predicted only for low spin electronic structures. Metal oxo complexes with d^2 electron counts that are high spin

(Figure 3.1, right) have been observed to react via one electron radical chemistry,¹¹⁻¹³ similar to the Radical Coupling (RC) mechanism described in Chapter 1 for O–O bond formation. This radical reactivity arises from one electron population of a π^* orbital of the metal oxo bond, imparting unpaired spin density on the oxygen atom. As tetragonal metal oxo complexes have been well studied, an electronic-structure/reactivity relationship has been established wherein d^0 , d^1 and low spin d^2 tetragonal metal oxo compounds are electrophilic and react via AB mechanisms, whereas high spin d^2 tetragonal metal oxo complexes can react via RC mechanisms.

This relationship between electron configuration and reactivity can be seen in the proposed mechanism for the epoxidation of olefins by $\text{Cr}^{\text{V}}(\text{porphinato})(\text{O})$ compounds. Organic radical chain products are formed suggesting that the $\text{Cr}^{\text{V}}(\text{porphinato})\text{O}$ compound reacts via a RC mechanism, despite the proposed electrophilic nature of the $\text{Cr}(\text{V})\text{--O}_{\text{oxo}}$ bond in a tetragonal ligand environment. Thorough kinetic analysis has shown that there is an electron transfer prior to the chemical reaction that forms an intermediate high spin $\text{Cr}(\text{IV})\text{--O}_{\text{oxo}}$ complex, which then proceeds to react with olefins via a one electron radical mechanism (Scheme 3.1) to give rise to the observed radical chain side products.¹⁴ More recently, electron transfer is observed to occur during $[\text{Cr}(\text{salen})(\text{O})]^+$ oxidations of thio-ethers.¹⁵ Thus, even in circumstances of electrophilic tetragonal metal oxo complexes, an electronic transfer is observed to occur to pre-form a high spin d^2 electronic structure.

Scheme 3.1



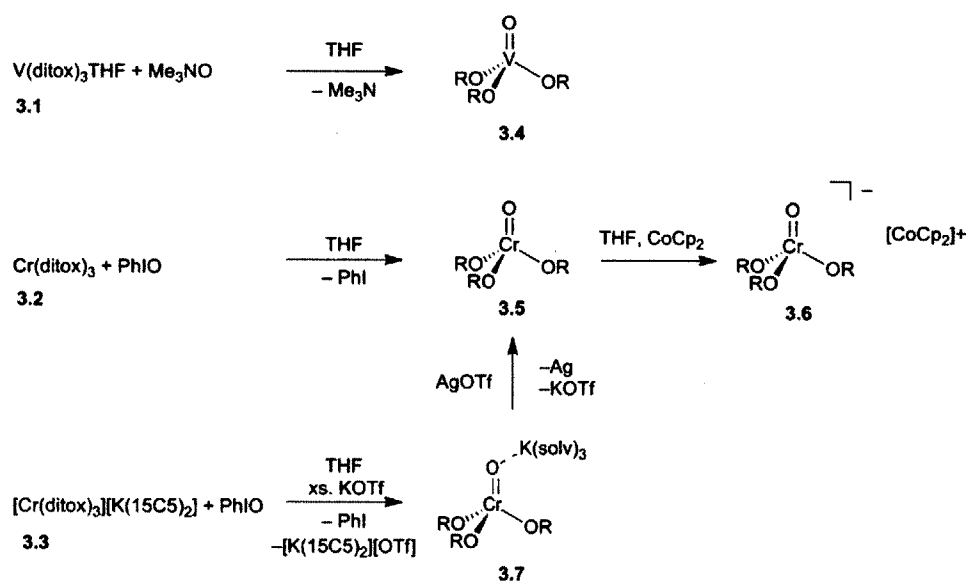
As pseudo-tetrahedral metal oxo complexes are less common than their tetragonal counterparts,¹⁶ the following chapter targets pseudo-tetrahedral d^0 , d^1 and d^2 metal oxo complexes of vanadium and chromium supported by a tris(ditox) ancillary ligand platform. Isolation of the desired compounds has afforded the opportunity to explore the electronic structure of pseudo-tetrahedral metal oxo complexes in oxygen rich ligand environments. In order to establish a structure-reactivity relationship analogous to those in tetragonal fields, a survey of reaction chemistry has been performed. As chromium and vanadium are oxophilic

metals are unlikely to participate in O–O bond formation reactions owing to the large metal oxo bond strength, metal-sulfido complexes were synthesized to more generally interrogate chalcogen–chalcogen bond formation process.

3.2 Pseudo-Tetrahedral d^0 , d^1 and d^2 Terminal Metal Oxo Complexes

3.2.1 Preparation. Scheme 3.2 outlines the preparative methods for the synthesis of high valent d^0 , d^1 and d^2 pseudo-tetrahedral metal oxo complexes of V(V), Cr(V) and Cr(IV). The compounds $V(\text{ditox})_3\text{THF}$ (**3.1**), $\text{Cr}(\text{ditox})_3$ (**3.2**), $[\text{Cr}(\text{ditox})_3][\text{K}(\text{15C5})_2]$, (**3.3**) were used as precursor complexes for the pseudo-tetrahedral terminal metal oxo complexes upon reactions with oxygen atom transfer reagents.

Scheme 3.2



The d^0 pseudo-tetrahedral complex $V(\text{ditox})_3(\text{O})$ (**3.4**) can be synthesized from **3.1**, $V(\text{ditox})_3\text{THF}$, upon addition of 1 equiv of Me_3NO in tetrahydrofuran. Within 5 min, the initially blue solution of **3.1** assumed a brown color. Removal of THF in vacuo, followed by addition of pentane to the remaining brown residue afforded a pale yellow solution. Upon filtration, concentration and cooling to $-40\text{ }^\circ\text{C}$ resulted in pale yellow crystals of **3.4**, $V(\text{ditox})_3(\text{O})$, which were collected in 55% yield. Notably, iodosyl benzene (PhIO) was unable to oxidize **3.1** to **3.4**. This is attributed to a kinetic effect, as THF is found to coordinate tightly to the open

coordination site of the vanadium center of **3.1**. The low solubility of PhIO in THF does not provide a high enough concentration of oxidant in solution to react with **3.1** at an appreciable rate. Attempts to reduce **3.4** to the d^1 $[\text{V}(\text{ditox})_3(\text{O})]^-$ with CoCp_2 , Na/Hg , and KC_8 were unsuccessful, which is in agreement with the observed difficulty in reducing vanadium–alkoxide complexes.¹⁷

The d^1 pseudo-tetrahedral complex $\text{Cr}(\text{ditox})_3(\text{O})$ (**3.5**) was synthesized from **3.2**, $\text{Cr}(\text{ditox})_3$, upon exposure to oxygen atom transfer reagents, such as Me_3NO and PhIO, as well as exposure to O_2 . Addition of an oxygen transfer reagent to **3.2** resulted in the initially turquoise solution assuming a dark red color within 2 min. The THF solvent was removed in vacuo and pentane was added to afford red pentane solution. After filtration and concentration, cooling to -40 °C resulted in **3.5** in 78% yield. Attempts to oxidize **3.5**, $\text{Cr}(\text{ditox})_3(\text{O})$ to the d^0 $[\text{Cr}(\text{ditox})_3(\text{O})]^+$ resulted in decomposition and non-specific reactivity.

The d^2 pseudo-tetrahedral complex $[\text{Cr}(\text{ditox})_3(\text{O})]^-$ can be synthesized from **3.5**, $\text{Cr}(\text{ditox})_3(\text{O})$. Treatment of **3.5** with 1 equiv of CoCp_2 in THF resulted in the red solution assuming a deep blue over the course of 2 h at room temperature. Upon recrystallization from diethyl ether, the blue $[\text{Cr}(\text{ditox})_3(\text{O})][\text{CoCp}_2]$, **3.6**, is isolated in 55% yield. Alternatively, $[\text{Cr}(\text{ditox})_3][\text{K}(\text{15C5})_2]$, **3.3**, can be treated with an oxygen atom transfer reagent (PhIO or Me_3NO) in THF to afford a similar blue solution. Addition of excess potassium triflate and subsequent removal of THF yielded a light blue residue. Recrystallization from Et_2O afforded $[\text{Cr}(\text{ditox})_3(\text{O})][\text{K}(\text{Et}_2\text{O})_3]$, **3.7**, in 63% yield. Of note, **3.6** features a terminal $\text{Cr}-\text{O}_{\text{oxo}}$ bond whereas the oxo ligand present in **3.7** coordinates to the potassium cation.

In summary, the d^0 $\text{V}(\text{ditox})_3(\text{O})$, d^1 $\text{Cr}(\text{ditox})_3(\text{O})$, and d^2 complexes $[\text{Cr}(\text{ditox})_3(\text{O})][\text{CoCp}_2]$ and $\text{Cr}(\text{ditox})_3(\text{O})\text{K}(\text{Et}_2\text{O})_3$ have been successfully synthesized via the treatment of reduced trigonal precursors **3.1-3.3** with oxygen atom transfer reagents.

3.2.2 Crystallography. X-ray diffraction of **3.4**, $\text{V}(\text{ditox})_3(\text{O})$, confirms the structure of the complex and that the metal resides in a pseudo-tetrahedral coordination environment with a terminal oxo ligand. The structure of **3.4** is presented in Figure 3.2. The $\text{V}-\text{O}_{\text{oxo}}$ bond distance is found to be 1.60 Å. This is within the range of typical $\text{V}-\text{O}_{\text{oxo}}$ bond lengths for tetragonal ancillary ligand fields, which range from 1.56 Å to 1.61 Å.¹⁸⁻²¹ The average $\text{V}-\text{O}_{\text{alk}}$ bond distance for **3.4** is 1.75 Å, which represents a contraction of on average 0.09 Å relative to the four-coordinate V(III) compound, **3.1**, $\text{V}(\text{ditox})_3\text{THF}$. The average internal $\text{O}_{\text{alk}}-\text{C}$ bond distance is

1.44 Å, which is elongated 0.01 Å from the $O_{alk}-C$ the V(III) precursor. The contraction of the $V-O_{alk}$ bond distance in concert with the elongation of the $O_{alk}-C$ bond distance follows the expected trends observed upon oxidation of divalent tris(ditox) complexes to trivalent tris(ditox) complexes described in Chapter 2. Oxidations at the metal center result in stronger $V-O_{alk}$ bond, which in turn weakens the $O_{alk}-C$ interactions within the ligand. The average oxo- $V-O_{alk}$ bond angle is observed to be 109.6° while the average $O_{alk}-V-O_{alk}$ bond angle is 109.4° . These bond angles are representative of a tetrahedral geometry.

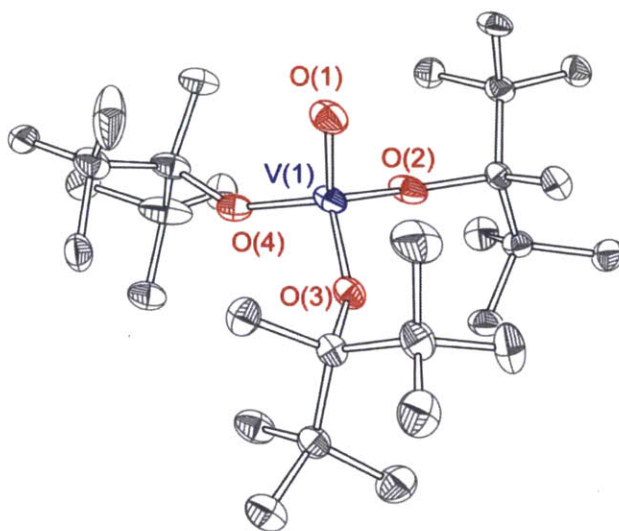


Figure 3.2. Single crystal X-ray diffraction structures for $V(ditox)_3(O)$, **3.4**. Thermal ellipsoids presented at 50% probability density. Hydrogen atoms omitted for clarity. Selected bond distances: $V(1)-O(1) = 1.605(2)$ Å, $V(1)-O(2) = 1.748(2)$ Å, $V(1)-O(3) = 1.757(2)$ Å, $V(1)-O(4) = 1.758(2)$ Å, $(O-C_{alk})_{avg} = 1.44$ Å. Selected bond angles: $O(1)-V(1)-O(2) = 109.78(6)^\circ$, $O(1)-V(1)-O(3) = 110.40(6)^\circ$, $O(1)-V(1)-O(4) = 108.59(6)^\circ$, $O(2)-V(1)-O(3) = 108.46(6)^\circ$, $O(2)-V(1)-O(4) = 110.72(6)^\circ$, $O(3)-V(1)-O(4) = 108.89(5)^\circ$.

^{51}V NMR analysis can be used to confirm that the solid state structure is maintained within a solution of **3.4**. Pribsch and Rehder have previously reported the ^{51}V NMR chemical shifts for a series of V(V) oxo complexes supported by a tris(alkoxide) ligand platform and two general trends were observed.²² The first observation was that more electron rich alkoxides result in upfield shifts as evidenced by $\delta(^{51}V) = -595.0$ ppm for $VO(OCH_2CH_2F)_3$ and $\delta(^{51}V) = -681.4$ ppm for $VO(O^tBu)_3$, with chemical shifts referenced to $\delta(^{51}V) = 0.0$ ppm for $VOCl_3$.²² The second observation was that smaller alkoxide ligands were found to oligomerize in solution at high concentrations resulting the chemical shift moving downfield. This is observed for the chemical shift of $VO(OMe)_3$ which is reported to be $\delta(^{51}V) = -598.2$ ppm at a concentration of

12 mmol/L and $\delta(^{51}\text{V}) = -547.5$ ppm at a concentration of 520 mmol/L.²² For a 22 mmol/L solution of **3.4** in C_6D_6 , the chemical shift is observed to be $\delta(^{51}\text{V}) = -691.5$ ppm relative to VOCl_3 . This indicates a slightly more electron rich ligand environment than that found for $\text{VO}(\text{O}'\text{Bu})_3$. The ^{51}V chemical shift is not observed to change at all at higher concentrations, as $\delta(^{51}\text{V}) = -691.5$ ppm at concentrations as high as 320 mmol/L. The ^{51}V chemical shift of **3.4** which is invariant with respect to concentration suggests that the molecular structure found for **3.4** persists in solution as the steric bulk of the ditox ligand inhibits oligomer formation.

Similar to the molecular structure observations for **3.4**, X-ray diffraction of single crystals of **3.5**, $\text{Cr}(\text{ditox})_3(\text{O})$, confirms the pseudo-tetrahedral geometry of the d^1 complex (Figure 3.3). The $\text{Cr}-\text{O}_{\text{oxo}}$ bond distance is observed to be 1.65 Å, which represents an elongation of 0.05 Å relative to the d^0 complex **3.4**. An elongation of the metal oxo bond upon addition of one electron suggests that within a pseudo-tetrahedral tris(alkoxide) platform, the energetically lowest d orbital is of metal oxo π^* character. In comparison to other $\text{Cr}(\text{V})-\text{O}_{\text{oxo}}$ bonds, the observed bond length for **3.5** is remarkably long. A search of the Cambridge Structural Database spanning 25 different mononuclear $\text{Cr}-\text{oxo}$ complexes displays an expected bond length range of a metal oxo triple bond: 1.49 Å-1.60 Å.²³⁻²⁸ This suggest an intrinsically weak $\text{Cr}-\text{O}_{\text{oxo}}$ bond within the pseudo-tetrahedral tris(alkoxide) ancillary ligand platform. The average $\text{Cr}-\text{O}_{\text{alk}}$ bond distance of **3.5** is found to be 1.76 Å. Notably, within error this bond length is identical to the average $\text{V}-\text{O}_{\text{alk}}$ bond distance in **3.4**, indicating that the orbital in which the d electron populated in **3.5** is essentially nonbonding with respect to the $\text{Cr}-\text{O}_{\text{alk}}$ bond. Further evidence of comparable metal-alkoxide bonding motifs in the d^0 complex **3.4** and the d^1 complex **3.5** can be found in similar average $\text{O}_{\text{alk}}-\text{C}$ bond distance (for **3.5** is 1.45 Å and for **3.4** is 1.45 Å). In considering the bond angles, the average $\text{O}_{\text{oxo}}-\text{Cr}-\text{O}_{\text{alk}}$ bond angle is observed to be 111.1° while the average $\text{O}_{\text{alk}}-\text{Cr}-\text{O}_{\text{alk}}$ bond angle is 107.7° . These bond angles indicate significant distortion from the ideal tetrahedral geometry, as the additional electron for the d^1 complex causes the metal oxo moiety to move farther away from the plane of the alkoxide ligands. Overall, the bond metrics lead to the conclusion that the first electron of metal oxo complexes in a pseudo-tetrahedral geometry supported by a tris(alkoxide) platform occupies an orbital that is primarily metal oxo π^* in nature.

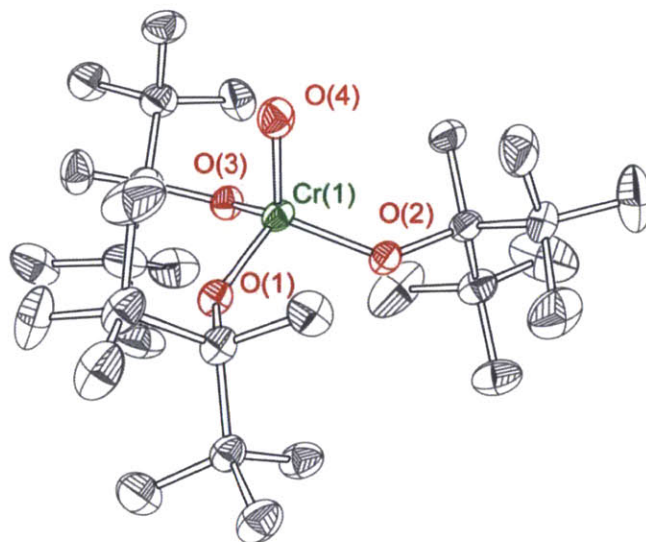


Figure 3.3. Single crystal X-ray diffraction structures for $\text{Cr}(\text{ditox})_3(\text{O})$, **3.5**. Thermal ellipsoids presented at 50% probability density. Hydrogen atoms omitted for clarity. Selected bond distances: $\text{Cr}(1)\text{--O}(4) = 1.649(2) \text{ \AA}$, $\text{Cr}(1)\text{--O}(1) = 1.773(2) \text{ \AA}$, $\text{Cr}(1)\text{--O}(2) = 1.759(2) \text{ \AA}$, $\text{Cr}(1)\text{--O}(3) = 1.762(2) \text{ \AA}$, $(\text{O}\text{--C}_{\text{alk}})_{\text{avg}} = 1.45 \text{ \AA}$. Selected bond angles: $\text{O}(4)\text{--Cr}(1)\text{--O}(1) = 109.95(8)^\circ$, $\text{O}(4)\text{--Cr}(1)\text{--O}(2) = 114.48(8)^\circ$, $\text{O}(4)\text{--Cr}(1)\text{--O}(3) = 108.92(8)^\circ$, $\text{O}(1)\text{--Cr}(1)\text{--O}(2) = 107.95(7)^\circ$, $\text{O}(2)\text{--Cr}(1)\text{--O}(3) = 105.99(7)^\circ$, $\text{O}(2)\text{--Cr}(1)\text{--O}(3) = 109.21(8)^\circ$.

Two separate crystal structures for a d^2 pseudo-tetrahedral complex have been obtained: $[\text{Cr}(\text{ditox})_3(\text{O})][\text{CoCp}_2]$, **3.6** (Figure 3.4), with an uncoordinated terminal oxo, as well as $\text{Cr}(\text{ditox})_3(\text{O})\text{K}(\text{Et}_2\text{O})_3$, **3.7** (Figure 3.5), with the terminal oxo interacting with a potassium cation. The $\text{Cr}\text{--O}_{\text{oxo}}$ bond distances for **3.6** and **3.7** are 1.64 \AA and 1.65 \AA , respectively, indicating that there is an approximately 1% elongation of the metal oxo bond length upon interaction with the potassium cation. Relative to the d^1 complex, **3.5**, there is no observable elongation of the metal oxo bond with the addition of a second electron. This suggests that the second d electron populates an orbital with minimal metal oxo π^* character. In comparison to $\text{Cr}(\text{IV})\text{--O}_{\text{oxo}}$ bond in tetragonal ligand fields, **3.6** and **3.7** contain longer than expected bond lengths. Typical $\text{Cr}(\text{IV})\text{--O}_{\text{oxo}}$ bond lengths fall within a range of $1.57\text{--}1.60$.^{11,29,30} As seen in the case of $\text{Cr}(\text{V})$ oxo complexes, the elongations observed in the pseudo-tetrahedral tris(ditox) platform relative to tetragonal platforms suggest a lower bond order for the $\text{Cr}\text{--O}_{\text{oxo}}$ bonds in **3.6** and **3.7**.

The average $\text{Cr}\text{--O}_{\text{alk}}$ bond distances for **3.6** and **3.7** are found to be 1.83 \AA and 1.84 \AA , respectively. These average bond lengths are 0.07 \AA longer than those found in **3.5** indicating that the second d electron populates a metal-alkoxide σ^* orbital. However, just as the d^1 compound **3.5** was seen to deviate from an idealized tetrahedral geometry, compounds **3.6** and

3.7 are observed to deviate further from a tetrahedral coordination sphere around the metal. For **3.6**, the average $O_{oxo}-Cr-O_{alk}$ bond angle is 114° while the average $O_{alk}-Cr-O_{alk}$ bond angle is found to be 105° . Unlike **3.5**, both Cr(IV) oxo complexes do not display an angular Jahn-Teller distortion within the ancillary ligand field, suggesting that the lowest orbitals within the d orbital manifold are degenerate to one another. For **3.7**, the average $O_{oxo}-Cr-O_{alk}$ bond angle is observed to 113° while the average $O_{alk}-Cr-O_{alk}$ bond angle is found to be 106° . Thus, the geometry of the d^2 metal complexes, while still close to pseudo-tetrahedral in nature, distorts significantly. Consequently, it is difficult to confidently assign the elongation of the chromium-alkoxide bonds of **3.6** and **3.7**, as well as the unchanged chromium oxo bonds relative to **3.5**, as being caused by additional population of the d orbital manifold or the result of the structural distortions.

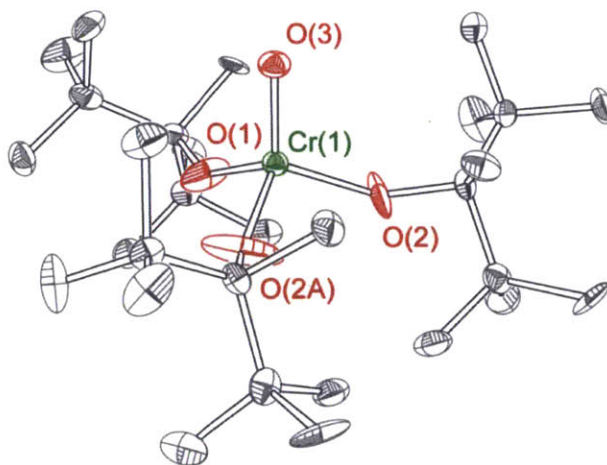


Figure 3.4. Single crystal X-ray diffraction structures for $[Cr(ditox)_3(O)][CoCp_2]$, **3.5**. Thermal ellipsoids presented at 50% probability density. Hydrogen atoms and $[CoCp_2]^+$ omitted for clarity. Selected bond distances: $Cr(1)-O(3) = 1.640(5) \text{ \AA}$, $Cr(1)-O(1) = 1.837(5) \text{ \AA}$, $Cr(1)-O(2) = 1.822(4) \text{ \AA}$, $(O-C_{alk})_{avg} = 1.32 \text{ \AA}$. Selected bond angles: $O(3)-Cr(1)-O(1) = 113.5(2)^\circ$, $O(3)-Cr(1)-O(2) = 113.6(2)^\circ$, $O(1)-Cr(1)-O(2) = 105.0(2)^\circ$, $O(2)-Cr(1)-O(2A) = 105.3(4)^\circ$.

X-ray crystallography confirms the assignment of **3.4-3.7** as pseudo-tetrahedral d^0 , d^1 and d^2 metal oxo complexes. Through an analysis of the bonding metric of **3.4-3.7** it can be concluded that the lowest orbital of the d orbital manifold for a metal oxo complex in a pseudo-tetrahedral geometry includes significant metal oxo π^* character. The elongation of the metal oxo bond by 0.05 \AA upon population of the d manifold, as well as significantly longer metal oxo

bonds in comparison to tetragonal ancillary ligands fields, indicates substantial weakening of the metal oxo bond with the addition of either one or two d electrons. Additionally, the structure of **3.7** shows an interaction of the metal oxo moiety with a potassium cation, suggesting that upon population of the d orbital manifold by two electron, the oxo behaves in a nucleophilic manner. However, the small 1% elongation of the Cr–O_{oxo} bond upon coordination of the potassium cation indicates that the nucleophilicity of the metal oxo remains weak.

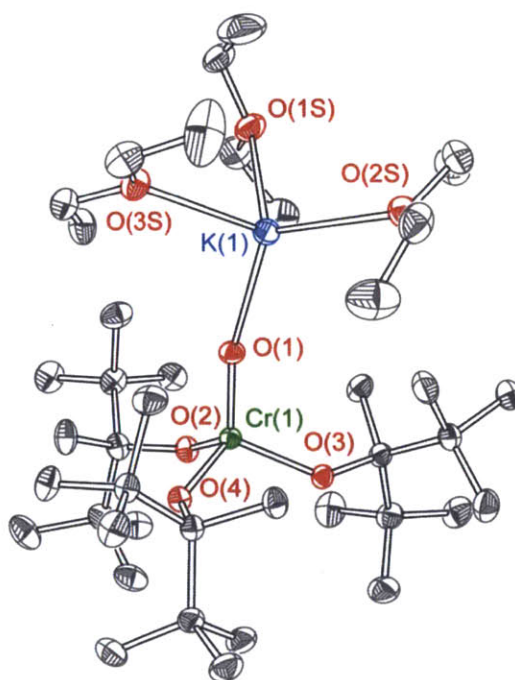


Figure 3.5. Single crystal X-ray diffraction structures for [Cr(ditox)₃(O)][K(Et₂O)₃], **3.6**. Thermal ellipsoids presented at 50% probability density. Hydrogen atoms omitted for clarity. Selected bond distances: Cr(1)–O(1) = 1.646(2) Å, Cr(1)–O(2) = 1.836(2) Å, Cr(1)–O(3) = 1.837(2) Å, Cr(1)–O(4) = 1.833(2) Å, O(1)–K(1) = 2.535(2) Å, (O–C_{alk})_{avg} = 1.43 Å. Selected bond angles: O(1)–Cr(1)–O(2) = 113.00(6)°, O(1)–Cr(1)–O(3) = 112.86(6)°, O(1)–Cr(1)–O(4) = 112.44(6)°, O(2)–Cr(1)–O(3) = 105.26(6)°, O(2)–Cr(1)–O(4) = 106.19(6)°, O(3)–Cr(1)–O(4) = 106.19(6)°.

3.2.3 Infrared Spectroscopy. Infrared spectroscopy of **3.4-3.6** was used to directly probe relevant vibrations for the d^0 , d^1 and d^2 pseudo-tetrahedral metal oxo complexes. There are two regions of interest for compounds **3.4-3.6**: 1100 cm⁻¹ to 800 cm⁻¹ is the region where the $\nu(\text{M}-\text{O}_{\text{oxo}})$ vibration for chromium oxo and vanadium oxo complexes are observed, and 750 cm⁻¹ to 550 cm⁻¹ is the range for $\nu(\text{M}-\text{O}_{\text{alk}})$ vibrations.

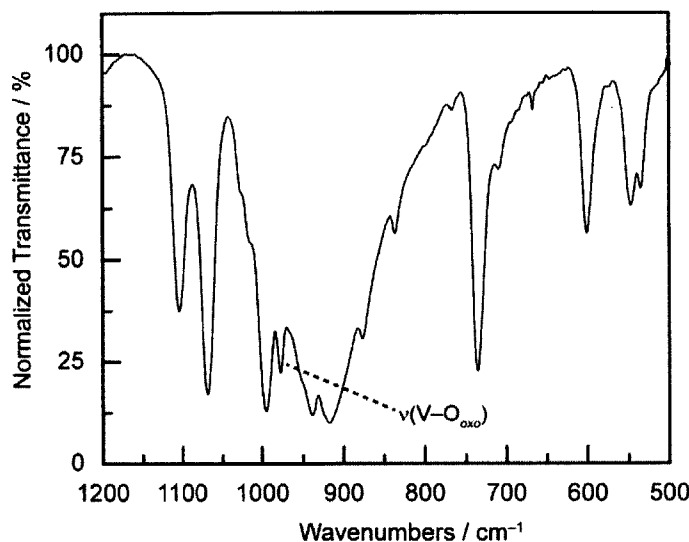


Figure 3.6. IR spectrum for **3.4**, $V(\text{ditox})_3(\text{O})$, from 1200 cm^{-1} to 500 cm^{-1} . The $\nu(\text{V}-\text{O}_{\text{oxo}})$ vibration is labeled and is assigned to a peak at 981 cm^{-1} . Vibrations corresponding to $\nu(\text{V}-\text{O}_{\text{alk}})$ are assigned at 735 cm^{-1} , 601 cm^{-1} , and 548 cm^{-1} .

The IR spectrum for the d^0 complex **3.4**, $V(\text{ditox})_3(\text{O})$, is shown in Figure 3.6. The broad $\nu(\text{C}-\text{C})$ bands of the ditox ligands that appear between 850 cm^{-1} and 950 cm^{-1} prohibit direct assignment of the $\nu(\text{V}-\text{O}_{\text{oxo}})$ vibration via isotopic labeling as a shift of the 981 cm^{-1} peak to lower energy becomes obscured. However, ^{18}O labeling of $\nu(\text{V}-\text{O}_{\text{oxo}})$ vibration of **3.4** causes the intensity of the 981 cm^{-1} peak to diminish greatly while the intensity of all other peaks in the 1100 cm^{-1} to 800 cm^{-1} region remains constant. We therefore assign the $\nu(\text{V}-\text{O}_{\text{oxo}})$ vibration to 981 cm^{-1} . Vanadium oxo stretching frequencies in tetragonal and trigonal bipyramidal ligand environments are found to be slightly higher in energy and fall within a range of 1150 cm^{-1} to 990 cm^{-1} .^{31,32} Lower energy frequencies are attributed to packing effects wherein there is an intermolecular interaction between the oxo ligand and a second vanadium metal center ($\text{V}-\text{O}_{\text{oxo}}\cdots\text{V}$) causing the internal $\text{V}-\text{O}_{\text{oxo}}$ bond to weaken.³³ As the intermolecular $\text{V}\cdots\text{O}_{\text{oxo}}$ distance is crystallographically found to be long (6.53 \AA), the lower energy vibrational frequency is indicative of an intrinsically weak $\text{V}-\text{O}_{\text{oxo}}$ bond.

The three peaks at 735 cm^{-1} and 603 cm^{-1} and 548 cm^{-1} are assigned to $\nu(\text{M}-\text{O}_{\text{alk}})$ vibrations. When compared to the $\nu(\text{M}-\text{O}_{\text{alk}})$ of the reduced precursor compound $V(\text{ditox})_3\text{THF}$, **3.1**, the high energy peak is observed to shift to higher energy upon oxidation (718 cm^{-1} in **3.1**). The shift of 17 cm^{-1} to higher energy is in agreement with the observation of shorter $\text{V}-\text{O}_{\text{alk}}$ bond

distances found crystallographically in **3.4** and the expectation of stronger ancillary ligand bonds upon oxidation. In general, the IR spectra of **3.4**, $V(\text{ditox})_3(\text{O})$, provides benchmark values for d^0 pseudo-tetrahedral metal oxo complexes for the $\nu(\text{M}-\text{O}_{\text{oxo}})$ and $\nu(\text{M}-\text{O}_{\text{alk}})$ vibrations (981 cm^{-1} and 735 cm^{-1} respectively), which are used as guides in assessing the effect of populating the d orbital manifold of the d^1 and d^2 compounds.

Figure 3.7 depicts the $\nu(\text{M}-\text{O}_{\text{oxo}})$ vibrational region for the d^1 complex **3.5**, $\text{Cr}(\text{ditox})_3(\text{O})$. The spectra for **3.5** prepared with an oxo moiety of natural isotopic abundance are shown in red. As there are several distinct peaks within this region, an isotopic labeling study was performed in order to discern the $\nu(\text{Cr}-\text{O}_{\text{oxo}})$ vibrations. Isotopically labeled compound ^{17}O -**3.5** and ^{18}O -**3.5** were prepared from isotopically labeled PhIO. A peak at 946 cm^{-1} in **3.5** shifts to 925 cm^{-1} in the spectrum of ^{17}O -**3.5** (Figure 3.7, green trace). The peak further shifts to 905 cm^{-1} in the IR spectrum of ^{18}O -**3.5** (Figure 3.7, blue trace). As such, the initial peak at 946 cm^{-1} in the spectrum of **3.5** is assigned to be the $\nu(\text{Cr}-\text{O}_{\text{oxo}})$ vibration. This is a significantly lower vibrational frequency than is typically found for $\text{Cr}(\text{V})$ oxo complexes in any ligand environments. The standard range for $\nu(\text{Cr}^{\text{V}}-\text{O}_{\text{oxo}})$ frequencies is 1100 cm^{-1} to 975 cm^{-1} .³⁴⁻³⁹

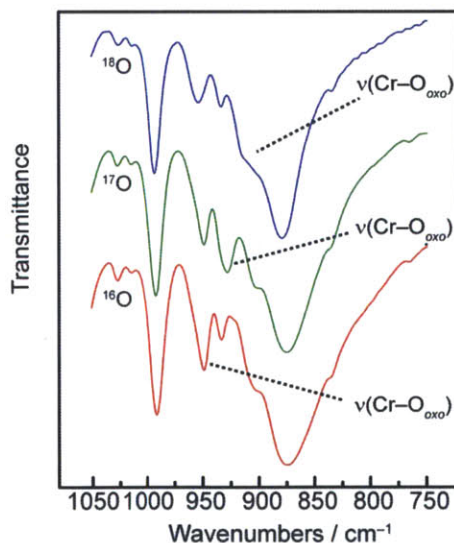


Figure 3.7. IR spectra for ^{16}O (red, natural abundance), ^{17}O (green, 50% labeled) and ^{18}O (blue, 70% labeled) isotopically labeled variant of **3.5**, $\text{Cr}(\text{ditox})_3(\text{O})$. The $\nu(\text{Cr}-\text{O}_{\text{oxo}})$ vibration is assigned to 946 cm^{-1} for ^{16}O -**3.5**, 925 cm^{-1} for ^{17}O -**3.5**, and 905 cm^{-1} for ^{18}O -**3.5**.

A metal oxo stretching frequency of 946 cm^{-1} for **3.5** represents a vibration that is 35 cm^{-1} lower in energy relative than that of the d^0 **3.4**. The decrease in the stretching frequency of the

metal oxo bond upon reduction from d^0 to d^1 is in agreement with the observed elongation of the metal oxo bond in the d^1 **3.5**. This observation supports the conclusion that the energetically lowest orbital in the d orbital manifold for metal oxo complexes in a tris(alkoxide) ancillary ligand platform has significant metal oxo π^* character. In considering the $\nu(\text{M}-\text{O}_{alk})$ vibration, the metal-alkoxide frequency at 735 cm^{-1} for d^0 **3.4** is observed to shift to lower energy in d^1 **3.5** and is assigned at 719 cm^{-1} . This indicates a significant weakening of the metal-alkoxide bond upon reduction to a d^1 configuration. The weaker bond strength was not observed in the crystal structure, as the metal-alkoxide bond distances are found to be identical in d^0 **3.4** and d^1 **3.5**.

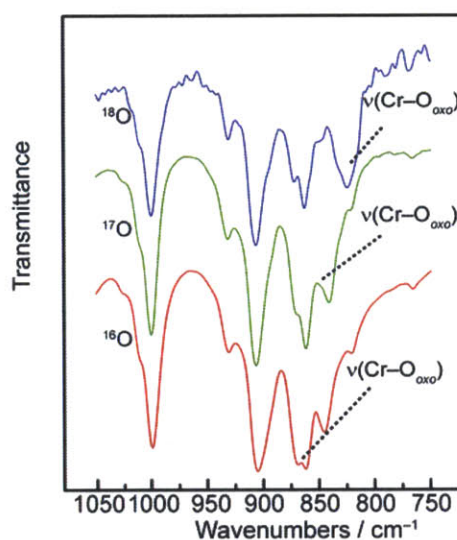


Figure 3.8. IR spectra for ^{16}O (red, natural abundance), ^{17}O (green, 50% labeled) and ^{18}O (blue, 70% labeled) isotopically labeled variant of **3.6**, $[\text{Cr}(\text{ditox})_3(\text{O})][\text{CoCp}_2]$. The $\nu(\text{Cr}-\text{O}_{oxo})$ vibration is assigned to 870 cm^{-1} for ^{16}O -**3.6**, $\sim 850\text{ cm}^{-1}$ for ^{17}O -**3.6**, and 825 cm^{-1} for ^{18}O -**3.6**.

As the d^2 **3.6**, $[\text{Cr}(\text{ditox})_3(\text{O})][\text{CoCp}_2]$, was crystallographically observed to have an equivalent Cr-oxo bond distance to that of the d^1 **3.5**, the $\nu(\text{M}-\text{O}_{oxo})$ vibration for **3.6** was also expected to be comparable to that of **3.5**. Figure 3.8 depicts the $\nu(\text{M}-\text{O}_{oxo})$ vibration region for the d^2 complex **3.6**. The spectrum for **3.6** prepared with an oxo moiety of natural isotopic abundance is shown in red. In a similar manner as was seen in the spectrum of **3.5**, there are several distinct peaks within the region this region for the IR spectra of **3.6**. Thus, a similar isotopic labeling study was performed in order to discern the $\nu(\text{Cr}-\text{O}_{oxo})$ vibration for d^2 **3.6**. Isotopically labeled compounds ^{17}O -**3.6** and ^{18}O -**3.6** were prepared via chemical reduction of

^{17}O -3.5 and ^{18}O -3.5 with CoCp_2 . Analysis of the resulting IR spectra shows a peak at 870 cm^{-1} in the spectrum of 3.6 shifting to 825 cm^{-1} in the spectrum of ^{18}O -3.6 (Figure 3.8, blue trace). As such, the initial peak at 870 cm^{-1} in the spectrum of 3.6 is assigned to be the $\nu(\text{Cr}-\text{O}_{\text{oxo}})$ stretching frequency. For the spectrum of ^{17}O -3.6, no peaks are seen at 870 cm^{-1} or 825 cm^{-1} (Figure 3.8, green trace). However, there are two overlapping peaks around 860 cm^{-1} and 840 cm^{-1} . It is believed that these peaks conceal the $\nu(\text{Cr}-\text{O}_{\text{oxo}})$ stretch for ^{17}O -3.6, and thus the $\nu(\text{Cr}-\text{O}_{\text{oxo}})$ vibration is assigned general as around 850 cm^{-1} for ^{17}O -3.6.

Comparing the $\nu(\text{M}-\text{O}_{\text{oxo}})$ stretching frequencies for d^0 3.4, d^1 3.5, and d^2 3.6, a clear trend of decreasing energy of the vibration with increased d electron count is found as the vibration shifts from 981 cm^{-1} to 946 cm^{-1} to 870 cm^{-1} . This suggests that despite no crystallographic evidence for the weakening of the metal oxo bond with the addition of a second d electron, the two energetically lowest d orbitals must be π^* with respect to the metal oxo moiety. Given the pseudo- C_{3V} symmetry of 3.4-3.6, the lowest d orbitals are assigned to be the degenerate e'' orbital, which includes the d_{xz} and d_{yz} orbitals. The d_{xz} and d_{yz} orbitals are π^* with respect to the metal oxo moiety and can readily receive two d electrons. Given the strong σ -donating ability of an oxo ligand, it is predicted that the energetically highest d orbital is the d_{z^2} . As such, a general d orbital splitting diagram is shown in Figure 3.9 is predicted for pseudo-tetrahedral metal oxo compounds.

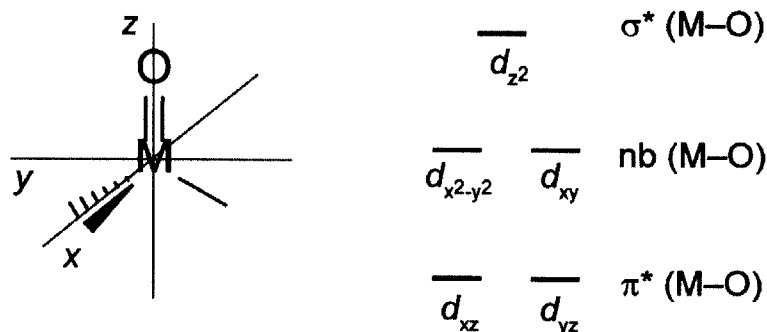


Figure 3.9. Generalized d orbital splitting diagram for pseudo-tetrahedral metal oxo derived from experimental observations.

3.2.4 Computational Analysis. DTF calculations were performed in order to assess the ordering of the d orbital manifold for pseudo-tetrahedral metal oxo complexes supported by a tris(ditox) platform. The calculations were performed using simplified models of ditox, wherein the t Bu groups have been replaced by Me groups thereby converting ditox to t BuO $^-$, resulting in the identity of the calculated species being Cr(O t Bu) $_3$ (O), **3.A**, and [Cr(O t Bu) $_3$ (O)] $^-$, **3.B**. Geometry optimizations of **3.A** and **3.B** accurately reproduce the pseudo-tetrahedral coordination environment found in **3.5** and **3.6**. The observed similarity of the Cr–O $_{oxo}$ bond distance in the d^1 **3.5** and the d^2 **3.6** was reproduced computationally for **3.A** and **3.B** (1.59 Å and 1.61 Å respectively). A frequency calculation confirmed the geometries as a local minimum as well as reproducing the decreased ν (Cr–O $_{oxo}$) stretching frequency between **3.5** and **3.6** (ν (Cr–O $_{oxo}$) = 1039 cm $^{-1}$ for **3.A**, ν (Cr–O $_{oxo}$) = 988 cm $^{-1}$ for **3.B**). Thus, the computation models **3.A** and **3.B** accurately mimic the three primary observed features of **3.5** and **3.6**: pseudo-tetrahedral coordination environment, similar metal oxo bond distances, and a decreased ν (Cr–O $_{oxo}$) stretching frequency upon reduction.

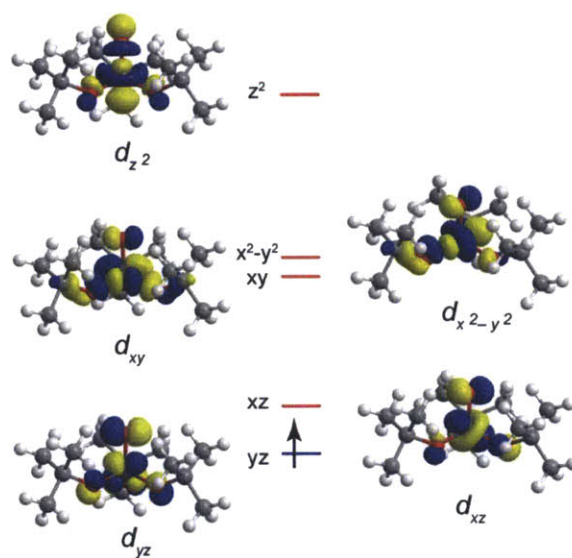


Figure 3.10. The computed α orbitals for the d orbital manifold for **3.A**, Cr(O t Bu) $_3$ (O), derived from DFT calculations. Depictions of molecular orbitals presented with an isovalue of 0.04.

The frontier d orbitals of **3.A** and **3.B** display the identical relative ordering of orbitals. The d orbital splitting diagram of **3.A** derived from DFT calculations and depictions of the α spins for the d orbitals are present in Figure 3.10. Of note, the d orbital splitting diagram for **3.B** is

similar; with the only significant difference being that for **3.B** the d_{z^2} orbital is much closer in energy to the $d_{x^2-y^2}$ and d_{xy} orbitals than is calculated for **3.A**.

The computed d orbital splitting diagrams for **3.A** and **3.B** are in agreement with the experimentally proposed d orbital splitting diagram (Figure 3.9). The strong σ -donating ability of the oxo ligand results in the greatest destabilization of the d_{z^2} orbital. The $d_{x^2-y^2}$ and d_{xy} orbitals remain σ^* with respect to the alkoxide ligands despite the alkoxide ligands residing significantly below the x/y plane. The oxygen p orbitals of the alkoxides preferentially orient towards the x/y plane and towards the $d_{x^2-y^2}$ and d_{xy} orbitals, as opposed to orienting away from the x/y plane and interacting with the d_{xz} and d_{yz} orbitals. The lowest energetic orbitals, d_{xz} and d_{yz} , are assigned to be π^* with respect to the metal oxo bond as well as π^* with respect to the metal alkoxide bonds. This assignment agrees with the experimental observation of a significant decrease of the strength of both the $\nu(\text{M}-\text{O}_{\text{oxo}})$ and $\nu(\text{M}-\text{O}_{\text{alk}})$ vibrations upon population of the d orbital manifold with one and two electrons.

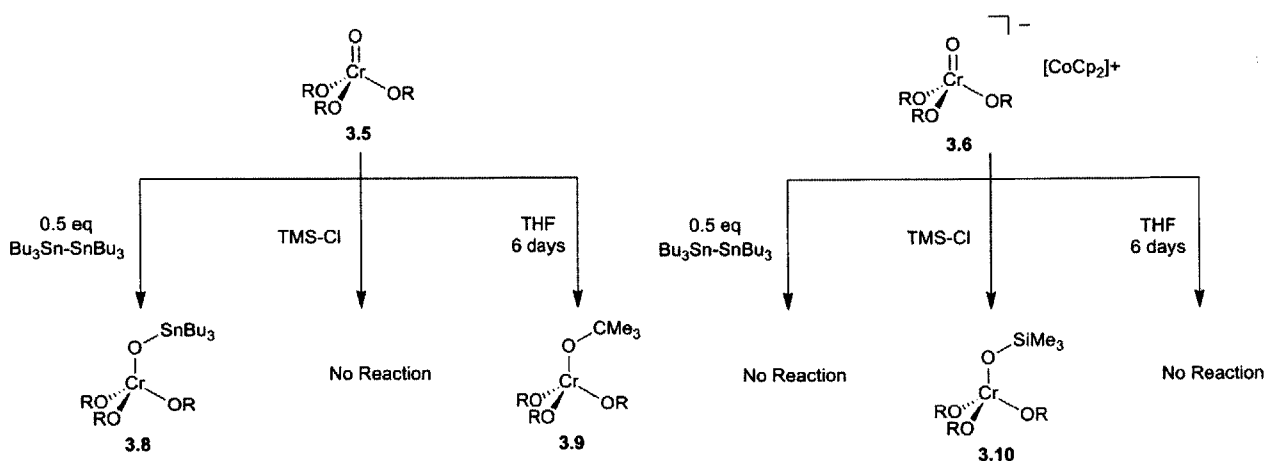
Establishing the d orbital splitting diagram as shown in Figure 3.10 allows the assignment of the bond order of the metal oxo interaction for the d^0 **3.4**, the d^1 **3.5**, and the d^2 **3.6** as 3, 2.5 and 2 respectively. Thus, the predicted reactivity trends are that the triple bond of **3.4** behaves as an electrophilic metal oxo in an AB mechanism; the metal oxo moiety of **3.5** should have unpaired spin density on the oxo moiety and react via one electron pathways in an RC mechanism; the double bond observed in **3.6** should behave as a nucleophile in an AB mechanism.

3.3 Reactivity Assay

In order to interrogate the propensity of **3.5**, $\text{Cr}(\text{ditox})_3(\text{O})$, and **3.6**, $[\text{Cr}(\text{ditox})_3(\text{O})][\text{CoCp}_2]$, to react in either 1 electron processes (RC mechanism) or 2 electron processes (AB mechanism), the compounds were each treated with bis(tributyltin) ($\text{Bu}_3\text{SnSnBu}_3$) and trimethylsilylchloride (TMSCl). The reagent $\text{Bu}_3\text{SnSnBu}_3$ was chosen to identify a RC mechanism as the Sn–Sn bond is susceptible to attack by radical reagents, such as 2-cyanoprop-2-yl radicals generated via the photolysis of azobisisobutyronitrile (AIBN), and propagates the radical behavior through the subsequent generation of 1 equiv of $\text{Bu}_3\text{Sn}\cdot$.^{40–42} The reagent TMSCl was utilized as it is susceptible to nucleophilic attack (AB mechanism) at the Si atom via an $\text{S}_{\text{N}}2$ pathway resulting the elimination of Cl^- .⁴³ Additionally, the general stabilities of **3.5** and

3.6 were evaluated by allowing solutions of each to rest for several days at room temperature. The results of these reactions are summarized in Scheme 3.3.

Scheme 3.3



Compound **3.5**, Cr(ditox)₃(O), has one d electron in a chromium oxo π* orbital and thus is expected to react in one electron RC pathways. Treatment of **3.5** with excess Bu₃SnSnBu₃ over the course of several hours results in a reaction to furnish the green Cr(IV) product **3.8**. The crystal structure of **3.8** (Figure 3.11) verifies a Cr(IV) formulation in which the oxo ligand is transformed into a stannoxo group, resulting in the pseudo-tetrahedral compound Cr(ditox)₃(OSnBu₃) in 55% isolated yield. Treatment of **3.5** with 1 equiv of TMSCl yielded no observable reaction. Allowing **3.5** to remain in solution at room temperature (THF, toluene, diethyl ether, pentane) results in slow decomposition to another green-brown Cr(IV) product, **3.9** in 37% yield. A crystal structure of **3.9** is presented in Figure 3.12 and identifies the product as Cr(ditox)₃(O^tBu). Compound **3.9** is proposed to form via a bimolecular reaction wherein **3.5** reacts with the ditox ligand of another equivalent of **3.5** which induces a radical transfer of ^tBu group to the high valent chromium oxo. Thus, both observed products, **3.8** and **3.9**, are thought to form via a RC-type of mechanism. This establishes the primary mechanism for a d¹ pseudo-tetrahedral metal oxo complex as radical in nature.

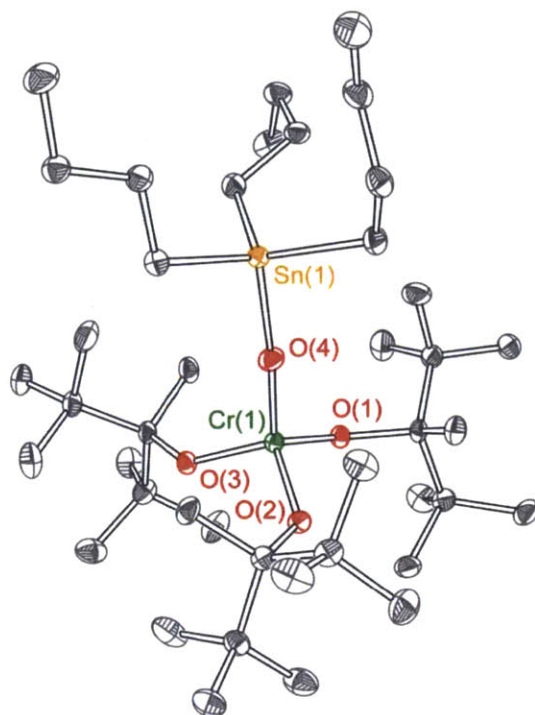


Figure 3.11. Single crystal X-ray diffraction structures for $\text{Cr}(\text{ditox})_3(\text{OSnBu}_3)$, **3.8**. Thermal ellipsoids presented at 50% probability density. Hydrogen atoms omitted for clarity. Selected bond distances: $\text{Cr}(1)\text{--O}(4) = 1.721(2) \text{ \AA}$, $\text{Cr}(1)\text{--O}(1) = 1.795(2) \text{ \AA}$, $\text{Cr}(1)\text{--O}(2) = 1.789(2) \text{ \AA}$, $\text{Cr}(1)\text{--O}(3) = 1.791(2) \text{ \AA}$, $\text{O}(4)\text{--Sn}(1) = 1.998(2) \text{ \AA}$, $(\text{O}\text{--C}_{\text{alk}})_{\text{avg}} = 1.44 \text{ \AA}$. Selected bond angles: $\text{O}(4)\text{--Cr}(1)\text{--O}(1) = 111.38(7)^\circ$, $\text{O}(4)\text{--Cr}(1)\text{--O}(2) = 111.38(7)^\circ$, $\text{O}(4)\text{--Cr}(1)\text{--O}(3) = 111.89(7)^\circ$, $\text{O}(1)\text{--Cr}(1)\text{--O}(2) = 107.81(7)^\circ$, $\text{O}(1)\text{--Cr}(1)\text{--O}(3) = 107.73(7)^\circ$, $\text{O}(2)\text{--Cr}(1)\text{--O}(3) = 106.42(7)^\circ$.

Compound **3.6**, $[\text{Cr}(\text{ditox})_3(\text{O})][\text{CoCp}_2]$ was exposed to the identical reaction conditions as **3.5**. No reaction is observed upon treatment of **3.6** with excess equivalents of $\text{Bu}_3\text{SnSnBu}_3$. Additionally, **3.6** is stable in solution at room temperature for several days and does not participate in the radical transfer of a $t\text{Bu}$ group to form an analogous structure to **3.9**. These two observations indicate that the d^2 pseudo-tetrahedral metal oxo compound **3.6** does not preferentially react in a one electron manner (RC mechanism). Electrochemically, solutions of **3.6** in THF are found to be resistant to reduction at negative potentials ca. -2.5 V vs. Fc/Fc^+ . The lack of reactivity is additionally attributed to the thermodynamic stability of the tetravalent chromium oxo moiety in a pseudo-tetrahedral tris(alkoxide) ligand platform. Upon treatment of **3.6** with TMSCl , an immediate white precipitate was observed and the original blue solution assumes a green color, indicating the formation of a Cr(IV) compound **3.10**. The identity of **3.10** is verified via crystallography as $\text{Cr}(\text{ditox})_3(\text{OTMS})$ (Figure 3.13). The formation of **3.10** proceeds via a nucleophilic attack on the Si atom followed by elimination of $[\text{CoCp}_2][\text{Cl}]$. The nucleophilic behavior of the chromium oxo of **3.6**, along with nucleophilic coordination of a K

cation in 3.7, indicates that d^2 pseudo-tetrahedral metal oxo complexes react primarily as nucleophiles in an AB-type of mechanism.

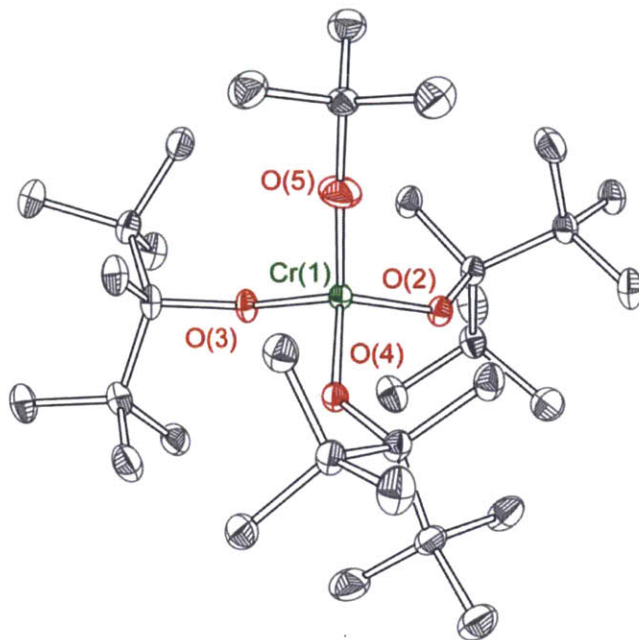


Figure 3.12. Single crystal X-ray diffraction structures for $\text{Cr}(\text{ditox})_3(\text{O}'\text{Bu})$, **3.9**. Thermal ellipsoids presented at 50% probability density. Hydrogen atoms omitted for clarity. Selected bond distances: $\text{Cr}(1)\text{--O}(5) = 1.751(2) \text{ \AA}$, $\text{Cr}(1)\text{--O}(2) = 1.796(2) \text{ \AA}$, $\text{Cr}(1)\text{--O}(3) = 1.782(2) \text{ \AA}$, $\text{Cr}(1)\text{--O}(4) = 1.781(2) \text{ \AA}$, $(\text{O}\text{--C}_{\text{alk}})_{\text{avg}}$ for ditox = 1.46 \AA . Selected bond angles: $\text{O}(5)\text{--Cr}(1)\text{--O}(2) = 113.321(8)^\circ$, $\text{O}(5)\text{--Cr}(1)\text{--O}(3) = 112.15(8)^\circ$, $\text{O}(5)\text{--Cr}(1)\text{--O}(4) = 112.30(8)^\circ$, $\text{O}(2)\text{--Cr}(1)\text{--O}(3) = 107.53(7)^\circ$, $\text{O}(2)\text{--Cr}(1)\text{--O}(4) = 105.55(7)^\circ$, $\text{O}(3)\text{--Cr}(1)\text{--O}(4) = 105.57(7)^\circ$.

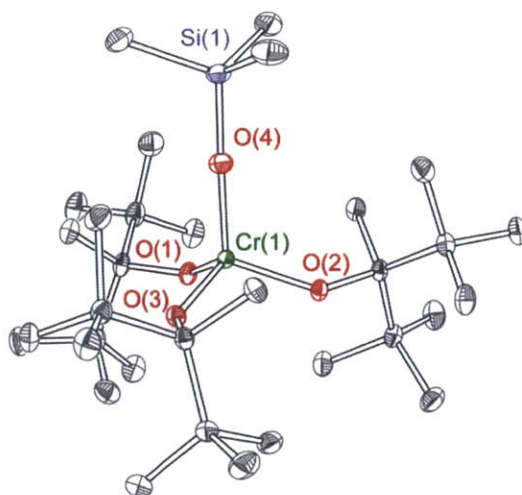


Figure 3.13. Single crystal X-ray diffraction structures for $\text{Cr}(\text{ditox})_3(\text{OTMS})$, **3.10**. Thermal ellipsoids presented at 50% probability density. Hydrogen atoms omitted for clarity. Selected bond distances: $\text{Cr}(1)\text{--O}(4) = 1.780(1) \text{ \AA}$, $\text{Cr}(1)\text{--O}(1) = 1.775(1) \text{ \AA}$, $\text{Cr}(1)\text{--O}(2) = 1.777(1) \text{ \AA}$, $\text{Cr}(1)\text{--O}(3) = 1.774(1) \text{ \AA}$, $\text{O}(4)\text{--Si}(1) = 1.998(2) \text{ \AA}$, $(\text{O}\text{--C}_{\text{alk}})_{\text{avg}}$ = 1.45 \AA . Selected bond angles: $\text{O}(4)\text{--Cr}(1)\text{--O}(1) = 111.41(5)^\circ$, $\text{O}(4)\text{--Cr}(1)\text{--O}(2) = 111.54(5)^\circ$, $\text{O}(4)\text{--Cr}(1)\text{--O}(3) = 110.74(5)^\circ$, $\text{O}(1)\text{--Cr}(1)\text{--O}(2) = 107.23(4)^\circ$, $\text{O}(1)\text{--Cr}(1)\text{--O}(3) = 108.04(4)^\circ$, $\text{O}(2)\text{--Cr}(1)\text{--O}(3) = 107.71(5)^\circ$.

Motivated by a desire to perform transformations that result in complexes more relevant to intermediates of water oxidation, terminal metal-hydroxide moieties synthesized from terminal metal oxo complexes were targeted. Unexpectedly, treatment of **3.5**, $\text{Cr}(\text{ditox})_3\text{O}$, with Bu_3SnH did not afford hydrogen atom transfer product, but rather resulted in the formation of **3.8**, $\text{Cr}(\text{ditox})_3(\text{OSnBu}_3)$, in low yields (17%). Analysis of the reaction progress by ^1H NMR indicated an increase of Hditox concentration during the course for the reaction. Based on these observations, it was surmised that Bu_3SnH addition resulted in the formation of 0.5 equiv of **3.8** as well as 0.5 equiv of $\text{Cr}(\text{ditox})_3(\text{OH})$, followed by fast decomposition of $\text{Cr}(\text{ditox})_3(\text{OH})$ to Hditox and unidentified $\text{Cr}(\text{IV})$ oxo products. To interrogate this further, 1 equiv of lutidinium hydrochloride was added to **3.7**, $\text{Cr}(\text{ditox})_3(\text{O})\text{K}(\text{Et}_2\text{O})_3$. The initially blue solution immediately formed a white precipitate and the solution assumed a blue-green color. Removal of the solvent followed by filtration and recrystallization from pentane afforded compound **3.11**. The identity of **3.11** was verified by crystallography and determined to be $[\text{Cr}(\text{ditox})_2(\text{O})]_2$ (Figure 3.14). The identification of **3.11** supports the notion of the inherent instability of $\text{Cr}(\text{ditox})_3(\text{OH})$ as protonation of ditox was found to occur preferentially over the protonation of the oxo.

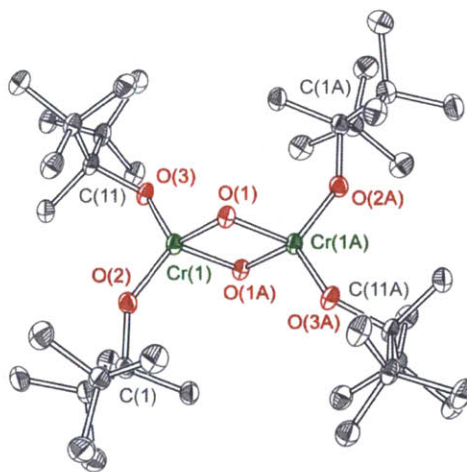
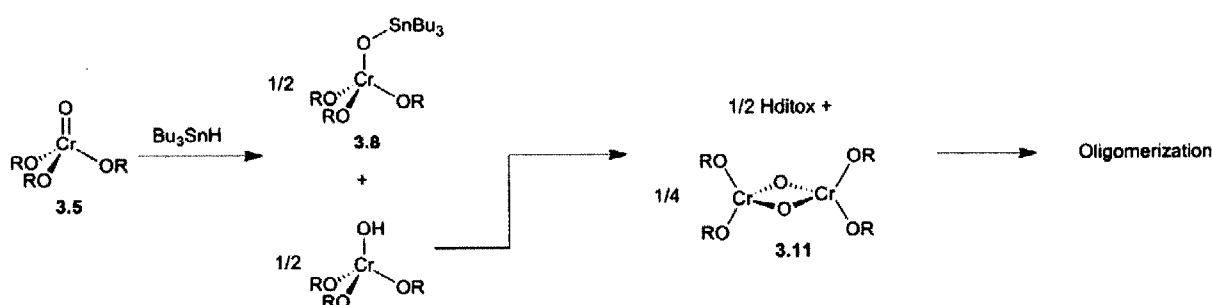


Figure 3.14. Single crystal X-ray diffraction structures for $[\text{Cr}(\text{ditox})_2(\text{O})]_2$, **3.11**. Thermal ellipsoids presented at 50% probability density. Hydrogen atoms omitted for clarity. Selected bond distances: $\text{Cr}(1)\text{--O}(1) = 1.767(2)$ Å, $\text{Cr}(1)\text{--O}(1\text{A}) = 1.843(2)$ Å, $\text{Cr}(1)\text{--O}(2) = 1.742(2)$ Å, $\text{Cr}(1)\text{--O}(3) = 1.760(2)$ Å, $(\text{O}\text{--C}_{\text{alk}})_{\text{avg}} = 1.45$ Å. Selected bond angles: $\text{O}(1)\text{--Cr}(1)\text{--O}(1\text{A}) = 85.33(8)^\circ$, $\text{O}(1)\text{--Cr}(1)\text{--O}(2) = 115.28(8)^\circ$, $\text{O}(1)\text{--Cr}(1)\text{--O}(3) = 117.74(5)^\circ$, $\text{O}(1\text{A})\text{--Cr}(1)\text{--O}(2) = 112.88(8)^\circ$, $\text{O}(1\text{A})\text{--Cr}(1)\text{--O}(3) = 103.16(8)^\circ$, $\text{Cr}(1)\text{--O}(1)\text{--Cr}(1\text{A}) = 94.67(8)^\circ$.

With the identification of **3.11** as $[\text{Cr}(\text{ditox})_2(\text{O})]_2$, the proposed mechanistic pathway for the reactivity upon treatment of **3.5** with Bu_3SnH is presented in Scheme 3.4. The $\text{Cr}(\text{ditox})_3(\text{OH})$ is proposed to form initially followed by elimination of Hditox and the formation of **3.11**. The implication of the elimination of Hditox from $\text{Cr}(\text{ditox})_3(\text{OH})$ is that the pK_a of the $\text{Cr}(\text{IV})$ –hydroxide is comparable to that of Hditox , which is estimated to be approximately 30 in organic solvents. Further oligomerization of **3.11** is proposed due to the tendency of low coordinate metal oxo complexes supported by alkoxides to form multi-metallic species.

Scheme 3.4



Interrogating the reactivity of pseudo-tetrahedral chromium oxo complexes with d^1 and d^2 electron counts establishes that d^1 complexes react preferentially via one electron radical pathways whereas d^2 complexes react primarily as nucleophiles. The reactivity patterns can be rationalized by consideration of the electronic structure of pseudo-tetrahedral metal oxo complexes wherein d^1 complexes have a bond order of 2.5 and unpaired spin density on the oxo moiety and d^2 complexes have a bond order of 2. Whereas the d^2 complexes are calculated to have unpaired spin density on the oxo moiety, the lower oxidation state for $\text{Cr}(\text{IV})$ versus $\text{Cr}(\text{V})$ diminishes the thermodynamic strength of $\text{Cr}(\text{IV})$ as an oxidation and leads to preferential nucleophilic behavior. However, radical chemistry mediated through a pseudo-tetrahedral $\text{Cr}(\text{IV})$ complex would be consistent with our understanding of the electronic structure of the complexes.

3.4 Pseudo-Tetrahedral Terminal Metal–sulfidos

3.4.1 Motivation for Sulfido Complexes. Compounds of early transition metals in the tris(ditox) ancillary ligand environments with sulfido ligands were targeted as these compounds afford the opportunity to study further the electronic structure of complexes with terminal chalcogen ligands at the aforementioned platform as well as potentially to study the chalcogen–

chalcogen bond forming process. Ligated sulfur atoms have been observed to catenize readily to form polysulfido ligands.⁴⁴⁻⁴⁸ This facility to which S–S bonds can be made is in stark contrast to the difficulty in which O–O bonds are formed.

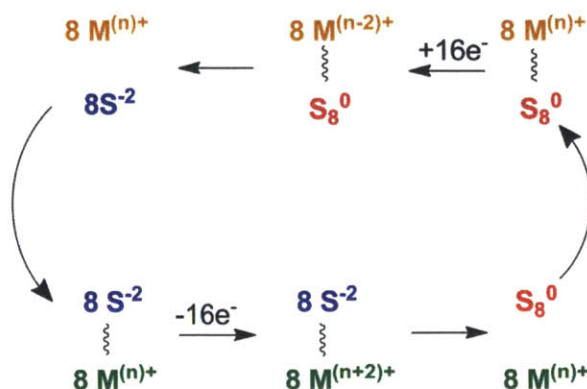


Figure 3.15. Cycle for metal catalyzed oxidation of S^{2-} and reduction of S_8 showing the possible requirement for the metal to access a range of 4 oxidation states.

Interest in terminal sulfur moieties stems from cyclcooctasulfur, S_8 , as a promising candidate for energy storage as a possible flow battery analyte due to its solubility and the potential for storing 16 electrons within the S_8^0 to 8S^{2-} redox transformation.⁴⁹⁻⁵³ Nevertheless, the chemistry occurring at the electrode of a flow battery is poorly understood. The full potential of the system is not fully realized as the 2-electron polysulfido transformation of 3S_2^{2-} to 2S_3^{2-} dominates. This process stores only 2 electrons within 6 sulfur atom. Conversely, the ability to facilitate the transformation between 8S^{2-} and S_8^0 would result in the storage of 16 electrons within 8 sulfur atoms, increasing the energy density stored from 1 electron per 3 sulfur atoms to 2 electrons per 1 sulfur atom. Ideally, a catalyst for the transformation would mediate both the oxidation and reduction events for the $8\text{S}^{2-}/\text{S}_8^0$ transformation as shown in Figure 3.15. Consequently, the metal center would likely need the ability to access a range 4 different oxidation states. Group 6 metals have the possibility to access such as range of oxidation states and thus could facilitate the desired transformation.

3.4.2 Synthetic Methods. The previous strategy employed for the generation of terminal metal oxo complexes involved the exposure of tris(ditox) metal complex precursors in reduced states with oxygen atom transfer reagents. An analogous strategy was sought for the generation of terminal sulfides whereby triphenylstibine sulfide (Ph_3SbS) was used as a sulfur atom transfer reagent. Treatment of a blue THF solution of $\text{V}(\text{ditox})_3(\text{THF})$, **3.1**, with 1 equiv of Ph_3SbS at

room temperature yielded no observed color change. Upon removal of THF, pentane was added to the reaction mixture form a dilute solution. Cooling the dilute pentane solution to $-40\text{ }^{\circ}\text{C}$ for 48 h affords large pale yellow crystals. Crystallography confirms the identity of the pale yellow crystals as Ph_3SbS , thus indicating no sulfur atom transfer to **3.1** occurs. Treatment of **3.2**, $\text{Cr}(\text{ditox})_3$, under analogous conditions similarly results in no observed sulfur atom transfer.

Sulfur atom transfer to **3.3**, $[\text{Cr}(\text{ditox})_3][\text{K}(\text{15C5})_2]$ was observed by the addition of a 1 equiv of Ph_3SbS to a blue THF solution of **3.3** that immediately turned brown. The THF was removed in vacuo and the resulting residue was washed extensively with pentane to remove Ph_3Sb . The remaining brown residue was taken up in an acetonitrile solution and filtered through celite. Upon concentration and cooling to $-40\text{ }^{\circ}\text{C}$ for 24 h, yellow crystals were obtained. The infrared spectrum of the yellow crystals showed a strong peak grow in at 485 cm^{-1} , which is assigned to the terminal $\nu(\text{M}-\text{S})$ stretching frequency. Crystallography confirms the nature of this species as the pseudo-tetrahedral complex $[\text{Cr}(\text{ditox})_3(\text{S})][\text{K}(\text{15C5})_2]$ (**3.12**), with a terminal Cr–S distance of 2.09 \AA (Figure 3.16, A). Unfortunately, the quality of the crystal structure is low, owing to the low symmetry (triclinic) and the large size of the unit cell size ($a = 22.083(2)$, $b = 46.622(4)$, $c = 22.553(2)$) resulting in 18 unique different orientations of the molecule to be refined. Each molecule has a substantially different orientation of the $[\text{K}(\text{15C5})_2]^+$ cation resulting in a large amount of unique ^tBu rotational disorder as well as 15-crown-5-ether positional disorder to be refined. Given the data sets acquired, complete refinement **3.12** could not be completed. However, the assignment of a terminal-sulfide ligand is confirmed and an estimation of 2.09 \AA for the Cr–S bond distance is made.

In a similar manner to the cation-exchange synthesis of **3.7**, $\text{Cr}(\text{ditox})_3(\text{O})\text{K}(\text{Et}_2\text{O})_3$, addition of 1 equiv of AgOTf to a brown solution of **3.12** in acetonitrile, results in the formation of a white precipitate while the solution maintains the brown color. The white precipitate can be filtered away and the acetonitrile solvent can be removed in vacuo. Addition of pentane to the resulting brown residue results in a brown pentane solution of **3.13**. The infrared spectrum of **3.13** shows that the assigned $\nu(\text{M}-\text{S})$ stretching frequency in **3.12** persists but has shifted to lower energy by 13 cm^{-1} and is observed at 472 cm^{-1} . Crystallography confirms the identity of **3.13** and as the trimer $[\text{Cr}(\text{ditox})_3(\text{S})\text{Ag}]_3$, which is depicted in Figure 3.16.B. The structure of **3.13** is analogous to that of **3.7** with a direct coordination of the terminal chalcogen atom to a coordinating cation. The structure of **3.7** shows solvent molecules (diethyl ether) coordinating to

the rest of the open sites of the potassium cation, whereas the structure of **3.13** shows that the silver cation coordinating to a second terminal sulfur atom. The direct coordination of the sulfur atoms by the silver cation causes the Cr–S bond distance to elongate relative to that found in **3.12** to 2.23 Å.

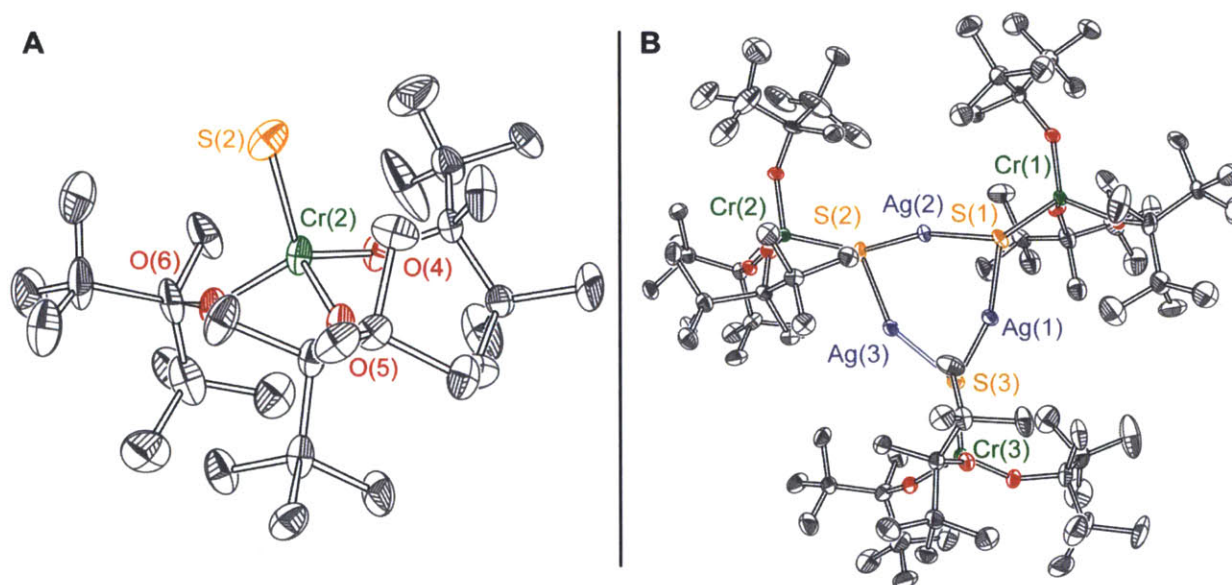


Figure 3.16. (A) Crystal structure of **3.12**, $[\text{Cr}(\text{ditox})_3(\text{S})][\text{K}(\text{15C5})_2]$. Thermal ellipsoids are presented at 50% probability density. Hydrogen atoms and $[\text{K}(\text{15C5})_2]^+$ cation omitted for clarity. The structure is incompletely refined, but shows a terminal Cr–S bond distance of 2.09 Å. (B) Crystal structure of **3.13**, $[\text{Cr}(\text{ditox})_3(\text{S})\text{Ag}]_3$. Thermal ellipsoids presented at 50% probability density. Hydrogen atoms omitted for clarity. Selected bond distances: Cr(1)–S(1) = 2.247(2) Å, Cr(2)–S(2) = 2.231(2) Å, 2.397(2) Å, Cr(3)–S(3) = 2.222(2) Å, S(1)–Ag(1) = 2.386(2) Å, S(1)–Ag(2) = 2.397(2) Å; S(2)–Ag(2) = 2.398(2) Å, S(2)–Ag(3) = 2.391(2) Å, S(3)–Ag(2) = 2.387(2) Å, S(3)–Ag(3) = 2.374(2) Å. Selected bond angles: $(\text{Cr}–\text{S}–\text{Ag})_{\text{avg}} = 118.7^\circ$, $(\text{Ag}–\text{S}–\text{Ag})_{\text{avg}} = 77.5^\circ$, $(\text{S}–\text{Ag}–\text{S})_{\text{avg}} = 157.7^\circ$.

3.4.3 Electrochemical Analysis. Cyclic voltammetry was performed on **3.12**, $[\text{Cr}(\text{ditox})_3(\text{S})][\text{K}(\text{15C5})_2]$ to assess the behavior of the pseudo-tetrahedral metal-sulfide upon exposure to oxidizing conditions. Cyclic voltammograms were collected with a 1.0 mM solution of **3.12** in acetonitrile with 0.1 M $[\text{TBA}][\text{PF}_6]$ as a supporting electrolyte. A glassy carbon electrode was used as a working electrode; the reference electrode was a high surface area Pt electrode. The voltammograms were referenced to Ag/AgNO_3 redox couple and were subsequently externally referenced to the Fc/Fc^+ redox couple. Under these conditions, the open circuit potential was -1.100 V.

Cyclic voltammograms acquired at a scan rate of 100 mV/s initially scanning in the anodic direction show an irreversible feature with an onset potential at -0.710 V. At a scan rate of 100

mV/s, the peak current potential was observed at -0.621 V. At further anodic potentials, an additional irreversible feature was observed at $+0.500$ V. The cathodic return scans displayed no electrochemical features, however, when the anodic scan was stopped prior to the feature at $+0.500$ V, the subsequent cathodic return scan displayed a broad irreversible feature with an onset potential of -0.890 V and a peak current potential of -1.152 V. The anodic feature at $+0.500$ V is thus assigned to a decomposition event and all subsequent anodic scans were stopped at -0.250 V.

When the initial scan was in the cathodic direction, no feature was observed at -1.152 V. Thus, the irreversible cathodic feature at -1.152 V is electrochemically related to the irreversible anodic feature at -0.621 V. In order to glean insight into the nature of the irreversible redox event at -0.621 V, a scan rate dependence for the peak potential was performed. The data (Figure 3.17) shows the peak current potential plotted versus $\log(\text{scan rate})$ shows a relationship between these two values of 61 mV/decade. A slope of approximately 60 mV/decade is indicative rate limiting electron transfer from the electrode to the substrate.⁵⁴ Consequently, further electrochemical methods are unable to elucidate mechanistic information regarding nature of the oxidation event observed. Additionally, similar analysis was performed on the cathodic electrochemical feature. However no clear scan rate dependence was observed. At faster scan rates, the entire feature became much broader and consequently the peak current potential could not be clearly identified.

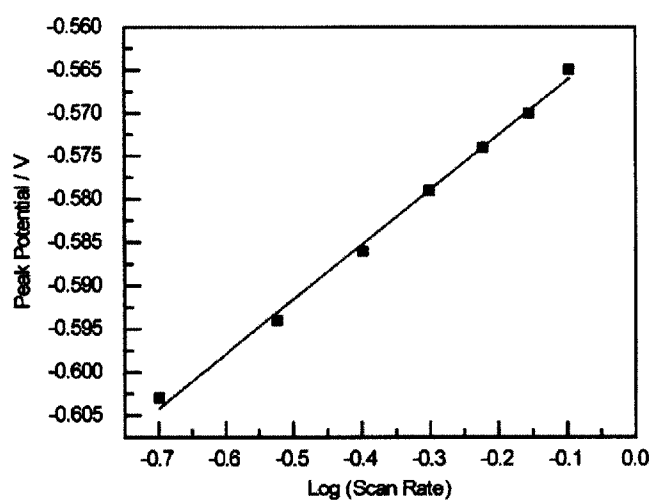


Figure 3.17. Peak potential versus $\log(\text{scan rate, V/s})$ plot for the electrochemical oxidation feature observed for 3.12, $[\text{Cr}(\text{ditox})_3(\text{S})][\text{K}(\text{15C5})_2]$. The data is fit to a slope of 61 mV/dec which is indicative of rate limiting electron transfer from the electrode.

To characterize the electrochemical oxidation feature observed for **3.12**, $[\text{Cr}(\text{ditox})_3(\text{S})][\text{K}(\text{15C5})_2]$, a titration experiment was performed in which FcOTf was added to solutions of **3.12** in THF. The additions were monitored via UV-vis spectroscopy for the appearance of a FcOTf absorption, which is assigned to 617 nm. The observation of the FcOTf absorption feature at 617 nm is indicative of complete oxidation of **3.12**. The electronic absorption data for the titration is presented in Figure 3.18. Due to the air sensitivity of the **3.12**, stock solutions of **3.12** and FcOTf were made inside a glovebox maintained under inert N_2 atmosphere. Each UV-vis sample was made independently with different ratios of stock solutions, which resulted in slight variations of in the baseline of each spectra acquired. Additionally, the increasing presence of a strong ferrocene absorption band at higher energy causes variations in the baselines for each sample, which can be seen in Figure 3.18.

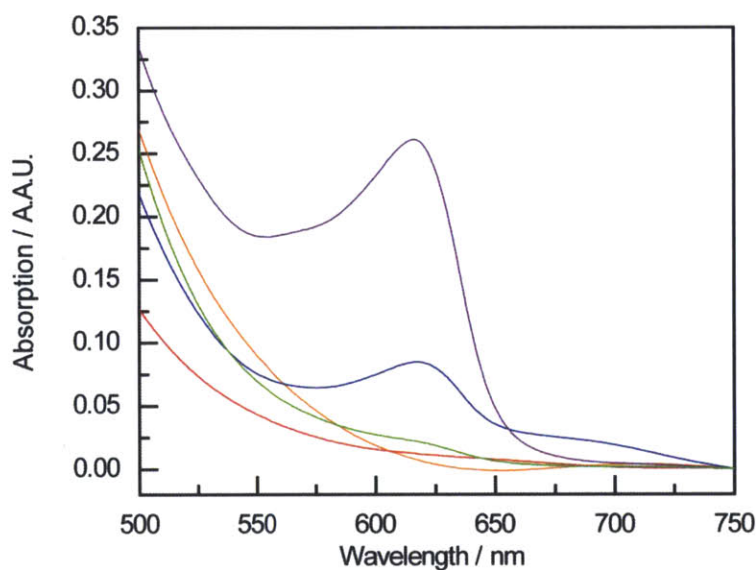


Figure 3.18. UV-vis spectra for the titration of $[\text{Cr}(\text{ditox})_3(\text{S})][\text{K}(\text{15C5})_2]$ with FcOTf: (red) 1.0 eq. FcOTf; (orange) 1.5 eq. FcOTf; (green) 2.0 eq FcOTf; (blue) 2.2 eq. Fc OTf; (purple) 3.0 eq FcOTf.

Upon addition of 1 equiv of FcOTf to a solution of $[\text{Cr}(\text{ditox})_3(\text{S})][\text{K}(\text{15C5})_2]$, **3.12**, no FcOTf absorption was observed at 617 nm. The addition of 1.5 equiv of FcOTf to **3.12** likewise resulted in no absorption feature at 617 nm, indicating that **3.12** can be oxidized more than once. A very small absorption at 617 nm can be seen with the addition of 2 equiv of FcOTf to **3.12**, suggesting that **3.12** is fully oxidized once treated with 2 equiv of oxidant. Subsequent samples with 2.2 equiv of FcOTf and 3 equiv of FcOTf show significant absorption at 617 nm. As the

titration of **3.12** with FcOTf showed significant absorption upon the addition of greater than 2 equiv of oxidant, $[\text{Cr}(\text{ditox})_3(\text{S})][\text{K}(\text{15C5})_2]$ is proposed to be able to undergo two one-electron oxidations. The anodic electrochemical feature at -0.621 V is similarly proposed to include two one-electron oxidation events.

Attempts to isolate the products of chemical oxidation of **3.12** and **3.13** via the addition of both 1 equiv and 2 equiv of a chemical oxidant, have been unsuccessful as intractable mixtures of chromium containing products are observed. Under conditions for crystallization (concentrated acetonitrile solution stored at -40 °C for 24 h) pale yellow crystals reproducibly form. These crystals can be mechanically separated from the mixture and have been determined by single crystal XRD (unit cell parameters were *Fddd* with $a=10.468$, $b=12.866$, $c=24.486$, which are in agreement for literature reports for cyclo- $\text{S}_{8-\alpha}$ ⁵⁵) as well as by infrared spectroscopy to be cyclo- S_8 . The typical yield of mechanically separated S_8 crystals was about 43%, which indicates possible preferential formation of S_8 relative to other possible polysulfides. However, it remains unknown as to whether or not the S_8 is formed chemically upon oxidation of **3.12** or **3.13**, or a result of the crystallization conditions employed.

3.4.4 Computational Analysis. The reproducible observation of S_8 upon the oxidation of $[\text{Cr}(\text{ditox})_3(\text{S})][\text{K}(\text{15C5})_2]$ suggests that the pseudo-tetrahedral oxidic ligand environment of the Cr(IV)–S moiety of **3.12** is capable to forming S–S bonds upon oxidation. To assess the underlying electronic structure of oxidized species, DFT calculations were performed on the truncated model systems $[\text{Cr}(\text{O}^t\text{Bu})_3(\text{S})]^-$, **3.C**, and $\text{Cr}(\text{O}^t\text{Bu})_3(\text{S})$, **3.D**. Geometry optimization were performed on **3.C** and **3.D** and the observed pseudo-tetrahedral geometries were determined to be ground state structures. The calculated geometry for **3.C** closely resemble the experimentally determined structure for the analogous compounds **3.12** and **3.13**, as the Cr–S bond distance was calculated to be 2.19 Å and the $\nu(\text{Cr}–\text{S})$ stretching frequency was calculated to be 462 cm^{-1} (as compared to the experimentally found frequency of 485 cm^{-1}).

The *d* orbital manifold for **3.C** and **3.D** are qualitatively similar to the *d* orbital splitting pattern of the comparable oxo compounds, **3.A** and **3.B**, the highest energy *d* orbital being d_{z^2} , followed by $d_{x^2-y^2}$ and d_{xy} , with d_{xz} and d_{yz} being the lowest energetic *d* orbitals. The *d* orbital manifold for **3.D**, $\text{Cr}(\text{O}^t\text{Bu})_3(\text{S})$, and relevant molecular orbital surfaces are presented in Figure 3.19. The *d* orbital splitting diagram for **3.D** shows a large energetic gap between the unoccupied

d_{xz} and occupied d_{yz} (1.9 eV). In the case of the d^2 **3.C**, the degenerate d_{xz} and d_{yz} orbitals are both occupied and reside about 3.4 eV below the d_{z^2} orbital.

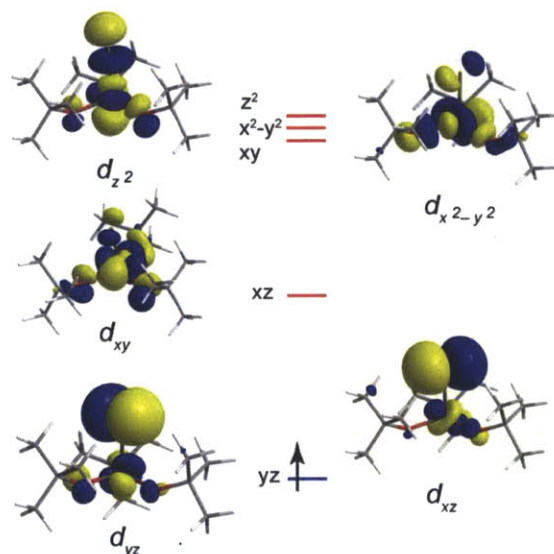


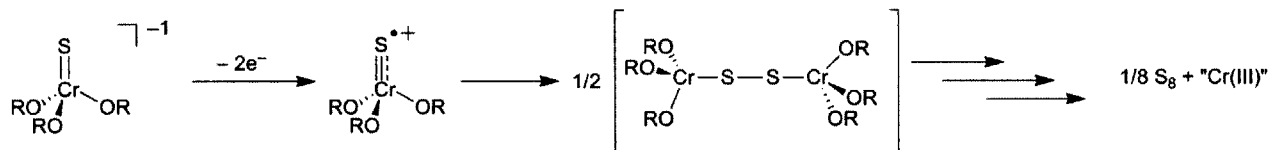
Figure 3.19 Computed frontier orbital diagram for the α spins of the calculated compound **3.D**, $\text{Cr}(\text{O}'\text{Bu})_3(\text{O})$, derived from DFT calculations. Molecular orbital surfaces presented at an isovalue of 0.04.

For both **3.C** and **3.D**, the molecular orbitals assigned to d_{xz} and d_{yz} are calculated to have significant parentage from sulfur p orbitals; approximately 50%. Thus the frontier orbitals are not of solely of d orbital parentage but rather are more accurately described as highly mixed $\text{Cr}(d)/\text{S}(p)$ molecular orbitals. This is rationalized as the more electropositive atomic orbitals of sulfur, relative to the atomic orbital of oxygen, are more energetically aligned with the atomic orbitals of the $\text{Cr}(\text{IV})$ or $\text{Cr}(\text{V})$ cations. In concert with the larger atomic orbital radii of sulfur relative to oxygen, this results in more balanced mixing with the chromium cation. Thus, while the frontier orbitals of the chromium oxo complexes (**3.A** and **3.B**) are calculated to be of 20% oxygen parentage, the frontier orbitals of **3.C** and **3.D** have significantly more sulfur character.

In considering the orbital frontier orbital parentage of **3.C** and **3.D**, the two one-electron oxidation events observed chemically and electrochemically for $[\text{Cr}(\text{ditox})_3(\text{S})][(\text{K}(15\text{C}5)_2)]$, **3.3**, can be thought to result in a species that closely resembles a $\text{Cr}^{\text{V}}(\text{ditox})_3(\text{S}^{\text{+}})$. Computations show that the two orbitals that are oxidized have ca. 50% chromium character, leading to a valency assignment of $\text{Cr}(\text{V})$ upon oxidation by 2 electrons. As these orbital also are of 50% sulfur character, a sulfur radical cationic is also proposed upon oxidation. The proposal of a

sulfur radical cation as an intermediate to S–S bond formation is furthered by an NBO analysis performed on theoretical compounds $[\text{Cr}(\text{O}'\text{Bu})_3\text{S}]^-$ ($S=3$), $\text{Cr}(\text{O}'\text{Bu})_3\text{S}$ ($S=2$) and $[\text{Cr}(\text{O}'\text{Bu})_3\text{S}]^+$ ($S=1$). The NBO charge distribution of $[\text{Cr}(\text{O}'\text{Bu})_3\text{S}]^-$ indicates a charge of -0.73 on the S atom and $+1.03$ on the Cr atom. The product of a one electron oxidation, $\text{Cr}(\text{O}'\text{Bu})_3\text{S}$, results in significant increase of charge on the S atom and a minimal increase of charge on the Cr atom as the NBO charge distribution is found to be -0.28 on the S atom and $+0.99$ on the Cr atom. The product of another one electron oxidation, $[\text{Cr}(\text{O}'\text{Bu})_3\text{S}]^+$, results in the further increase of the charge on the sulfur atom to $+0.13$. Overall, the calculated two electron oxidation of $[\text{Cr}(\text{O}'\text{Bu})_3\text{S}]^-$ to $[\text{Cr}(\text{O}'\text{Bu})_3\text{S}]^+$ results in an increase of charge on the sulfur atom from -0.73 to $+0.13$. Extrapolating this electronic structure to the oxidized form of **3.13**, Scheme 3.5 outlines the proposed chemistry occurring upon oxidation of **3.13**.

Scheme 3.5



The initial Cr(IV)–sulfido complex is oxidized twice to result in a transient Cr(V)–sulfido radical cation. Two Cr(V)–sulfido radical cation complexes are proposed to couple in a mechanism similar to the RC mechanism for O–O bond formation. The result would be a Cr(V)–S₂–Cr(V) complex analogous to a bridging peroxy structure. Further steps involving the catenation of the ligand S₂²⁻ occurs followed by elimination of the experimentally observed S₈ molecule as well as an ill-defined Cr(III) compound, as the experimental reaction mixture appears to have formed via non-specific reactivity.

3.5 Concluding Remarks

Treatment of the early transition metal tris(ditox) complexes **3.1-3.3** with oxygen atom transfer reagents results in series of d^0 , d^1 and d^2 metal oxo complexes. X-ray crystallography confirms the pseudo-tetrahedral coordination geometry of the metal oxo complexes. Spectroscopic observations in concert with theoretical calculations verify that the electronic structure of the pseudo-tetrahedral metal oxo complexes **3.4-3.7** as involving low lying d_{xz} and

d_{yz} orbitals which are of π^* character with respect to the metal oxo bond and contain approximately 20% oxo character. Consequently, population of the d orbital manifold by one or two electrons results in weakening of the metal oxo bond as the bond order lowers from 3 to 2.5 to 2 respectively across the d^0 , d^1 and d^2 series.

The d^1 pseudo-tetrahedral metal oxo compound **3.5**, $\text{Cr}(\text{ditox})_3(\text{O})$, is found to preferentially react via one electron radical pathways (RC mechanism), which is in contrast to d^1 tetragonal metal oxo compounds that typically react as electrophiles (AB mechanism). The d^2 pseudo-tetrahedral compounds **3.6** and **3.7** are observed to react in two electron pathways, preferentially as nucleophiles (AB mechanism), which contrasts common reactivity pathways of tetragonal metal oxo species that either react as electrophiles (low spin) or via one electron radical pathways (high spin). Overall, contrasting reactivity trends can be found for pseudo-tetrahedral metal oxo complexes relative to comparable isoelectronic tetragonal species that can be rationalized due to the nature of the electronic structure of pseudo-tetrahedral metal oxo complexes.

As early transition metals are oxophilic, metal oxo species of Group V and Group IV are not reported to participate in O–O bond formation processes. Analogous pseudo-tetrahedral metal sulfido complexes were sought in order to interrogate thermodynamically accessible chalcogen–chalcogen bond formations in a general manner. The tris(ditox) Cr(IV) sulfido complexes **3.12** and **3.13** were prepared. Electrochemical analysis in concert with chemical oxidant titration shows the pseudo-tetrahedral Cr(IV) sulfido species are able to be oxidized by 2 electrons. Upon oxidation of the Cr(IV) sulfido species with 2 equiv of a chemical oxidant, cyclo- S_8 was observed along with the nonspecific decomposition of the chromium ditox complex. DTF calculations suggest that the electronic structure of the oxidized chromium-sulfido is described as a $\text{Cr}(\text{V})\text{--S}^{+}$. It is proposed that cyclo- S_8 is generated from the radical coupling of terminal sulfide moieties.

These results suggest that pseudo-tetrahedral tris(alkoxide) metal chalcogen complexes support electronic structures with significant unpaired spin density on the chalcogen moiety. As complexes of less oxophilic later transition metal complexes are synthesized, the weaker metal oxo bonds should afford a broader range of thermodynamically accessible chemistry proceeding through a *radical coupling* mechanism as opposed to an AB mechanism.

3.6 Experimental Methods and Computational Details

3.6.1 General methods. All reactions involving air-sensitive materials were executed in a nitrogen-filled glovebox. Solvents were purified using SG Water Glass Contour Solvent System and stored over 4-Å molecular sieves. Compounds were routinely characterized by IR, NMR, XRD, and elemental analyses; selected compounds were characterized by EPR. IR spectra of powdered samples were recorded on a PerkinElmer Spectrum 400 FT-IR/FT-FIR Spectrometer outfitted with a Pike Technologies GladiATR attenuated total reflectance accessory with a monolithic diamond crystal stage and pressure clamp. All NMR spectra were recorded at the MIT Department of Chemistry Instrumentation Facility on a Varian Mercury 300 NMR Spectrometer or a Varian Inova-500 NMR Spectrometer in C₆D₆ or in CD₃CN solvents at room temperature. EPR spectra of Cr(ditox)₃(O) were recorded at the MIT Department of Chemistry Instrumentation Facility on a Bruker EMX EPR spectrometer (X band, G = 9.860 GHz) in pentane at room temperature. Elemental analyses were performed by Midwest Microlab LLC. Methyl lithium (1.6 M in ether), 2,2,4,4-tetramethyl-3-pentanone, FeCl₃, VCl₃(THF)₃, CrCl₃(THF)₃, FeBr₃, CoCl₂, 15-crown-5-ether, and Ph₃SbS were purchased from Aldrich. PhI¹⁷O and PhI¹⁸O were prepared according to literature procedures.⁵⁶ The preparation of V(ditox)₃THF, **3.1**, can be found in section 2.9.8. The preparation of Cr(ditox)₃, **3.2**, can be found in section 2.9.9. The preparation of [Cr(ditox)₃][K(15C5)₂], **3.3**, can be found in section 2.9.3.

3.6.2 Preparation of V(ditox)₃(O) (3.4). A suspension of 11 mg (0.14 mmol) of Me₃NO in THF was added to the stirred blue solution of V(ditox)₃THF (74 mg, 0.13 mmol) in THF. The mixture assumed a dark brown color within 5 min. The solution was stirred at room temperature for 2.5 h, volatiles were removed in vacuo, and the product was recrystallized from a pentane solution that was allowed to stand at -40 °C for 24 h, giving V(ditox)₃(O) in 55% yield (37 mg, 0.069 mmol) as off white crystals. ¹H NMR (C₆D₆, 300 MHz) δ = 1.65 ppm (s, Me, 3H), 1.27 ppm (s, ^tBu, 18H). IR (cm⁻¹) = 1476 (m), 1392 (m), 1367, (m), 1232 (w), 1102 (s), 1068 (s), 994 (s), 981 (s), 915 (s), 734, (s), 598 (m), 544 (w), 533 (w). Anal Calcd (Found) for C₃₀H₆₃O₄V: C, 66.9 (66.8); H, 11.8 (11.6).

3.6.3 Preparation of Cr(ditox)₃(O) (3.5). A suspension of 37 mg (0.17 mmol) of PhIO in THF (2 mL) was added to the stirred blue-green solution of Cr(ditox)₃ (99 mg, 0.17 mmol) in THF. The mixture assumed a red-orange color within 2 min and the solution became

homogeneous. The solution was stirred at room temperature for 1 h, volatiles were removed in vacuo, and the product was recrystallized from pentane solution that was allowed to stand at -40 °C for 24 h, giving $\text{Cr}(\text{ditox})_3(\text{O})$ in 78% yield (72 mg, 0.13 mmol) as dark red crystals. ^1H NMR (C_6D_6 , 300 MHz) δ = 3.9 ppm (s, Me, 3H), 1.22 ppm (s, ^tBu , 18H). IR ($\text{Cr}-^{16}\text{O}$, cm^{-1}) = 1475 (m), 1391 (m), 1368 (m), 1232 (w), 1201 (w), 1100 (s), 1065 (s), 990 (s), 946 (s), 931 (sh), 870 (s), 860 (s), 716 (s), 601 (m), 546 (w), 528 (w). Anal Calcd (Found) for $\text{C}_{30}\text{H}_{63}\text{O}_4\text{Cr}$: C, 66.8 (66.4); H, 11.8 (11.6).

3.6.4 Preparation of $[\text{Cr}(\text{ditox})_3(\text{O})][\text{CoCp}_2]$ (3.6). A solution of 12 mg (0.068 mmol) of CoCp_2 in THF (2 mL) was added to the stirred red solution of $\text{Cr}(\text{ditox})_3(\text{O})$ (35 mg, 0.065 mmol) in THF at room temperature. The mixture assumed a blue color, and the solution was left to stir for 1 h. The solvent was removed in vacuo, the blue residue was washed with a pentane/diethyl ether mixture (3:1), dissolved in as THF/diethyl ether mixture (1:3 mL) and precipitated by the addition of pentane, giving a blue crystalline solid. Recrystallization (vapor diffusion) from THF/ether at -40 °C yielded pure $[\text{Cr}(\text{ditox})_3(\text{O})][\text{CoCp}_2]$ as blue needle-like crystals in 55% yield (26 mg, 0.036 mmol). IR ($\text{Cr}-^{16}\text{O}$, cm^{-1}): 1476 (m), 1414 (m), 1387 (w), 1382 (m), 1360 (s), 1104 (s), 1083 (s), 998 (s), 931 (sh), 904 (s), 870 (s), 860, (m), 674 (s), 603 (m), 551 (w), 528 (w). Anal. Calcd (Found) for $\text{C}_{30}\text{H}_{63}\text{O}_4\text{Cr}$: C, 65.9 (65.4); H, 10.1 (9.8).

3.6.5 Preparation of $\text{Cr}(\text{ditox})_3(\text{O})\text{K}(\text{Et}_2\text{O})_3$ (3.7). A suspension of 44 mg (0.20 mmol) of PhIO in THF (4 mL) was added to the stirred light blue solution of $[\text{Cr}(\text{ditox})_3][\text{K}(\text{15C5})_2]$ (200 mg, 0.199 mmol) in THF. The solution assumed a dark blue color within 2 min and became homogeneous. The solution was stirred at room temperature for 1 h. The solution was filtered through celite and the volatiles were removed in vacuo. To the resulting blue solid, KOTf was added (172 mg, 0.997 mmol) along with 7 mL of Et_2O . The suspension was stirred for 1 h, the blue solution was filtered through celite and the volatiles were removed in vacuo. To the residue, 5 mL of pentane were added and the mixture was stirred for 30 min and filtered through celite to afford a blue pentane solution. The pentane was removed in vacuo to afford a blue solid which was recrystallized from a concentrated Et_2O solution that was allowed to stand at -40 °C for 24 h, giving $\text{Cr}(\text{ditox})_3(\text{O})\text{K}(\text{Et}_2\text{O})_3$ in 63% yield (103 mg, 0.134 mmol) as blue crystals. IR ($\text{Cr}-^{16}\text{O}$, cm^{-1}) = 1485 (m), 1396 (sh), 1387 (m), 1360 (m), 1298 (w), 1239 (w), 1214 (m), 1131 (m), 1068 (sh), 1060 (sh), 1045 (s), 1008 (sh), 990 (s), 975 (s), 875 (s), 833 (w), 815 (m), 788(s) 730

(w), 655 (m), 632 (m), 584 (m), 540 (w), 525 (w). Anal Calcd (Found) for $C_{42}H_{93}O_7KCr$: C, 62.8 (63.0); H, 11.8 (11.7).

3.6.6 Preparation of $Cr(ditox)_3(OSnBu_3)$ (3.8). A solution of 22 mg (0.0379 mmol, 0.5 equiv) of $Bu_3SnSnBu_3$ in diethyl ether (1 mL) was added to the stirred red solution of $Cr(ditox)_3(O)$ (41 mg, 0.075 mmol) in diethyl ether. The color of the solution changed to green within 2 h. The solution was stirred at room temperature for 24 h, filtered, volatiles were removed in vacuo, and the product was recrystallized from pentane solution that was allowed to stand at $-40\text{ }^\circ\text{C}$ for 24 h, and then dried for 48 h, giving the product in 55% yield (34 mg, 0.041 mmol) as green crystals. IR (cm^{-1}): 1480 (m), 1452(w), 1387 (m), 1368 (m), 1102 (s), 1074 (s), 994 (s), 886 (s), 805 (s), 700 (s), 607 (s), 553 (w). Anal. Calcd (Found) for $C_{54}H_{118}O_4CrSn$: C, 60.8 (60.4); H, 10.9 (10.3).

3.6.7 Preparation of $Cr(ditox)_3(O^tBu)$ (3.9). In the presence of 2,3-dimethylbuta-1,3-diene, 200 mg (2.43 mmol) of 2,3-dimethylbuta-1,3-diene were added to the stirred red solution of $Cr(ditox)_3(O)$ (39 mg, 0.072 mmol) in THF (2 mL). After 3 d the solution assumed a green-brown color. The volatiles were removed in vacuo to afford a green-brown residue. The residue was recrystallized from solution of pentane that is allowed to stand at $-40\text{ }^\circ\text{C}$ to afford $Cr(ditox)_3(O^tBu)$ as green crystals in 37% yield (16 mg, 0.026 mmol). IR (cm^{-1}): 1477 (m), 1390 (m), 1368 (m), 1235 (w), 1198 (w), 1102 (s), 1064 (s), 991 (s), 931 (w), 870 (s), 867 (s), 719 (s), 600 (m), 549 (w), 530 (w). Anal Calcd (Found) for $C_{34}H_{72}O_4Cr$: C, 68.4 (68.6); H 12.2 (12.1).

3.6.8 Preparation of $Cr(ditox)_3(OSiMe_3)$ (3.10). To the stirred blue solution of 92 mg (0.138 mmol) of $[Cr(ditox)_3(O)][CoCp_2]$ in 2 mL of THF was added 15 mg (0.138 mmol) of Me_3SiCl in 1 mL of THF. The reaction mixture immediately assumed a green color and a white precipitated. The solution was filtered through celite and the volatiles were removed. Recrystallization from pentane solution that is allowed to stand at $-40\text{ }^\circ\text{C}$ for 24 h afforded the product in 77% yield (65 mg, 0.11 mmol) of $Cr(ditox)_3(OSiMe_3)$ obtained as pale green crystals. IR (cm^{-1}): 1480 (m), 1475 (w), 1388 (m), 1370 (m), 1245 (m), 1100 (s), 1070 (s), 992 (m), 950 (s), 932 (sh), 887 (sh), 828 (m), 746 (m), 708 (s), 695 (sh), 605 (m), 552 (w). Anal Calcd (Found) for $C_{33}H_{72}O_4SiCr$: C, 64.7 (64.9); H, 11.8 (11.7).

3.6.9 Preparation of $[Cr(ditox)_2O]_2$ (3.11). To the stirred blue solution of 100 mg (0.125 mmol) of $Cr(ditox)_3(O)K(Et_2O)_3$ in 3 mL of THF was added 18 mg (0.13 mmol) of the lutidinium hydrochloride. The reaction mixture immediately assumed a green-blue color. The

solution was filtered and the volatiles were removed in vacuo. The pentane was added to the blue-green residue and filtered. Recrystallization from a pentane solution that is allowed to stand at $-40\text{ }^{\circ}\text{C}$ for 24 h afforded the product in 21% yield (10 mg, 0.030 mmol) of $[\text{Cr}(\text{ditox})_2(\text{O})]_2$. IR (cm^{-1}): 1481 (m), 1389, (m), 1372 (w), 1360 (m), 1242 (w), 1217 (w), 1127 (s), 1094 (s), 1060 (m), 1045 (s), 1019 (s), 990 (sh), 979 (s), 864 (w), 838 (m), 819 (m), 792 (s), 629 (m), 618 (sh), 570 (s), 546 (m), 525 (m), 477 (m), 466 (sh). Anal. Calcd (Found) for $\text{C}_{40}\text{H}_{84}\text{O}_6\text{Cr}_2$: C, 61.2 (62.8); H, 11.0 (11.1).

3.6.10 Preparation of $[\text{Cr}(\text{ditox})_3(\text{S})][\text{K}(\text{15C5})_2]$ (3.12). A solution of 77 mg (0.20 mmol) of Ph_3SbS in THF (2 mL) was added to the stirred light blue solution of $[\text{Cr}(\text{ditox})_3][\text{K}(\text{15C5})_2]$ (200 mg, 0.199 mmol) in THF. The solution assumed a green-brown color within 2 min and dark precipitate is observed. The volatiles were removed in vacuo and the remaining brown residue was washed three times with 10 mL of pentane. Acetonitrile (10 mL) was added to the brown solid to result in a green-brown solution. The solution was filtered through celite and the solution was concentrated to 1 mL. Allowing the solution to stand at $-40\text{ }^{\circ}\text{C}$ for 24 h afforded the crystalline product in 53% yield (109 mg, 0.105 mmol). IR (cm^{-1}): 1475 (m), 1442 (m), 1429 (m), 1395 (m), 1385 (m), 1352 (m), 1300 (m), 1289 (m), 1237 (m), 1119 (s), 1102 (s), 1090(s), 1081 (s), 1038 (m), 1030 (sh), 998 (m), 940 (m), 902 (s), 854 (m), 821 (m), 726 (w), 699 (sh), 677 (s), 665 (sh), 600 (m), 551 (w), 520 (w), 510 (w), 485 (s). Anal. Calcd (Found) for $\text{C}_{50}\text{H}_{103}\text{O}_{13}\text{SKCr}$: C, 56.9 (58.0); H, 10.5 (10.0).

3.6.11 Preparation of $[\text{Cr}(\text{ditox})_3(\text{S})\text{Ag}]_3$ (3.13). A solution of 77 mg (0.20 mmol) of Ph_3SbS in THF (2 mL) was added to the stirred light blue solution of $[\text{Cr}(\text{ditox})_3][\text{K}(\text{15C5})_2]$ (200 mg, 0.199 mmol) in THF. Within 2 min the solution assumed a green-brown color and a dark precipitate is observed. The solution was allowed to stir for 1 h at which time 240 mg (1.00 mmol) of AgOTf was added to the reaction mixture. The solution was allowed to stir for an addition 30 min. The volatiles were removed in vacuo and the remaining brown residue was treated with 7 mL of pentane to afford a green-yellow pentane solution. The solution was filtered through celite and the solution was concentrated to 1 mL. Allowing the solution to stand at $-40\text{ }^{\circ}\text{C}$ for 24 h afforded the crystalline product in 66% yield (87 mg, 0.13 mmol). IR (cm^{-1}): 1489 (m), 1480 (m), 1432 (w), 1406 (m), 1393 (m), 1372 (m), 1359 (sh), 1330 (w), 1257 (w), 1238 (m), 1200(m), 1159 (w), 1105 (s), 1050 (s), 1019 (w), 995 (s), 952 (w), 934 (w), 878 (s), 814 (s),

781 (m), 728 (m), 716 (sh), 695 (m), 668 (w), 629 (m), 600 (m), 550 (w), 532 (w), 520 (sh), 487 (sh), 473 (s), 455 (sh). Anal. Calcd (Found) for $C_{30}H_{63}O_3SAgCr$: C, 53.8 (54.3); H, 10.0 (9.6).

3.6.12 Crystallographic Details. Crystals were mounted on a Bruker three circle goniometer platform equipped with an APEX detector. A graphite monochromator was employed for wavelength selection of the Mo $K\alpha$ radiation ($\lambda = 0.71073 \text{ \AA}$). Data were processed and refined using the program SAINT supplied by Siemens Industrial Automation. Structures were solved by direct methods in SHELXS and refined by standard difference Fourier techniques in the SHELXTL program suite (6.10 v., Sheldrick G. M., and Siemens Industrial Automation, 2000). Hydrogen atoms were placed in calculated positions using the standard riding model and refined isotropically; all other atoms were refined anisotropically. Rigid bond restraints were used in all refinement models. In the structure of **3.4** one of the ditox ligands is disordered over two positions; the disorder was modeled adequately. In addition, t Bu groups of another ditox ligand are disordered over two positions. The $-\text{CH}_3$ groups of the t Bu were satisfactorily modeled, however the disorder in the central (quaternary) carbon atoms could not be resolved, leading to somewhat longer than expected C–C bonds for one conformation and shorter C–C bonds than expected. In the structure of **3.6**, $[\text{Cr}(\text{ditox})_3(\text{O})][\text{CoCp}_2]$, both the anion and the cation are disordered over two positions. The disorder in the structure of $[\text{Cr}(\text{ditox})_3(\text{O})]^-$ for **3.6** involves two enantiomers of C_3 symmetry; the disorder in the orientation of the ditox ligands was fully modeled. However, the disorder in the oxygen donor atoms of the alkoxide ligands could not be resolved, resulting in the large thermal ellipsoids. There is no disorder in the positions of the chromium atom and the apical oxo ligand. Structure **3.7**, **3.9** and **3.10** contained disordered solvent molecules. While the disorder in the structures of **3.7** and **3.10** were modeled, no appropriate model could be found for **3.9**. Therefore, electron density associated with the disordered solvent was removed using SQUEEZE program.

3.6.13 Computational Details. Density functional theory (DFT) calculations were performed with the hybrid functional Becke–3 parameter exchange functional⁵⁷ and the Lee–Yang–Parr nonlocal correlation functional (B3LYP)⁵⁸ as implemented in the Gaussian 03, Revision B.05 software package.⁵⁹ An effective core potential (ECP) representing the 1s2s2p core was used for chromium (LANL2DZ).⁶⁰ The double- ζ quality correlation-consistent polarized ccc–pvdz basis set by Dunning and coworkers was used on all oxygen atoms, while double- ζ quality basis sets (D95) were used on carbon and hydrogen.⁶¹ The calculations were

performed on simplified models of **3.5**, **3.6**, and **3.12** (**3.A**, **3.B** and **3.C**, respectively) where ^tBu groups are replaced by methyl groups. The theoretical product of a one electron oxidation for **3.C** was also calculated (**3.D**). All spin states were calculated as high spin and all geometries were confirmed as local minima structures by calculating the Hessians and checking that no negative eigenvalues were present. Figure 3.10 shows the molecular orbitals for **3.A** and Figure 3.19 shows the molecular orbitals for **3.D**. Cartesian coordinates for **3.A-3.D** can be found in Tables 3.10-Table 3.13 respectively.

3.7 Crystallographic Tables and Computational Model Coordinate Tables

Table 3.1. Crystallographic data and structural refinement parameters for V(ditox)₃(O) (3.4).

Identification code	data_3	
Empirical formula	C ₃₀ H ₆₃ O ₄ V	
Formula weight	538.74 g/mol	
Temperature	-173(2) °C	
Wavelength	0.70173 Å	
Crystal system	Monoclinic	
Space group	C2/c	
Unit cell dimensions	$a = 33.621(4)$ Å	$\alpha = 90.00^\circ$
	$b = 8.166(1)$ Å	$\beta = 101.540(2)^\circ$
	$c = 23.801(3)$ Å	$\gamma = 90.00^\circ$
Volume	6402.7(2) Å ³	
Z	8	
Density (calculated)	1.118 Mg/m ³	
Absorption coefficient	0.339 mm ⁻¹	
F(000)	2384	
Crystal size	0.25 × 0.20 × 0.15 mm ³	
θ range for data collection	1.92 to 27.50°	
Index ranges	-43 ≤ h ≤ 43, -10 ≤ k ≤ 10, -30 ≤ l ≤ 30	
Reflections collected	23234	
Independent reflections	7376 [$R_{\text{int}} = 0.0520$]	
Completeness to $\theta = 28.28^\circ$	99.9%	
Absorption correction	Empirical SADABS	
Max. and min. transmission	0.9509 and 0.9200	
Refinement method	Full-matrix least-squared on F^2	
Data / restraints/ parameters	7378 / 0 / 476	
^a Goodness-of-fit on F^2	1.033	
^{b,c} Final R indices [$I > 2\sigma(I)$]	$R_1 = 0.0396$, $wR_2 = 0.0974$	
^{b,c} R indices (all data)	$R_1 = 0.0545$, $wR_2 = 0.1096$	
Largest diff. peak and hole	0.407 and -0.523 e/Å ⁻³	

^a GOF = $(\sum w(F_o^2 - F_c^2)^2 / (n - p))^{1/2}$ where n is the number of data and p is the number of parameters refined.

^b $R_1 = \sum ||F_o - |F_c|| / \sum |F_o|$

$${}^c wR_2 = \left(\frac{\sum (w(F_o^2 - F_c^2)^2)}{\sum (w(F_o^2)^2)} \right)^{1/2}$$

Table 3.2. Crystallographic data and structural refinement parameters for Cr(ditox)₃(O) (3.5).

Identification code	data_4	
Empirical formula	C ₃₀ H ₆₃ O ₄ Cr	
Formula weight	539.80 g/mol	
Temperature	-173(2) °C	
Wavelength	0.70173 Å	
Crystal system	Monoclinic	
Space group	C2/c	
Unit cell dimensions	$a = 33.803(4) \text{ \AA}$	$\alpha = 90.00^\circ$
	$b = 8.288(1) \text{ \AA}$	$\beta = 101.702(2)^\circ$
	$c = 23.240(3) \text{ \AA}$	$\gamma = 90.00^\circ$
Volume	6375.6(2) Å ³	
Z	8	
Density (calculated)	1.125 Mg/m ³	
Absorption coefficient	0.388 mm ⁻¹	
F(000)	2392	
Crystal size	0.40 × 0.35 × 0.15 mm ³	
θ range for data collection	1.23 to 27.57°	
Index ranges	-43 ≤ h ≤ 43, -10 ≤ k ≤ 10, -30 ≤ l ≤ 29	
Reflections collected	60479	
Independent reflections	7329 [R _{int} = 0.0655]	
Completeness to $\theta = 28.28^\circ$	99.3%	
Absorption correction	Empirical SADABS	
Max. and min. transmission	0.9441 and 0.8602	
Refinement method	Full-matrix least-squared on F^2	
Data / restraints/ parameters	7378 / 0 / 337	
^a Goodness-of-fit on F^2	1.023	
^{b,c} Final R indices [I > 2σ(I)]	$R_1 = 0.0509$, $wR_2 = 0.1261$	
^{b,c} R indices (all data)	$R_1 = 0.0746$, $wR_2 = 0.1429$	
Largest diff. peak and hole	0.588 and -0.400 e/Å ⁻³	

^a GOF = $(\sum w(F_o^2 - F_c^2)^2 / (n - p))^{1/2}$ where n is the number of data and p is the number of parameters refined.

^b $R_1 = \sum ||F_o - |F_c|| / \sum |F_o|$

^c $wR_2 = \left(\frac{\sum (w(F_o^2 - F_c^2)^2)}{\sum (w(F_o^2)^2)} \right)^{1/2}$

Table 3.3. Crystallographic data and structural refinement parameters for [Cr(ditox)₃(O)][CoCp₂] (3.6).

Identification code	data_6	
Empirical formula	C ₄₀ H ₅₈ O ₄ CoCr	
Formula weight	713.79 g/mol	
Temperature	-173(2) °C	
Wavelength	0.70173 Å	
Crystal system	Orthorhombic	
Space group	<i>Pmn2₁</i>	
Unit cell dimensions	<i>a</i> = 13.575(2) Å	$\alpha = 90.00^\circ$
	<i>b</i> = 11.915(2) Å	$\beta = 90.00^\circ$
	<i>c</i> = 12.428(2) Å	$\gamma = 90.00^\circ$
Volume	2010.2(5) Å ³	
Z	2	
Density (calculated)	1.179 Mg/m ³	
Absorption coefficient	0.718 mm ⁻¹	
F(000)	762	
Crystal size	0.25 × 0.10 × 0.05 mm ³	
θ range for data collection	1.71 to 24.99°	
Index ranges	-16 ≤ <i>h</i> ≤ 16, -14 ≤ <i>k</i> ≤ 14, -14 ≤ <i>l</i> ≤ 14	
Reflections collected	26133	
Independent reflections	3697 [R _{int} = 0.1181]	
Completeness to $\theta = 28.28^\circ$	99.9%	
Absorption correction	Empirical SADABS	
Max. and min. transmission	0.9650 and 0.8409	
Refinement method	Full-matrix least-squared on <i>F</i> ²	
Data / restraints/ parameters	7378 / 1 / 384	
^a Goodness-of-fit on <i>F</i> ²	1.036	
^{b,c} Final R indices [I > 2σ(I)]	<i>R</i> ₁ = 0.0524, <i>wR</i> ₂ = 0.1245	
^{b,c} R indices (all data)	<i>R</i> ₁ = 0.0677, <i>wR</i> ₂ = 0.1365	
Largest diff. peak and hole	0.648 and -0.487 e/Å ⁻³	

^a GOF = $(\sum w(F_o^2 - F_c^2)^2 / (n - p))^{1/2}$ where *n* is the number of data and *p* is the number of parameters refined.

^b $R_1 = \sum ||F_o - |F_c|| / \sum |F_o|$

^c $wR_2 = \left(\frac{\sum (w(F_o^2 - F_c^2)^2)}{\sum (w(F_o^2)^2)} \right)^{1/2}$

Table 3.4. Crystallographic data and structural refinement parameters for Cr(ditox)₃(O)K(Et₂O)₃ (3.7).

Identification code	10290	
Empirical formula	C ₄₂ H ₉₃ O ₇ KCr	
Formula weight	801.26 g/mol	
Temperature	-173(2) °C	
Wavelength	0.70173 Å	
Crystal system	Orthorhombic	
Space group	<i>P</i> 2 ₁ 2 ₁ 2 ₁	
Unit cell dimensions	<i>a</i> = 20.155(2) Å	$\alpha = 90.00^\circ$
	<i>b</i> = 22.077(2) Å	$\beta = 90.00^\circ$
	<i>c</i> = 22.077(2) Å	$\gamma = 90.00^\circ$
Volume	9823.6(2) Å ³	
Z	8	
Density (calculated)	1.084 Mg/m ³	
Absorption coefficient	0.358 mm ⁻¹	
F(000)	3552	
Crystal size	0.25 × 0.25 × 0.20 mm ³	
θ range for data collection	1.30 to 28.38°	
Index ranges	-26 ≤ <i>h</i> ≤ 26, -29 ≤ <i>k</i> ≤ 29, -29 ≤ <i>l</i> ≤ 29	
Reflections collected	204086	
Independent reflections	24477 [<i>R</i> _{int} = 0.0554]	
Completeness to $\theta = 28.28^\circ$	99.6%	
Absorption correction	Empirical SADABS	
Max. and min. transmission	0.9213 and 0.8737	
Refinement method	Full-matrix least-squared on <i>F</i> ²	
Data / restraints/ parameters	24477 / 0 / 1053	
^a Goodness-of-fit on <i>F</i> ²	1.036	
^{b,c} Final R indices [<i>I</i> > 2σ(<i>I</i>)]	<i>R</i> ₁ = 0.0359, <i>wR</i> ₂ = 0.0888	
^{b,c} R indices (all data)	<i>R</i> ₁ = 0.0457, <i>wR</i> ₂ = 0.0947	
Largest diff. peak and hole	0.595 and -0.259 e/Å ⁻³	

^a GOF = $(\sum w(F_o^2 - F_c^2)^2 / (n - p))^{1/2}$ where *n* is the number of data and *p* is the number of parameters refined.

^b $R_1 = \sum ||F_o - |F_c|| / \sum |F_o|$

^c $wR_2 = \left(\frac{\sum (w(F_o^2 - F_c^2)^2)}{\sum (w(F_o^2)^2)} \right)^{1/2}$

Table 3.5. Crystallographic data and structural refinement parameters for Cr(ditox)₃(OSnBu₃) (**3.8**).

Identification code	data_6	
Empirical formula	C ₄₂ H ₉₀ O ₄ SnCr	
Formula weight	829.83 g/mol	
Temperature	-173(2) °C	
Wavelength	0.70173 Å	
Crystal system	Monoclinic	
Space group	<i>P2₁/c</i>	
Unit cell dimensions	<i>a</i> = 19.660(2) Å	$\alpha = 90.00^\circ$
	<i>b</i> = 11.218(2) Å	$\beta = 108.632(2)^\circ$
	<i>c</i> = 21.884(3) Å	$\gamma = 90.00^\circ$
Volume	4573.4(9) Å ³	
Z	4	
Density (calculated)	1.205 Mg/m ³	
Absorption coefficient	0.819 mm ⁻¹	
F(000)	1792	
Crystal size	0.40 × 0.25 × 0.15 mm ³	
θ range for data collection	1.09 to 28.65°	
Index ranges	-26 ≤ <i>h</i> ≤ 26, -15 ≤ <i>k</i> ≤ 15, -29 ≤ <i>l</i> ≤ 29	
Reflections collected	93541	
Independent reflections	11574 [<i>R</i> _{int} = 0.0762]	
Completeness to $\theta = 28.28^\circ$	99.4%	
Absorption correction	Empirical SADABS	
Max. and min. transmission	0.8871 and 0.7354	
Refinement method	Full-matrix least-squared on <i>F</i> ²	
Data / restraints/ parameters	11574 / 0 / 457	
^a Goodness-of-fit on <i>F</i> ²	1.023	
^{b,c} Final R indices [<i>I</i> > 2σ(<i>I</i>)]	<i>R</i> ₁ = 0.0336, <i>wR</i> ₂ = 0.0654	
^{b,c} R indices (all data)	<i>R</i> ₁ = 0.0539, <i>wR</i> ₂ = 0.0737	
Largest diff. peak and hole	0.592 and -0.445 e/Å ⁻³	

^a GOF = $(\sum w(F_o^2 - F_c^2)^2 / (n - p))^{1/2}$ where *n* is the number of data and *p* is the number of parameters refined.

^b $R_1 = \sum ||F_o - |F_c|| / \sum |F_o|$

^c $wR_2 = \left(\frac{\sum (w(F_o^2 - F_c^2)^2)}{\sum (w(F_o^2)^2)} \right)^{1/2}$

Table 3.6. Crystallographic data and structural refinement parameters for Cr(ditox)₃(O^tBu) (3.9).

Identification code	data_07	
Empirical formula	C ₃₄ H ₇₂ O ₄ Cr	
Formula weight	596.92 g/mol	
Temperature	-173(2) °C	
Wavelength	0.70173 Å	
Crystal system	Orthorhombic	
Space group	<i>Pccn</i>	
Unit cell dimensions	$a = 18.701(2) \text{ \AA}$	$\alpha = 90.00^\circ$
	$b = 37.603(3) \text{ \AA}$	$\beta = 90.00^\circ$
	$c = 11.330(1) \text{ \AA}$	$\gamma = 90.00^\circ$
Volume	7699.0(9) Å ³	
Z	8	
Density (calculated)	1.030 Mg/m ³	
Absorption coefficient	0.327 mm ⁻¹	
F(000)	2656	
Crystal size	0.25 × 0.20 × 0.20 mm ³	
θ range for data collection	1.08 to 27.51°	
Index ranges	-23 ≤ <i>h</i> ≤ 23, -48 ≤ <i>k</i> ≤ 47, -14 ≤ <i>l</i> ≤ 14	
Reflections collected	81384	
Independent reflections	8837 [<i>R</i> _{int} = 0.0983]	
Completeness to $\theta = 28.28^\circ$	99.8%	
Absorption correction	Empirical SADABS	
Max. and min. transmission	0.9375 and 0.9227	
Refinement method	Full-matrix least-squared on <i>F</i> ²	
Data / restraints/ parameters	8837 / 0 / 376	
^a Goodness-of-fit on <i>F</i> ²	1.053	
^{b,c} Final R indices [<i>I</i> > 2σ(<i>I</i>)]	<i>R</i> ₁ = 0.0539, <i>wR</i> ₂ = 0.1131	
^{b,c} R indices (all data)	<i>R</i> ₁ = 0.0867, <i>wR</i> ₂ = 0.1244	
Largest diff. peak and hole	0.417 and -0.425 e/Å ⁻³	

^a GOF = $(\sum w(F_o^2 - F_c^2)^2 / (n - p))^{1/2}$ where *n* is the number of data and *p* is the number of parameters refined.

^b $R_1 = \sum ||F_o - |F_c|| / \sum |F_o|$

^c $wR_2 = \left(\frac{\sum (w(F_o^2 - F_c^2)^2)}{\sum (w(F_o^2)^2)} \right)^{1/2}$

Table 3.7. Crystallographic data and structural refinement parameters for Cr(ditox)₃(OTMS) (3.10).

Identification code	data_8	
Empirical formula	C ₃₆ H ₈₁ O ₅ SiCr	
Formula weight	674.10 g/mol	
Temperature	-173(2) °C	
Wavelength	0.70173 Å	
Crystal system	Orthorhombic	
Space group	<i>Iba2</i>	
Unit cell dimensions	$a = 19.150(2) \text{ \AA}$	$\alpha = 90.00^\circ$
	$b = 36.173(4) \text{ \AA}$	$\beta = 90.00^\circ$
	$c = 11.332(2) \text{ \AA}$	$\gamma = 90.00^\circ$
Volume	7849.7(2) Å ³	
Z	8	
Density (calculated)	1.141 Mg/m ³	
Absorption coefficient	0.358 mm ⁻¹	
F(000)	3000	
Crystal size	0.30 × 0.25 × 0.15 mm ³	
θ range for data collection	1.13 to 28.33°	
Index ranges	-25 ≤ h ≤ 25, -46 ≤ k ≤ 48, -15 ≤ l ≤ 15	
Reflections collected	77879	
Independent reflections	9781 [R _{int} = 0.0416]	
Completeness to $\theta = 28.28^\circ$	99.9%	
Absorption correction	Empirical SADABS	
Max. and min. transmission	0.9482 and 0.9001	
Refinement method	Full-matrix least-squared on F^2	
Data / restraints/ parameters	9781 / 2 / 425	
^a Goodness-of-fit on F^2	1.050	
^{b,c} Final R indices [I > 2σ(I)]	$R_1 = 0.0281, wR_2 = 0.0701$	
^{b,c} R indices (all data)	$R_1 = 0.0309, wR_2 = 0.722$	
Largest diff. peak and hole	0.416 and -0.229 e/Å ⁻³	

^a GOF = $(\sum w(F_o^2 - F_c^2)^2 / (n - p))^{1/2}$ where n is the number of data and p is the number of parameters refined.

^b $R_1 = \sum ||F_o - |F_c|| / \sum |F_o|$

$$^c wR_2 = \left(\frac{\sum (w(F_o^2 - F_c^2)^2)}{\sum (w(F_o^2)^2)} \right)^{1/2}$$

Table 3.8. Crystallographic data and structural refinement parameters for [Cr(ditox)₂(O)]₂ (3.11).

Identification code	[Cr(ditox) ₂ (O)] ₂	
Empirical formula	C ₂₀ H ₄₂ O ₃ Cr	
Formula weight	382.54 g/mol	
Temperature	-173(2) °C	
Wavelength	0.70173 Å	
Crystal system	Triclinic	
Space group	P-1	
Unit cell dimensions	$a = 8.079(1) \text{ \AA}$	$\alpha = 77.841(1)^\circ$
	$b = 11.758(1) \text{ \AA}$	$\beta = 73.996(1)^\circ$
	$c = 12/020(1) \text{ \AA}$	$\gamma = 80.348(1)^\circ$
Volume	1065.6(2) Å ³	
Z	2	
Density (calculated)	1.192 Mg/m ³	
Absorption coefficient	0.551 mm ⁻¹	
F(000)	420	
Crystal size	0.20 × 0.10 × 0.10 mm ³	
θ range for data collection	2.30 to 26.37°	
Index ranges	-10 ≤ h ≤ 10, -14 ≤ k ≤ 14, -15 ≤ l ≤ 15	
Reflections collected	18336	
Independent reflections	4350 [$R_{\text{int}} = 0.0518$]	
Completeness to $\theta = 28.28^\circ$	99.9%	
Absorption correction	Empirical SADABS	
Max. and min. transmission	0.9257 and 0.9257	
Refinement method	Full-matrix least-squared on F^2	
Data / restraints/ parameters	4350 / 0 / 231	
^a Goodness-of-fit on F^2	1.032	
^{b,c} Final R indices [$I > 2\sigma(I)$]	$R_1 = 0.0459$, $wR_2 = 0.1169$	
^{b,c} R indices (all data)	$R_1 = 0.0646$, $wR_2 = 0.1267$	
Largest diff. peak and hole	1.628 and -0.455 e/Å ⁻³	

^a GOF = $(\sum w(F_o^2 - F_c^2)^2 / (n - p))^{1/2}$ where n is the number of data and p is the number of parameters refined.

^b $R_1 = \sum ||F_o - |F_c|| / \sum |F_o|$

^c $wR_2 = \left(\frac{\sum (w(F_o^2 - F_c^2)^2)}{\sum (w(F_o^2)^2)} \right)^{1/2}$

Table 3.9. Crystallographic data and structural refinement parameters for [Cr(ditox)₃(S)Ag]₃ (3.13).

Identification code	Cr(ditox) ₃ SAg	
Empirical formula	C ₉₀ H ₁₈₉ O ₉ S ₃ Ag ₃ Cr ₃	
Formula weight	1991.282 g/mol	
Temperature	-173(2) °C	
Wavelength	0.70173 Å	
Crystal system	Triclinic	
Space group	P-1	
Unit cell dimensions	$a = 16.836(2) \text{ \AA}$	$\alpha = 76.620(1)^\circ$
	$b = 17.091(2) \text{ \AA}$	$\beta = 82.952(1)^\circ$
	$c = 19.742(2) \text{ \AA}$	$\gamma = 66.892(1)^\circ$
Volume	5079.8(6) Å ³	
Z	2	
Density (calculated)	1.302 Mg/m ³	
Absorption coefficient	0.987 mm ⁻¹	
F(000)	1062	
Crystal size	0.30 × 0.20 × 0.20 mm ³	
θ range for data collection	1.06 to 25.03°	
Index ranges	-20 ≤ h ≤ 20, -20 ≤ k ≤ 20, -23 ≤ l ≤ 23	
Reflections collected	85024	
Independent reflections	17953 [R _{int} = 0.0803]	
Completeness to $\theta = 28.28^\circ$	99.9%	
Absorption correction	Empirical SADABS	
Max. and min. transmission	0.9257 and 0.9257	
Refinement method	Full-matrix least-squared on F^2	
Data / restraints/ parameters	17953 / 867 / 1012	
"Goodness-of-fit on F^2 "	1.017	
^{b,c} Final R indices [I > 2σ(I)]	$R_1 = 0.0555$, $wR_2 = 0.1342$	
^{b,c} R indices (all data)	$R_1 = 0.0860$, $wR_2 = 0.1540$	
Largest diff. peak and hole	2.298 and -1.594 e/Å ⁻³	

^a GOF = $(\sum w(F_o^2 - F_c^2)^2 / (n - p))^{1/2}$ where n is the number of data and p is the number of parameters refined.

^b $R_1 = \sum ||F_o - |F_c|| / \sum |F_o|$

^c $wR_2 = \left(\frac{\sum (w(F_o^2 - F_c^2)^2)}{\sum (w(F_o^2)^2)} \right)^{1/2}$

Table 3.10. Cartesian coordinates for the DFT optimized geometry for the model of 3.A, Cr(O^tBu)₃(O).

	<i>x</i>	<i>y</i>	<i>z</i>
O	13.08072	7.787448	9.18411
O	14.60589	10.06211	9.01035
O	13.0903	9.260332	6.872332
C	15.0992	11.21828	9.88743
C	14.44449	12.50508	9.366699
H	14.69324	12.67516	8.313723
H	14.82405	13.35558	9.945714
H	13.35524	12.48333	9.484834
C	12.15941	6.932056	10.06222
C	11.93078	7.69274	11.37507
H	12.87779	7.876984	11.89353
H	11.2968	7.085071	12.03198
H	11.41627	8.645361	11.20647
C	12.27017	9.842456	5.714681
C	10.7983	9.489217	5.96834
H	10.65787	8.404798	6.029447
H	10.19386	9.863007	5.132981
H	10.42292	9.957711	6.885198
C	16.61883	11.18288	9.659419
H	16.86325	11.3581	8.606849
H	17.09029	11.9709	10.25947
H	17.03973	10.21926	9.963545
C	14.70351	10.88152	11.33317
H	15.12901	9.921335	11.64383
H	15.09575	11.65836	12.00059
H	13.61456	10.85539	11.45483
C	10.86928	6.711196	9.257512
H	10.32437	7.650224	9.106389
H	11.08659	6.256138	8.285367
H	10.21358	6.029071	9.812283
C	12.97752	5.644768	10.24827
H	12.40562	4.943167	10.86815
H	13.18338	5.166308	9.285535
H	13.92832	5.851822	10.74988
C	12.86111	9.120765	4.493249
H	13.92864	9.337577	4.385991
H	12.72789	8.037059	4.573122
H	12.34537	9.465992	3.588655
C	12.53592	11.35528	5.702521
H	13.6073	11.56471	5.614143
H	12.03035	11.79944	4.836651
H	12.14245	11.83913	6.603945
O	11.9465	10.19331	9.091261
Cr	13.13973	9.354648	8.557556

Table 3.11. Cartesian coordinates for the DFT optimized geometry for the $S = 1$ model of **3.B**, $[\text{Cr}(\text{O}^t\text{Bu})_3(\text{O})]^-$.

	<i>x</i>	<i>y</i>	<i>z</i>
O	1.177498	1.051388	0.380866
O	0.413508	-1.73173	0.102567
O	-1.67277	0.325595	0.506824
C	1.739716	-2.26533	0.177284
C	2.612923	-1.77722	-1.00765
H	2.125182	-2.02694	-1.95854
H	3.612327	-2.23915	-0.9838
H	2.72354	-0.68765	-0.95842
C	1.322998	2.465621	0.209493
C	1.930123	2.760028	-1.18676
H	2.919546	2.28884	-1.26953
H	2.037734	3.84121	-1.36589
H	1.283518	2.32711	-1.9598
C	-2.96307	-0.23094	0.233588
C	-3.6117	0.548128	-0.93975
H	-3.72922	1.605185	-0.66395
H	-4.59854	0.139408	-1.20784
H	-2.94962	0.495897	-1.81288
C	1.586804	-3.80649	0.118836
H	1.121889	-4.09496	-0.83327
H	2.557763	-4.31705	0.2119
H	0.929809	-4.13964	0.932976
C	2.383095	-1.83816	1.521859
H	1.775268	-2.21231	2.357119
H	3.408884	-2.2263	1.627263
H	2.399025	-0.74357	1.573133
C	-0.03619	3.196322	0.361321
H	-0.72815	2.883248	-0.42932
H	-0.49549	2.933832	1.3215
H	0.098086	4.287957	0.306083
C	2.293657	2.934642	1.323235
H	2.499921	4.013894	1.256789
H	1.857818	2.714492	2.306485
H	3.241163	2.385965	1.240328
C	-3.79413	-0.04291	1.527762
H	-3.32942	-0.60614	2.347644
H	-3.80028	1.018937	1.806494
H	-4.83271	-0.38572	1.401677
C	-2.87023	-1.73898	-0.11574
H	-2.31771	-2.26914	0.668491
H	-3.87317	-2.18108	-0.22131
H	-2.32174	-1.88024	-1.05532
O	-0.24379	0.187327	-2.00603
Cr	-0.10729	-0.03396	-0.41053

Table 3.12. Cartesian coordinates for the DFT optimized geometry for the S=1 model of **3.C**, [Cr (O'Bu)₃(S)]⁻.

	<i>x</i>	<i>y</i>	<i>z</i>
Cr	0.000141	-0.002516	0.099534
O	-1.67394	-0.084038	-0.58894
O	0.766627	1.489385	-0.587347
O	0.907769	-1.414122	-0.585231
C	0.548555	2.886644	-0.310451
C	-2.776831	-0.968548	-0.311657
C	2.230034	-1.916879	-0.310465
C	2.680897	-2.625093	-1.612116
H	1.950194	-3.397902	-1.883805
H	2.727385	-1.896736	-2.432028
H	3.66893	-3.094616	-1.493658
C	-0.931038	3.172001	0.042924
H	-1.587594	2.79902	-0.752063
H	-1.20033	2.65636	0.972299
H	-1.095363	4.252601	0.173077
C	-2.28367	-2.388465	0.056872
H	-1.620142	-2.770776	-0.72785
H	-1.71337	-2.354915	0.992672
H	-3.135505	-3.074497	0.179878
C	1.471486	3.312447	0.856141
H	1.33395	4.374808	1.109568
H	1.245047	2.698075	1.735875
H	2.522284	3.14658	0.582217
C	0.937876	3.630425	-1.612174
H	0.855597	4.721138	-1.492629
H	1.970972	3.379423	-1.885454
H	0.280929	3.310342	-2.431175
C	-3.607915	-1.015513	-1.618055
H	-2.998168	-1.432979	-2.429639
H	-4.512518	-1.630055	-1.497034
H	-3.904637	0.002226	-1.902966
C	-3.616586	-0.372101	0.843412
H	-3.996101	0.618164	0.557027
H	-4.469991	-1.020344	1.095122
H	-2.980624	-0.252763	1.728718
C	2.143069	-2.92752	0.857915
H	1.487483	-3.764527	0.581501
H	3.135205	-3.325474	1.120823
H	1.709784	-2.426737	1.73213
C	3.210208	-0.771405	0.039141
H	2.894463	-0.279312	0.966709
H	4.230734	-1.162324	0.169985
H	3.209557	-0.018889	-0.75834
S	-0.003232	-0.00133	2.260215

Table 3.13. Cartesian coordinates for the DFT optimized geometry for the model of **3.D**, Cr(O^tBu)₃(S).

	<i>x</i>	<i>y</i>	<i>z</i>
Cr	0.003286	-0.028613	-0.154738
O	0.188903	1.625977	-0.67566
O	1.34574	-1.038928	-0.648508
O	-1.536267	-0.661975	-0.676463
C	2.733462	-1.298371	-0.247391
C	-0.200748	2.967057	-0.214676
C	-2.552294	-1.627897	-0.230198
C	-3.398522	-1.894907	-1.493034
H	-3.848857	-0.963001	-1.854167
H	-2.769436	-2.305302	-2.291297
H	-4.201179	-2.610896	-1.273069
C	3.395177	0.012938	0.222242
H	3.337142	0.77269	-0.565966
H	2.896419	0.404166	1.117138
H	4.451397	-0.161054	0.46468
C	-1.609441	2.918726	0.412287
H	-2.315966	2.443771	-0.278699
H	-1.600382	2.351391	1.350058
H	-1.961903	3.935367	0.628454
C	2.719228	-2.362623	0.867114
H	3.742003	-2.591628	1.193892
H	2.152606	-2.008377	1.737309
H	2.252125	-3.286129	0.505314
C	3.411666	-1.834417	-1.525829
H	4.458022	-2.09916	-1.324882
H	2.8864	-2.726043	-1.886888
H	3.385533	-1.075357	-2.316305
C	-0.198351	3.825418	-1.49754
H	-0.955412	3.462129	-2.20244
H	-0.414806	4.874569	-1.257154
H	0.781092	3.771923	-1.986335
C	0.856662	3.461662	0.792021
H	1.84114	3.522641	0.312767
H	0.589165	4.459295	1.164718
H	0.924102	2.777358	1.644753
C	-3.400343	-0.983	0.883003
H	-3.850054	-0.047697	0.528433
H	-4.207282	-1.661413	1.189609
H	-2.782618	-0.765356	1.762241
C	-1.855676	-2.914911	0.25593
H	-1.226984	-2.706141	1.1286
H	-2.605754	-3.665789	0.53666
H	-1.226418	-3.332197	-0.539153
S	0.049944	-0.068855	2.055433

3.8 References

- (1) Haynes, W. M. ed. *CRC Handbook of Chemistry and Physics*, 93rd Edition (Internet Version 2013), CRC Press/Taylor and Francis, Boca Raton FL.
- (2) Gray, H. B.; Hare, C. R. *Inorg. Chem.* **1962**, *1*, 363.
- (3) Maurya, M. R. *Coord. Chem. Rev.* **2003**, *237*, 163.
- (4) Srinivasan, K.; Kochi, J. K. *Inorg. Chem.* **1985**, *24*, 4671.
- (5) Ostovic, D; Bruce, T. C. *Acc. Chem. Res.* **1992**, *25*, 314.
- (6) Bousquet, C.; Gilheany, D. G. *Tet. Lett.*, **1995**, *36*, 7739.
- (7) Brandt, P.; Norrby, P-O.; Daly, A. M.; Gilheany, D. G. *Chem. Eur. J.* **2002**, *8*, 4299.
- (8) Gross, Z.; Gray, H. B. *Adv. Synth. Catal.* **2004**, *346*, 165.
- (9) Holm, R. H. *Chem. Rev.* **1987**, *87*, 1401.
- (10) Purohit, S.; Koley, A. P.; Prasad, L. S.; Manoharan, P. T.; Ghosh, S. *Inorg. Chem.* **1989**, *28*, 3735.
- (11) Qin, K. I. Incarvito, A. L.; Rheingold, A. L.; Theopold, K. H. *J. Am. Chem. Soc.* **2002**, *124*, 14008.
- (12) Khenkin, A. M; Hill, C. L. *J. Am. Chem. Soc.* **1993**, *115*, 8178.
- (13) Sevvel, R.; Rajagopal, S.; Srinivasan, C.; Alhaji, N. I.; Chellamani, A. *J. Org. Chem.* **2000**, *65*, 3334.
- (14) Garrison, J. M; Ostovic, D.; Bruice, T. C. *J. Am. Chem. Soc.* **1989**, *111*, 4960.
- (15) Venkataramanan, N. S.; Rajagopal, S; Suvitha, A.; Kawazoe, Y. *J. Phys. Org. Chem.* **2009**, *22*, 650.
- (16) Hay-Motherwell, R. S.; Wilkonson, G.; Hussain-Bates, B.; Hursthouse, M. B. *Polyhedron* **1993**, *12* 2009.
- (17) Groyzman, S.; Villagran, D.; Freedman, D. E.; Nocera, D. G. *Chem. Comm.* **2011**, *47*, 10242.
- (18) Nielsen, K.; Fehrmann, R.; Eriksen, K. M.; *Inorg. Chem.* **1993**, *32*, 4825.
- (19) Santoni, G.; Licini, G.; Rehder, D. *Chem. Eur. J.* **2003**, *9*, 4700.
- (20) Sutradhar, M.; Mukherjee, G.; Drew, M. G. D.; Ghosh, S. *Inorg. Chem.* **2005**, *45*, 5150.
- (21) Azuma, N.; Ozawa, T. *Polyhedron* **1994**, *13*, 1715.
- (22) Pribsch, W.; Rehder, D. *Inorg. Chem.* **1990**, *29*, 3013.

- (23) Siddall, T.L.; Miyaura, N.; Huffman, J. C.; Kochi, J. K. *Chem. Comm.* **1983**, 1185.
- (24) Kapre, R.; Ray, K.; Sylvestre, I.; Weyhermuller, T.; George, S. D.; Neese, F.; Wieghardt, K. *Inorg. Chem.* **2006**, *45*, 3499.
- (25) Wistuba, T.; Limberg, C.; Kircher, P. *Angew. Chem., Int. Ed.* **1999**, *38*, 3037.
- (26) Srinivasan, K.; Kochi, J.K. *Inorg. Chem.* **1985**, *24*, 4671.
- (27) Krumpolc, M.I DeBoer, B. G.; Rocek, J. *J. Am. Chem. Soc.* **1978**, *100*, 145.
- (28) Garcia-Monforte, M. A.; Alonso, P. J.; Arauzo, A. B.; Martin, A.; Menjon, B.; Rillo, C. *Dalt. Trans.* **2012**, *41*, 1297.
- (29) Lin, H-M.; Sheu, H-S.; Wang, C-C.; Che, C-M.; Wang, Y. *J. Chin. Chem Soc. (Taipei)* **1999**, *46*, 487.
- (30) Budge, J. R.; Gatehouse, B. M. K.; Nesbit, M. C.; West, B. O. *Chem. Comm.* **1981**, 370.
- (31) Cummins, C. C.; Schrock, R. R.; Davis, W. M. *Inorg. Chem.* **1994**, *33*, 1448.
- (32) Vuletic, N.; Djordjevic, C. *J. Chem. Soc. Dalt.* **1973**, 1137.
- (33) Nakajima, K.; Kojima, K.; Kojima, M.; Fujita, J. *Bull. Chem. Soc. Jpn.* **1990**, *63*, 2620.
- (34) O'Reilly, M.; Falkowski, J. M.; Ramachandran, V.; Pati, M.; Abboud, K. A.; Dalal, N. S.; Gray, T. G.; Veige A. S. *Inorg. Chem.* **2009**, *48*, 10901.
- (35) Collins, T. J.; Slebodnick, C.; Uffelman, E. S. *Inorg. Chem.* **1990**, *29*, 3433.
- (36) Egorova, O. A.; Tsay, O. G.; Khatua, S.; Huh, J. O.; Churchill, D. G. *Inorg. Chem.* **2009**, *48*, 4634.
- (37) Odom, A. L.; Mindiola, D. J.; Cummins, C. C. *Inorg. Chem.* **1999**, *38*, 3290.
- (38) Morse, D. B.; Rauchfuss, T. B.; Wilson, S. R. *J. Am. Chem. Soc.* **1988**, *110*, 8234.
- (39) Czernuszewicz, R. S.; Mody, V.; Czader, A.; Galezowski, M.; Gryko, D. T. *J. Am. Chem. Soc.* **2009**, *131*, 14214.
- (40) Jasperse, C. P.; Curran, D. P.; Fevig, T. L. *Chem. Rev.* **1991**, *91*, 1237.
- (41) Harendza, M. Junngebauer, J.; Labman, K.; Neumann, W. P.; Tews, H. *SYNLETT*, **1993**, 286.
- (42) Janzen, E. G.; Blackburn, B. J. *J. Am. Chem. Soc.* **1969**, *91*, 4481.
- (43) Bento, A. P.; Bickelhaupt, M. *J. Org. Chem.*, **2007**, *72*, 2201.
- (44) Meyer, B. *Chem. Rev.* **1976**, *76*, 367.
- (45) Baird, N. C. *J. Comp. Chem.*, **1984**, *5*, 35.

- (46) McCall, J. M.; Shaver, A. *J. Organomet. Chem.* **1980**, *193*, C37.
- (47) Wakatsuki, Y.; Yamazaki, H.; Cheng, C. *J. Organomet. Chem.* **1989**, *372*, 437.
- (48) Harrup, M. K.; Hill, C. L. *Inorg. Chem.* **1994**, *33*, 5448.
- (49) Zhao, P.; Zhang, H.; Zhou, H.; Yi, B. *Electrochimica Acta* **2005**, *51*, 1091.
- (50) Zhou, H.; Zhang, H.; Zhao, P.; Yi, B. *Electrochimica Acta* **2006**, *51*, 6304.
- (51) Scamman, D. P.; Reade, G.W.; Roberts, E. P. *J. Power Sources* **2009**, *189*, 1220.
- (52) Mikhaylik, Y. V.; Akridge, J. R. *J. Electrochem. Soc.* **2004**, *151*, A1969.
- (53) Steudel, R.; Steudel, Y. *Chem. Eur. J.* **2013**, *19*, 3162.
- (54) Savéant, J.-M. Single Electron Transfer at an Electrode. In *Elements of Molecular and Biomolecular Electrochemistry – An Electrochemical Approach to Electron Transfer Chemistry*; John Wiley & Sons Inc.: Hoboken, New Jersey, 2006; pp 53.
- (55) Meyer, B. *Chem. Rev.* **1976**, *76*, 367.
- (56) Schardt, B. C.; Hill, C. L. *Inorg. Chem.* **1983**, *22*, 1563.
- (57) (a) Becke, A. D. *Phys. Rev. A* **1988**, *38*, 3098. (b) Becke, A. D. *J. Chem. Phys.* **1993**, *98*, 1372. (c) Becke, A. D. *J. Chem Phys.* **1993**, *98*, 5648.
- (58) Lee, C.; Yang, W.; Parr, R. G. *Phys Rev. B* **1988**, *37*, 785.
- (59) Gaussian 03, Revision C.02, Frisch, M. J.; Trucks, G. W.; Schlegel, H. B.; Scuseria, G. E.; Robb, M. A.; Cheeseman, J. R.; Montgomery, Jr., J. A.; Vreven, T.; Kudin, K. N.; Burant, J. C.; Millam, J. M.; Iyengar, S. S.; Tomasi, J.; Barone, V.; Mennucci, B.; Cossi, M.; Scalmani, G.; Rega, N.; Petersson, G. A.; Nakatsuji, H.; Hada, M.; Ehara, M.; Toyota, K.; Fukuda, R.; Hasegawa, J.; Ishida, M.; Nakajima, T.; Honda, Y.; Kitao, O.; Nakai, H.; Klene, M.; Li, X.; Knox, J. E.; Hratchian, H. P.; Cross, J. B.; Bakken, V.; Adamo, C.; Jaramillo, J.; Gomperts, R.; Stratmann, R. E.; Yazyev, O.; Austin, A. J.; Cammi, R.; Pomelli, C.; Ochterski, J. W.; Ayala, P. Y.; Morokuma, K.; Voth, G. A.; Salvador, P.; Dannenberg, J. J.; Zakrzewski, V. G.; Dapprich, S.; Daniels, A. D.; Strain, M. C.; Farkas, O.; Malick, D. K.; Rabuck, A. D.; Raghavachari, K.; Foresman, J. B.; Ortiz, J. V.; Cui, Q.; Baboul, A. G.; Clifford, S.; Cioslowski, J.; Stefanov, B. B.; Liu, G.; Liashenko, A.; Piskorz, P.; Komaromi, I.; Martin, R. L.; Fox, D. J.; Keith, T.; Al-Laham, M. A.; Peng, C. Y.; Nanayakkara, A.; Challacombe, M.; Gill, P. M. W.; Johnson, B.; Chen, W.; Wong, M. W.; Gonzalez, C.; and Pople, J. A.; Gaussian, Inc., Wallingford CT, 2004.

(60) (a) Wadt, W. R.; Hay, P. J. *J. Chem Phys.* **1985**, *82*, 284. (b) Hay P. J.; Wadt, W. R. *J. Chem. Phys.* **1985**, *82*, 299.

(61) (a) Dunning, T. H., Jr. *J. Chem. Phys.* **1989**, *90*, 1007. (b) Dunning, T. H.; Hay, P. J. *In Modern Theoretical Chemistry. 3. Methods of Electronic Structure Theory*; Schaefer, H. F., III, Ed.; Plenum Press: New York, 1977. (c) Woon, D. E.; Dunning, T. H. *J. Chem. Phys.* **1993**, *98*, 1358.

CHAPTER 4

Oxidation of Iron in the Tris(ditox) Ancillary Ligand Platform

4.1 Introduction

High valent iron oxo moieties are important intermediates in critical oxidation processes in nature including the activation of C–H bonds.^{1–4} This hallmark reactivity of iron based enzymes has provided an imperative for the syntheses of iron oxo complexes with the aim of engendering efficient and potent oxidation chemistry.⁵ Additionally, high valent late metal oxo moieties in general have been identified as probable intermediates in water oxidation processes. Tetravalent iron with a terminal oxo functionality provides an intriguing synthetic target due to the d^4 electron configuration. As alluded to in Chapter 1, the d^4 configuration is particularly interesting for terminal metal oxo complexes as two scenarios are possible. First, the proper energetic arrangement of the d orbitals along with a low spin electronic configuration could potentially afford an electrophilic metal oxo moiety susceptible to nucleophilic attack. Second, high spin state configurations could afford kinetically viable unpaired spin density localized on the oxo functionality poised for radical coupling or bond activation. As such, synthetic Fe(IV) oxo complexes have been an area of much research while trying to understand the relationship between ancillary ligand fields to the reactivity and property of the Fe(IV) oxo functionality

Though originally elusive,⁶ mononuclear species containing non-heme Fe(IV) oxo functionalities have now been realized⁷ with high valent iron centers supported in tetragonal^{8–14} and trigonal bipyramidal^{15–21} ligand fields. The majority of these complexes feature a primary coordination sphere comprising four or five coordinate polydentate nitrogen donors. The ligand field of the Fe(IV) oxo functionality has been found to be particularly important in tuning the spin state of the metal center. A key feature to the reactivity of non-heme Fe(IV) oxo complexes is the accessibility of a quintet high spin state. Whereas Fe(IV) oxo complexes can be isolated in the intermediate triplet spin state,⁹ supporting DFT calculations suggest that a thermally accessible quintet state affords the minimum barrier towards C–H bond activation.^{22,23} As such, ligand modifications have afforded more accessible high spin states, and in some cases a high spin ground state, with faster rates of reaction observed.^{24–26} In view of our interest in the use of metal oxo complexes to promote energy conversion reactions,^{27,28} we have explored the coordination chemistry of metals in the exceptionally weak ligand field engendered by the tris(alkoxide) platform of ditox (Hditox = $t\text{Bu}_2\text{MeCOH}$).²⁹ The steric bulk of ditox is reduced relative to its tritox^{30,31} brethren by virtue of the replacement of one $t\text{Bu}$ group by Me. Ditox enables the preferential formation of tris(alkoxide) metal complexes, as we have recently

demonstrated for 3d transition metals ($M = V, Cr$). Such an alkoxide ligand platform provides an oxidation-resistant ligand environment of very weak field. Spectroscopic, structural, computational and reactivity studies on the pseudo-tetrahedral d^0-d^2 $[M(\text{ditox})_3O]$ ($M = V, Cr$) oxo complexes have demonstrated that the d electrons occupy metal oxo π^* orbitals with all frontier orbitals possessing significant oxo character. Thus, a tris(ditox) metal oxo system possessing more than two d electrons is expected to be highly reactive as a result of substantial unpaired electron density on the oxo.

4.2 O–O bond Formation versus C–H Bond Activation

In considering homogenous late transition metal oxo complexes for O–O bond formation, C–H bond activation from organic molecules becomes an unavoidable consequence. Organic solvents provide many practical benefits for fundamental studies, such as high purity as well as a diverse range of polarity and solubility properties. However, organic solvents such as tetrahydrofuran, acetonitrile diethyl ether, pentane and benzene, also introduce large concentrations of relatively weak C–H bond into the reaction mixture. The same highly oxidizing properties of metal oxo complexes that are desirable for the study of O–O bond formation^{27,32–34} inherently make the metal oxo species competent for C–H bond activation.^{35–38} Highly oxidizing potentials and possible unpaired electron density on the metal oxo moiety prime the species for C–H bond homolysis. Consequently, C–H bond activation can be crudely interpreted as a surrogate for O–O bond formation processes, as complexes suitable of O–O bond formation will likely participate in C–H bond activation as well.

Ultimately, O–O bond formation process can occur preferentially to C–H bond activation if accessibility to C–H bonds is limited. For homogeneous molecular systems, this requires the design of the ligand scaffold affording an increases local concentration of the reactants necessary for O–O bond formation.³⁹ In examples where this is achieved, selectivity for O–O bond formation is never in perfect yields, resulting in eventual decomposition and either low yield for O–O bonds or poor turn over numbers for water oxidation catalysts. Heterogeneous systems, on the other hand have been designed to use metal-oxide catalysts in water, which eliminated C–H bonds from the reaction mixture entirely. This strategy has been effective enough afford commercialization of electrolyzer, but also requires that the metal catalyst is stabilized in an oxidation resistant and oxygen atom-rich ancillary ligand field. Given the dearth of

investigations into the nature of high valent late metals in oxygen rich ligand environment, this provides further motivation to study the behavior high valent iron compounds supported by alkoxide ancillary ligand environments

In an effort to interrogate the nature of high valent mononuclear iron supported by the oxygen rich tris(ditox) ancillary ligand environment, the possibility of C–H bond activation as a surrogate for O–O bond formation will be embraced. In lieu of designing a ligand scaffold to increase a local concentration of a desired reaction partner, simplified mononuclear species will be studied in order to glean insight into the unperturbed nature of the observed reactivity. Furthermore, embracing C–H bond activation afford the ability to directly compare the reactivity in the pseudo-tetrahedral geometry to the abundance of C–H bond activation reports for high valent iron oxo complexes supported by tetragonal and trigonal bipyramidal ancillary ligand field.

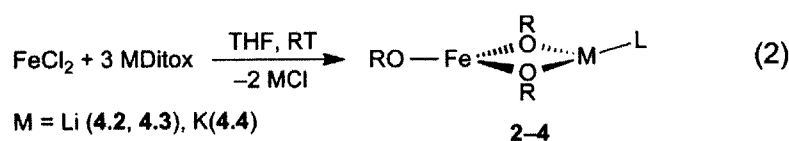
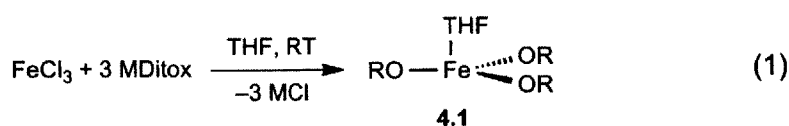
4.3 Synthesis and Characterization of Fe Ditox Compounds

The preparative reaction chemistry employed to obtain the iron ditox compounds is illustrated in Figure 4.1. Homoleptic iron tris(alkoxide) complexes were prepared by salt metathesis reactions between corresponding iron halides and alkali metal alkoxides. As described in Chapter 2, a trivalent tris(ditox)₃ iron complex Fe(ditox)₃THF (**4.1**) is prepared via the reaction of 3 equiv of Li(ditox) or K(ditox) with FeCl₃ in THF at room temperature, (eq 1) to afford a yellow solution. Filtration followed by recrystallization from pentane at –40 °C yields analytically pure products in 64% yield for Li(ditox) and 71% yield for K(ditox).

The synthesis of a trigonal planar divalent tris(ditox) iron complex is described in Chapter 2 wherein the coordinating cation (potassium) is sequestered in between two crown-ether molecules. However, in order to have a greater variety of divalent iron compounds with which to utilize, different variations of a divalent iron tris(ditox) compounds were prepared with coordinating cations (lithium and potassium) allowed to coordinate directly to the alkoxide ligands. These compounds provide divalent tris(alkoxide) complexes with enhanced solubility properties, especially in non-polar organic solvents such as pentane and cyclohexane.

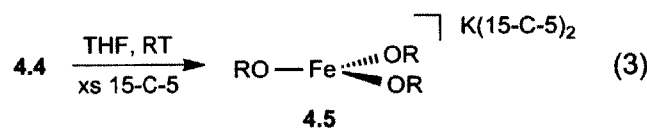
Treatment of 3 equiv of Li(ditox) with FeCl₂ in THF or diethyl ether at room temperature results in the formation a green solution of Fe(ditox)₃Li(L) (L = diethyl ether (**4.2**), THF (**4.3**)) in 63% and 71% yields, respectively, after filtration and recrystallization from pentane (eq 2, Figure

1). The potassium analogue, $\text{Fe}(\text{ditox})_3\text{K}(\text{THF})_2$ (**4.4**) was obtained in 67% yield using $\text{K}(\text{ditox})$. Of note, the alkali cation of **4.2–4.4** is coordinated by two ditox ligands. As presented in Chapter 2, the trigonal planar complex $[\text{Fe}(\text{ditox})_3]^-$ can be directly generated by treatment of **4.4** with excess 15-crown-5-ether resulting in $[\text{Fe}(\text{ditox})_3][\text{K}(\text{15C5})_2]$ (**4.5**). Attempts to sequester Li cation from **4.2** or **4.3** proved more problematic. As such, **4.5** was exclusively used as an anionic mononuclear trigonal planar iron tris(alkoxide) synthon. Treatment of **4.4** with 18-crown-6-ether, a more commonly used reagent for potassium sequestration, was not tractable for removal of potassium



M = Li (**4.2, 4.3**), K(**4.4**)

L = Et₂O (**4.2**), THF (**4.3**), 2 THF(**4.4**)



15-C-5 = 15-crown-5-ether

Figure 4.1. Preparative methods for trivalent and divalent iron-tris(ditox) complexes.

Single crystal X-ray diffraction studies were performed on compounds **4.1, 4.3–4.5**. Compound **4.1** is shown to be a distorted trigonal monopyramid with a THF molecule coordinating the axial position (Chapter 2, Figure 2.6.C); the structure of the compound is isomorphous with the previously reported $\text{V}(\text{ditox})_3\text{THF}$.²⁹ The average $\text{Fe}-\text{O}_{\text{alk}}$ bond distance is 1.82 Å. The alkoxide-iron bond angle is slightly distorted from an idealized trigonal planar angle of 120°, $\text{O}(1)_{\text{alk}}-\text{Fe}(1)-\text{O}(2)_{\text{alk}} = 113^\circ$, with the apical THF molecule slightly positioned over this contracted angle. The other two $\text{O}_{\text{alk}}-\text{Fe}-\text{O}_{\text{alk}}$ bond angles are refined to 119° and 120° resulting in a sum of the angles equal to 352°, indicating that the coordinated THF results in an iron atom that is slightly above the plane of the ditox ligands.

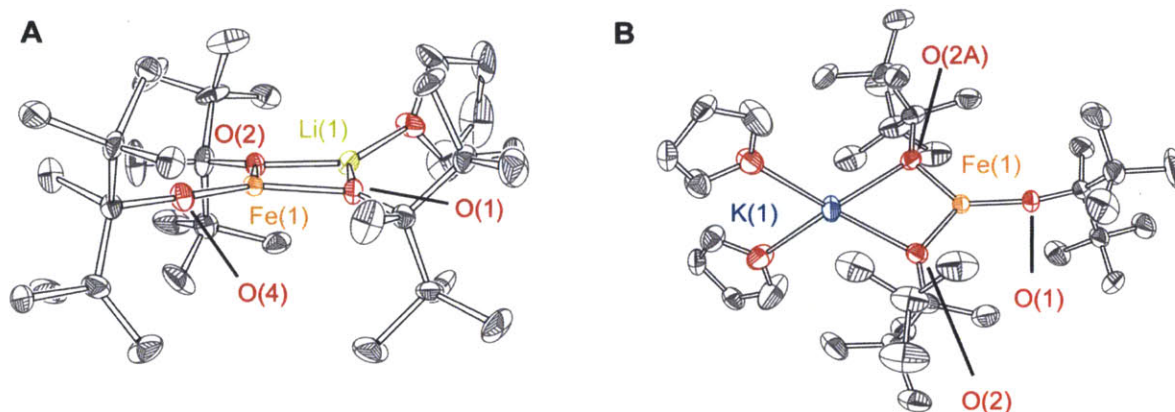


Figure 4.2 (A) Crystal Structure of $\text{Fe}(\text{ditox})_3\text{Li}(\text{THF})$ (**4.3**), 50% probability ellipsoids. Hydrogen atoms omitted for clarity. Selected bond distances: $\text{Fe}(1)\text{--O}(1) = 1.912(4)$ Å, $\text{Fe}(1)\text{--O}(2) = 1.922(4)$ Å, $\text{Fe}(1)\text{--O}(4) = 1.796(1)$ Å, $\text{Li}(1)\text{--O}(1) = 1.863(12)$ Å, $\text{Li}(1)\text{--O}(2) = 1.859(12)$ Å, $\text{Li}(1)\text{--O}(3) = 1.902(4)$ Å. Selected bond angles: $\text{O}(1)\text{--Fe}(1)\text{--O}(2) = 88.9(1)^\circ$, $\text{O}(1)\text{--Fe}(1)\text{--O}(4) = 135.6(2)^\circ$, $\text{O}(2)\text{--Fe}(1)\text{--O}(4) = 135.6(2)^\circ$. **(B)** Crystal structure of $\text{Fe}(\text{ditox})_3\text{K}(\text{THF})_2$ (**4.4**), 50% probability ellipsoids. H atoms are omitted for clarity. Selected bond distances: $\text{Fe}(1)\text{--O}(1) = 1.826(2)$ Å, $\text{Fe}(1)\text{--O}(2) = 1.903(1)$ Å, $\text{K}(1)\text{--O}(2) = 2.585(1)$ Å. Selected bond angles: $\text{O}(1)\text{--Fe}(1)\text{--O}(2) = 130.1(1)^\circ$, $\text{K}(1)\text{--O}(2)\text{--Fe}(1) = 95.8(1)^\circ$, $\text{O}(2)\text{--Fe}(1)\text{--O}(2A) = 99.8(1)^\circ$.

$\text{Fe}(\text{II})$ complexes **4.3** and **4.4** (Figures 4.2 (A) and (B) respectively) assume a Y-shaped geometry with alkali cations coordinated directly to two ditox ligands. The average $\text{Fe}\text{--O}_{alk}$ bond distance of the alkoxides coordinated to the alkali cation increase to 1.91 Å when compared to **4.1**. The terminally bound alkoxide ligands in **4.3** have a bond length that is 1.80 Å, shorter than that found in **4.1**, whereas the bond length of the terminal alkoxide of **4.4** is slightly elongated to 1.83 Å. Since the bond lengths of the alkoxides coordinated to the cations are essentially identical in **4.3** and **4.4**, the differences in bond lengths of the terminal alkoxide ligand of these complexes likely arise from the Y-shaped distortion owing to the size of the alkali metal cation. The contracted bond angle of **4.3** is 90° whereas the contracted bond angle of **4.4** is 100° . Thus, as the coordinating alkali metal induces a smaller contracted bond angle, the terminally bound alkoxide appears to bind the metal more tightly. In both **4.3** and **4.4**, the sum of the all the angles are exactly 360° , indicating that the Fe atom resides in the plane of the alkoxides for both complexes. In the absence of an alkali metal cation template, no distortion is observed. The crystal structure of **4.5** is shown in Figure 2.4.C within Chapter 2. All three bond angles of **4.5** are 120° and the average $\text{Fe}\text{--O}_{alk}$ bond distance is 1.87 Å.

The $\nu(\text{M}\text{--O}_{alk})$ stretching region in the FTIR of **4.5** shows two strong absorptions at 632 cm^{-1} and 576 cm^{-1} . As is expected upon oxidation, these features shift to higher energy in **4.1** to 686 cm^{-1} and 590 cm^{-1} . Upon coordination of a potassium cation in **4.4**, with concomitant

contraction of one of the of $O_{alk}-Fe-O_{alk}$ bond angles to 100° , the higher energy band splits into two peaks that are separated by 14 cm^{-1} . With Li coordination in **4.3** and further angle contraction, this splitting increases to 32 cm^{-1} . Thus the contraction of the $O_{alk}-Fe-O_{alk}$ bond angle appears to be correlated with the higher energy $\nu(M-O_{alk})$ stretching feature.

Solution magnetic measurement (Evans method) is consistent with a high spin electronic ground state for **4.1–4.5**. The room temperature magnetic moment of **4.1** is $\mu_{eff} = 5.09\text{ BM}$, which is slightly lower than the spin-only value for a d^6 ion but comparable to other high spin Fe(III) systems. The room temperature solution magnetic moments of $\mu_{eff} = 4.70\text{ BM}$ for the series of Fe(II) compounds (**4.2–4.5**) are consistent with high spin $S = 2$ metal centers.

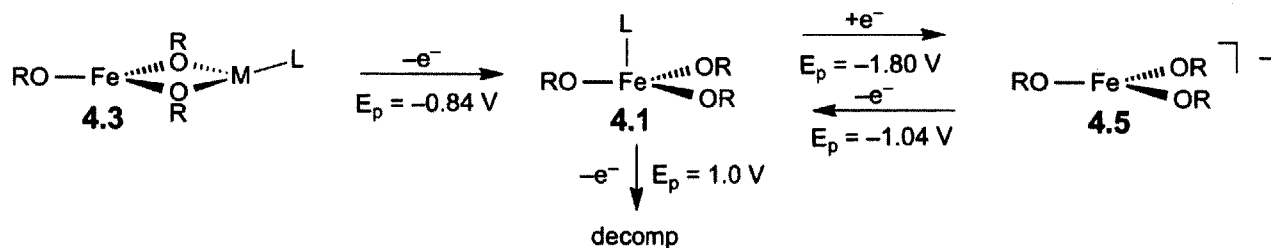
4.4 Oxidation Chemistry

The electrochemical behavior of **4.1**, **4.3** and **4.5** is summarized in Scheme 4.1. Cyclic voltammograms of **4.3**, $Fe(ditox)_3Li(THF)$, in a $0.1\text{ M TBAPF}_6/THF$ solution, show a broad irreversible oxidation wave with a peak current at -0.84 V vs. $FeCp_2/FeCp_2^+$ attributable to the Fe(III)/Fe(II) couple and loss of coordinated lithium. **5** displays a sharper irreversible oxidation wave with a peak current at -1.04 V vs. $FeCp_2/FeCp_2^+$. The cathodic shift of the electrochemical oxidation of **4.5** as compared to **4.3** indicates that the removal of the bound lithium cation and subsequent bond angle changes requires ca. 200 mV of overpotential.

Upon completion of an anodic sweep wherein **4.3** and **4.5** have been electrochemically oxidized, a subsequent cathodic sweep of both oxidized species show another broad irreversible feature with peak potential at -1.80 V vs. $FeCp_2/FeCp_2^+$ for both complexes. The identical cathodic feature is observed upon the reduction of independently prepared **4.1**, $Fe(ditox)_3$, suggesting that the electrochemical oxidation of either **4.3** or **4.5** result in the formation **4.1**. The process is consistent with electrochemical irreversibility owing to the weak coordination of ligands in the apical position of **4.1**.

At more anodic potentials, **4.3** and **4.5** exhibit a sharp irreversible feature at 1.0 V versus $FeCp_2/FeCp_2^+$. The electrochemistry is consistent with the oxidation of the Fe(III) complex; the resulting product quickly decomposes. Notably, **4.1** also shows a similarly sharp irreversible oxidation at the same potential. It appears therefore that the formation of Fe(IV) in this system is feasible even in the absence of a strongly donating apical ligand.

Scheme 4.1



Attempts to attain a high valent Fe oxo species focused on the reactivity of Fe(II) and Fe(III) tris(ditox) complexes with common oxo-transfer reagents, as outlined in Figure 4.3. The Fe(III) complex, **4.1**, did not exhibit any reactivity with iodosyl-benzene (PhIO) over the course of a week at room temperature. In contrast, **4.1** reacted immediately with Me₃NO but not in an oxidative transformation but rather to replace the apical THF to furnish **4.6**. The structure of **4.6** (Figure 4.4) exhibits pseudo-tetrahedral geometry at the Fe(III) center, which is ligated by three ditox ligand and ONMe₃. The N–O bond distance in **4.6** is 1.397(2) Å, which falls within a usual range of values (1.38–1.40 Å) found for unactivated ONMe₃ (as provided by a CSD search that delivered 32 structures).^{40–42}

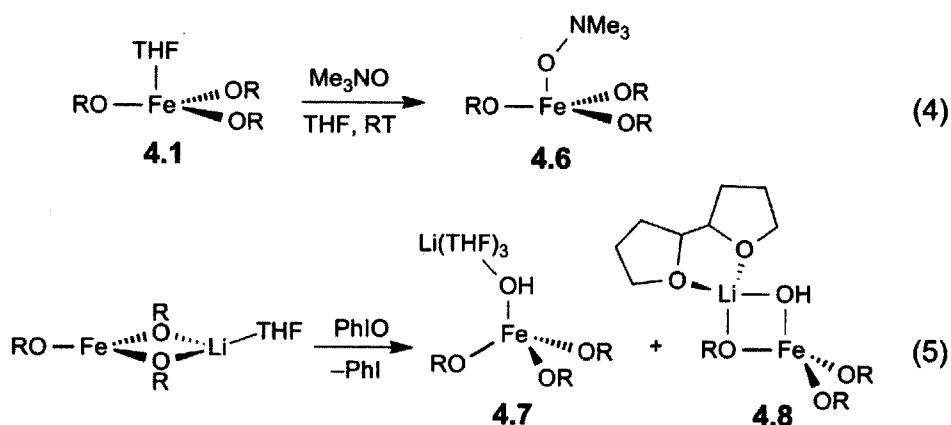


Figure 4.3. Reactivity of trigonal Fe(III) ditox compounds with oxo transfer reagents.

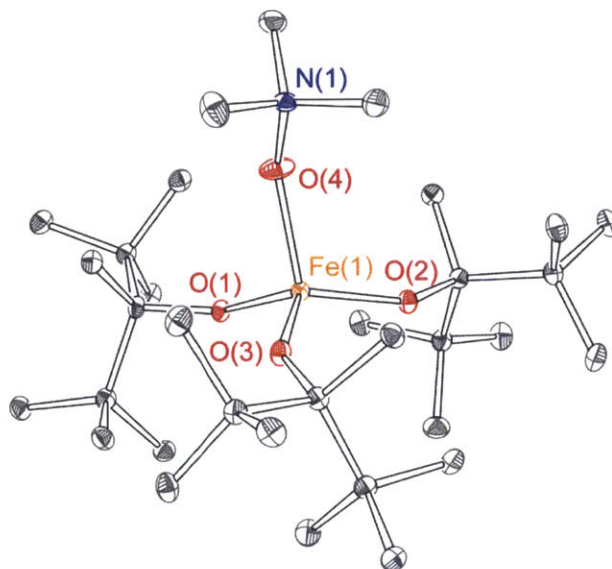


Figure 4.4. Crystal structure of $\text{Fe}(\text{ditox})_3(\text{ONMe}_3)$ (**4.6**), 50% probability ellipsoids. Hydrogen atoms omitted for clarity. Selected bond distances: $\text{Fe}(1)\text{--O}(1) = 1.840(1) \text{ \AA}$, $\text{Fe}(1)\text{--O}(2) = 1.843(2) \text{ \AA}$, $\text{Fe}(1)\text{--O}(3) = 1.838(2) \text{ \AA}$, $\text{Fe}(1)\text{--O}(4) = 1.979(2) \text{ \AA}$, $\text{O}(4)\text{--N}(1) = 1.397(2) \text{ \AA}$. Selected bond angles: $\text{O}(1)\text{--Fe}(1)\text{--O}(2) = 113.9(1)^\circ$, $\text{O}(1)\text{--Fe}(1)\text{--O}(3) = 112.2(1)^\circ$, $\text{O}(2)\text{--Fe}(1)\text{--O}(3) = 112.6(1)^\circ$, $\text{O}(1)\text{--Fe}(1)\text{--O}(4) = 107.4(1)^\circ$, $\text{O}(2)\text{--Fe}(1)\text{--O}(4) = 112.9(1)^\circ$, $\text{O}(3)\text{--Fe}(1)\text{--O}(4) = 96.6(1)^\circ$, $\text{Fe}(1)\text{--O}(4)\text{--N}(1) = 137.2(1)^\circ$.

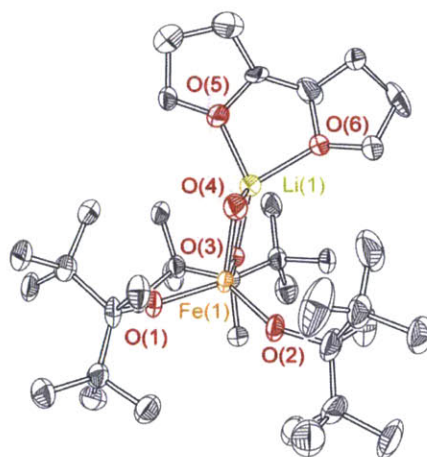


Figure 4.5. Crystal structure of $\text{Fe}(\text{ditox})_3(\text{OH})\text{Li}(\text{C}_8\text{O}_2\text{H}_{14})$, (**8**), 50% probability. H atoms and alternative conformations of ^tBu groups are omitted for clarity. Selected bond distance: $\text{Fe}(1)\text{--O}(1) = 1.836(2) \text{ \AA}$, $\text{Fe}(1)\text{--O}(2) = 1.823(2) \text{ \AA}$, $\text{Fe}(1)\text{--O}(3) = 1.919(2) \text{ \AA}$, $\text{Fe}(1)\text{--O}(4) = 1.920(2) \text{ \AA}$, $\text{Li}(1)\text{--O}(3) = 1.949(5) \text{ \AA}$, $\text{Li}(1)\text{--O}(4) = 1.885(7) \text{ \AA}$, $\text{Li}(1)\text{--O}(5) = 1.995(5) \text{ \AA}$, $\text{Li}(1)\text{--O}(6) = 2.014(5) \text{ \AA}$. Selected bond angles: $\text{O}(1)\text{--Fe}(1)\text{--O}(2) = 111.4(1)^\circ$, $\text{O}(1)\text{--Fe}(1)\text{--O}(3) = 111.5(1)^\circ$, $\text{O}(2)\text{--Fe}(1)\text{--O}(3) = 121.8(1)^\circ$, $\text{O}(1)\text{--Fe}(1)\text{--O}(4) = 111.4(1)^\circ$, $\text{O}(2)\text{--Fe}(1)\text{--O}(4) = 110.6(1)^\circ$, $\text{O}(3)\text{--Fe}(1)\text{--O}(4) = 87.9(1)^\circ$, $\text{O}(3)\text{--Li}(1)\text{--O}(4) = 88.0(2)^\circ$.

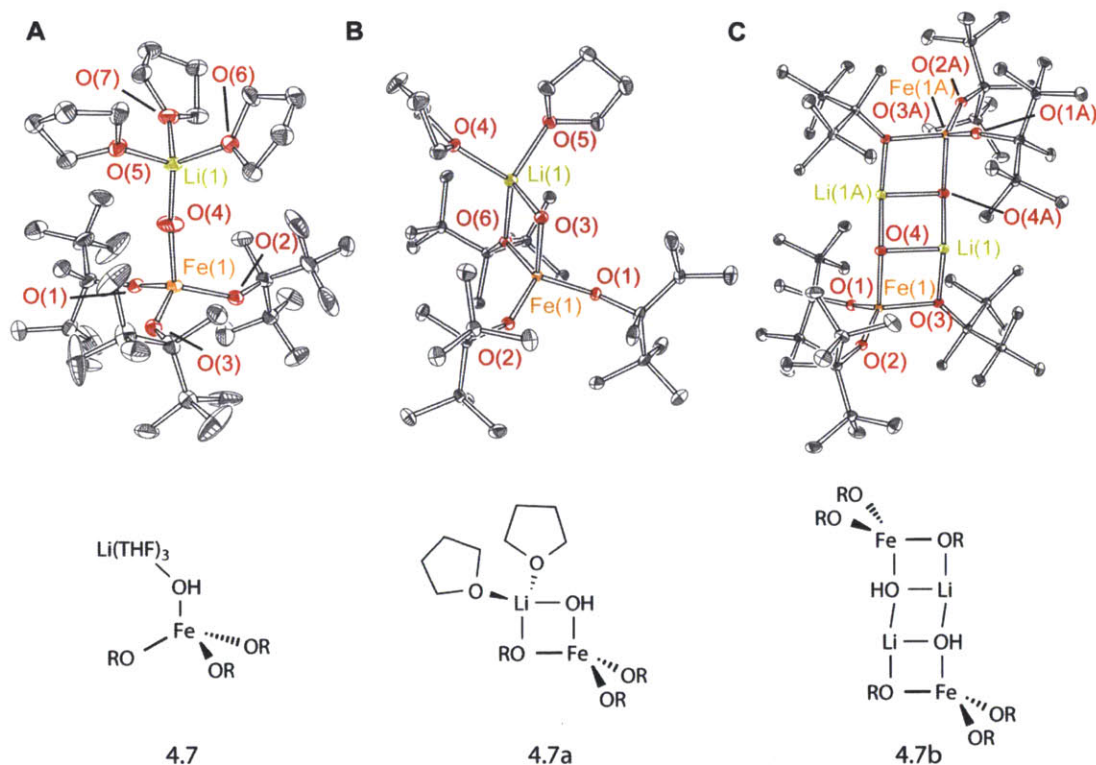


Figure 4.6. (A) Crystal structure of $\text{Fe}(\text{ditox})_3(\text{OH})\text{Li}(\text{THF})_3$, (**4.7**), 30% probability ellipsoids. H atoms, co-crystallized solvent molecules, and alternative conformations of ${}^t\text{Bu}$ groups are omitted for clarity. Selected bond distances: $\text{Fe}(1)\text{--O}(1) = 1.842(5) \text{ \AA}$, $\text{Fe}(1)\text{--O}(2) = 1.860(4) \text{ \AA}$, $\text{Fe}(1)\text{--O}(3) = 1.850(5) \text{ \AA}$, $\text{Fe}(1)\text{--O}(4) = 1.945(5) \text{ \AA}$, $\text{Li}(1)\text{--O}(4) = 1.794(11) \text{ \AA}$. Selected bond angles: $\text{O}(1)\text{--Fe}(1)\text{--O}(2) = 111.2(2)^\circ$, $\text{O}(1)\text{--Fe}(1)\text{--O}(3) = 111.4(2)^\circ$, $\text{O}(2)\text{--Fe}(1)\text{--O}(3) = 110.9(2)^\circ$, $\text{O}(1)\text{--Fe}(1)\text{--O}(4) = 107.4(3)^\circ$, $\text{O}(2)\text{--Fe}(1)\text{--O}(4) = 109.5(2)^\circ$, $\text{O}(3)\text{--Fe}(1)\text{--O}(4) = 106.3(3)^\circ$, $\text{Fe}(1)\text{--O}(4)\text{--Li}(1) = 173.5(6)^\circ$. (B) Crystal structure of $\text{Fe}(\text{ditox})_3(\text{OH})\text{Li}(\text{THF})_2$, (**4.7a**), 50% probability ellipsoids. H atoms, co-crystallized solvent molecules, and alternative conformations of ${}^t\text{Bu}$ groups are omitted for clarity. Selected bond distances: $\text{Fe}(1)\text{--O}(1) = 1.840(1) \text{ \AA}$, $\text{Fe}(1)\text{--O}(2) = 1.834(1) \text{ \AA}$, $\text{Fe}(1)\text{--O}(3) = 1.916(2) \text{ \AA}$, $\text{Fe}(1)\text{--O}(6) = 1.919(1) \text{ \AA}$, $\text{Li}(1)\text{--O}(4) = 1.875(4) \text{ \AA}$, $\text{Li}(1)\text{--O}(6) = 2.029(3) \text{ \AA}$. Selected bond angles: $\text{O}(1)\text{--Fe}(1)\text{--O}(2) = 110.7(1)^\circ$, $\text{O}(1)\text{--Fe}(1)\text{--O}(6) = 110.4(1)^\circ$, $\text{O}(2)\text{--Fe}(1)\text{--O}(6) = 123.7(1)^\circ$, $\text{O}(1)\text{--Fe}(1)\text{--O}(3) = 111.2(1)^\circ$, $\text{O}(2)\text{--Fe}(1)\text{--O}(3) = 111.2(1)^\circ$, $\text{O}(6)\text{--Fe}(1)\text{--O}(3) = 87.4(1)^\circ$, $\text{Fe}(1)\text{--O}(3)\text{--Li}(1) = 96.2(2)^\circ$. (C) Structure $[\text{Fe}(\text{ditox})_3(\text{OH})\text{Li}]_2$, (**4.7b**), 30% probability ellipsoids. H atoms are omitted for clarity. Selected bond distances: $\text{Fe}(1)\text{--O}(1) = 1.812(5) \text{ \AA}$, $\text{Fe}(1)\text{--O}(2) = 1.804(5) \text{ \AA}$, $\text{Fe}(1)\text{--O}(3) = 1.913(5) \text{ \AA}$, $\text{Fe}(1)\text{--O}(4) = 1.981(5) \text{ \AA}$, $\text{Li}(1)\text{--O}(3) = 1.880(2) \text{ \AA}$, $\text{Li}(1)\text{--O}(4) = 1.990(2) \text{ \AA}$. Selected bond angles: $\text{O}(1)\text{--Fe}(1)\text{--O}(2) = 121.2(2)^\circ$, $\text{O}(1)\text{--Fe}(1)\text{--O}(3) = 108.8(2)^\circ$, $\text{O}(2)\text{--Fe}(1)\text{--O}(3) = 117.0(2)^\circ$, $\text{O}(1)\text{--Fe}(1)\text{--O}(4) = 110.2(2)^\circ$, $\text{O}(2)\text{--Fe}(1)\text{--O}(4) = 106.6(2)^\circ$, $\text{O}(3)\text{--Fe}(1)\text{--O}(4) = 87.7(2)^\circ$, $\text{O}(3)\text{--Li}(1)\text{--O}(4) = 88.3(5)^\circ$.

Unlike **4.1**, compound **4.3** reacts with oxygen atom transfer reagents, such as PhIO, in THF at room temperature with facility. Dissolution of solid PhIO causes solutions of **4.3** to turn from pale green to pale yellow within ca. 30 sec. In the absence of the Fe(II) complex, no dissolution of PhIO is observed within several hours. Fractional recrystallization of the oxidation products (from pentane and ether/THF phases) yielded two Fe(III)–OH products in 25% and 23% yields, respectively: **4.7**, $[\text{Fe}(\text{ditox})_3(\text{OH})\text{Li}(\text{THF})_3]$ with three THF molecules filling the coordination

environment around the lithium cation; and, **4.8**, $\text{Fe}(\text{ditox})_3(\mu_2\text{-OH})\text{Li}(\text{C}_8\text{O}_2\text{H}_{14})$ with a coupled THF chelate that coordinates to Li. Structures of the compounds **4.7** and **4.8**, shown in Figures 4.5 and 4.6.A, respectively, feature distorted tetrahedral geometry at the metal centers. Both compounds display the expected OH stretch in the IR spectra (3700 cm^{-1} and 3630 cm^{-1}). Compound **4.8** is especially noteworthy, as it contains the 2,2'-bi-tetrahydrofuran ligand, which is also evident in ESI-MS. 2,2'-bi-THF has been previously prepared from THF via hydrogen atom abstraction using radical reagents.^{43,44}

Chemical analysis of **4.7** is complicated by the variability of the coordination environment imposed by Li, as shown in Figure 4.6. Drying compound **4.7** under vacuum led to a partial loss of THF to yield a solid mixture of **4.7** and **4.7a**, $\text{Fe}(\text{ditox})_3(\mu_2\text{-OH})\text{Li}(\text{THF})_2$. Although **4.7a** and **4.7** are not easily separated from each other, we were able to discern the identity of **4.7a** by the single crystal X-ray diffraction (from the bulk sample of **4.7**). The molecular structure of **4.7a** is shown in Figure 4.6.B. Compound **4.7a** differs from compound **4.7** in that it only has two THF molecules coordinated to the lithium cation as well as one Fe-bound alkoxide in a manner analogous to the connectivity observed in **4.8**. Unlike **4.8**, Compound **4.7a** has two THF molecules which are uncoupled ligated to the lithium cation. The structural concordance of **4.7a** and **4.8** may explain the similarity in the OH stretching frequency of **4.7a** and **4.8**, both approximately 3630 cm^{-1} , as opposed to that of **4.7**, which has an OH stretching frequency at 3700 cm^{-1} . ESI-MS of both **4.7a** and **4.8** show peaks consistent with the $[\text{Fe}(\text{ditox})_3(\text{OH})]^-$ ($m/z = 544.4$) and $[\text{Fe}(\text{ditox})_3(\text{OH})(\text{OH}_2)]^-$ ($m/z = 562.4$) ions. Exposure of the bright yellow transparent crystals of **4.7** to vacuum leads to an immediate loss of crystallinity.

Recrystallization of **4.7** in the absence of THF affords crystals of $[\text{Fe}(\text{ditox})_3(\text{OH})\text{Li}]_2$ (**4.7b**) (Figure 4.6.B) in low yield. Compound **4.7b** differs from **4.7** and **4.7a** in that no solvent molecules are bound to the lithium cation. In order to complete the coordination environment around the lithium cation, **4.7b** effectively dimerizes to give “ $\text{Fe}(\text{ditox})_3(\text{OH})\text{Li}$ ” units. Each Li atom has a coordination number of three that is achieved by its coordination to two hydroxide ligands and one Fe-bound alkoxide.

Eventual formation of an Fe(III)-OH via an oxygen atom transfer (OAT), and possible formation of an oxidized intermediate, is accompanied by formal hydrogen atom abstraction. Such reactivity is displayed by the oxidation of the trigonal planar divalent species **4.5**, $[\text{Fe}(\text{ditox})_3][\text{K}(\text{15C5})_2]$, to yield a terminal Fe(III)-OH moiety (**4.9**). The structure of **4.9** (Figure

4.7) is noteworthy, as the terminal hydroxide is completely embedded inside crown ether. The absence of an OH stretching frequency in the FTIR spectrum of **4.9** is likely due to strong hydrogen bonding to the 15-crown-5- ether. Within the solid state structure, a distance between the oxygen of the metal bound hydroxide and an oxygen atom on the 15-crown-5-ether ring is determined to 3.20 Å, which is consistent with a hydrogen bonding model. IR spectroscopy provides further confirmation of the metal–hydroxide observed in **4.9**. A new strong feature in the $\nu(\text{M–OH})$ range, 543 cm^{-1} , is observed in the IR spectrum of **4.9** which shifts to lower energy upon preparation with PhI^{18}O (510 cm^{-1}).

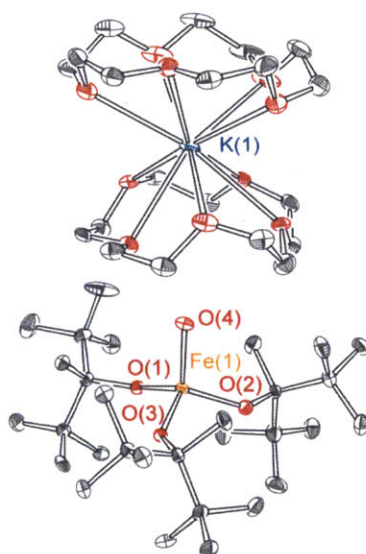


Figure 4.7. Structure $[\text{Fe}(\text{ditox})_3(\text{OH})][\text{K}(15\text{C}5)_2]$, (**4.9**), 50% probability ellipsoids. H atoms are omitted for clarity. Selected bond distances: $\text{Fe}(1)\text{--O}(1) = 1.868(2)\text{ \AA}$, $\text{Fe}(1)\text{--O}(2) = 1.859(1)\text{ \AA}$, $\text{Fe}(1)\text{--O}(3) = 1.859(1)\text{ \AA}$, $\text{Fe}(1)\text{--O}(4) = 1.890(1)\text{ \AA}$. Selected bond angles: $\text{O}(1)\text{--Fe}(1)\text{--O}(2) = 108.0(1)^\circ$, $\text{O}(1)\text{--Fe}(1)\text{--O}(3) = 111.1(1)^\circ$, $\text{O}(2)\text{--Fe}(1)\text{--O}(3) = 109.2(1)^\circ$, $\text{O}(1)\text{--Fe}(1)\text{--O}(4) = 110.0(0)^\circ$, $\text{O}(2)\text{--Fe}(1)\text{--O}(4) = 111.4(1)^\circ$, $\text{O}(3)\text{--Fe}(1)\text{--O}(4) = 107.2(2)^\circ$.

To determine the source of the hydroxyl proton, the OAT reaction was performed in THF-d_8 . Reaction in deuterio-THF yielded both OH and OD, in ca. 50:50 ratio as determined by IR ($\nu(\text{O–H}) = 3700\text{ cm}^{-1}$, 3630 cm^{-1} , $\nu(\text{O–D}) = 2730\text{ cm}^{-1}$, 2677 cm^{-1}). The deuteration of the hydroxide confirms that THF is a prominent source of the H atom. However, the presence of the protio form also suggests that the abstracted H atom can originate or be mediated by other sources of hydrogen atoms, such as advantageous water, glassware or a $t\text{Bu}$ group of a ditox ligand located in a vicinity of the apical position. Regarding the ligand possibly mediating H-atom transfer (oxidized intermediate abstracts H-atom from ligand generating a radical on the ligand that subsequently abstracts an H-atom from solvent), no ^2H signal was observed in the ^2H

NMR spectrum of the hydrolyzed ligand after oxidations were performed. Thus, the ditox ligand could possibly be an additional H atom source and not a mediator, as it does not incorporate any deuterium. The reaction in silylated glassware does not change the ratio of the products, implying that the H atom does not originate from the glass. Exchange of the proton on the metal bound hydroxide with trace water cannot be ruled out as well. Thus, despite these ambiguities, the approximately 50% incorporation of deuterium shows that hydrogen atom abstraction from solvent is the primary pathway for reactivity upon oxygen atom transfer. Performing the OAT reaction in the presence of compounds possessing weak C–H bonds (e.g., 1,4-cyclohexadiene) yields **4.7** in isolated yields of ca. 90%.

Complete atom transfer to the Fe(II) center would produce a Fe(IV) oxo intermediate, $[\text{Fe(IV)(ditox)}_3(\text{O})]^-$. Accordingly, efforts were pursued to isolate or observe an Fe(IV) oxo intermediate under a variety of reaction conditions. Temperatures were investigated as low as $-78\text{ }^\circ\text{C}$. However, the formation of the Fe(III)–OH was instantaneous with mixing. The oxidative potency of the intermediate is further in evidence by its indiscriminate reaction with solvent. The formation of Fe(III)–OH complexes (both compounds **4.7** and **4.9**) is immediate even when solvents are used that possess thermodynamically strong C–H bonds (pentane, cyclohexane, and benzene). Whereas Fe(IV) oxo intermediates are often able to be observed via in situ generation of the oxo in acetonitrile at cold temperatures,^{7,8,18} in the case of **4.5**, the oxidative intermediate reacts with acetonitrile at $-40\text{ }^\circ\text{C}$ to furnish the C–H activation product, $[\text{Fe(ditox)}_3(\text{H}_2\text{CCN})][\text{K(15C5)}_2]$ (**4.10**), which was isolated and structurally characterized (Figure 4.8). The identity of the activated acetonitrile moiety is confirmed crystallography as the two metal-unbound atoms to the triatomic ligand were best refined as carbon and nitrogen with a C–N bond distance of 1.163 Å. The IR spectrum of the product also confirms the presence of a C–N triple bond with as a sharp intense peak at 2140 cm^{-1} . In addition to this C–H activated acetonitrile complex, FTIR of the reaction mixture shows the presence of Fe(III)–OH product **4.9**, indicating that C–H abstraction from CH_3CN by the oxidative intermediate is a likely reaction pathway. **4.9** does not react with CH_3CN , ruling out that **4.10** is furnished by **4.9** and CH_3CN . Unfortunately, the **4.9** and **4.10** have similar solubility properties and thus **4.10** can only be isolated via mechanical separation of crystals.

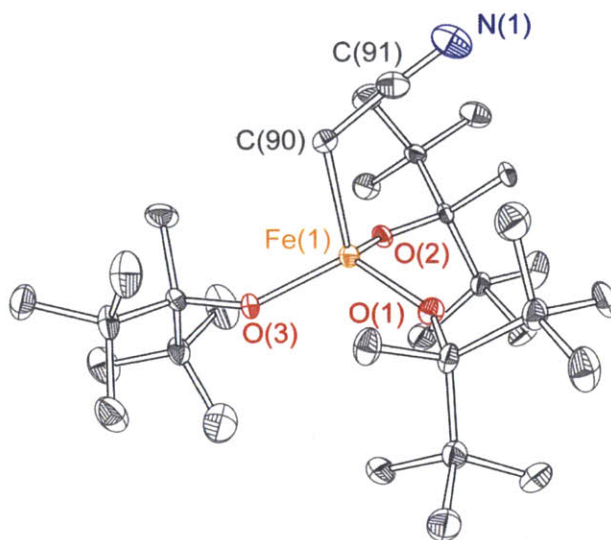


Figure 4.8. Structure $[\text{Fe}(\text{ditox})_3(\text{CH}_2\text{CN})][\text{K}(\text{15C5})_2]$ (**4.10**), 50% probability ellipsoids. H atoms and $\text{K}(\text{15C5})_2$ are omitted for clarity. Selected bond distances: $\text{Fe}(1)\text{--O}(1) = 1.859(2)$ Å, $\text{Fe}(1)\text{--O}(2) = 1.845(2)$ Å, $\text{Fe}(1)\text{--O}(3) = 1.846(2)$ Å, $\text{Fe}(1)\text{--C}(90) = 2.141(3)$ Å, $\text{C}(90)\text{--C}(91) = 1.406(5)$ Å, $\text{C}(91)\text{--N}(1) = 1.163(4)$ Å. Selected bond angles: $\text{O}(1)\text{--Fe}(1)\text{--O}(2) = 111.6(1)^\circ$, $\text{O}(1)\text{--Fe}(1)\text{--O}(3) = 114.6(1)^\circ$, $\text{O}(2)\text{--Fe}(1)\text{--O}(3) = 110.0(1)^\circ$, $\text{O}(1)\text{--Fe}(1)\text{--C}(90) = 107.9(1)^\circ$, $\text{O}(2)\text{--Fe}(1)\text{--C}(90) = 107.9(1)^\circ$, $\text{O}(3)\text{--Fe}(1)\text{--C}(90) = 104.4(1)^\circ$, $\text{C}(90)\text{--C}(91)\text{--N}(1) = 176.6(4)^\circ$.

The oxidized intermediate can be intercepted with selected substrates. Oxidations of phosphines to phosphine oxides by amine-*n*-oxides have been shown to be prohibitively slow. For example, pyridine-*N*-oxide is unable to oxidize phosphines in the absence of a metal-based catalyst.⁴⁵ The ability of oxidize phosphines is observed for Fe(II) ditox precursors treated with Me_3NO in the presence of Ph_3P . Ph_3PO is immediately observed by ^{31}P NMR in 80% yield (per mole of Me_3NO added) when **4.4** or **4.5** in 1,2-difluorobenzene is treated with Me_3NO in the presence of Ph_3P . This reaction is catalytic as treatment of 1 equiv of **4.4** with 10 equiv of NMe_3O and 10 equiv of PPh_3 shows formation of 7.5 equiv of PPh_3O . When THF is used as a solvent under similar conditions, the yield of the PPh_3O diminishes to ca. 20%. We attribute this decrease in phosphine oxidation to competitive hydrogen atom abstraction with the C–H bond of THF. This contention is supported by the observation of Fe(III)–OH stretching vibrations in the FTIR of the reaction mixture. These results together suggest a common intermediate for phosphine oxidation and hydrogen atom abstraction.

4.5 Computation of Fe(IV)–oxo Intermediate

DFT calculations at the B3LYP level using the Gaussian 03 suite were performed to assess the viability of a Fe(IV) oxo intermediate. We utilized models of the putative Fe(IV) oxo, **4.7** and **4.9**, where the ditox ligands are replaced by $t\text{BuO}^-$ groups in order to simplify the computation. This simplification has been found to provide accurate and reliable results with similar types of compounds.²⁹

Our initial computational efforts focused on the electronic structure of a tris(alkoxide) Fe(IV) oxo complex. We calculated two models: one as the free Fe(IV) oxo anion, $[\text{Fe}(\text{O}^i\text{Bu})_3(\text{O})]^-$ (**4.A**), and the other as the neutral complex with an associated lithium cation, $\text{Li}[\text{Fe}(\text{O}^i\text{Bu})_3(\text{O})]$ (**4.B**). The electronic structure of each of these models was probed for its appropriate ground state multiplicity. The energies of the singlet, triplet and quintet states were computed while relaxing the geometry to their basal state. We found that the quintet state was the most stable for both the **4.A** and **4.B** as compared to the singlet and triplet states (Table 4.1). This result is in agreement with the prediction that a weak equatorial ligand field should favor high spin states and poor ancillary donor ligands should destabilize the high valent oxo state.⁴⁶

Table 4.1. Calculated multiplicities, selected parameters and relative energies referenced to quintet state respectively for $[\text{Fe}(\text{O}^i\text{Bu})_3(\text{O})]^-$ (**4.A**) and $[\text{Fe}(\text{O}^t\text{Bu})_3(\text{O})\text{Li}]$ (**4.B**).

	$d(\text{Fe}-\text{O}_{\text{oxo}})_{\text{avg}}$	$d(\text{Fe}-\text{O}_{\text{alk}})_{\text{avg}}$	Rel. Energy(kcal/mol)
A			
Quintet	1.63 Å	1.86 Å	0
Triplet	1.61 Å	1.87 Å	+13
Singlet	1.58 Å	1.81 Å	+12
B			
Quintet	1.68 Å	1.80 Å	0
Triplet	1.70 Å	1.78 Å	+21
Singlet	1.65 Å	1.74 Å	+19

The optimized geometry of the anionic quintet state predicts a $\text{Fe}-\text{O}_{\text{oxo}}$ distance of 1.63 Å, which is in good agreement with experimentally found Fe(IV)– O_{oxo} bond distances. Analysis of the ancillary ligand environment of the quintet, triplet and singlet spin states indicates that in order to stabilize lower spin states, $\text{Fe}-\text{O}_{\text{alk}}$ bond distances must shorten and $\text{O}_{\text{alk}}-\text{Fe}-\text{O}_{\text{alk}}$ must be constricted relative to tetrahedral bond angles. These geometrical distortions are exacerbated by the increased steric bulk afforded by ditox relative to $t\text{BuO}^-$. Therefore, it is likely that the quintet state of $[\text{Fe}(\text{ditox})_3(\text{O})]^-$ is even more stabilized relative to the computed model **4.A**. This is noteworthy as even in cases where other Fe(IV) oxo complexes are predicted to be high spin,

the high spin state is typically much closer in energy to an intermediate spin state (~8 kcal/mol).²²

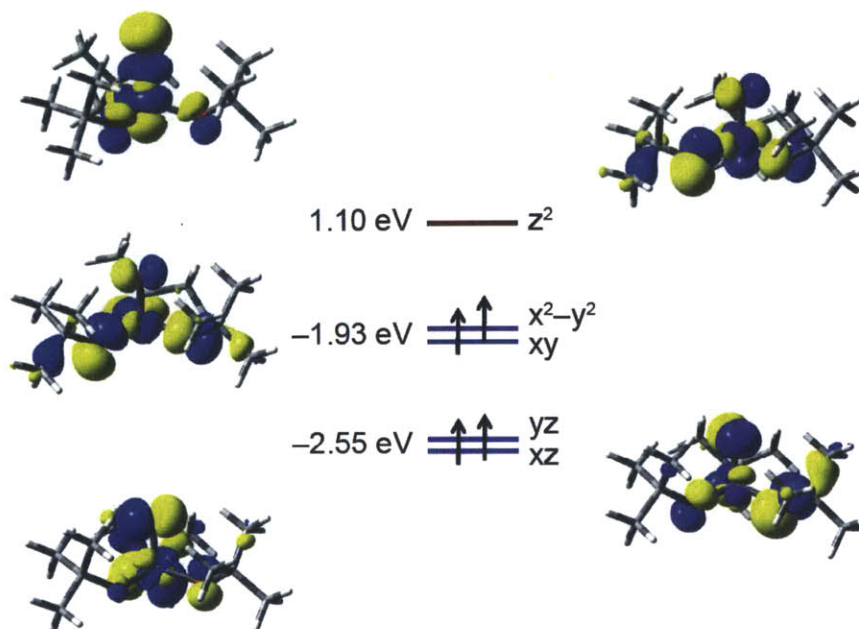


Figure 4.9. Molecular orbital diagram the quintet ground state of $[\text{Fe}(\text{O}^t\text{Bu})_3(\text{O})]^-$ for the α orbitals shown with an isovalue of 0.4.

The electronic structure of the **4.A** follows from an orbital parentage that is similar to the previously reported $\text{Cr}(\text{ditox})_3(\text{O})$ analogue (Table 4.2).²⁹ The frontier orbitals of the quintet state models have significant d-orbital character. The four SOMOs correspond to the doubly degenerate sets of d_{xz} and d_{yz} , and d_{xy} and $d_{x^2-y^2}$ (Figure 4.9). A significant amount of spin density (14%) is found to reside on the oxygen atom, due to the substantial oxo orbital character in the SOMOs.

Table 4.2 Calculated atomic orbital composition of frontier molecule orbitals for **4.A**, $[\text{Fe}(\text{O}^t\text{Bu})_3(\text{O})]^-$.

Orbital		O (oxo)	Fe	O (alkoxide)
LUMO	z^2	30%	44%	17%
SOMO	x^2-y^2	7%	22%	46%
SOMO-1	xy	7%	21%	47%
SOMO-2	yz	19%	12%	38%
SOMO-3	xz	24%	13%	36%

The neutral model **4.B** shows that the quintet state model is further stabilized compared to the singlet and triplet states by 19 and 21 kcal/mol, respectively. The lithium cation is found between the oxygen atom from the oxo functional group and an oxygen atom from the alkoxide. The calculated Fe–O_{oxo} bond distance of the neutral quintet state is predicted to be 1.68 Å. The electronic structure of neutral **4.B** quintet state model is similar to that of the free anionic model where the SOMOs correspond to the doubly degenerate sets of (d_{xz} , d_{yz}) and (d_{xy} , $d_{x^2-y^2}$). The quintet model of **4.B** shows that significant radical O character from the oxo group is also observed in the SOMOs although the radical character in the d_{xy} and $d_{x^2-y^2}$ orbitals is slightly attenuated compared to the Li-free anionic model (Table 4.3).

Table 4.3. Calculated atomic orbital composition of frontier molecule orbitals for **4.B**, Fe(O^tBu)₃(O)Li.

Orbital	O (oxo)	Fe	O (alkoxide)	Li	
LUMO	z^2	20%	42%	26%	1%
SOMO	x^2-y^2	13%	22%	40%	1%
SOMO-1	xy	7%	19%	47%	2%
SOMO-2	yz	5%	13%	49%	1%
SOMO-3	xz	27%	7%	41%	1%

We also wished to estimate a possible mechanistic pathway for the activation of THF as observed experimentally (vide supra). A simple solvation model with one THF molecule was targeted for its relative ease of computation. Similar to the unsolvated Li[Fe(IV)–O_{oxo}] model **4.B**, the structure with one THF coordinated to the lithium cation, Li[Fe(IV)–O_{oxo}]THF, has a ground state optimized geometry with the lithium cation situated between the oxygen atom from the oxo group and an oxygen atom from an alkoxide. However, single crystal X-ray diffraction data of Fe(ditox)₃(OH)Li(THF)₃ shows a different structural conformations with the lithium cation coordinated to the terminal hydroxide and solvent molecules, not the alkoxides. Additionally, structural data of Cr(Ditox)₃(O)K(Et₂O)₃ does not show the alkali cation coordinated to an alkoxide ligand as the potassium coordinates to the terminal oxo and three solvent molecules exclusively. The similarity of these experimentally characterized analogous compounds supports the belief that in practical solvent environments a conformation in which the lithium cation is not interacting with the alkoxides is the ground state (Figure 4.10, Left). As

such, the ground state structure of $\text{Fe}(\text{O}^t\text{Bu})_3(\text{O})\text{Li}(\text{THF})$ will be taken to be without the lithium cation coordinated to the alkoxide ligand.

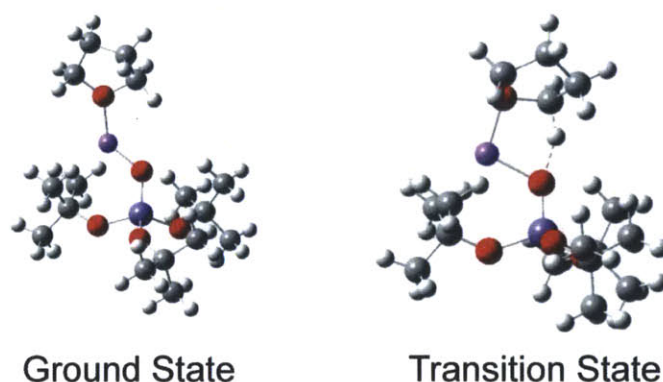


Figure 4.10. Optimized structures for the ground state geometry of $\text{Fe}(\text{O}^t\text{Bu})_3(\text{O})\text{Li}(\text{THF})$ and the corresponding transition state for hydrogen atom abstraction from α carbon of the coordinated THF.

With knowledge of the nature of the initial ground state, a reaction coordinate for C–H bond activation of THF via a high valent $\text{Fe}(\text{O}^t\text{Bu})_3(\text{O})\text{Li}$ complex was calculated and a transition state structure for C–H bond activation was determined (Figure 4.10, right). The calculated transition state is found to include an α -H from the solvated THF activated to produce a loosely associated Fe–OH moiety. This transition state structure is the lowest energy barrier towards C–H bond activation and lies at an accessible 7.6 kcal/mol higher than ground state. A radical intermediate structure is calculated along the reaction coordinate with a fully formed Fe(III)–OH functionality along with a radical localized on the THF associated to the lithium cation. The organic THF radical intermediate can be easily envisioned to react with a second THF radical to produce the bis-THF adduct **4.8**. This calculated mechanism provides an accessible pathway for the observed THF activation.

4.7 Discussion

The reported metathetical preparation and characterization of **4.1–4.5** represent a successful return to the original synthetic strategy employed by Thiessen and Koerner, who first isolated a homoleptic Fe(III)–alkoxide by the treatment of ferric chloride with sodium ethoxide.⁴⁷ Iron–alkoxide complexes have historically been difficult to isolate in a monometallic form because the alkoxide tends to engender multimetallic species by assuming a bridging coordination between metals.⁴⁸ The facile isolation of rare monomeric iron-tris(alkoxide)

complexes reported here shows that proper tuning of the steric bulk of the alkoxide ligand is an effective strategy for discouraging the formation of multimetallic complexes, a feature that has plagued the alkoxide coordination chemistry.

Owing to the dearth of structurally characterized homoleptic iron-tris(alkoxide) complexes, it is difficult to thoroughly compare the observed metric parameters of **4.1–4.5** to other compounds. Two exemplars of Fe(II) or Fe(III) tris(alkoxide) complexes have been structurally characterized. Cantalupo and coworkers have shown that the Fe(II) center of Fe(OC₄F₉)₃K(18-crown-6)₂⁴⁹ is three coordinate with the K⁺ cation coordinating to two of the fluorinated alkoxide ligands. An Fe(OAr)₃ aryloxide complex (Ar = 2,6, diphenylbenzene) has been structurally characterized as well.⁵⁰ The d(Fe–O_{alk}) bond distances of **4.3** and **4.4** are uniformly shorter than those of Fe(OC₄F₉)₃K(18-crown-6)₂ by approximately 0.05 Å. This indicates stronger bonding interactions between the iron and the alkoxides in **4.3** and **4.4**, which is likely important in stabilizing compounds **4.1–4.5** by discouraging ligand disproportionation and formation of tetrakis(alkoxide) complexes.

Iron(II) ditox complexes in the presence of OAT reagents exhibit unparalleled activity. All observed products including the formation of the Fe(III)–OH and the 2,2'–bi–tetrahydrofuran ligand products is consistent with H–atom abstraction by a Fe(IV) oxo intermediate. However, we cannot rule out an alternative mechanism similar to the one proposed for Mn–corroles,⁵¹ in which the oxidant species is actually the PhIO adduct of Fe(II). Regardless of the precise nature of the intermediate, the observed oxidation chemistry of **4.2–4.5** in the presence of OAT reagents is distinguished by exceptionally fast rates of reaction and by the indiscriminate nature in which hydrogen atom transfer occurs. One challenge with identifying the oxidative intermediate is its exceptional reactivity. Established procedures for observing Fe(IV) oxo complexes typically involves the utilization of acetonitrile as a solvent at low temperatures. However, compounds **4.2–4.5** all furnish an Fe(III)–OH as well as C–H activated products such as **4.10**, [Fe(ditox)₃(CH₂CN)][K(15C5)₂] in acetonitrile at temperatures as low as –40° C. This reactivity contrasts the chemistry of typical iron oxo complexes that are capable of activating substrates possessing BDEs as high as 110 kcal/mol but fail to do so for kinetic reasons.^{52–54} For example, based on the empirical Evans-Polanyi relationship, though [(N4Py)Fe^{IV}(O)]²⁺ should react with a C–H bonds possessing BDE of 95 kcal/mol at a rate of ~10^{–4} M^{–1} s^{–1}, the complex does not react with acetonitrile.^{9,10,55,56} Similarly, the Evans-Polanyi relationship predicts that

$[(\text{bpy})_2(\text{py})\text{Ru}(\text{O})]^{2+}$ should react with C–H bonds of a BDE of 95 kcal/mol at a rate of $10^{-5} \text{ M}^{-1} \text{ s}^{-1}$. But no reaction with acetonitrile is observed despite the much greater concentration of neat acetonitrile as compared to substrate.^{57,58} On this basis, the reaction rates of typical iron oxo compounds can conservatively be estimated to react with acetonitrile at rates that are least two orders of magnitude slower than what is expected based on the BDE of acetonitrile. Conversely, UV-vis spectra of reaction mixtures of Fe(II) ditox complexes in the presence of OAT reagents show complete conversion to product in approximately a second. If one assumes reaction by pseudo-first order kinetics, the reaction rates for the oxidative intermediate can be estimated utilizing the Eyring equation and the relationship $k = \ln(2)/t_{1/2}$. If a complete reaction is taken to represent seven half-lives (99.2% complete), a pseudo first order rate constant of approximately 10 s^{-1} is obtained. Admittedly, this is a crude estimate of the rate constant for reaction but it is in accordance with the instantaneous reactions observed at low temperatures as well as the low activation barrier calculated found from transition state DFT calculations ($\sim 8 \text{ kcal/mol}$).

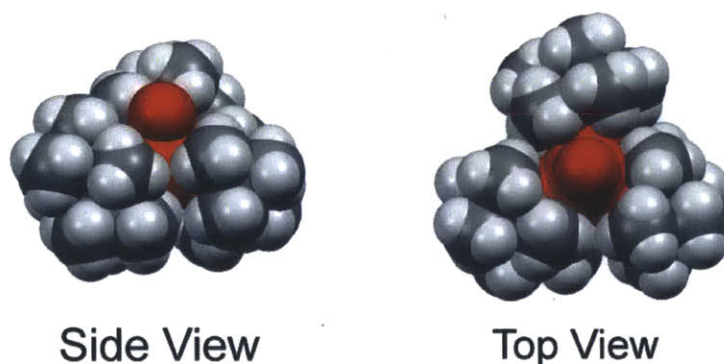


Figure 4.11. Space filling models of **4.9** depicting the accessibility of an apical oxygen atom (red) in a pseudo-tetrahedral geometry.

The exceptional reactivity of Fe ditox compounds with acetonitrile under oxidizing conditions is ascribed to steric and electronic factors. A clear rate dependence on steric crowding about Fe enforced by the ancillary ligand has been observed by Que and coworkers.²⁵ Using the structure of **4.9** as a guidepost, a space filling model can be generated that shows a potentially accessible axial coordination site in which the Fe oxo or Fe–OAT adduct could reside within the ditox platform (Figure 4.11). Whereas the exact Fe–O_{oxo} bond distance shown in the space filling model is too long for an Fe–O_{oxo} by 0.3 Å, the pseudo-tetrahedral geometry is similar to that of the structurally characterized early metal oxo complexes in tris(ditox) ligand environments.²⁹

The model shows that the steric bulk of the ditox ligands is directed away from the axial coordination environment, thus providing insight as to the exceptional reactivity of the putative pseudo-tetrahedral Fe tris(ditox) intermediate. Thus, the manner in which the steric bulk of the ligands is seen to not be directed towards the terminal oxygen atom does accurately model an accessible axial position towards substrates for a pseudo-tetrahedral Fe–tris(ditox) system.

Electronic structure calculations support enhanced reaction rates, particularly for an oxidizing intermediate in which OAT is complete. The weak ligand field of ditox together with a pseudo-tetrahedral environment engenders a high spin quintet state for a Fe(IV)–oxo intermediate. In addition, the ligand field orthogonal to the Fe–O_{oxo} bond (d_{xy} , $d_{x^2-y^2}$) is thought to promote high spin behavior.⁴⁶ Accessibility of such a high spin state has been shown to increase reaction rates.²² Theoretical predictions by Neese correlate accessibility of high spin states in Fe(IV) oxo complexes to the ligand field strength orthogonal to the metal oxo bond axis.

Calculations of early metal oxo complexes supported by a tris(ditox) ancillary ligand field show that the primary interaction between the metal and the alkoxide is a σ O_{alk(p)}–M(d_{xy} , $d_{x^2-y^2}$) bond; essentially identical to the primary bonding motifs in a trigonal bipyramidal geometry. Thus, by lowering the ancillary ligands below the x/y plane, the pseudo-tetrahedral geometry creates poor orbital overlap with the d_{xy} , $d_{x^2-y^2}$ causing these orbitals to be lower in energy relative to pseudo-octahedral and pseudo-trigonal bipyramidal geometries. This in turn favors electronic population of d_{xy} , and $d_{x^2-y^2}$ over pairing electrons in d_{xz} and d_{yz} resulting in stabilization of a high spin state.

A weak ligand field orthogonal to the Fe–O_{oxo} bond axis could be essential to the high reactivity observed in the oxidized Fe-ditox system as well as explain the highly reactive nature of an Fe(III) oxo recently reported by Smith and coworkers.⁵⁹ Smith's transient pseudo-tetrahedral Fe(III) oxo is reported to be more difficult to isolate than many Fe(V) oxo complexes and Fe(IV) oxo complexes while performing similar C–H bond activation and OAT chemistries.⁶⁰ Our report of Fe in a tris(ditox) ligand platform supports the emerging trend of the importance of high spin states induced by ancillary ligand fields in Fe oxo complexes, possible over high oxidation states, as the contributing factor to highly reactive and difficult to isolate metal oxo complexes.^{16-18, 24-26, 56,57}

4.7 Concluding Remarks

An oxygen-rich pseudo-tetrahedral coordination sphere with strong π -donation is appealing as it engenders an extremely weak ligand field as compared to tetragonal nitrogen-donor coordination environments. Towards this end, we have prepared Fe supported within the trigonal tris(alkoxide) platform. Alkoxide ligands typically have been ineffective at stabilizing three coordinate ancillary ligand fields because they are prone to bridging metals centers to result in multi-nuclear complexes.⁶¹ While the use of the sterically crowded alkoxides has been shown to discourage the formation of bridging multi-nuclear species, they are typically too bulky to afford tris(alkoxide) ancillary ligand spheres.⁶² The ditox environment circumvents these issues to afford a trigonal, mononuclear Fe center pre-disposed to high spin states. Consistent with this contention, OAT to the Fe(II) ditox platform results in a oxidative intermediate that readily activates C–H bonds including those of solvents generally unreactive to high valent iron oxo compounds, especially those coordinated by nitrogen donor ligands in a tetragonal field. In summary, the steric and electronic factors of a tris(ditox) ligand field about Fe together support exceptional oxidative reactivity.

4.8 Experimental Methods and Computational Details

4.8.1 General Considerations. All reactions involving air-sensitive materials were performed in a nitrogen-filled glovebox. Solvents were purified using SG Water Glass Contour Solvent System and stored over 4-Å molecular sieves. Compounds were routinely characterized by IR, elemental analyses, and the X-ray analysis; selected compounds were characterized by NMR, cyclic voltammetry and ESI-MS. IR spectra of powdered samples were recorded on a PerkinElmer Spectrum 400 FT-IR/FT-FIR Spectrometer outfitted with a Pike Technologies GladiATR attenuated total reflectance accessory with a monolithic diamond crystal stage and pressure clamp. Cyclic voltammetry (CV) experiments were performed using a glassy carbon working electrode (0.07 cm²), a platinum wire auxiliary electrode and a Ag/AgNO₃ (0.1 M) reference electrode in 0.1 M NBu₄PF₆ acetonitrile/THF solutions at room temperature using a BASI CV50W in a glove box. The potentials were referenced to ferrocene/ferrocenium couple by recording the CV of the ferrocene before and after each scan. All NMR spectra were recorded at the MIT Department of Chemistry Instrumentation Facility on a Varian Mercury 300 NMR spectrometer in C₆D₆ at room temperature. Magnetic moments were determined in C₆D₆ at room temperature on a Varian Mercury 300 NMR Spectrometer using Evans method.⁶³ Pascal constants were used to estimate diamagnetic correction. Silylated glassware was obtained by swirling the reaction vessels with Me₃SiCl and drying them thereafter under vacuum. UV-vis measurements were recorded on a Varian Cary 5000 spectrometer and references to appropriate solvent. All UV-vis measurements were performed on sample in solutions of THF. Elemental analyses were performed by Midwest Microlab LLC. Methyl lithium (1.6 M in ether), 2,2,4,4-tetramethyl-3-pentanone, 15-crown-5-ether, FeCl₃, and FeCl₂ were purchased from Aldrich. PhIO was purchased from Alfa Aesar. ONMe₃ was purchased from Aldrich and sublimed twice before use. ^tBu₂MeCOLi and ^tBu₂MeCOH (Liditox and Hditox hereafter) were prepared according to literature procedures.⁶⁴ Compounds **4.1** and **4.5** were prepared as described in Chapter 2.

4.8.2 Preparation of Fe(ditox)₃Li(OEt₂) (4.2). 271 mg (1.65 mmol) of Liditox in 2 mL of ether was added in one portion to the stirred off-white ether suspension (2 mL) of FeCl₂ (89.0 mg, 1.55 mmol), and the reaction was left to stir overnight. The resulting brown solution was filtered and concentrated. Light blue-green solid was recrystallized from pentane (2 mL) at -40 °C, to give [Fe(ditox)₃Li(OEt₂)] in 62.5% yield (210 mg, 0.344 mmol). Anal. Calcd. (Found) for

$C_{34}H_{73}FeLiO_4$: C, 67.08 (66.80); H, 12.09 (11.90). IR (cm^{-1}): 1391 (w), 1383 (m), 1370 (m), 1359 (m), 1178 (w), 1127 (m), 1103 (m), 1089 (s), 1062 (s), 1014 (m), 999 (s), 943 (m), 931 (m), 907 (s), 866 (w), 832 (w), 793 (w), 684 (m), 646 (m), 585 (s), 564 (m), 515 (br, m), 489 (m). UV-vis: 748 nm($71 M^{-1}, cm^{-1}$) $\mu_{eff} = 4.68 \mu B$

4.8.3 Preparation of $Fe(ditox)_3Li(THF)$ (4.3). 725 mg (4.42 mmol) of Liditox in 3 mL of THF was added in one portion to the stirred off-white THF slurry (2 mL) of $FeCl_2$ (186 mg, 1.47 mmol). The solution became homogenous and assumed a green color. After 1 h, volatiles were removed, and the residue was extracted with pentane (3 mL). Pentane solution was concentrated to ca. 1 mL, and left at $-40\text{ }^\circ C$ for 12 h to give $[Fe(ditox)_3Li(THF)]$ in 70.7% yield (627 mg, 1.04 mmol). Anal. Calcd. (Found) for $C_{34}H_{73}FeLiO_4$: C, 67.31 (67.21); H, 11.80 (11.61). IR (cm^{-1}): 1482 (m), 1472 (m), 1391 (w), 1382 (m), 1372 (m), 1361 (m), 1131 (m), 1111 (s), 1094 (s), 1036 (m), 1021 (m), 1009 (m), 1000 (m), 940 (m), 932 (m), 910 (s), 885 (m), 870 (m), 681 (m), 649 (m), 586 (s), 567 (sh), 520 (br, m), 468 (w), 453 (w). UV-vis: 748 nm($71 M^{-1}, cm^{-1}$) $\mu_{eff} = 4.66 \mu B$

4.8.4 Preparation of $Fe(ditox)_3K(THF)_2$ (4.4). 1.00 g (5.09 mmol) of Kditox in 3 mL of THF were added in one portion to the stirred pale yellow THF slurry (2 mL) of $FeBr_2$ (366 mg, 1.70 mmol). The solution became homogenous and assumed a green color. After 2 h, volatiles were removed, and the residue was extracted with pentane (5 mL) and filtered through Celite. Pentane solution was collected and concentrated to ca. 1 mL, and left to stand at $-40\text{ }^\circ C$ for 24 h to give **4.4** in 67.2% yield (810 mg, 1.14 mmol). Anal. Calcd. (Found) for $C_{38}H_{79}FeKO_5$: C, 64.19 (63.89); H, 11.20 (10.96). IR (cm^{-1}): 1483 (m), 1393 (sh), 1383 (m), 1358 (m), 1214 (w), 1128 (s), 1106 (s), 1074 (vs), 1051 (vs), 1009 (vs), 976 (s), 894 (w), 839 (m), 819 (m), 796 (s), 635 (m), 621 (m), 569 (s), 537 (w), 526 (w). UV-vis: 748 nm ($71 M^{-1}, cm^{-1}$). UV-vis: 773 nm($90 M^{-1}, cm^{-1}$) $\mu_{eff} = 4.71 \mu B$

4.8.5 Preparation of $Fe(ditox)_3(ONMe_3)$ (4.6). 7.0 mg (0.088 mmol) of Me_3NO was dissolved in 2 mL of THF and added to the stirred yellow solution of **4.1** (26.0 mg, 0.044 mmol) in 2 mL of ether. The resulting yellow solution was stirred for 1 h, filtered, and the volatiles were removed in vacuo. Yellow-brown residue was extracted with 2 mL of ether, filtered, and the solution was concentrated to ca. 0.5 mL volume. Yellow crystals of **4.6** are obtained from solution at $-40\text{ }^\circ C$ for 24 h in 80% yield (21 mg, 0.035 mmol). Anal. Calcd. (Found) for $C_{33}H_{72}NO_4Fe$: C, 65.75 (65.65); H, 12.04 (11.81); N, 2.32 (2.10). IR (cm^{-1}): 1395 (w), 1386 (m),

1367 (m), 1236 (w), 1099 (vs), 1088 (vs), 1004 (s, C–O), 939 (s), 923 (s), 870 (w), 767 (m), 704 (m), 686 (m), 598 (m), 549 (m), 477 (m). UV-vis : no notable features. $\mu_{\text{eff}} = 6.10 \mu\text{B}$.

4.8.6 Preparation of $\text{Fe}(\text{ditox})_3(\text{OH})\text{Li}(\text{THF})_n$, $n = 3$ (4.7**), $n = 2$ (**4.7a**), $n = 0$ (**4.7b**) and $\text{Fe}(\text{ditox})_3(\text{OH})\text{Li}(\text{di-THF})$ (**4.8**).** Solid iodosyl benzene (74.0 mg, 0.337 mmol) was added to the stirred green solution of 204 mg (0.337 mmol) of **4.3** in 3 mL of THF. The resulting heterogeneous mixture quickly became homogeneous (ca. 30 sec), and the initial brown solution turned yellow–orange (ca. 1 min). After 2 min, volatiles were removed in vacuo. The resulting mixture was extracted with pentane (3 mL). Crystallization from pentane leads to the formation of 61 mg (0.088 mmol, 23%) of yellow crystals of **4.8** in two crops. Anal. Calcd. (Found) for $\text{C}_{42}\text{H}_{88}\text{FeLiO}_7$: C, 65.78 (65.41); H, 11.33(11.23). IR (cm^{-1}): 3630 (OH), 1386 (w), 1362 (w), 1084 (vs), 1000 (s), 931 (m), 911 (s), 866 (w), 793 (m), 683 (m), 654 (w), 595 (m), 568 (w), 529 (br, m), 471 (m), 451 (w). ESI-MS⁺ (m/z) 143.1 [$\text{di-THF} + \text{H}$]⁺, 291.1 [(di-THF)₂Li]⁺ ESI-MS⁻ (m/z) 405.3 [$\text{Fe}(\text{ditox})_2(\text{OH})(\text{OH}_2)$]⁻, 562.4 [($\text{Fe}(\text{ditox})_3(\text{OH})(\text{OH}_2)$)]⁻. UV-vis : no notable features.

The crude insoluble solid was taken up from pentane in a mixture of ether/THF (3:1 mL). Slow evaporation of the solution yields 76 mg of a mixture of **4.7** and **4.7a** as yellow crystals (0.096 mmol, ca. 25% yield). The identity of the major product (ca. 90%), containing three THF molecules ($\text{Fe}(\text{ditox})_3(\text{OH})\text{Li}(\text{THF})_3$) (**4.7**), and the minor product (ca. 10%) containing two THF molecules ($\text{Fe}(\text{ditox})_3(\text{OH})\text{Li}(\text{THF})_2$) (**4.7a**) was proven by XRD, and confirmed by IR. Non-dried sample of the mixture of **4.7** and **4.7a**, covered with Paratone N–oil, contains mostly pure **4.7** (by unit cell determination). The presence of **4.7a** in a dried sample of **4.7** is signified by two OH resonances in the IR spectrum at 3630 cm^{-1} and 3700 cm^{-1} . Exposure of the bright yellow transparent crystals of **4.7** to vacuum leads to an immediate loss of crystallinity. The IR of the dried material shows two peaks at 3700 cm^{-1} and 3630 cm^{-1} . Prolonged drying under vacuum or crystallization of the compound from THF–deficient solution (ca. 3:0.2 mL ether:THF) increases the amount of $\text{Fe}(\text{ditox})_3(\text{OH})\text{Li}(\text{THF})_2$ (**4.7a**) as determined by IR. **4.7** and **4.7a** cannot be separated completely as the recrystallization of **4.7/4.7a** in the absence of THF forms [$\text{Fe}(\text{ditox})_3(\text{OH})\text{Li}$]₂ (**4.7b**) in low yield.

Solid iodosobenzene (46.0 mg, 0.205 mmol) was added to the stirred green solution of 126 mg (0.205 mmol) of $\text{Fe}(\text{ditox})_3\text{Li}(\text{THF-}d_8)$, **4.3- d^8 THF**, and 330.0 mg (4.125 mmol, ca. 20.12 equiv) of 1,4–cyclohexadiene in 3 mL of THF. The resulting heterogeneous mixture quickly

became homogeneous (ca. 30 sec), and bright yellow (ca. 1 min). After 1 min, volatiles were removed in vacuo. The resulting mixture was extracted with pentane/THF (3 × 0.5 mL) mixture. Solvents concentration under vacuum to ca 0.5 mL led to the formation of yellow crystals. Crystals were dried to give Fe(ditox)₃(OH)Li(THF)₃ **7** and ca. 10% Fe(ditox)₃(μ₂-OH)Li(THF)₂ **4.7a** in ca. 92% yield {same cmpd – do not know what is going on here} (145 mg, 0.189 mmol).

Characterization of **4.7/4.7a**: ESI-MS⁻ (m/z) 544.2 [Fe(ditox)₃(OH)]⁻, 562.4 [(Fe(ditox)₃(OH)(OH₂))]⁻ Anal. Calcd. (Found) for C₄₂H₈₈FeLiO₇: C, 65.69 (64.40); H, 11.55 (11.21). Repeated attempts to obtain EA showed low percent of C, consistent with the loss of THF and/or decomposition. IR (cm⁻¹): 3700(w), 3630 (w), 1391 (w), 1383 (m), 1370 (m), 1359 (m), 1178 (w), 1127 (m), 1103 (m), 1089 (s), 1062 (s), 1014 (m), 999 (s), 943 (m), 931 (m), 907 (s), 866 (w), 832 (w), 793 (w), 684 (m), 646 (m), 585 (s), 564 (m), 515 (br, m), 489 (m). UV-vis: no notable features.

4.8.7 Preparation of [Fe(ditox)₃(OH)][K(15-crown-5-ether)₂] (4.9). Solid iodosyl benzene (108 mg, 0.492 mmol) was added to the stirred green solution of 500 mg (0.492 mmol) of **4.5** in 6 mL of THF. The resulting heterogeneous mixture quickly became homogeneous (ca. 1 min), and turned yellow-orange. After 2 min, volatiles were removed in vacuo. The resulting mixture was washed 3 × 5 mL of pentane each time. Remaining solid extracted with diethyl ether/THF mixture (5 × 1 mL) and filtered through Celite. The yellow-orange solution was concentrated to ca. 1 mL and left to stand at -40 °C for 24 h to yield pale yellow crystals. Crystals were collected and dried in vacuo to give **4.9** in 65.8% yield (335 mg, 0.324 mmol). An alternative method of preparation involves the use of Me₃NO in place of PhIO in the same molar ratios reported. Anal. Calcd. (Found) for C₅₀H₁₀₄FeKO₁₄: C, 58.63 (58.66); H, 10.23 (9.91). IR (cm⁻¹): 1484 (m), 1476 (sh), 1443 (w), 1383 (m), 1372 (sh), 1355 (s), 1303 (m), 1290 (m), 1253 (m), 1245 (m), 1120 (vs), 1105 (sh), 1092 (sh), 1079 (vs), 1053 (sh), 1042 (s), 1014 (s), 979 (s), 941 (s), 907 (sh), 856 (s), 830 (m), 808 (s), 667 (sh), 635 (s), 577 (s), 543 (br, s), 530 (sh), 411 (sh), 462 (vw). UV-vis: no notable features. μ_{eff} = 6.10 μB.

4.8.8 X-ray crystallographic details. Crystals were mounted on a Bruker three circle goniometer platform equipped with an APEX detector. A graphite monochromator was employed for wavelength selection of the Mo Kα radiation (λ = 0.71073 Å). Data were processed and refined using the program SAINT supplied by Siemens Industrial Automation. Structures were solved by direct methods in SHELXS and refined by standard difference Fourier techniques

in the SHELXTL program suite (6.10 v., Sheldrick G. M., and Siemens Industrial Automation, 2000). Hydrogen atoms were placed in calculated positions using the standard riding model and refined isotropically; all other atoms were refined anisotropically. The structure of **4** had one disordered THF molecule that was satisfactorily modeled. The structure of **4.7** contains four molecules of disordered solvent for one molecule of the metal complex, which leads to the overall low quality of the structure. Three molecules were modeled, whereas the fourth could not be modeled satisfactorily. Therefore, electron density associated with the disordered solvent was removed using SQUEEZE program. PLATON indicated pseudo-trigonal symmetry (P-3) for **4.7**. In the structure of **4.9**, both the 15-crown-5-ether molecules were disordered. One of the 15-crown-5-ether was successfully modeled. However, heavy restraints on the anisotropy of several carbon atoms of the 15-crown-5-ether molecule interacting with the Fe-OH had to be utilized for the minor orientation. The Fe-OH hydrogen atom was detected from the electron density difference map for structure **4.9**. In the structure of **4.8** two enantiomers of di-THF ligand co-crystallize at the same position. In the structures of **4.3**, **4.7**, **8** and **4.9**, some of the ^tBu groups were disordered; the disorder was modeled satisfactorily in separate parts.

4.8.9 Computational Details. Density functional theory (DFT) calculations were performed with the hybrid functional Becke-3 parameter exchange functional⁶⁵ and the Lee-Yang-Parr nonlocal correlation functional (B3LYP)⁶⁶ as implemented in the Gaussian 03, Revision B.05 software package.⁶⁷ An effective core potential (ECP) representing the 1s2s2p core was used for iron (LANL2DZ).⁶⁸ The double- ζ quality correlation-consistent polarized ccc-pvdz basis set by Dunning and coworkers was used on all oxygen atoms, while double- ζ quality basis sets (D95) were used on carbon and hydrogen.⁶⁹

The calculations were performed on simplified models of $[\text{Fe}(\text{ditox})_3(\text{O})]^-$ and $\text{LiFe}(\text{ditox})_3(\text{O})$ where the ^tBu groups are replaced by methyl groups. All geometries were confirmed as local minima structures by calculating the Hessians and checking that no negative eigenvalues were present. Figure 4.9 pictorially depicts the calculated spin density for the models of $[\text{Fe}(\text{ditox})_3(\text{O})]^-$ and $\text{LiFe}(\text{ditox})_3(\text{O})$. Tables 4.13 list the Cartesian coordinates of the optimized geometries of the model of $[\text{Fe}(\text{ditox})_3(\text{O})]^-$.

4.9 Crystallographic Tables and Computational Cartesian Coordinate Tables

Table 4.4. Crystallographic data and structural refinement parameters for Fe(ditox)₃Li(THF) (4.3).

Identification code	compd_3_Fe(ditox) ₃ Li(THF)	
Empirical formula	C ₃₄ H ₆₅ O ₄ LiFe	
Formula weight	600.65 g/mol	
Temperature	-173(2) °C	
Wavelength	0.70173 Å	
Crystal system	Monoclinic	
Space group	P2 ₁	
Unit cell dimensions	$a = 9.146(1) \text{ \AA}$	$\alpha = 90.00^\circ$
	$b = 16.534(2) \text{ \AA}$	$\beta = 92.818(1)^\circ$
	$c = 12.176(1) \text{ \AA}$	$\gamma = 90.00^\circ$
Volume	1839.0(2) Å ³	
Z	2	
Density (calculated)	1.085 Mg/m ³	
Absorption coefficient	0.441 mm ⁻¹	
F(000)	660	
Crystal size	0.25 × 0.20 × 0.20 mm ³	
θ range for data collection	2.08 to 28.27°	
Index ranges	-12 ≤ h ≤ 11, -21 ≤ k ≤ 21, -16 ≤ l ≤ 16	
Reflections collected	35289	
Independent reflections	9072 [R _{int} = 0.0440]	
Completeness to θ = 28.28°	99.7%	
Absorption correction	Empirical SADABS	
Max. and min. transmission	0.9170 and 0.8978	
Refinement method	Full-matrix least-squared on F ²	
Data / restraints/ parameters	9072 / 375 / 471	
^a Goodness-of-fit on F ²	1.034	
^{b,c} Final R indices [I > 2σ(I)]	R ₁ = 0.0461, wR ₂ = 0.1085	
^{b,c} R indices (all data)	R ₁ = 0.0641, wR ₂ = 0.1204	
Largest diff. peak and hole	0.481 and -0.523 e/Å ⁻³	

^a GOF = $(\sum w(F_o^2 - F_c^2)^2 / (n - p))^{1/2}$ where n is the number of data and p is the number of parameters refined.

^b R₁ = $\sum ||F_o - |F_c|| / \sum |F_o|$

^c wR₂ = $\left(\frac{\sum (w(F_o^2 - F_c^2)^2)}{\sum (w(F_o^2)^2)} \right)^{1/2}$

Table 4.5. Crystallographic data and structural refinement parameters for Fe(ditox)₃K(THF)₂ (**4.4**).

Identification code	compd_4_Fe(ditox)3K(THF)2	
Empirical formula	C ₃₈ H ₇₉ O ₅ KFe	
Formula weight	710.981g/mol	
Temperature	-173(2) °C	
Wavelength	0.70173 Å	
Crystal system	Monoclinic	
Space group	C2/c	
Unit cell dimensions	$a = 18.420(2) \text{ \AA}$	$\alpha = 90.00^\circ$
	$b = 15.879(1) \text{ \AA}$	$\beta = 122.454(1)^\circ$
	$c = 16.7830(1) \text{ \AA}$	$\gamma = 90.00^\circ$
Volume	4142.2(4) Å ³	
Z	4	
Density (calculated)	1.140 Mg/m ³	
Absorption coefficient	0.496 mm ⁻¹	
F(000)	1252	
Crystal size	0.40 × 0.30 × 0.20 mm ³	
θ range for data collection	1.83° to 28.70°	
Index ranges	-24 ≤ h ≤ 24, -21 ≤ k ≤ 21, -22 ≤ l ≤ 22	
Reflections collected	43649	
Independent reflections	5364 [R _{int} = 0.0374]	
Completeness to $\theta = 28.28^\circ$	99.9%	
Absorption correction	Empirical SADABS	
Max. and min. transmission	0.9257 and 0.9257	
Refinement method	Full-matrix least-squared on F ²	
Data / restraints/ parameters	5364 / 374 / 358	
^a Goodness-of-fit on F ²	1.026	
^{b,c} Final R indices [I > 2σ(I)]	R ₁ = 0.0333 wR ₂ = 0.0891	
^{b,c} R indices (all data)	R ₁ = 0.0403, wR ₂ = 0.0950	
Largest diff. peak and hole	0.327 and -0.300 e/Å ⁻³	

^a GOF = $(\sum w(F_o^2 - F_c^2)^2 / (n - p))^{1/2}$ where n is the number of data and p is the number of parameters refined.

^b R₁ = $\sum ||F_o - |F_c|| / \sum |F_o|$

^c wR₂ = $\left(\frac{\sum (w(F_o^2 - F_c^2)^2)}{\sum (w(F_o^2)^2)} \right)^{1/2}$

Table 4.6. Crystallographic data and structural refinement parameters for Fe(ditox)₃(ONMe₃) (4.6).

Identification code	cmpd_6_Fe(ditox)3(ONMe3)	
Empirical formula	C ₃₃ H ₇₂ O ₄ NFe	
Formula weight	602.77 g/mol	
Temperature	-173(2) °C	
Wavelength	0.70173 Å	
Crystal system	Monoclinic	
Space group	P2 ₁ /n	
Unit cell dimensions	$a = 9.932(2) \text{ \AA}$	$\alpha = 90.00^\circ$
	$b = 19.091(2) \text{ \AA}$	$\beta = 100.376(2)^\circ$
	$c = 18.937(2) \text{ \AA}$	$\gamma = 90.00^\circ$
Volume	3532.0(8) Å ³	
Z	4	
Density (calculated)	1.134 Mg/m ³	
Absorption coefficient	0.460 mm ⁻¹	
F(000)	1340	
Crystal size	0.205 × 0.20 × 0.20 mm ³	
θ range for data collection	1.53° to 25.00°	
Index ranges	-11 ≤ h ≤ 11, -22 ≤ k ≤ 22, -22 ≤ l ≤ 22	
Reflections collected	56173	
Independent reflections	6227 [R _{int} = 0.0784]	
Completeness to $\theta = 28.28^\circ$	99.9%	
Absorption correction	Empirical SADABS	
Max. and min. transmission	0.9136 and 0.8936	
Refinement method	Full-matrix least-squared on F^2	
Data / restraints/ parameters	6227 / 0 / 376	
^a Goodness-of-fit on F^2	1.023	
^{b,c} Final R indices [I > 2σ(I)]	$R_1 = 0.0377$, $wR_2 = 0.0811$	
^{b,c} R indices (all data)	$R_1 = 0.0568$, $wR_2 = 0.0904$	
Largest diff. peak and hole	0.386 and -0.308 e/Å ⁻³	

^a GOF = $(\sum w(F_o^2 - F_c^2)^2 / (n - p))^{1/2}$ where n is the number of data and p is the number of parameters refined.

^b $R_1 = \sum ||F_o - |F_c|| / \sum |F_o|$

^c $wR_2 = \left(\frac{\sum (w(F_o^2 - F_c^2)^2)}{\sum (w(F_o^2)^2)} \right)^{1/2}$

Table 4.7. Crystallographic data and structural refinement parameters for Fe(ditox)₃(OH)Li(THF)₃ (**4.7**).

Identification code	compd_7_Fe(ditox) ₃ (OH)Li(THF) ₃	
Empirical formula	C ₅₂ H ₁₁₂ O ₁₀ LiFe	
Formula weight	1882.32 g/mol	
Temperature	-173(2) °C	
Wavelength	0.70173 Å	
Crystal system	Triclinic	
Space group	<i>P</i> -1	
Unit cell dimensions	<i>a</i> = 11.990(5) Å	<i>α</i> = 119.693(9)°
	<i>b</i> = 17.034(5) Å	<i>β</i> = 90.078(6)°
	<i>c</i> = 17.077(6) Å	<i>γ</i> = 90.019(5)°
Volume	3029 (2) Å ³	
Z	1	
Density (calculated)	1.053 Mg/m ³	
Absorption coefficient	0.296 mm ⁻¹	
F(000)	1066	
Crystal size	0.30 × 0.25 × 0.25 mm ³	
<i>θ</i> range for data collection	2.18 to 23.50°	
Index ranges	-12 ≤ <i>h</i> ≤ 12, -18 ≤ <i>k</i> ≤ 18, -18 ≤ <i>l</i> ≤ 18	
Reflections collected	29984	
Independent reflections	7909 [<i>R</i> _{int} = 0.0638]	
Completeness to <i>θ</i> = 28.28°	99.8%	
Absorption correction	Empirical SADABS	
Max. and min. transmission	0.9297 and 0.9164	
Refinement method	Full-matrix least-squared on <i>F</i> ²	
Data / restraints/ parameters	7909 / 537 / 616	
^a Goodness-of-fit on <i>F</i> ²	1.039	
^{b,c} Final R indices [<i>I</i> > 2σ(<i>I</i>)]	<i>R</i> ₁ = 0.1042, <i>wR</i> ₂ = 0.2708	
^{b,c} R indices (all data)	<i>R</i> ₁ = 0.1325, <i>wR</i> ₂ = 0.2876	
Largest diff. peak and hole	1.020 and -0.626 e/Å ⁻³	

^a GOF = $(\sum w(F_o^2 - F_c^2)^2 / (n - p))^{1/2}$ where *n* is the number of data and *p* is the number of parameters refined.

^b $R_1 = \sum ||F_o - |F_c|| / \sum |F_o|$

$${}^c wR_2 = \left(\frac{\sum (w(F_o^2 - F_c^2)^2)}{\sum (w(F_o^2)^2)} \right)^{1/2}$$

Table 4.8. Crystallographic data and structural refinement parameters for Fe(ditox)₃(OH)Li(THF)₂ (4.7a).

Identification code	cmpd_7a_Fe(ditox)3(OH)Li(THF)2	
Empirical formula	C ₃₈ H ₈₀ O ₆ LiFe	
Formula weight	695.81 g/mol	
Temperature	-173(2) °C	
Wavelength	0.70173 Å	
Crystal system	Triclinic	
Space group	<i>P</i> -1	
Unit cell dimensions	<i>a</i> = 12.1070(5) Å	<i>α</i> = 87.035(1)°
	<i>b</i> = 12.5462(5) Å	<i>β</i> = 70.968(1)°
	<i>c</i> = 16.0073(7) Å	<i>γ</i> = 62.728(1)°
Volume	2029.2(2) Å ³	
<i>Z</i>	2	
Density (calculated)	1.139 Mg/m ³	
Absorption coefficient	0.411 mm ⁻¹	
F(000)	770	
Crystal size	0.30 × 0.25 × 0.15 mm ³	
<i>θ</i> range for data collection	1.84° to 27.56°	
Index ranges	-15 ≤ <i>h</i> ≤ 15, -16 ≤ <i>k</i> ≤ 16, -20 ≤ <i>l</i> ≤ 20	
Reflections collected	40543	
Independent reflections	9361 [<i>R</i> _{int} = 0.0532]	
Completeness to <i>θ</i> = 28.28°	99.8%	
Absorption correction	Empirical SADABS	
Max. and min. transmission	0.9409 and 0.8865	
Refinement method	Full-matrix least-squared on <i>F</i> ²	
Data / restraints/ parameters	9361 / 1 / 520	
^a Goodness-of-fit on <i>F</i> ²	1.016	
^{b,c} Final <i>R</i> indices [<i>I</i> > 2σ(<i>I</i>)]	<i>R</i> ₁ = 0.0402, <i>wR</i> ₂ = 0.0905	
^{b,c} <i>R</i> indices (all data)	<i>R</i> ₁ = 0.0587, <i>wR</i> ₂ = 0.0998	
Largest diff. peak and hole	0.736 and -0.384 e/Å ⁻³	

^a GOF = $(\sum w(F_o^2 - F_c^2)^2 / (n - p))^{1/2}$ where *n* is the number of data and *p* is the number of parameters refined.

$$^b R_1 = \sum ||F_o - |F_c|| / \sum |F_o|$$

$$^c wR_2 = \left(\frac{\sum (w(F_o^2 - F_c^2)^2)}{\sum (w(F_o^2)^2)} \right)^{1/2}$$

Table 4.9. Crystallographic data and structural refinement parameters for [Fe(ditox)₃(OH)Li]₂ (**4.7b**).

Identification code	compd_7b_Fe(ditox) ₃ (OH)Li_dimer	
Empirical formula	C ₃₀ H ₆₄ O ₄ LiFe	
Formula weight	551.60 g/mol	
Temperature	-173(2) °C	
Wavelength	0.70173 Å	
Crystal system	Triclinic	
Space group	<i>P</i> -1	
Unit cell dimensions	<i>a</i> = 11.145(2) Å	<i>α</i> = 69.484(2)°
	<i>b</i> = 11.463(2) Å	<i>β</i> = 81.278(3)°
	<i>c</i> = 15.124(2) Å	<i>γ</i> = 63.207(2)°
Volume	1615.3(4) Å ³	
Z	2	
Density (calculated)	1.134 Mg/m ³	
Absorption coefficient	0.496 mm ⁻¹	
F(000)	610	
Crystal size	0.15 × 0.15 × 0.10 mm ³	
<i>θ</i> range for data collection	2.05° to 26.41°	
Index ranges	-13 ≤ <i>h</i> ≤ 13, -14 ≤ <i>k</i> ≤ 14, -18 ≤ <i>l</i> ≤ 18	
Reflections collected	28943	
Independent reflections	6601 [<i>R</i> _{int} = 0.1006]	
Completeness to <i>θ</i> = 28.28°	99.4%	
Absorption correction	Empirical SADABS	
Max. and min. transmission	0.9521 and 0.9293	
Refinement method	Full-matrix least-squared on <i>F</i> ²	
Data / restraints/ parameters	6601 / 0 / 350	
^a Goodness-of-fit on <i>F</i> ²	1.123	
^{b,c} Final R indices [<i>I</i> > 2σ(<i>I</i>)]	<i>R</i> ₁ = 0.0886, <i>wR</i> ₂ = 0.1245	
^{b,c} R indices (all data)	<i>R</i> ₁ = 0.1245, <i>wR</i> ₂ = 0.3000	
Largest diff. peak and hole	2.035 and -0.469 e/Å ⁻³	

^a GOF = $(\sum w(F_o^2 - F_c^2)^2 / (n - p))^{1/2}$ where *n* is the number of data and *p* is the number of parameters refined.

^b $R_1 = \sum ||F_o - |F_c|| / \sum |F_o|$

^c $wR_2 = \left(\frac{\sum (w(F_o^2 - F_c^2)^2)}{\sum (w(F_o^2)^2)} \right)^{1/2}$

Table 4.10. Crystallographic data and structural refinement parameters for Fe(ditox)₃(OH)Li(THF)₂ (4.8).

Identification code	cmpd_8_Fe(ditox) ₃ (OH)Li(THF) ₂	
Empirical formula	C ₃₈ H ₇₈ O ₆ LiFe	
Formula weight	693.79 g/mol	
Temperature	-173(2) °C	
Wavelength	0.70173 Å	
Crystal system	Triclinic	
Space group	<i>P</i> -1	
Unit cell dimensions	<i>a</i> = 12.082(1) Å	<i>α</i> = 89.912(1)°
	<i>b</i> = 12.592(1) Å	<i>β</i> = 70.503(1)°
	<i>c</i> = 15.886(2) Å	<i>γ</i> = 64.822(1)°
Volume	2032.0(2) Å ³	
<i>Z</i>	2	
Density (calculated)	1.134 Mg/m ³	
Absorption coefficient	0.411 mm ⁻¹	
F(000)	766	
Crystal size	0.30 × 0.25 × 0.20 mm ³	
<i>θ</i> range for data collection	1.38° to 27.44°	
Index ranges	-15 ≤ <i>h</i> ≤ 15, -16 ≤ <i>k</i> ≤ 16, -20 ≤ <i>l</i> ≤ 20	
Reflections collected	39884	
Independent reflections	9250 [<i>R</i> _{int} = 0.0357]	
Completeness to <i>θ</i> = 28.28°	99.6%	
Absorption correction	Empirical SADABS	
Max. and min. transmission	0.9224 and 0.8867	
Refinement method	Full-matrix least-squared on <i>F</i> ²	
Data / restraints/ parameters	9250 / 0 / 576	
^a Goodness-of-fit on <i>F</i> ²	1.022	
^{b,c} Final <i>R</i> indices [<i>I</i> > 2σ(<i>I</i>)]	<i>R</i> ₁ = 0.0660, <i>wR</i> ₂ = 0.1831	
^{b,c} <i>R</i> indices (all data)	<i>R</i> ₁ = 0.0766, <i>wR</i> ₂ = 0.1947	
Largest diff. peak and hole	1.637 and -0.896 e/Å ⁻³	

^a GOF = $(\sum w(F_o^2 - F_c^2)^2 / (n - p))^{1/2}$ where *n* is the number of data and *p* is the number of parameters refined.

$$^b R_1 = \sum ||F_o - |F_c|| / \sum |F_o|$$

$$^c wR_2 = \left(\frac{\sum (w(F_o^2 - F_c^2))^2}{\sum (w(F_o^2))^2} \right)^{1/2}$$

Table 4.11. Crystallographic data and structural refinement parameters for [Fe(ditox)₃(OH)][K(15C5)₂] (4.9).

Identification code	cmpd_9_Fe(ditox)3(OH)_K(15C5)2	
Empirical formula	C ₅₀ H ₁₀₃ O ₁₃ KFe	
Formula weight	1007.27 g/mol	
Temperature	-173(2) °C	
Wavelength	0.70173 Å	
Crystal system	Triclinic	
Space group	<i>P</i> -1	
Unit cell dimensions	<i>a</i> = 11.414(1) Å	<i>α</i> = 99.317(1)°
	<i>b</i> = 16.199(1) Å	<i>β</i> = 90.255(1)°
	<i>c</i> = 17.684(1) Å	<i>γ</i> = 109.732(1)°
Volume	3031.1(3) Å ³	
Z	2	
Density (calculated)	1.170 Mg/m ³	
Absorption coefficient	0.392 mm ⁻¹	
F(000)	2208	
Crystal size	0.20 × 0.20 × 0.20 mm ³	
<i>θ</i> range for data collection	1.17° to 26.37°	
Index ranges	-14 ≤ <i>h</i> ≤ 14, -20 ≤ <i>k</i> ≤ 20, -22 ≤ <i>l</i> ≤ 22	
Reflections collected	55329	
Independent reflections	12406 [<i>R</i> _{int} = 0.0457]	
Completeness to <i>θ</i> = 28.28°	99.9%	
Absorption correction	Empirical SADABS	
Max. and min. transmission	0.9257 and 0.9257	
Refinement method	Full-matrix least-squared on <i>F</i> ²	
Data / restraints/ parameters	12406 / 2015 / 1069	
^a Goodness-of-fit on <i>F</i> ²	0.993	
^{b,c} Final R indices [<i>I</i> > 2σ(<i>I</i>)]	<i>R</i> ₁ = 0.0472, <i>wR</i> ₂ = 0.1143	
^{b,c} R indices (all data)	<i>R</i> ₁ = 0.0664, <i>wR</i> ₂ = 0.1264	
Largest diff. peak and hole	0.886 and -0.569 e/Å ⁻³	

^a GOF = $(\sum w(F_o^2 - F_c^2)^2 / (n - p))^{1/2}$ where *n* is the number of data and *p* is the number of parameters refined.

^b $R_1 = \sum ||F_o - |F_c|| / \sum |F_o|$

$$^c wR_2 = \left(\frac{\sum (w(F_o^2 - F_c^2)^2)}{\sum (w(F_o^2)^2)} \right)^{1/2}$$

Table 4.12. Crystallographic data and structural refinement parameters for [Fe(ditox)₃(CH₂CN)][K(15C5)₂] (4.10).

Identification code	cmpd_10_Fe(ditox)3(CH2CN)_K(15C5)2	
Empirical formula	C ₅₂ H ₁₀₅ O ₁₃ NFeK	
Formula weight	1047.32 g/mol	
Temperature	-173(2) °C	
Wavelength	0.70173 Å	
Crystal system	Monoclinic	
Space group	P2 ₁ /n	
Unit cell dimensions	$a = 20.214(1) \text{ \AA}$	$\alpha = 90.00^\circ$
	$b = 15.117(1) \text{ \AA}$	$\beta = 113.692(1)^\circ$
	$c = 20.883(1) \text{ \AA}$	$\gamma = 90.00^\circ$
Volume	5843.4(5) Å ³	
Z	4	
Density (calculated)	1.190 Mg/m ³	
Absorption coefficient	0.386 mm ⁻¹	
F(000)	2292	
Crystal size	0.40 × 0.20 × 0.20 mm ³	
θ range for data collection	1.81° to 25.35°	
Index ranges	-24 ≤ h ≤ 17, -17 ≤ k ≤ 13, -1 ≤ l ≤ 27	
Reflections collected	10200	
Independent reflections	6337 [R _{int} = 0.0557]	
Completeness to $\theta = 28.28^\circ$	99.9%	
Absorption correction	Empirical SADABS	
Max. and min. transmission	0.9257 and 0.9257	
Refinement method	Full-matrix least-squared on F^2	
Data / restraints/ parameters	6337 / 608 / 634	
^a Goodness-of-fit on F^2	0.987	
^{b,c} Final R indices [I > 2σ(I)]	$R_1 = 0.0393$, $wR_2 = 0.0997$	
^{b,c} R indices (all data)	$R_1 = 0.0557$, $wR_2 = 0.1073$	
Largest diff. peak and hole	0.369 and -0.22 e/Å ⁻³	

^a GOF = $(\sum w(F_o^2 - F_c^2)^2 / (n - p))^{1/2}$ where n is the number of data and p is the number of parameters refined.

^b $R_1 = \sum ||F_o - |F_c|| / \sum |F_o|$

^c $wR_2 = \left(\frac{\sum (w(F_o^2 - F_c^2)^2)}{\sum (w(F_o^2)^2)} \right)^{1/2}$

Table 4.13. Cartesian coordinates for the DFT optimized geometry for the S = 2 model of $[\text{Fe}(\text{O}^i\text{Bu})_3(\text{O})]^-$ (**4.B**).

	x	y	z
Fe	0.04100300	-0.02635100	-0.11964000
O	1.79138600	-0.14121900	-0.73783000
O	-0.86947100	-1.57301300	-0.64334000
C	-1.08578500	2.76685700	-0.09430500
C	3.01514500	-0.49251600	-0.10279700
C	-1.96856100	-2.27645600	-0.08832100
O	-0.84732700	1.50099000	-0.70017100
O	0.10841700	0.06229100	1.51312300
C	-1.54776600	-2.91970400	1.25951900
H	-2.38297800	-3.45710200	1.73577700
H	-0.72207100	-3.62413000	1.09096100
H	-1.18904900	-2.13245300	1.93367000
C	-2.36145600	-3.37988600	-1.10645500
H	-1.49472100	-4.02660400	-1.29577100
H	-3.19660600	-3.99775400	-0.74077400
H	-2.65153100	-2.91579100	-2.05852700
C	-3.16952100	-1.31887700	0.13490200
H	-2.89257000	-0.54376400	0.85910100
H	-3.42323000	-0.82118700	-0.81000100
H	-4.05484200	-1.85701600	0.50901700
C	2.87751000	-1.86466100	0.61010100
H	2.09141900	-1.79955900	1.37133500
H	2.58179300	-2.63073600	-0.11892300
H	3.82101100	-2.17006200	1.08997300
C	4.08707700	-0.58266900	-1.21971200
H	4.16015000	0.38259300	-1.73798900
H	5.07646100	-0.84774600	-0.81550800
H	3.78620100	-1.34081000	-1.95457100
C	3.40514600	0.60120100	0.92628600
H	4.35290900	0.36563500	1.43582100
H	3.50686300	1.56895000	0.41649400
H	2.60481600	0.68811600	1.67032100
C	-2.10446400	2.61097800	1.06584000
H	-3.05290900	2.21630800	0.67652900
H	-1.70515300	1.89602800	1.79459100
H	-2.29875600	3.57111800	1.56884700
C	-1.67240600	3.68238500	-1.20049000
H	-1.92175900	4.68247400	-0.81238100

H	-0.94519800	3.78770700	-2.01637800
H	-2.58047800	3.22313000	-1.61262200
C	0.24004600	3.36759000	0.44319400
H	0.96532900	3.44986400	-0.37671200
H	0.08594100	4.36403900	0.88671400
H	0.65904300	2.69601200	1.20082800

4.10 References

- (1) Sono, M., Roach, M. P., Coulter, E. D., and Dawson, J. H. *Chem. Rev.* **1996**, *96*, 2841.
- (2) Meunier, B., de Visser, S. P., and Shaik, S. *Chem. Rev.* **2004**, *104*, 3947.
- (3) Peloquin, J. M., Campbell, K. A., Randall, D. W., Evanchik, M. A., Pecoraro, V. L., Armstrong, W. H., and Britt, R. D. *J. Am. Chem. Soc.* **2000**, *122*, 10926.
- (4) McEvoy, J. P., and Brudvig, G. W. *Chem. Rev.* **2006**, *106*, 4455.
- (5) Sun, C.-L.; Li, B.-J.; Shi, Z.-J. *Chem. Rev.* **2011**, *111*, 1293.
- (6) Holm, R. H. *Chem. Rev.* **1987**, *87*, 1401.
- (7) Nam, W. *Acc. Chem. Res.* **2007**, *40*, 522.
- (8) Que, L., Jr. *Acc. Chem. Res.* **2007**, *40*, 493.
- (9) Rohde, J.-U.; In, J.-H.; Lim, M. H.; Brennessel, W. W.; Bukowski, M. R.; Stubna, A.; Münck, E.; Nam, W.; Que, L., Jr. *Science* **2003**, *299*, 1037.
- (10) Lim, M. H.; Rohde, J.-U.; Stubna, A.; Bukowski, M. R.; Costas, M.; Ho, R. Y. N.; Münck, E.; Nam, W.; Que, L., Jr. *Proc. Natl. Acad. Sci. U.S.A.* **2003**, *100*, 3665.
- (11) Grapperhaus, C. A.; Mienert, B.; Bill, E.; Weyhermüller, T.; Wieghardt, K. *Inorg. Chem.* **2000**, *39*, 5306.
- (12) Klinker, E. J.; Kaizer, J.; Brennessel, W. W.; Woodrum, N. L.; Cramer, C. J.; Que, L., Jr. *Angew. Chem. Int. Ed.* **2005**, *44*, 3690.
- (13) de Visser, S. P.; Oh, K.; H, A.-R.; Nam, W. *Inorg. Chem.* **2007**, *46*, 4632.
- (14) Hong, S.; Lee, Y.-M.; Cho, K.-B.; Sundaravel, K.; Cho, J.; Kim, M. J.; Shin, W.; Nam, W. *J. Am. Chem. Soc.* **2011**, *133*, 11876.
- (15) Harman, W. H.; Chang, C. J. *J. Am. Chem. Soc.* **2007**, *129*, 15128.
- (16) Lacy, D. C.; Gupta, R.; Stone, K. L.; Greaves, J.; Ziller, Joseph W.; Hendrich, M. P.; Borovik, A. S. *J. Am. Chem. Soc.* **2010**, *132*, 12188.
- (17) England, J.; Martinho, M.; Farquhar, E. R.; Frisch, J. R.; Bominaar, E. L.; Münck, E.; Que, L., Jr. *Angew. Chem. Int. Ed.* **2009**, *48*, 3622.
- (18) Bigi, J. P.; Harman, W. H.; Lassalle-Kaiser, B.; Robles, D. M.; Stich, T. A.; Yano, J.; Britt, R. D.; Chang, C. J. *J. Am. Chem. Soc.* **2012**, *134*, 1536.
- (19) Rohde, J.-U.; Stubna, A.; Bominaar, E. L.; Münck, E.; Nam, W.; Que Jr., L. *Inorg. Chem.* **2006**, *45*, 6435.

- (20) Seo, M. S.; Kim, N. H.; Cho, K. B.; So, J. E.; Park, S. K.; Clémancey, M.; Garcia-Serres, R.; Latour, J.-M.; Shaik, S.; Nam, W. *Chem. Sci.* **2011**, *2*, 1039.
- (21) Ye, W.; Ho, D. M.; Friedle, S.; Palluccio, T. D.; Rybak-Akimova, E. V. *Inorg. Chem.* **2012**, *51*, 5006.
- (22) Hirao, H.; Kumar, D.; Que, L., Jr.; Shaik, S. *J. Am. Chem. Soc.* **2006**, *128*, 8590.
- (23) Janardanan, D.; Wang, Y.; Schyman, P.; Que, L., Jr.; Shaik, S. *Angew. Chem. Int. Ed.* **2010**, *49*, 3342.
- (24) England, J.; Guo, Y.; Farquhar, E. R.; Young, V. G.; Münck, E.; Que, L., Jr. *J. Am. Chem. Soc.* **2010**, *132*, 8635.
- (25) England, J.; Guo, Y.; Van Heuvelen, K. M.; Cranswick, M. A.; Rohde, G. T.; Bominaar, E. L.; Münck, E.; Que, L., Jr. *J. Am. Chem. Soc.* **2011**, *133*, 11880.
- (26) Gupta, R.; Lacy, D. C.; Bominaar, E. L.; Borovik, A. S.; Hendrich, M. P. *J. Am. Chem. Soc.* **2012**, *134*, 9775.
- (27) Betley, T. A.; Wu, Q.; Van Voorhis, T.; Nocera, D. G. *Inorg. Chem.* **2008**, *47*, 1849.
- (28) Nocera, D. G. *Inorg. Chem.* **2009**, *48*, 10001.
- (29) Groysman, S.; Villagrán, D.; Nocera, D. G. *Inorg. Chem.* **2010**, *49*, 10759.
- (30) Wolczanski, P. T. *Polyhedron* **1995**, *14*, 3335.
- (31) Murray, B. D.; Power, P. P. *J. Am. Chem. Soc.* **1984**, *106*, 7011.
- (32) Ertem, M. Z.; Cramer, C. J. *Dalton Trans.* **2012**, *41*, 12213.
- (33) Wada, T.; Ohtsu, H.; Tanaka, K. *Chem. Eur. J.* **2012**, *18*, 2374.
- (34) Wang, L.-P.; Van Voorhis, T. *J. Phys. Chem. Lett.* **2011**, *2*, 2200.
- (35) Mayer, J. M. *Acc. Chem. Res.* **1998**, *31*, 441.
- (36) Yin, G. *Coord. Chem. Rev.* **2010**, *254*, 1826.
- (37) Bakac, A. *J. Am. Chem. Soc.* **2000**, *122*, 1092.
- (38) Yin, G.; Danby, A. M.; Kitko, D.; Carter, J. D.; Scheper, W. M.; Busch, D. H. *J. Am. Chem. Soc.* **2008**, *130*, 16245.
- (39) Dogutan, D. K.; McGuire, R. Jr.; Nocera, D. G. *J. Am. Chem. Soc.* **2011**, *133*, 9178.
- (40) Hong, S.; Gupta, A. K.; Tolman, W. B. *Inorg. Chem.* **2009**, *49*, 6323.
- (41) Caron, A.; Palenik, G. J.; Goldish, E.; Donohue, J. *Acta Cryst.* **1964**, *17*, 102.

- (42) Jin, S.; Nieuwenhuyzen, M.; Robinson, W. T.; Wilkins C. J. *Acta Cryst..C: Cryst. Struct. Commun.* **1992**, *48*, 274
- (43) Naarmann, H.; Beaujean, M.; Merényi, R.; Viehe, H. G. *Polym. Bull.* **1980**, *2*, 363
- (44) Brown, S. H.; Crabtree, R. H. *J. Am. Chem. Soc.* **1989**, *111*, 2935.
- (45) Cai, X.; Majumdar, S.; Fortman, G. C.; Frutos, L. M.; Temprado, M; Clough, C. R.; Cummins, C. C.; Germain, M. E.; Palluccio, T.; Rybak-Akimova, E .V.; Captain, B.; Hoff, C. D. *Inorg. Chem.* **2011**, *50* 9620.
- (46) Neese, F. *J. Inorg Biochem.* **2006**, *100*, 716.
- (47) Thiessen, P. A.; Koerner, O. *Z. anorg. Chem.* **1929**, *180*, 65.
- (48) Bradley, D. C.; Mehrotra, R. C.; Rothwell, I. P.; Singh, A. *Alkoxo and Aryloxo Derivatives of Metals*; Academic Press: London, 2001.
- (49) Cantalupo, S. A.; Lum, J. S.; Buzzeo, M. C.; Moore, C.; DiPasquale, A. G.; Rheingold, A. L.; Doerrler, L. H. *Dalton Trans.* **2010**, *39*, 374.
- (50) Boyle, T. J.; Ottley, L. A. M.; Apblett, C. A.; Stewart, C. A.; Hoppe, S. M.; Hawthorne, K. L.; Rodriguez, M. A. *Inorg. Chem.* **2011**, *50*, 6174.
- (51) Zdilla, M. J.; Abu-Omar, M. M. *Inorg. Chem.* **2008**, *47*, 10718.
- (52) Hodgkiss, J. M., Rosenthal, J. and Nocera, D. G. (2007) The Relation between Hydrogen Atom Transfer and Proton-coupled Electron Transfer in Model Systems, in *Hydrogen-Transfer Reactions* (eds J. T. Hynes, J. P. Klinman, H.-H. Limbach and R. L. Schowen), Wiley-VCH Verlag GmbH & Co. KGaA, Weinheim, Germany.
- (53) Roelfes, G.; Lubben, M.; Hage, R.; Que Jr., L.; Feringa, B. L. *Chem. Eur. J.* **2000**, *6*, 2152.
- (54) Hirao, H.; Que Jr., L; Nam, W.; Shaik, S. *Chem. Eur. J.* **2008**, *14*, 1740.
- (55) Decker, A.; Rhode, J. U.; Que Jr., L.; Solomon, E. I. *J. Am. Chem. Soc.* **2004**, *126*, 5378.
- (56) Kaizer, J.; Klinker, E. J.; Oh, N. Y.; Rhode, J. U.; Songm, W. J.; Stubna, A.; Kim, J.; Munck E.; Nam, W.; Que Jr., L. *J. Am. Chem. Soc.* **2004**, *126*, 472.
- (57) Bryant, J. R.; Mayer, J. M. *J. Am. Chem. Soc.* **2003**, *125*, 10351.
- (58) Bryant, J. R.; Matsuo, T.; Mayer, J. M. *Inorg. Chem.* **2004**, *43*, 1587.
- (59) Smith, J. M.; Mayberry, D. E.; Margarit, C. G.; Sutter, J.; Wang, H.;Meyer, K.; Bontchev, R. P. *J. Am. Chem. Soc.* **2012**, *134*, 6516.
- (60) McDonald, A. R.; Que Jr., L. *Coord. Chem. Rev.* **2013**, *257*, 414.

- (61) Mehrotra, R. C. *Inorganica Chimica Acta, Reviews*, **1967**, *1*, 99.
- (62) Power, P. P. *J. of Organomet. Chem.*, **2004**, *689*, 3904.
- (63) Evans, D. F. *J. Chem. Soc.* **1959**, 2003.
- (64) Napolitano, E.; Giovani, E.; Ceccarelli, N.; Pelosi, P. *J. Agric. Food Chem.* **1996**, *44*, 2806.
- (65) (a) Becke, A. D. *Phys. Rev. A* **1988**, *38*, 3098. (b) Becke, A. D. *J. Chem. Phys.* **1993**, *98*, 1372. (c) Becke, A. D. *J. Chem Phys.* **1993**, *98*, 5648.
- (66) Lee, C.; Yang, W.; Parr, R. G. *Phys Rev. B* **1988**, *37*, 785.
- (67) Gaussian 03, Revision C.02, Frisch, M. J.; Trucks, G. W.; Schlegel, H. B.; Scuseria, G. E.; Robb, M. A.; Cheeseman, J. R.; Montgomery, Jr., J. A.; Vreven, T.; Kudin, K. N.; Burant, J. C.; Millam, J. M.; Iyengar, S. S.; Tomasi, J.; Barone, V.; Mennucci, B.; Cossi, M.; Scalmani, G.; Rega, N.; Petersson, G. A.; Nakatsuji, H.; Hada, M.; Ehara, M.; Toyota, K.; Fukuda, R.; Hasegawa, J.; Ishida, M.; Nakajima, T.; Honda, Y.; Kitao, O.; Nakai, H.; Klene, M.; Li, X.; Knox, J. E.; Hratchian, H. P.; Cross, J. B.; Bakken, V.; Adamo, C.; Jaramillo, J.; Gomperts, R.; Stratmann, R. E.; Yazyev, O.; Austin, A. J.; Cammi, R.; Pomelli, C.; Ochterski, J. W.; Ayala, P. Y.; Morokuma, K.; Voth, G. A.; Salvador, P.; Dannenberg, J. J.; Zakrzewski, V. G.; Dapprich, S.; Daniels, A. D.; Strain, M. C.; Farkas, O.; Malick, D. K.; Rabuck, A. D.; Raghavachari, K.; Foresman, J. B.; Ortiz, J. V.; Cui, Q.; Baboul, A. G.; Clifford, S.; Cioslowski, J.; Stefanov, B. B.; Liu, G.; Liashenko, A.; Piskorz, P.; Komaromi, I.; Martin, R. L.; Fox, D. J.; Keith, T.; Al-Laham, M. A.; Peng, C. Y.; Nanayakkara, A.; Challacombe, M.; Gill, P. M. W.; Johnson, B.; Chen, W.; Wong, M. W.; Gonzalez, C.; and Pople, J. A.; Gaussian, Inc., Wallingford CT, 2004.
- (68) (a) Wadt, W. R.; Hay, P. J. *J. Chem Phys.* **1985**, *82*, 284. (b) Hay P. J.; Wadt, W. R. *J. Chem. Phys.* **1985**, *82*, 299.
- (69) (a) Dunning, T. H., Jr. *J. Chem. Phys.* **1989**, *90*, 1007. (b) Dunning, T. H.; Hay, P. J. *In Modern Theoretical Chemistry. 3. Methods of Electronic Structure Theory*; Schaefer, H. F., III, Ed.; Plenum Press: New York, 1977. (c) Woon, D. E.; Dunning, T. H. *J. Chem. Phys.* **1993**, *98*, 1358.

CHAPTER 5

HX Splitting Mediated by Rh–Rh Bimetallic Complexes

5.1 Introduction

The basic issues regarding the science of renewable energy conversion and storage have made the subject of molecular inorganic chemistry an imperative. Previous chapters have addressed the use of homogeneous metal oxo complexes to fundamentally interrogate the manner in which the electronic environment of the metal oxo moiety imparts reactivity with relevance to water splitting. This chapter will investigate issues relevant to HX (HX = hydrohalic acid) splitting. Like water splitting, the 2 electron 2 proton process of the conversion of 2 equiv of HX into H₂ and X₂ is endergonic as well and stores a comparable amount of energy per electron as compared to water splitting (Table 5.1).^{1,2} The mechanistically less complicated 2-electron 2-proton process of HX splitting affords the opportunity to begin addressing issues beyond the fundamental nature of the transformation and instead move towards issues involved in molecular system design and integration. This chapter will focus on the molecular chemistry associated with direct light energy to energy storage via molecular photocatalysts for HX splitting.

Table 5.1. Gibbs Free Energy for HX splitting reactions (X=F, OH, Cl, Br, I).

	Reaction	ΔG_f° (kcal/mol)
2HF _(g)	—————> H _{2(g)} + F _{2(g)}	130.5
H ₂ O _(g)	—————> H _{2(g)} + 1/2O _{2(g)}	54.6
2HCl _(g)	—————> H _{2(g)} + Cl _{2(g)}	45.5
2HBr _(g)	—————> H _{2(g)} + Br _{2(l)}	25.5
2HI _(g)	—————> H _{2(g)} + I _{2(s)}	-0.4

Sunlight is of carbon-neutral energy that is large enough to meet the future global energy demands.³⁻⁷ However, the intermittency in the availability of the sunlight fosters the need for chemical storage, and direct photogeneration of fuels via HX splitting is a promising avenue for achieving cost-effective solar energy storage with high energy density and scalability.⁸ In a photocatalytic cycle for HX splitting, there are three main steps to consider: (i) HX oxidation addition(s) with metal complexes, (ii) H₂ liberation either by thermally or photochemically induced protonolysis or reductive elimination, and (iii) X₂ photoelimination to regenerate the starting catalytic species. This generalized photocatalytic cycle is shown in Scheme 5.1.

Previous efforts in the Nocera group have focused on mixed valent bimetallic catalysts as two-electron mixed-valent catalysts as the M–M bond that is conserved across the d^0-d^0 , d^1-d^1 ,

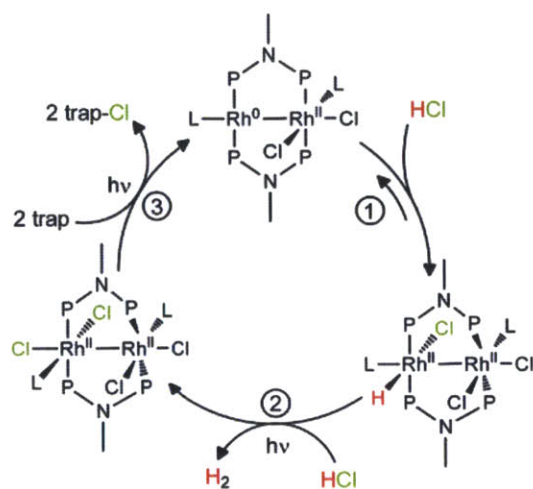
d^7-d^7 oxidation series have been proposed to act as a chromophore to drive both H_2 - and X_2 -forming reactions.⁹⁻¹² Initial reports for first generation catalysts for H_2 photogeneration were successful, however the stability of the catalyst was low and halogen traps were needed in the system to facilitate the halogen elimination reaction. Further work has been dedicated to optimizing the X_2 photoelimination step,¹³⁻¹⁷ which limited the efficiencies of the first-generation catalysts.^{9,18} This chapter will address photocatalytic HCl splitting by a new mixed-valent dirhodium architecture.^{19,20} Rational ligand design has been shown to significantly enhance catalyst performance. Additionally, kinetic studies and DFT calculations have provided key insights into a catalytically competent intermediate for the X_2 photoelimination reaction.

5.2 Photocatalytic Hydrogen Evolution from $Rh_2(tfepma)_2(CN^tBu)_2Cl_2$

The class of compounds studied is mixed valent dirhodium bimetallic complexes with the general formula $Rh_2^{0,II}(tfepma)_2(L)_2Cl_2$, where two *tfepma* ligands bridge the two rhodium centers (*tfepma* = $CH_3N[P(OCH_2CF_3)_2]_2$). “L” is a neutral capping ligand, which is CN^tBu for the previously reported complex **5.1**, $Rh_2^{0,II}(tfepma)_2(CN^tBu)_2Cl_2$.¹⁹ Complex **5.1** is prepared by the room temperature reaction of $[Rh^I(COD)Cl]_2$ (COD = 1,5-cyclooctadiene) with 2 equiv of *tfepma* and CN^tBu . **5.1** has been previously characterized by the $^{31}P\{^1H\}$ NMR spectrum (20 °C, CD_2Cl_2) which shows two distinct signals at 124.4 ppm and 145.1 ppm, indicative of a coordination asymmetry as a result of the two-electron mixed valence core.¹⁹ Furthermore, **5.1** has been structurally characterized confirming the two electron mixed valency as well as a Rh–Rh bond, as the internuclear distance between the rhodium centers was found to be 2.680 Å.¹⁹

An open coordination site on the Rh^0 center has been shown to allow for oxidative addition of HX and thus access to and interrogation of the products of oxidation addition.^{19,20} Compound **5.1** was found to undergo reversible oxidative addition of HCl to form a mixture of two isomeric hydrido-halide species, $Rh_2^{II,II}(tfepma)_2(CN^tBu)_2Cl_3H$ (**5.2**). Additionally, oxidation of **5.1** by Cl_2 or $PhICl_2$ afforded the two-electron oxidized congener $Rh_2^{II,II}(tfepma)_2(CN^tBu)_2Cl_4$ (**5.3**), which has been shown to photoeliminate Cl_2 in the presence of a trap. Both **5.2** and **5.3** have been similarly characterized to **5.1** as being two electron mixed valent with a formal Rh–Rh bond.

Scheme 5.1



Since complex **5.1** had demonstrably promoted two key steps of an HX splitting photocatalysts (HX oxidative addition and regeneration from X_2 photoelimination) we sought to identify conditions under which the hydrido complex **5.2** could liberate H_2 , thus allowed the photocycle shown in Scheme 5.1. To be closed. Whereas anaerobic solutions of hydride complex **5.2** are indefinitely stable to HCl in the dark, irradiation with white light ($\lambda_{\text{exc}} > 296 \text{ nm}$) results in photoconversion as depicted in step (ii) of Scheme 5.1. The reaction progress is readily monitored by NMR (^{31}P and ^1H) and UV-vis absorption spectroscopy. After 3 h of photolysis in CD_2Cl_2 , the ^{31}P NMR spectrum clearly shows the formation of the $\text{Rh}_2^{\text{II,II}}\text{Cl}_4$ product **5.3** (multiplet at 112 ppm) and after 21 h the ^1H NMR spectrum indicates the formation of H_2 as evidenced by a sharp singlet at 4.60 ppm. The observation of H_2 , and not HD or D_2 , demonstrates that the hydrogen originates from HCl and not from solvent decomposition.

The UV-vis absorption spectra (Figure 5.3, left) confirms the build-up of **5.3** followed by a period of minimal spectral evolution, where hydrogen production, HCl oxidative addition and Cl_2 elimination appear to be occurring at comparable rates. After more than an hour of photolysis at concentrations appropriate for UV-vis measurements (ca. $25 \mu\text{M}$ of **5.2**), degradation of the complex is evidenced by the diminishing absorption features in the 300-400 nm range (Figure 5.1, right), as well as the growth of featureless absorption further into the UV region. GC measurements of the overhead gases confirm H_2 as the exclusive gaseous products under these conditions.

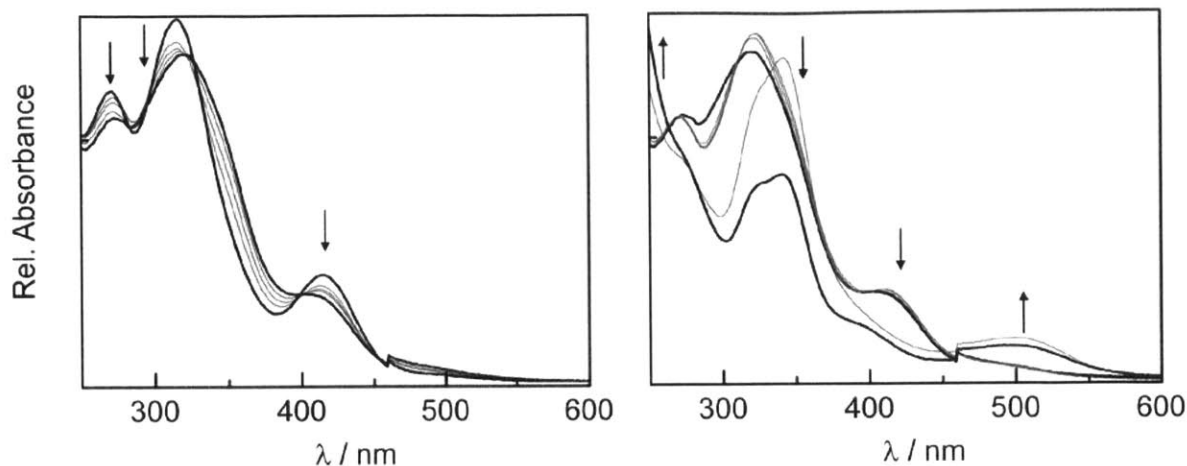


Figure 5.1. UV-vis traces of a photoysis experiment monitoring the progression of the absorption feature of a solution of **5.1** with excess HCl under photolytic conditions. **(Left)** The early time points (0, 0.5, 1, 2, and 4 min) show the apparent buildup of product with isosbestic points at 323, 401 and 451 nm. **(Right)** The longer time points (4, 6, 8, 10, 88, 200 min) show an initial steady state regime between 6-10 min followed by degradation.

The catalytic activity of **5.1** was interrogated by measurement of the amount of hydrogen production as a function of time, with photolytic conditions analogous to those described above. Figure 5.2 depicts the turnover number (TON) of the catalyst as a function of the irradiation time. The production of hydrogen is comparatively rapid during the first 12 h, with 2 TON during this period, highlighting the catalytic nature of the reaction. The activity diminished during the next 12 h and ceased after about 36 h. A precipitate was observed after as little as 6 h of photolysis, providing further evidence for catalysts degradation under these conditions.

The capping ligand, CN^tBu, was suspected to be the cause of degradation. Decomposition reactions of bound isocyanides have been extensively studied on electron-rich late transition metals, such as Pd(II).²¹⁻²³ Moreover, the ability of CN^tBu to lose the ^tBu cation is well established, providing yet another degradation pathway.²⁴ The nature of the decomposition observed here is unclear, but we reasoned that the straightforward substitution of CN^tBu for 1-adamantylisocyanide (CNAd), which provides enhanced steric protection for the reactive C–N triple bonded fragment and is incapable of planarizing to form a sp²-hybridized tertiary cation would enhance the catalyst's stability.

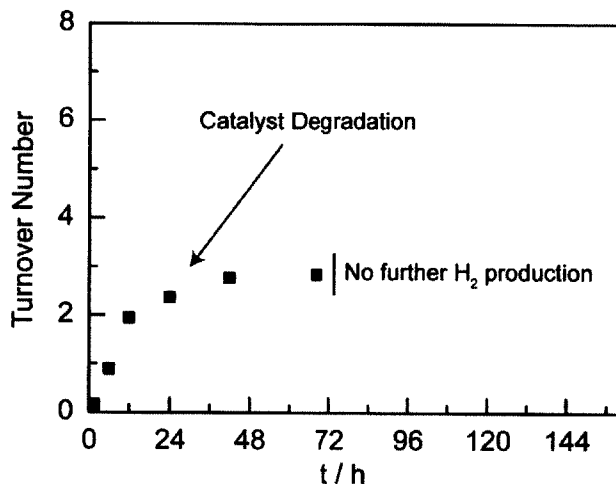


Figure 5.2. Turnover numbers (TON) of H_2 produced by 1 mM THF solution of $\text{Rh}_2^{0,\text{II}}(\text{tfepma})_2(\text{CN}^t\text{Bu})_2\text{Cl}_2$. Decomposition is observed with minimal additional hydrogen formation beyond 24 h.

5.3 Photocatalytic Hydrogen Evolution from $\text{Rh}_2(\text{tfepma})_2(\text{CNAd})_2\text{Cl}_2$

The synthesis of $\text{Rh}_2^{0,\text{II}}(\text{tfepma})_2(\text{CNAd})_2\text{Cl}_2$ (**5.4**) was analogous to that of **5.1** with the addition of two equiv of CNAd and tfepma to $[\text{Rh}(\text{COD})\text{Cl}]_2$ at room temperature. ^1H NMR experiments show that two isomers of the hydride product $\text{Rh}_2^{\text{II,II}}(\text{tfepma})_2(\text{CNAd})_2\text{Cl}_3\text{H}$ (**5.5**) are formed upon treatment with excess HCl, as judged from the ^1H NMR and $^3\text{P}\{^1\text{H}\}$ NMR spectra. Whereas treatment of **5.4** with PhICl_2 affords a mixture of isomeric oxidized products, aerobic oxidation of hydride complex **5.5** in the presence of HCl exclusively generates the valence symmetric, pseudo- C_{2h} symmetric product $\text{Rh}_2^{\text{II,II}}(\text{tfepma})_2(\text{CNAd})_2\text{Cl}_4$ (**5.6**), whose X-ray structure is depicted in Figure 5.3.A. The other isomer that is observed upon oxidation if PhICl_2 can be isolated by slow crystallization from toluene and is identified to be the valence asymmetric complex $\text{Rh}_2^{\text{I,III}}(\text{tfepma})_2(\text{CNAd})_2\text{Cl}_3$ (**5.7**). The X-ray structure of **5.7** is presented in Figure 5.3.B. As the valence symmetric complex **5.6** is the particular $\text{Rh}_2^{\text{II,II}}\text{Cl}_4$ isomer formed as an intermediate during photocatalytic H_2 production (*vide infra*), here we consider its photochemical profile.

Photolysis of a THF solution of **5.6** with $\lambda_{\text{exc}} > 305$ nm leads to chlorine elimination, with THF acting as a trap. The reaction proceeds cleanly, as determined by the UV-vis progression depicted in Figure 5.4. The final spectrum is identical to that of an authentic sample of $\text{Rh}_2^{0,\text{II}}$ complex **5.4**, and isosbestic points are maintained.

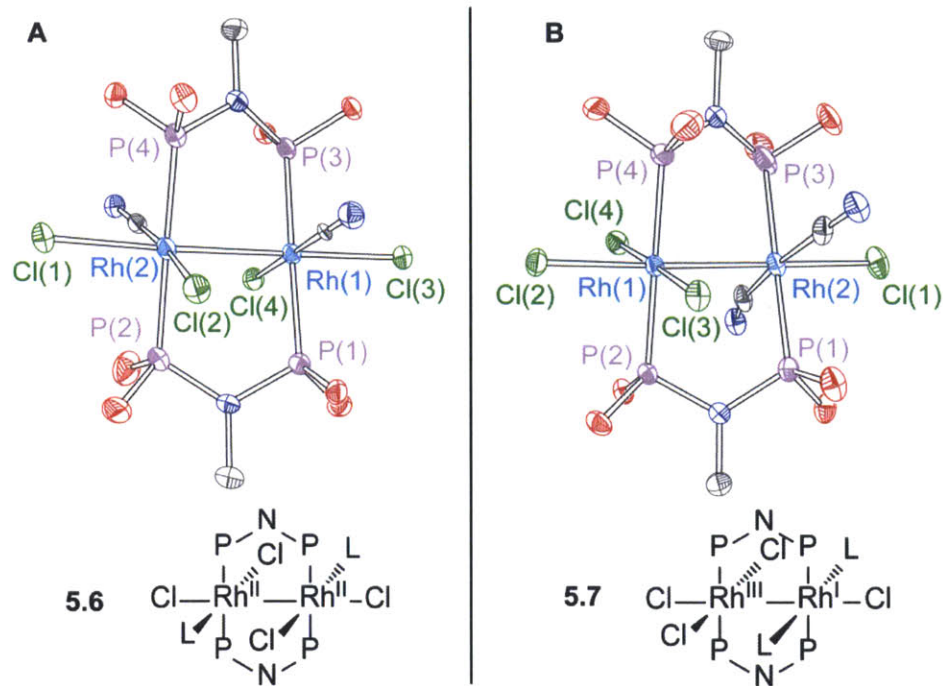


Figure 5.3. (A) X-ray structure of $\text{Rh}_2^{\text{II,II}}(\text{tfepma})_2(\text{CNad})\text{Cl}_4$, **5.6**. Thermal ellipsoids presented at 50% probability. Hydrogen atoms, the $-\text{CH}_2\text{CF}_3$, and the adamantyl groups are omitted for clarity. Selected bond distances: $\text{Rh}(1)-\text{Rh}(2) = 2.7137(4) \text{ \AA}$, $\text{Rh}(1)-\text{Cl}(3) = 2.3624(8) \text{ \AA}$, $\text{Rh}(1)-\text{Cl}(4) = 2.3519(9) \text{ \AA}$, $\text{Rh}(2)-\text{Cl}(1) = 2.486(1) \text{ \AA}$, $\text{Rh}(2)-\text{Cl}(2) = 2.4468(9) \text{ \AA}$. (B) X-ray structure of $\text{Rh}_2^{\text{I,III}}(\text{tfepma})_2(\text{CNad})\text{Cl}_4$, **5.7**. Thermal ellipsoids presented at 50% probability. Hydrogen atoms, the $-\text{CH}_2\text{CF}_3$, and the adamantyl groups are omitted for clarity. Selected bond distances: $\text{Rh}(1)-\text{Rh}(2) = 2.7137(4) \text{ \AA}$, $\text{Rh}(1)-\text{Cl}(2) = 2.4468(8) \text{ \AA}$, $\text{Rh}(1)-\text{Cl}(3) = 2.3624(8) \text{ \AA}$, $\text{Rh}(1)-\text{Cl}(4) = 2.3519(9) \text{ \AA}$, $\text{Rh}(2)-\text{Cl}(1) = 2.486(1) \text{ \AA}$.

Photolysis of **5.4** in the presence of excess acid with $\lambda_{\text{exc}} > 305 \text{ nm}$ in THF showed a behavior similar to that of **5.1** (Figure 5.1). The spectral evolution of the photolysis in the presence of acid is shown in Figure 5.5. Over the course of 10 min, the 325 nm band attributed to the hydride complex **5.5** decreases, while an increase in absorbance at 350 nm indicated the build-up of $\text{Rh}_2^{\text{II,II}}\text{Cl}_4$ complex **5.6**. After ca. 15 min the reaction reaches a steady state, with minimal ensuing spectral changes. Significantly, no signs of decomposition are observed after 120 min, in contradistinction to that observed for the CN^iBu -ligated system, where substantial decomposition is evident after 88 min. GC measurements of the headspace gasses showed H_2 as the only gaseous product.

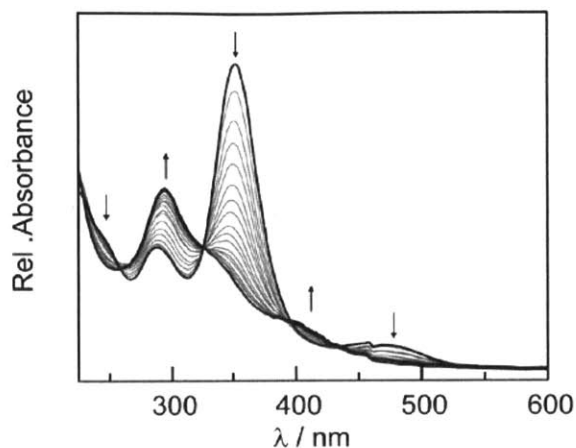


Figure 5.4. Spectral evolution of the photolysis of **5.6** (43 μM) in THF, using broad band light with $\lambda_{\text{exc}} > 305$ nm. Spectra were recorded every minute for a total of 20 min showing the conversion to **5.4**.

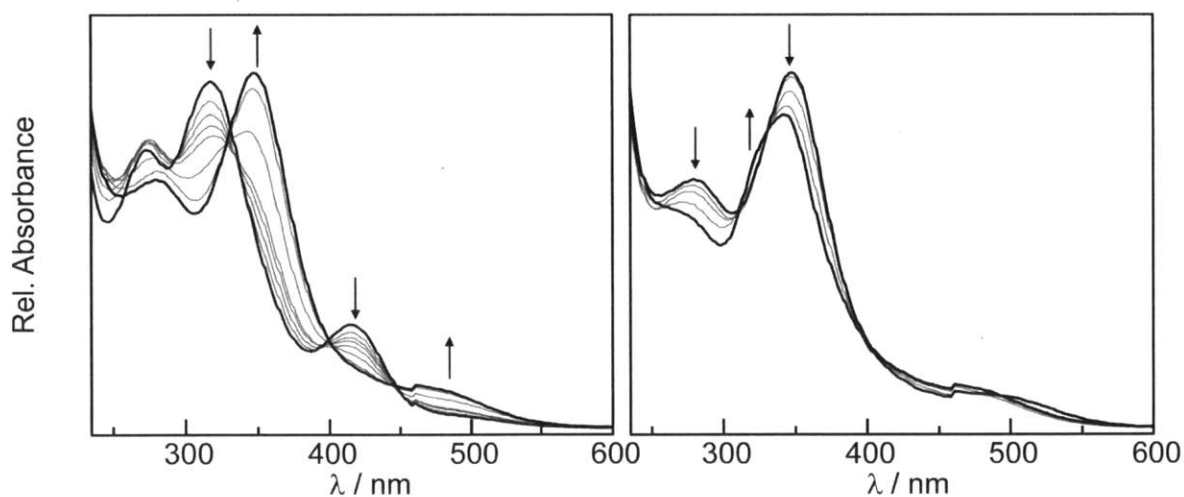


Figure 5.5. Spectral evolution for the photolysis of **5.5** in THF obtained after the addition of excess HCl to **5.4** (31 μM), using broad-band light with $\lambda_{\text{exc}} > 305$ nm. (Left) Early time points 0, 40, 60, 90 sec and 2, 5, 10 and 15 min showing the buildup of **5.6**. (Right) Late time points 15, 20, 30, 60 and 120 min showing minimal degradation of reaction mixture.

The amount of hydrogen production over time was measured by Toepler pump experiments, with the results for **5.4** shown in Figure 5.6. At early time points, **5.1** exhibits slightly higher activity, but at longer time points, **5.1** degrades and consequently **5.4** out produces **5.1**. H_2 photoreduction of **5.4** occurs at a steady rate for times exceeding 144 h.

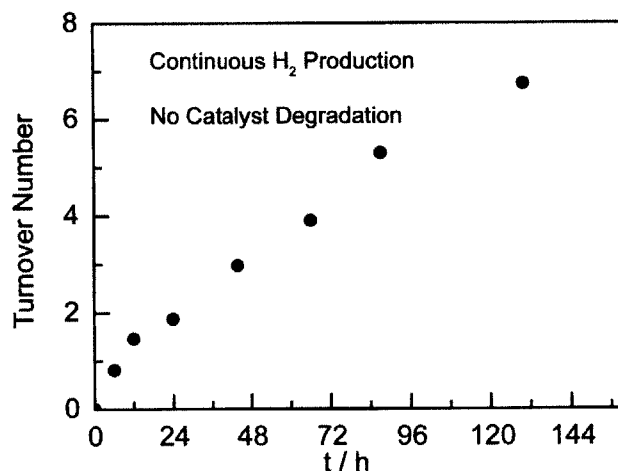


Figure 5.6. Turnover numbers (TON) for H₂ production by a 1 mM THF solution of Rh₂^{0,II}(tfepma)₂(CNAd)₂Cl₂, **5.4**, in photocatalytic conditions in the presence of excess HCl over time.

For the CNAd–ligated system, after *ca.* 1 equivalent of H₂ has been produced the rate of hydrogen production reaches a steady state. For $t = 6$ h, 0.81 equiv of H₂ have been produced, after which H₂ production monotonically and linearly increases, indicating that sustained H₂ production over long time scales with modest steady-state turnover frequency (TOF) of 1.3 per day. The data suggests that the chlorine photoelimination step, (iii) in Scheme 1 is turnover-limiting as observed in previous dirhodium photocatalysts. This step was previously measured to have a quantum yield of 0.63% for complex **5.3**, which corresponds roughly to one turnover per day under photocatalytic conditions described here. Consistent with turnover-limiting X₂ elimination, Rh₂^{II,II}Cl₄ complexes (**5.3** and **5.6**) build in concentration during photolysis (see Figure 5.2 and 5.6), and the first turnover of H₂ is noticeably faster.

As such, improved photocatalytic performance requires that X₂ elimination is facilitated without the detriment of H₂ production, a condition thus far not met in complexes that undergo efficient X₂ elimination. The challenge remains to develop a system where both H₂ evolution and X₂ elimination are comparatively favorable. Nonetheless, the isocyanide–ligated mixed valent dirhodium complexes (**5.1** and **5.4**) are competent HCl splitting photocatalysts. **5.1** exhibits minimal TON owing to catalyst degradation arising from reactivity of the CN^tBu capping ligand. This degradation is circumvented with the replacement of CN^tBu with CNAd. This simple ligand substitution greatly enhances the longer term photocatalyst performance; H₂ photoactivity of the CNAd–ligated system is observed to be indefinitely stable. This work highlights the need for robust capping ligands for use in catalytic HX splitting and identifies the capping ligand as a

likely source of catalyst instability in previous systems.⁹ Despite a low turnover frequency, **5.4** is found to be a competent photocatalyst for H₂ formation from HCl with highly reproducible catalyst performance. As such, the halogen photoelimination chemistry will be interrogated further.

5.4 X₂ Photoelimination from Rh₂(tfepma)₂(CNAd)₂Cl₄ Isomers

As X₂ photoelimination is found to be rate limiting in the HX splitting cycle for **5.4**, Rh₂^{0,II}(tfepma)₂(CNAd)₂Cl₂, insight into the nature of the X₂ photoelimination process could lead to system modifications resulting in more efficient photocatalytic performance. While developing the aforementioned dirhodium platforms for H₂ photogeneration, two oxidized dirhodium tetrachloride valence isomers were isolated: the valence symmetric Rh₂^{II,II}Cl₄ complex, **5.6**, and the two electron mixed valent Rh₂^{I,III}Cl₄ complex, **5.7**. The isolation of two oxidized valence isomers afford the opportunity to assess the efficiency in which X₂ elimination can occur from both isomers and determine the potential importance of the two-electron mixed valence state for X₂ photoelimination as both isomers are reduced under identical photolytic conditions.

Photolysis of a THF solution of valence asymmetric compound **5.7**, Rh₂^{I,III}Cl₄, which displays features at 329 nm and 379 nm, with a 1000 W Hg/Xe lamp ($\lambda > 295$ nm) resulted in the consumption of **5.7** and eventual formation of the reduced complex **5.4**, Rh₂^{0,II}(tfepma)₂(CNAd)₂Cl₂. The spectral evolution of this transformation can be seen in Figure 5.7.A. The lack of isosbestic points in the spectra obtained during photolysis of **5.7** indicated the evolution of a steady-state intermediate, which is assigned by ¹H and ³¹P NMR to be the valence symmetric complex **5.6** (Rh₂^{II,II}Cl₄) during the conversion of **5.7** to **5.4**.

Complex **5.7** displayed wavelength-selective photochemistry. Photolysis of **5.7** with a 380 nm long-pass filter used to selectively excite the lower energy absorption band of **5.7** ($\lambda_{\text{max}} = 379$ nm) resulted in exclusive isomerization of **5.7** to **5.6**. These results establish that photoreduction of **5.7** to **5.4** is driven by excitation into the 329 nm absorbance band whereas isomerization of **5.7** to **5.6** arises from excitation into the 379 nm absorption band. Independent photolysis of a THF solution of valence symmetric **5.6**, which displays an absorbance feature at 352 nm, afforded the photoreduction product **5.4**, (Rh₂^{0,II}Cl₄). The spectral evolution of the photolysis of **5.6** is

presented in Figure 5.8.A. Well-anchored isosbestic points are observed in UV-vis photolysis spectrum of **5.6**, excluding the evolution of a steady state intermediate.

With the knowledge of the molar absorptivities of complexes **5.4**, **5.6**, and **5.7**, the concentration of each of these species during photolysis was determined using least-squares spectral fitting of the UV-vis spectra. As shown in Figure 5.7.B, the concentration of **5.6**, $\text{Rh}_2^{\text{II,II}}\text{Cl}_4$, initially builds and subsequently decays during the photolysis of **5.7**, $\text{Rh}_2^{\text{I,III}}\text{Cl}_4$. Similar analysis was carried out on the photolysis of **5.6**, $\text{Rh}_2^{\text{II,II}}\text{Cl}_4$, and confirmed that no appreciable concentration of **5.7**, $\text{Rh}_2^{\text{I,III}}\text{Cl}_4$, complexes evolved with time (Figure 5.8.B). The observed photoreduction chemistry of both mixed valent **5.7** and valence symmetric **5.6** provided the first opportunity to experimentally probe the importance of mixed valency in halogen elimination from dirhodium complexes.

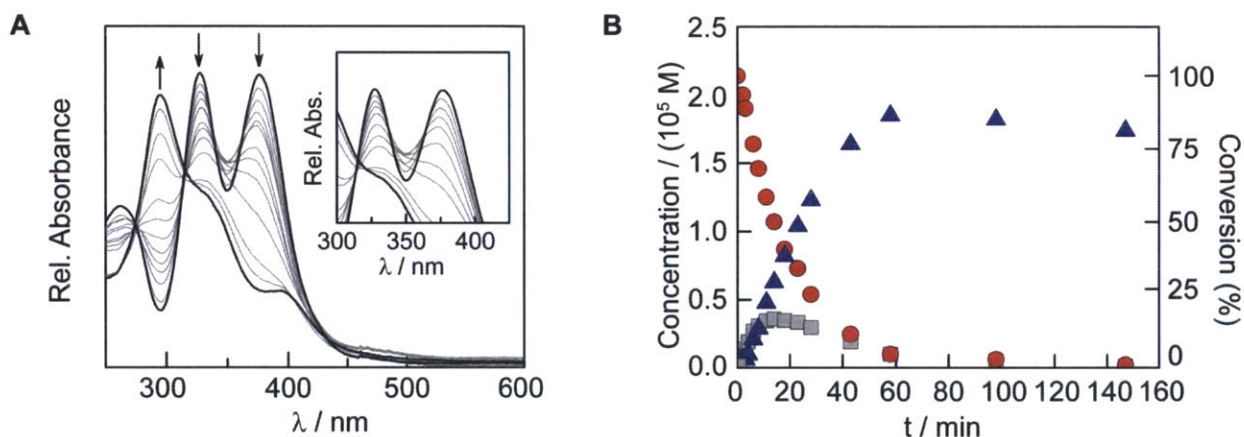


Figure 5.7. (A) Spectral evolution during photolysis of valence asymmetric $\text{Rh}_2^{\text{I,III}}\text{Cl}_4$ complex **5.7** in THF. Inset: Expanded spectrum to show that isosbestic points are not observed, consistent with evolution of a steady-state intermediate during the photolysis of **5.7**. (B) Concentration profiles of **5.7** (red circle), **5.6** (gray square) and **5.4** (blue triangle) during the photolysis of **5.7**.

In order to assess the relative efficiencies of halogen elimination from $\text{Rh}_2^{\text{I,III}}\text{Cl}_4$ complex **5.7** and $\text{Rh}_2^{\text{II,II}}\text{Cl}_4$ complex **5.6**, we determined the quantum yields for photoelimination from each of these complexes. Direct comparison of halogen elimination efficiencies was complicated by competing elimination and isomerization reactions in the photochemical manifold of **5.7**. At early times during the photolysis of $\text{Rh}_2^{\text{I,III}}\text{Cl}_4$ complex **5.7**, the observed quantum yield for the consumption of **5.7** ($\Phi_{320} = 0.36\%$), represents both photoreduction of **5.7** to **5.4**, as well of photoisomerization of **5.7** to **5.6**. The quantum yield of photoisomerization was determined by

evaluating the consumption of **5.7** during the period of photolysis in which the concentration of **5.6** is approximately constant (after approximately 20% of **5.7** has been consumed). In this pseudo-steady-state regime, the quantum efficiency of photoisomerization was determined to be 0.07%. By difference, the quantum efficiency of photoreduction of **5.7** was determined to be 0.29% and the quantum efficiency of halogen photoelimination from $\text{Rh}_2^{\text{II,II}}\text{Cl}_4$ complex **5.6** was determined to be 0.47%. Thus photoreduction of **5.6** is slightly more efficient than of **5.7**.

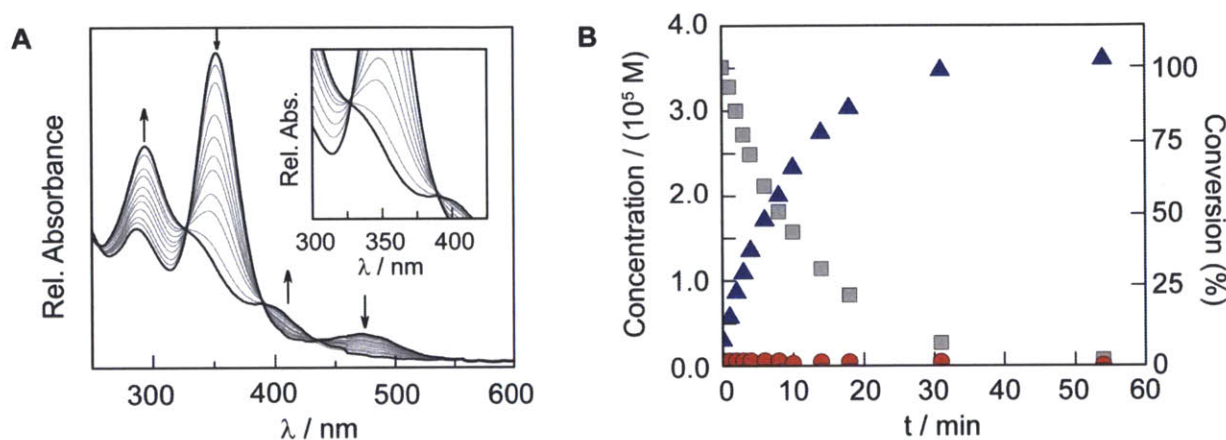
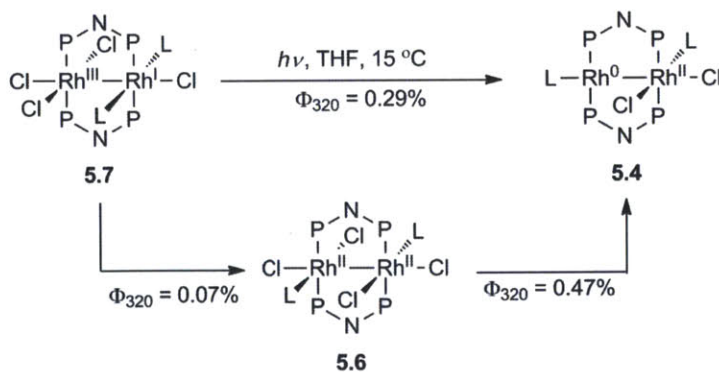


Figure 5.8. (A) Spectral evolution during photolysis of valence symmetric $\text{Rh}_2^{\text{II,II}}\text{Cl}_4$ complex **5.6** in THF. Inset: Expanded spectrum to show that isosbestic points are observed, precluding a steady-state intermediate. (B) Concentration profiles of **5.7** (red circle), **5.6** (gray square) and **5.4** (blue triangle) during the photolysis of **5.6**.

Scheme 5.2



Based on the similarity of the quantum yields for photoreduction of complexes **5.7** and **5.6**, respectively, we posited that a common intermediate may be accessed in the photochemical manifold of these complexes. To evaluate this contention, flash laser photolysis ($\lambda_{\text{exc}} = 355 \text{ nm}$) of complexes **5.7** and **5.6** was carried out and the transient absorption (TA) difference spectra

shown in Fig. 5.9 were obtained. The TA spectrum of **5.7** exhibits ground-state bleaches at 329 and 379 nm and a spectral growth at ~ 440 nm. The new spectral feature at ~ 440 nm is not an absorption feature of either **5.6** or **5.4** and thus represents a species that is not observed in the steady-state photolysis experiment. Flash laser photolysis of complex **5.6** revealed a TA spectrum with a ground-state bleach at ~ 350 nm and also a spectral growth at ~ 440 nm. Excepting a narrower line-shape for the absorbance feature of **5.7**, the transient absorption spectra of **5.7** and **5.6** are very similar for $\lambda_{\text{exc}} > 400$ nm. This narrowing of the 440 nm TA signal of **5.7** obviously is due to a superposition of a ground state bleach centered at ~ 460 nm with the spectral growth at ~ 440 nm. Owing to the similarities of the transient profiles of **5.7** and **5.6** at $\lambda > 400$ nm, we propose that photolysis of **5.7** and **5.6** affords a common intermediate.

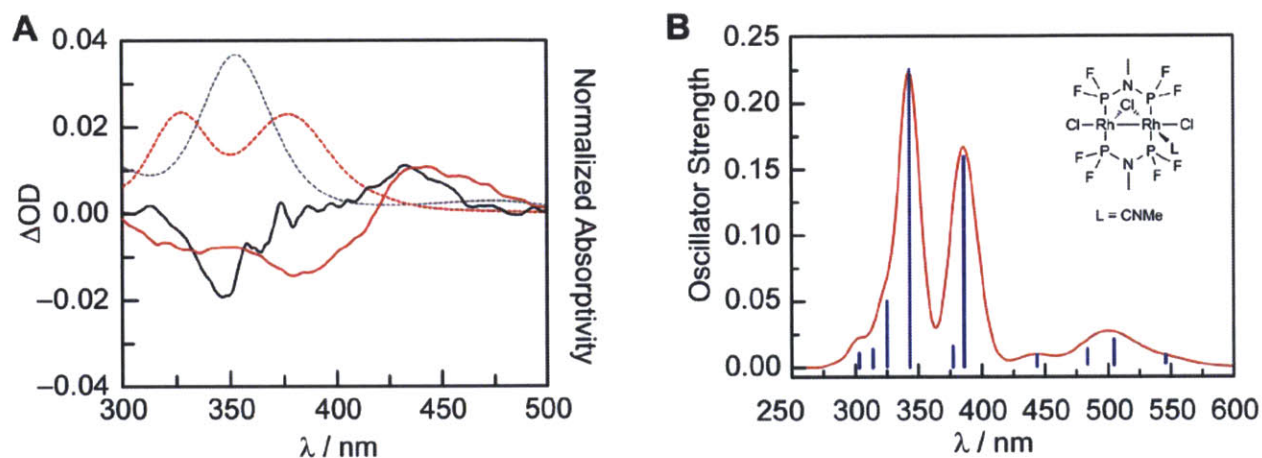


Figure 5.9 (A) Transient absorption spectra obtained by laser flash photolysis ($\lambda_{\text{exc}} = 355$ nm) of complexes **5.7** (solid red) and **5.6** (solid black), respectively. Spectra are normalized to the absorbance at ~ 440 nm. Normalized absorption spectra of **5.7** (dashed red) and **5.6** (dashed black) are also shown. (B) Relevant oscillators (solid blue bars) from TD-DFT calculations for **5.C**, $\text{Rh}_2(\text{dfpma})_2(\text{CNMe})\text{Cl}_3$ with simulated absorption spectrum overlaid (solid red line) showing absorption feature at low energy (500 nm).

To gain insight into the nature of the excited states of **5.7** and **5.6** that lead to the observed photochemical intermediates, time-dependent DFT (TD-DFT) calculations were performed with Gaussian 03²⁵ and the B3LYP functionals^{26,27} using model complexes $\text{Rh}^{\text{I,III}}(\text{dfpma})_2(\text{CNMe})_2\text{Cl}_4$ (**5.A**) and $\text{Rh}^{\text{II,II}}(\text{dfpma})_2(\text{CNMe})_2\text{Cl}_4$ (**5.B**) (Figure 5.10). In model structures **5.A** and **5.B**, the adamantyl isocyanide ligand was replaced with a methyl isocyanide and the bridging tfepma ligands were replaced with *bis*(difluorophosphinyl)methylamine (dfpma) ligands. Similar structural truncations have been validated in TD-DFT calculations of several heterobimetallic complexes.^{12,14,28} The optimized geometries and computed absorption spectra of

5.A and **5.B** reproduced both the metrical parameters and experimental absorption spectra of **5.7** and **5.6**, respectively. The calculated absorption spectra for **5.A** and **5.B** are shown in Figure 5.10. The two main absorption features found in **5.7** are replicated in the calculated spectra of **5.A**. Similarly, the one main absorption feature of **5.6** is replicated in the calculated spectra of **5.B**. Furthermore, the overall absorption of **5.B** is calculated to be more intense than that of **5.A**, which is experimentally found (**5.6** more intense than **5.7**).

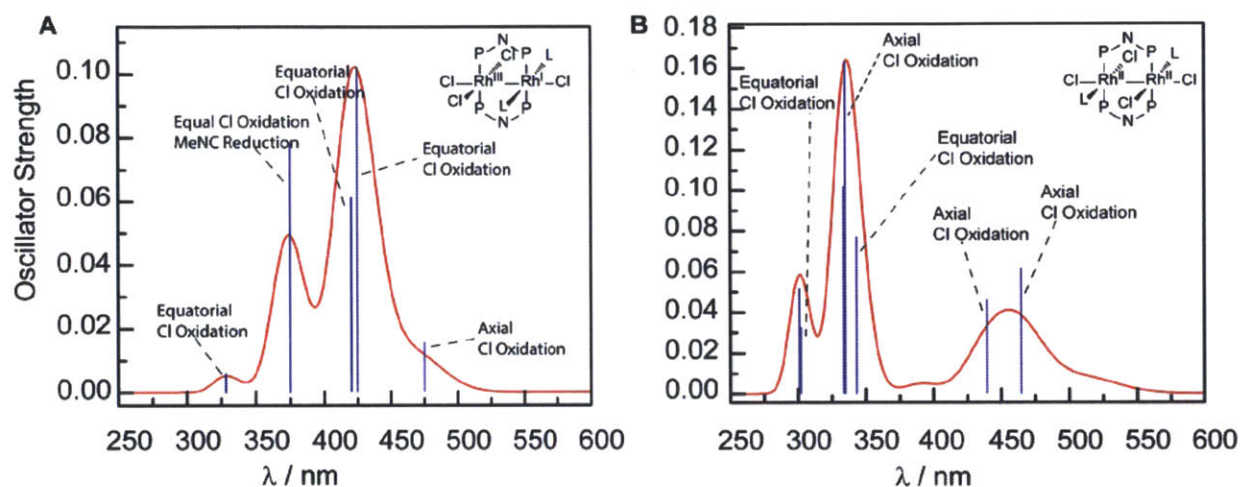


Figure 5.10. (A) Relevant oscillators (solid blue bars) from TD–DFT calculations for **5.A** with simulated absorption spectrum overlaid (solid red line). (B) Relevant oscillators (solid blue bars) from TD–DFT calculations for **5.B** with simulated absorption spectrum overlaid (solid red line).

The computed excited states of both structures **5.A** and **5.B** are dominated by ligand-to-metal charge transfer (LMCT) character (Figure 5.11). We have considered the strongest oscillator strength in the spectral absorbance envelop near 320 nm; evaluation of the orbital parentage of the major absorbance revealed that in both complexes, the LMCT excitations are primarily Cl (p) \rightarrow Rh (d) + dfpma (p) transitions. For $\text{Rh}_2^{\text{I,III}}\text{Cl}_4$ structure **5.A**, the transition is calculated to occur from a ground state orbital that is 30% Rh, 60% Cl, and 7% dfpma to an excited state orbital that is 40% Rh, 8% Cl, 36% dfpma. Similarly, valence symmetric $\text{Rh}_2^{\text{II,II}}\text{Cl}_4$ complex **5.B**, excitation results in a transition from a ground state orbital that is 20% Rh, 73% Cl, and 2% dfpma, to an excited state orbital that is 42% Rh, 15% Cl, and 30% dfpma. In contrast, analysis of the absorbance feature of **5.4** near $\lambda_{\text{max}} = 379$ nm, which results in

isomerization of **5.7** to **5.6** when excited, features transitions that reduce both the Rh(III) center and the Cl ligands.

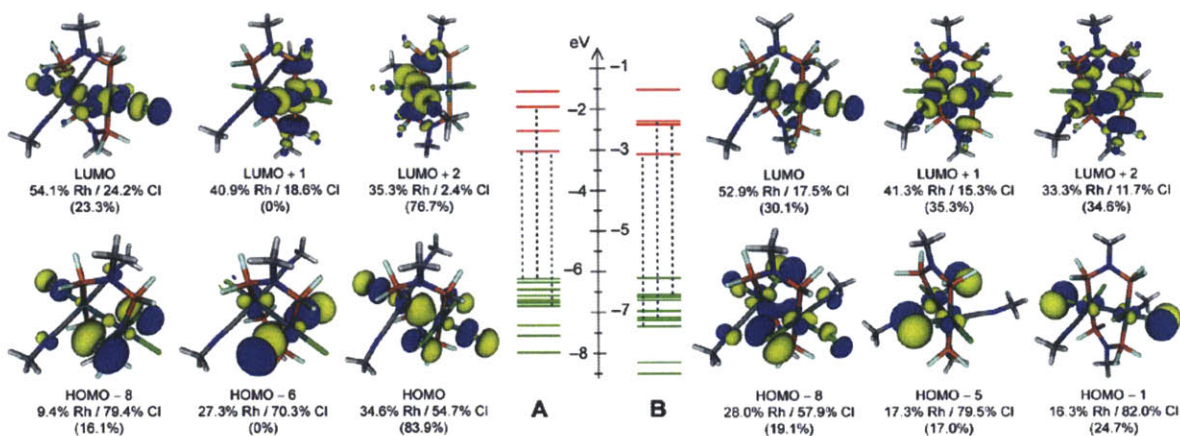
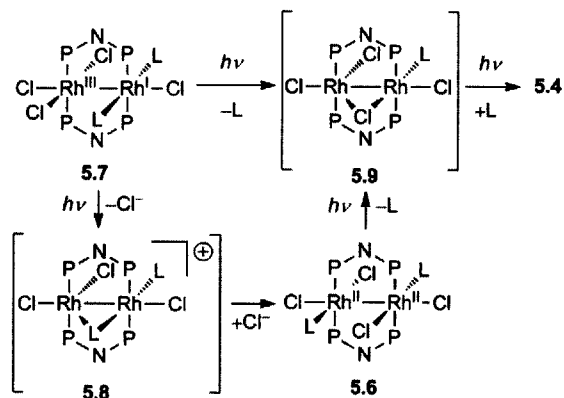


Figure 5.11. TD-DFT calculations of model structures **5.A** (A) and **5.B** (B) indicate LMCT excited state in both complexes. Contributions of Rh-based and Cl-based orbitals are given for each individual MO. Contributions of each MO to the overall electronic transformation are given within parentheses.

In analogy to the hydride-bridged transition states, which have been proposed for H_2 evolving reactions from diiridium complexes,^{4,12} we propose that the photointermediate in the TA spectrum is chloride-bridged structure **5.9** (Scheme 5.3). Accessing intermediate **5.9** from either mixed-valent complex **5.7** or valence-symmetric complex **5.6** could be accomplished by photochemically promoted dissociation of an isocyanide ligand. This ligand dissociation could proceed heterolytically, as shown in Scheme 5.3, or homolytically, to generate unsaturated intermediates reduced by one electron as compared with **5.4**. The TD-DFT calculations support this proposal. The computed excited states of both **5.A** and **5.B** are dissociative with respect to the Rh–isocyanide bond, which is consistent with loss of an isocyanide to generate the coordination site needed for a chloride-bridged structure. Additionally, the TD-DFT electronic absorption spectrum for a computed structural of a model compound for **5.9**, $Rh_2(dfpma)_2(CNMe)Cl_3$ (**5.C**) shows a low energy absorption feature similar to that observed in the TA experiments. Isomerization of **5.7** to **5.6** may be accomplished by a similar mechanism, in which dissociation of chloride, not isocyanide, would generate an open coordination site to accommodate a bridging isocyanide (i.e. intermediate **5.8**). Re-coordination of chloride to the formerly Rh(III) center would affect net isomerization. Such a proposal is supported by the observation that the lower energy excitation of **5.7**, which is dissociative with respect to the

Rh(III)–Cl bonds and thus could generate a vacant coordination site for a bridging isocyanide ligand, promotes isomerization of **5.7** to **5.6** (i.e. structure **5.8**).

Scheme 5.3



5.5 Cl₂ Photoelimination from Rh₂(tfepma)₂(CNAr)(μ-Cl)Cl₃ Complexes

In the mechanism outlined in Scheme 5.3, dirhodium complexes with bridging chloride and isocyanide ligands are the intermediates in chlorine elimination and isomerization, respectively. With interest in establishing that the proposed bridging-ligand geometries are accessible in phosphazane-supported dirhodium architectures, as well as directly interrogating the photochemistry of chloride-bridged dirhodium complexes, a new family of ligand-bridged dirhodium complexes was prepared (Figure 5.12 top). Treatment of [Rh^I(cod)Cl]₂ in THF with tfepma and either 4-fluorophenyl or 4-methoxyphenyl isocyanide resulted in the formation of isocyanide bridged complexes **5.10** and **5.11**, respectively. Complexes **5.10** and **5.11** do not react with excess isocyanide. Oxidation of Rh₂^ICl₂ complexes **5.10** and **5.11** with PhCl₂ afforded chloride-bridged structures **5.12** and **5.13**, respectively. Analysis of the IR spectra of **5.10** and **5.11** confirmed that the isocyanide ligand migrates from a bridging to terminal binding coordination position upon oxidation; the isocyanide stretching frequency in **5.10** (1736 cm⁻¹) moves to higher energy in **5.12** (2181 cm⁻¹). The structures of complexes **5.10–5.13** have all been established by single-crystal x-ray diffraction. Importantly, access to isolable models of proposed intermediate **5.9** allowed comparison of the absorption spectra of the model complexes with the absorption features observed in the TA spectra. In the absorption spectra of both **5.12** and **5.13**, an absorption feature centered at ~450 nm is observed, which is consistent with our assignment of intermediate **5.9** in the TA spectra as well as a TD-DFT calculation of th

truncated model **5.C**, $\text{Rh}_2(\text{dfpma})_2(\text{CNMe})(\mu\text{-Cl})\text{Cl}_2$, (dfpma = *bis*(difluorophosphinyl)-methylamine) (Figure 5.10.B).

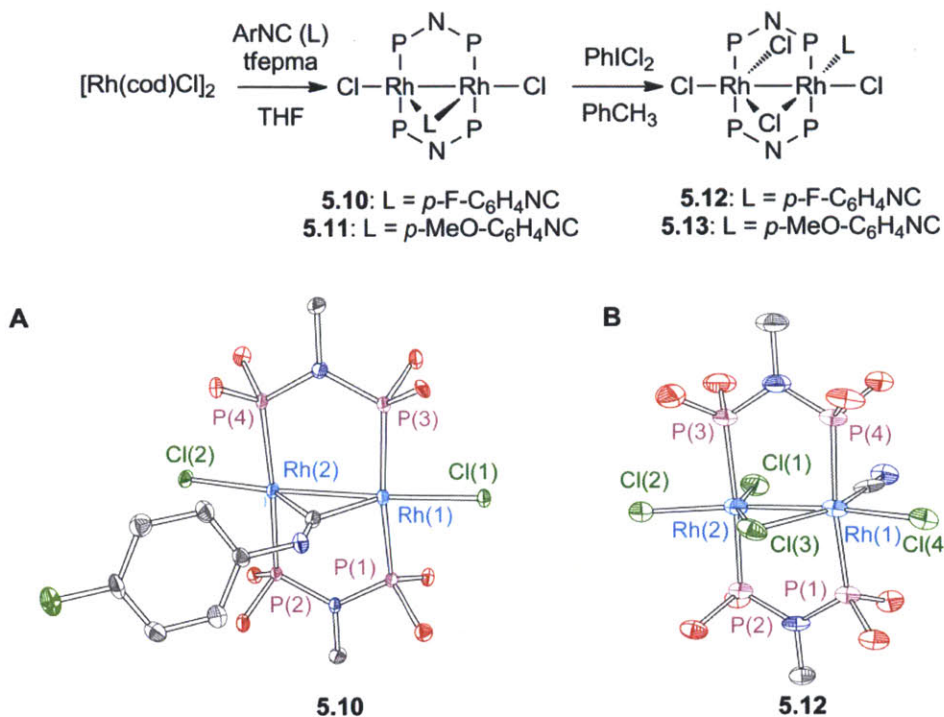


Figure 5.12. (Top) Synthesis of isocyanide-bridged (**5.10** and **5.11**) and chloride-bridged (**5.12** and **5.13**) dirhodium complexes, P–N–P = *bis*(trifluoroethoxy)phosphinyl)-methylamine (tfepma). (A) X-ray structure of $\text{Rh}_2^{\text{II}}(\text{tfepma})_2\mu_2\text{-}(\text{CN-}i>p\text{-F-C}_6\text{H}_4)\text{Cl}_2$, **5.10**. Thermal ellipsoids presented at 50% probability. Hydrogen atoms, and the $-\text{CH}_2\text{CF}_3$ groups are omitted for clarity. Selected bond distances: Rh(1)–Rh(2) = 2.6880(4) Å, Rh(1)–Cl(1) = 2.347(1) Å, Rh(2)–Cl(2) = 2.348(1) Å. (B) X-ray structure of $\text{Rh}_2^{\text{II}}(\text{tfepma})_2(\text{CN-}i>p\text{-F-C}_6\text{H}_4)(\mu_2\text{-Cl})\text{Cl}_3$, **5.12**. Thermal ellipsoids presented at 50% probability. Hydrogen atoms, the $-\text{CH}_2\text{CF}_3$, and the aryl groups are omitted for clarity. Selected bond distances: Rh(1)–Rh(2) = 2.6260(8) Å, Rh(1)–Cl(4) = 2.449(2) Å, Rh(1)–Cl(3) = 2.423(2) Å, Rh(2)–Cl(1) = 2.331(2) Å, Rh(2)–Cl(2) = 2.454(2) Å, Rh(3)–Cl(3) = 2.405(2) Å.

With chloride-bridged dirhodium complexes in hand, the photoreactivity of these species was investigated. Photolysis of a THF solution of chloride-bridged complex **5.12** effected photoreduction, yielding $\text{Rh}_2^{\text{II}}\text{Cl}_2$ complex **5.10** (Figure 5.13). During the observed photoreduction, the isocyanide ligand moved from a terminal binding mode to a bridging geometry, which may be responsible for the ability to observe photoreduction products in the absence of exogenous stabilizing ligands. We note that no reduction was observed upon thermolysis of complex **5.12** at 80 °C in the dark. The observation of a photochemically, but not thermally, promoted reduction of **5.12** suggests that photoreduction of complexes **5.7** and **5.6**

proceeds by two sequential photochemical reactions, the first of which generates chloride-bridged intermediate **5.9** from which photoelimination proceeds.

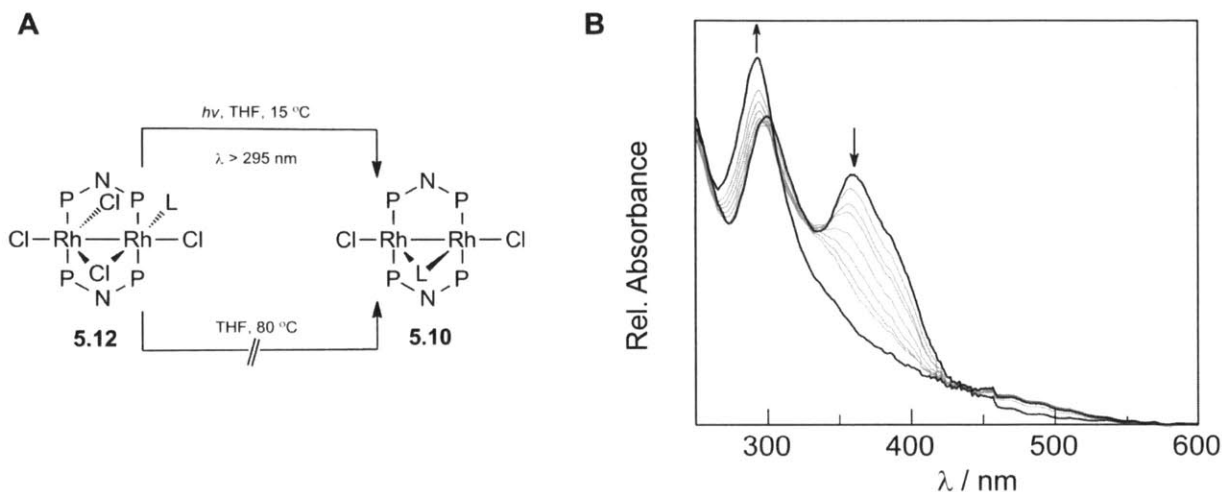


Figure 5.13. (A) Chloride-bridged dirhodium complex **5.12** undergoes photochemical, but not thermal, chlorine elimination to afford $\text{Rh}_2^{\text{II}}\text{Cl}_2$ complex **5.10**. (B) Spectral evolution during photolysis of chloride-bridged complex **5.12**.

5.6 Concluding Remarks

Coordinationally unsaturated dirhodium complexes **5.1** and **5.4** have been shown to be competent hydrogen evolving photocatalysts. Through the ligand modification of CN^tBu (**5.1**) to CNAd (**5.4**) the stability of the photocatalyst greatly improved. This identifies the nature of the capping ligand as the cause of the instability in **5.1**. Furthermore, the stability of **5.4** with the CNAd capping ligand suggests that the Rh -phosphazane-halogen core of the molecules is intrinsically stable under operating conditions. The turnover frequency remains low (1 turnover/day) but the stability appears indefinite.

Regarding halogen photoelimination, formal chlorine photoelimination occurs from both mixed-valent $\text{Rh}_2^{\text{I,III}}\text{Cl}_4$ complex **5.7** and valence-symmetric $\text{Rh}_2^{\text{II,II}}\text{Cl}_4$ complex **5.6** with similar efficiencies. Transient absorption studies suggest that the photochemistry of **5.7** and **5.6** proceed through a common intermediate, which propose to be chloride-bridged structure **5.9**. The presence of a common intermediate (i.e. **5.9**) in the photochemical manifold of both complex **5.6** as well as **5.7** implies that the observed differences in photoreduction efficiency between complexes **5.6** and **5.7** is due to the differing efficiencies associated with accessing **5.9**, and not

to the halogen elimination reaction itself. The observation of photochemically, but not thermally, promoted reduction of isolated models of intermediate **5.9** (i.e. chloride-bridged complex **5.12**) suggests that overall photoreduction of **5.7** and **5.6** proceeds by two sequential photochemical steps: ligand dissociation followed by halogen elimination. New HX-splitting photocatalysts, in which photochemically promoted ligand dissociation is not prerequisite for halogen elimination, may be more efficient because photoreduction would require one, not two, photochemical events. We therefore postulate that the highest photoelimination quantum efficiencies will be achieved for complexes that can directly assume a halide-bridged structure.

5.7 Experimental Details and Computational Methods

5.7.1 General Considerations. All reactions were carried out in an N₂-filled glovebox. Anhydrous solvents were obtained by filtration through drying columns.²⁹ NMR spectra were recorded at the MIT Department of Chemistry Instrument Facility (DCIF) on a Varian Mercury 300 MHz spectrometer, operating at 300 MHz for ¹H acquisitions and at 121.5 MHz for ³¹P acquisitions. NMR chemical shifts are reported in ppm with the residual solvent resonance as internal standard. ³¹P NMR chemical shifts were referenced to an external 85% D₃PO₄ standard. IR spectra were recorded on a Perkin Elmer Spectrum 400 FT-IR/FT-FIR spectrometer outfitted with a Pike Technologies GladiATR attenuated total reflectance accessory with a monolithic diamond stage and pressure clamp. Samples were suspended in Nujol[®] for all IR measurements. UV-vis spectra were recorded at 293 K in quartz cuvettes on a Spectral Instruments 400 series diode array and were blanked against the appropriate solvent. Photochemical reactions were performed using a 1000 W high-pressure Hg/Xe arc lamp (Oriel) and the beam was passed through a water-jacketed filter holder containing the appropriate long-pass filter, an iris and a collimating lens. [Rh(cod)Cl]₂ was obtained from Strem Chemicals and used without purification. HCl (4M dioxane solution) and ^tBuNC were purchased from Sigma Aldrich and used without purification. Isotopically labeled solvent *d*₈-THF and CD₂Cl₂ were purchased from Cambridge Isotopes and stored over 4Å sieves. Phosphazane ligand tfepma³⁰ and AdNC³¹ were prepared as described in the literature. Complexes **5.1**, **5.2** and **5.3** were prepared according to procedures we have previously reported.

5.7.2 Preparation of Rh₂^{0,II}(tfepma)₂(CNAd)₂Cl₂ (5.4**).** To a saturated CH₂Cl₂ solution of [Rh^I(COD)Cl]₂ (157 mg, 0.318 mmol) was added tfepma (309.6 mg, 0.6356 mmol, 1.999 equiv) to effect an immediate color change from yellow to dark brown/yellow. Addition of AdNC (102.5 mg, 0.6357 mmol, 1.999 equiv) in CH₂Cl₂ afforded a red solution that faded to orange over the course of 5 min. The solution was allowed to stir for 10 h during which time an orange solid formed. The mixture was concentrated to dryness, suspended in a mixture of 1 mL CH₂Cl₂/15 mL hexanes and allowed to settle. The supernatant was removed and the solid dried under vacuum to yield 452 mg (90.6% yield) of Rh₂(tfepma)₂(CNAd)₂Cl₂ as a yellow powder. ¹H NMR (300 MHz, CH₂Cl₂) δ/ppm: 4.40-5.09 (br, m, 16H), 2.87 (pseudoquintet, 6H), 2.10 (br, m, 6H), 1.96 (br, m, 6H), 1.90 (br, m, 6H), 1.67 (br, m, 12H). ³¹P{¹H} NMR (121.5 MHz,

CD₂Cl₂) δ /ppm: 145.1 (m, 2P), 124.5 (m, 2P). IR: $\nu_{\text{CN}} = 2126, 2157 \text{ cm}^{-1}$. Anal. Found (Calcd) for C₄₀H₅₂Cl₂F₂₄N₄O₈P₄Rh₂: C, 30.53 (30.49); H, 3.33 (3.29); N, 3.56 (3.37).

5.7.3 Preparation of Rh₂^{II,II}(tfepma)₂(CNAd)₂Cl₃H (5.5). A J-Young NMR tube was charged with a 0.7 mL *d*₈-THF solution of **5.4** (25 mg, 0.016 mmol) and freeze pumped thaw degassed on a high vacuum manifold. HCl(g) (25 equiv) was generated by adding 2 mL of sulfuric acid to anhydrous NaCl (23 mg) and vacuum transferred to the NMR tube and three additional FPT cycles were executed. Two isomers are obtained (~6:1 ratio). Major isomer: ¹H NMR (300 MHz, *d*₈-THF) δ /ppm: 5.51-4.35 (br, m, 16H), 2.95 (pseudopentet, 6H), 2.11 (br, m, 18H), 1.65 (br, m, 12H), -14.57 (dt, ¹J_{Rh-H} = 13.5 Hz and ²J_{P-H} = 9.2 Hz, Rh-H, 1H). ³¹P{¹H} NMR (121.5 MHz, THF-*d*₈) δ /ppm: 138.1 (m, 2P), 116.7 (m, 2P). Minor isomer: ¹H NMR (300 MHz, THF-*d*₈) δ /ppm: ~5.51-~4.35 (br, m, 16H, overlapped with major isomer), 3.00 (pseudopentet, 6H), 2.21-2.09 (br, m, 18H, overlapped with major isomer), 1.69 (br, m, 12H, overlapped with major isomer), -18.93 (dt (apparent quartet), ¹J_{Rh-H} = ²J_{P-H} = 15.3 Hz, Rh-H, 1H). ³¹P{¹H} NMR (121.5 MHz, THF-*d*₈) δ /ppm: 132.3 (m, 2P), 116.1 (m, 2P, overlapped with major isomer).

5.7.4 Preparation of Rh₂^{II,II}(tfepma)₂(CNAd)₂Cl₄ (5.6). A solution of **5.4** (50.0 mg, 0.0318 mmol) in 0.6 mL of THF was treated with HCl (75 μ L of 4.3 dioxane solution, 0.32 mmol, 10 equiv) with no appreciable color change. The solution was transferred to a screw-cap NMR tube fitted with a septum. The headspace was purged with 1 atm of O₂ for ca. 1 min, at which time the tube was shaken manually and then allowed to stand at room temperature. After 20 min the O₂ addition was repeated, and after 40 min ³¹P{¹H} NMR indicates clean, quantitative conversion to **5.6**. The solution was transferred to a scintillation vial and concentrated under vacuum to yield a dark orange residue. The product was redissolved in a mixture of 2 mL of dichloromethane and 2 mL of hexane. The orange solution was concentrated in vacuo overnight to afford 45 mg of **5.6**•0.25(hexane) (85% yield). ¹H NMR and combustion analysis are both consistent with the presence of 0.25 equiv of hexane in the isolated product. ¹H NMR (500 MHz, CD₂Cl₂) δ /ppm: 5.05-5.16 (br, m, 4H), 4.86-5.00 (br, m, 8H), 4.49-5.59 (br, m, 4H), 3.03 (pseudopentet, 6H), 2.13 (br, s, 6H), 2.03 (br, d, 12H), 1.66 (br, m, 12H). ³¹P{¹H} (121.5 MHz, CD₂Cl₂) δ /ppm: 112.6 (m, 4P). Anal Found (Calcd) for C₄₀H₅₂Cl₄F₂₄N₄O₈P₄Rh₂•0.25(C₆H₁₄): C, 29.92 (30.01); H, 3.36 (3.33), N, 3.36 (3.34). Crystals suitable for X-ray diffraction were grown from THF/toluene solution as orange blocks.

5.7.5 Preparation of $\text{Rh}_2^{\text{I,III}}(\text{tfepma})_2(\text{CNAd})_2\text{Cl}_4$ (5.7). To a saturated solution of **5.4** (50.0 mg, 3.18×10^{-5} mol, 1.00 equiv) in PhCH_3 was added PhICl_2 (17.5 mg, 6.36×10^{-5} mol, 2.00 equiv) as a solid. The reaction solution was heated to 80 °C for 10 h, during which time a green solid precipitated. The reaction mixture was cooled to -20 °C for 20 min, at which time the green solid was collected, washed with pentane, and dried in vacuo to afford 46 mg of the title complex (88% yield). ^1H NMR (300 MHz, $\text{THF-}d_8$) δ/ppm : 5.21–4.73 (m, 16H), 3.10 (pseudoquintet, $J = 4.1$ Hz, 6H), 2.11 (s, 18H), 1.71 (s, 12H). $^{31}\text{P}\{^1\text{H}\}$ NMR (121.5 MHz, $\text{THF-}d_8$) δ/ppm : 113.8 (m, 4P). IR: $\nu_{\text{CN}} = 2211 \text{ cm}^{-1}$. Anal. Found (Calcd) for $\text{C}_{40}\text{H}_{52}\text{Cl}_4\text{F}_{24}\text{N}_3\text{O}_8\text{P}_4\text{Rh}_2$: C, 29.08 (29.22); H, 3.21 (3.19); N, 3.12 (3.42). Crystals suitable for single-crystal diffraction analysis were obtained from a PhCH_3 solution.

5.7.6 Preparation of $\text{Rh}_2(\text{tfepma})_2(\mu\text{-}p\text{-F-C}_6\text{H}_4\text{NC})\text{Cl}_2$ (5.10). To a solution of $[\text{Rh}^{\text{I}}(\text{cod})\text{Cl}]_2$ (33.0 mg, 6.70×10^{-5} mol, 1.00 equiv) in THF (4.0 mL), tfepma (65.3 mg, 1.34×10^{-4} mol, 2.00 equiv) and *p*-fluorophenylisocyanide (16.3 mg, 1.34×10^{-4} mol, 2.00 equiv) was added sequentially. The dark red reaction solution was stirred at 23 °C for 4 h. Solvent was removed in vacuo and the residue was taken up in THF (1 mL) and hexanes (10 mL). The supernatant was removed and the solid residue was dried in vacuo to afford 59 mg of the title complex (59% yield) as an orange solid. ^1H NMR (300 MHz, CD_2Cl_2) δ/ppm : 7.30 (dd, $J = 9.0$ Hz, $J = 4.9$ Hz, 2H), 7.05 (dd, $J = 8.3$ Hz, $J = 8.3$ Hz, 2H), 4.72–4.55 (m, 16H), 2.79 (pseudoquintet, $J = 3.5$ Hz, 6H). ^{31}P NMR (121.5 MHz, CD_2Cl_2) δ/ppm : 130.8 (m, 4P). IR: $\nu_{\text{CN}} = 1736 \text{ cm}^{-1}$. Crystals suitable for single-crystal diffraction analysis were obtained from a PhCH_3 solution.

5.7.7 Preparation of $\text{Rh}_2(\text{tfepma})_2(\mu\text{-}p\text{-MeO-C}_6\text{H}_4\text{NC})\text{Cl}_2$ (5.11). To a solution of $[\text{Rh}^{\text{I}}(\text{cod})\text{Cl}]_2$ (163 mg, 3.31×10^{-4} mol, 1.00 equivalent) in THF (5.0 mL), tfepma (322 mg, 6.61×10^{-4} mol, 2.00 equiv) and *p*-methoxyphenylisocyanide (88.7 mg, 6.61×10^{-4} mol, 2.00 equiv) was added sequentially. The reaction solution was stirred at 23 °C for 4 h. Solvent was removed in vacuo and the residue was taken up in THF (2 mL) and hexanes (15 mL). The supernatant was removed and the solid residue was dried in vacuo to afford 298 mg of the title complex (65% yield). ^1H NMR (300 MHz, CD_2Cl_2) δ/ppm : 7.26 (d, $J = 9.0$ Hz, 2H), 6.85 (d, $J = 9.0$ Hz, 2H), 4.72–4.50 (m, 16H), 2.76 (pseudoquintet, $J = 3.5$ Hz, 6H). ^{31}P NMR (121.5 MHz, $\text{THF-}d_8$)

δ /ppm: 132.2 (m, 4P). IR: $\nu_{\text{CN}} = 1783 \text{ cm}^{-1}$. Crystals suitable for single-crystal diffraction analysis were obtained from a PhCH₃ solution.

5.7.8 Preparation of Rh₂(tfepma)₂(μ -*p*-F-C₆H₄NC)Cl₄ (5.12). To a solution of Rh₂(tfepma)₂(μ -*p*-F-C₆H₄NC)Cl₂ (5.10) (127.0 mg, 9.25×10^{-5} mol, 1.00 equivalent) in PhCH₃ at 23 °C was added PhICl₂ (26.7 mg, 9.71×10^{-5} mol, 1.05 equiv) as a solid in one portion. The color of the reaction mixture turned from orange to dark red. After stirring for 2 h at 23 °C, solvent was removed in vacuo and the residue was taken up in PhCH₃ (1 mL) and cooled to -30 °C for 1 h. The supernatant was removed and the solid residue was dried in vacuo to afford 125 mg of the title complex (94% yield) as a dark orange solid. ¹H NMR (300 MHz, CD₂Cl₂) δ /ppm: 7.48 (dd, $J = 9.2 \text{ Hz}$, $J = 4.6 \text{ Hz}$, 2H), 7.16 (dd, $J = 8.2 \text{ Hz}$, $J = 8.2 \text{ Hz}$, 2H), 4.92–4.60 (m, 12H), 4.56–4.44 (m, 2H), 4.38–4.28 (m, 2H), 3.02 (pseudoquintet, $J = 3.8 \text{ Hz}$, 6H). ³¹P NMR (121.5 MHz, CD₂Cl₂) δ /ppm: 119.5–113.1 (m, 4P). ¹⁹F NMR (275 MHz, CD₂Cl₂) δ /ppm: -73.7 (m, 24F), -105.0 (m, 24F). IR: $\nu_{\text{CN}} = 2181 \text{ cm}^{-1}$. Crystals suitable for single-crystal diffraction analysis were obtained from a PhCH₃ solution.

5.7.9 Preparation of Rh₂(tfepma)₂(μ -*p*-MeO-C₆H₄NC)Cl₄ (5.13). To a solution of Rh₂(tfepma)₂(μ -*p*-MeO-C₆H₄NC)Cl₂ (5.11) (88.0 mg, 6.35×10^{-5} mol, 1.00 equivalent) in PhCH₃ (2 mL) at 23 °C was added PhICl₂ (19.2 mg, 6.98×10^{-5} mol, 1.10 equiv) as a solid in one portion. The color of the reaction mixture turned from orange to dark red. After stirring for 2 h at 23 °C, solvent was removed in vacuo and the residue was taken up in PhCH₃ (0.7 mL) and cooled to -30 °C for 1 h. The supernatant was removed and the solid residue was dried in vacuo to afford 81 mg of the title complex (88% yield) as a red-orange solid. ¹H NMR (300 MHz, CD₂Cl₂) δ /ppm: 7.41 (d, $J = 9.0 \text{ Hz}$, 2H), 6.93 (d, $J = 9.1 \text{ Hz}$, 2H), 4.94–4.64 (m, 12H), 4.54–4.44 (m, 2H), 4.40–4.30 (m, 2H), 3.85 (s, 3H), 3.03 (pseudoquintet, $J = 3.5 \text{ Hz}$, 6H). ³¹P NMR (121.5 MHz, THF-*d*₈) δ /ppm: 119.8–113.4 (m, 4P). IR: $\nu_{\text{CN}} = 2189 \text{ cm}^{-1}$. Crystals suitable for single-crystal diffraction analysis were obtained from a PhCH₃ solution.

5.7.10 Crystallographic Details. Crystals were mounted on a Bruker three circle goniometer platform equipped with an APEX detector. A graphite monochromator was employed for wavelength selection of the Mo K α radiation (0.71073 Å). The data were processed and refined using the program SAINT supplied by Siemens Industrial Automation. Structures were solved by Patterson methods or direct methods in SHELXS and refined by

standard difference Fourier techniques in the SHELXTL program suite (6.10 v. Sheldrick, G.M., and Siemens Industrial Automation, 2000). Hydrogen atoms bonded to carbon were placed in calculated positions using the standard riding model and refined isotropically; all non-hydrogen atoms were refined anisotropically. The structure $\text{Rh}_2^{\text{II,II}}(\text{tfepma})_2(\text{CNAd})_2\text{Cl}_4$, **5.6**, had one disordered trifluoroethoxy group that was satisfactorily modeled. Rotationally disordered CF_3 groups were modeled with the anisotropy of several of the minor fluorine positions constrained.

5.7.11 Toepler pump measurements. Photolysis experiments were carried out in high-vacuum cells comprising a 1-cm fused quartz cuvette and a 20-mL solvent reservoir isolated from each other and the atmosphere by Teflon valves. HCl (from the reaction of NaCl with H_2SO_4) was transferred into the cell. Irradiation was carried out on samples maintained at 20 °C. After irradiation, the reaction solution was frozen, and noncondensable gas passed through three U-traps maintained at 90 K and collected with a Toepler pump. The noncondensable gas was then combusted over hot CuO to confirm H_2 content.

Control experiments showed no production of H_2 , as determined by Toepler pump gas collection. Irradiation of a 50-mL solution of 0.1 M HCl in THF with light ($\lambda > 338$ nm) for 12 h gave only an insignificant quantity of noncondensable gas, which did not burn over CuO. Similarly, no H_2 was collected from solution of **5.1** or **5.4** in THF containing excess HCl maintained at 20 °C in the dark for 12 h.

5.7.12 Photolysis of 5.7 and 5.6. Stock solutions of $\text{Rh}_2^{\text{I,III}}\text{Cl}_4$ complex **5.7** (17.6 mg, 1.07×10^{-5} mol) in 10.0 mL THF and $\text{Rh}_2^{\text{II,II}}\text{Cl}_4$ complex **5.6** (6.4 mg, 3.3×10^{-6} mol) were prepared in an N_2 -filled dry box. Reaction solutions were prepared by dilution of an appropriate volume of the stock solution with THF to 4.0 mL total volume. Reaction solutions were transferred to 1 cm quartz cuvettes and photolyzed with a 1000 W Hg/Xe arc lamp equipped with an appropriate long-pass filter. Reaction samples were periodically removed from the light source and UV-vis spectra were obtained. Photolysis continued until further evolution of $\text{Rh}_2^{0,\text{II}}\text{Cl}_2$ complex **5.4** was no longer detected.

5.7.13 Spectral Fitting to Obtain Concentration Plots for Photolysis of 5.6 and 5.7. In order to determine the concentration of reaction components during the photolysis reactions of complexes **5.7** and **5.6**, a least-squares spectral fitting algorithm was carried out. In order to accomplish this analysis, first, the wavelength-dependent molar absorptivity values of complexes **5.4**, **5.6**, and **5.7** were determined. These molar absorptivity values, in combination with the UV-

vis spectra that were obtained during photolysis allowed the concentration of each reaction component to be determined at each time point for which a UV-vis spectrum was obtained. A model was used in which an absorbance was calculated for each wavelength using the equation:

$$A_{\lambda,\text{model}} = c_1\varepsilon_{1,\lambda} + c_2\varepsilon_{2,\lambda} + c_3\varepsilon_{3,\lambda} \quad (1)$$

A spreadsheet was then generated in which the difference between the computed A_{λ} and the experimentally observed A_{λ} was computed for a given set of concentrations (c_1 , c_2 , and c_3). This difference is the error between the computed model and the experimentally observed absorbance. By optimizing the concentrations of each of the reaction components, the square of the error was minimized:

$$(\text{Error})^2 = \sum_{300 \text{ nm}}^{450 \text{ nm}} (A_{\lambda,\text{model}} - A_{\lambda,\text{exp}})^2 \quad (2)$$

This protocol was repeated for each of the UV-vis spectra that were obtained during the photolysis of complex **5.7** and **5.6**.

5.7.14 Determination of Quantum Yields. Quantum yields were determined using 320 nm monochromatic light, which was generated with a 320 nm Hg line filter on a 1000 W Hg/Xe arc lamp. Potassium ferrioxalate was used as a chemical actinometer.³² The photo flux was determined from the average of actinometric measurements before and after irradiation of the reaction samples. Each quantum yield determination was carried out in triplicate. Experimental details are reported below.

The quantum yield for the photoconversion of **5.6** to **5.4** was determined by analyzing consumption of **2** as a function of photon flux. The following equation was used to determine the quantum yield:

$$\Phi = \frac{n_x t_{\text{Fe}} \Phi_{\text{Fe}} (1 - 10^{-A})_{\text{Fe}}}{n_{\text{Fe}} t_x \Phi_{\text{Fe}} (1 - 10^{-A})_x} \quad (3)$$

where n_x and n_{Fe} are the number of moles of **5.4** and Fe^{2+} generated during the photolysis reactions of **5.6** and ferrioxalate, respectively, t_x and t_{Fe} are the amounts of time that the samples

of **5.4** and ferrioxalate were photolyzed for, Φ_{Fe} is the quantum yield of ferrioxalate reduction at 320 nm, and $(1-10^{-A})_x$ and $(1-10^{-A})_{\text{Fe}}$ are the fraction of incident light absorbed by the ferrioxalate standard and the reaction mixture during photolysis. The term $(1-10^{-A})_{\text{Fe}}$ was assumed to be unity and the term $(1-10^{-A})_x$ was calculated with the equation:

$$(1 - 10^{-A})_x = \frac{A_x}{A_{\text{tot}}} (1 - 10^{-A})_{\text{tot}} \quad (4)$$

where A_{tot} is the total absorbance of the sample at the exciting wavelength and A_x is the absorbance attributable to the starting material (**5.6** in this case), which was calculated using the known concentration of **5.6** and the molar absorptivity at the exciting wavelength. The quantum yield of isomerization of **5.7** to **5.6** was determined during the reaction regime where the concentration of **5.6** was nearly constant; samples were photolyzed to ~20% consumption of **5.4** before quantum yield determinations were carried out. Using the equation:

$$\frac{d[\mathbf{5.6}]}{dt} = 0 = \Phi_{\mathbf{5.7,5.6}}(1 - 10^{-A})_{\mathbf{5.7}} + \Phi_{\mathbf{5.6,5.4}}(1 - 10^{-A})_{\mathbf{5.6}} \quad (5)$$

as well as the known concentrations of **A** and **B**, and the quantum yield of photoreduction of **5.6**, the quantum yield of isomerization was determined. Finally, analysis of the early time points of the photolysis of **5.7** allowed an overall quantum yield for consumption of **5.7** to be determined, using equation 6. This observed quantum yield, coupled with the equation:

$$\Phi_{\text{obs}} = \Phi_{\mathbf{5.7,5.6}} + \Phi_{\mathbf{5.7,5.4}}(1 - 10^{-A})_{\mathbf{5.7}} \quad (6)$$

5.7.15 Time Resolved Photochemical Experiments General Considerations. THF solutions of complexes **5.7** and **5.6** were prepared in 50-mL Schlenk flasks in an N₂-filled glovebox. Solutions were flowed through a 3-mm diameter, 1-cm pathlength flow cell (Starna, type 585.2) using a peristaltic pump and positive argon pressure. Nanosecond transient absorption (TA) measurements were made with the pump light provided by the third harmonic (355 nm) of a Quanta-Ray Nd:YAG laser (Spectra-Physics) running at 10 Hz. Probe white light was provided by a 75 W Xe-arc lamp (Photon Technologies Inc.). The signal light passed

through a Triax 320 spectrometer, where it was dispersed by a 300 nm × 250 nm blazed grating and collected with either an intensified gated CCD camera (ICCD, CCD 30-11, Andor Technology, 1024 × 256 pixels, 26 μm²) for TA spectra or a photomultiplier tube (PMT) for TA single-wavelength kinetics. PMT outputs were collected and averaged with a 1GHz oscilloscope (LeCroy 9384CM). A TTL pulse synchronized with the Q-switch of the Infinity laser was delayed 99 ms before triggering the shutter for the probe light. Electronic delays were created with SRS DG535 delay generators (Stanford Research Systems). These delay boxes, in combination with electronic shutters (Uniblitz), were used to create the necessary pulse sequence.

5.7.16 Computational Details. Density functional theory (DFT) calculations were performed with the hybrid functional Becke-3 parameter exchange functional³³ and the Lee-Yang-Parr non-local correlation functional (B3LYP)²⁶ as implemented in the Gaussian 03, Revision B.05 software package.²⁵ An effective core potential (ECP) representing the 1s2s2p core was used for rhodium (LANL2DZ).³⁴ The 6-31G* basis set³⁵ was used for hydrogen, carbon, phosphorus, fluorine and chloride. All geometry optimizations were performed in C1 symmetry with subsequent vibrational frequency analysis to confirm that each stationary point was a minimum on the potential energy surface. The calculations were performed on simplified models of **5.7**, **5.6**, and **5.12** in which the CF₃CH₂O⁻ functional groups of tfepma have been replaced by F⁻ (dfpma) and the adamantyl functional groups of adamantyl isocyanide or aryl isocyanide have been replaced by CH₃ (**5.A**, **5.B** and **5.C** respectively). Orbitals were visualized using *Molekel* 5.3.³⁶

The percentage of rhodium, chloride, dfpma, and MeNC character in the occupied (canonical) molecular orbitals (MO's) and virtual orbitals discussed for complexes **5.A**, **5.B**, and **5.C** from a full population analysis using the following equation:

$$\% \text{Orbital Character}(i) = \frac{\sum \varphi_{(i)}^2}{\sum \varphi_{(all)}^2} \times 100$$

Where $\sum \varphi_{(i)}^2$ ($i = \text{Rh, Cl, P, F, C, H}$) is the sum of the squares of the eigenvalues associated with the atomic orbitals (AO's) of interest and $\sum \varphi_{(all)}^2$ is the sum of the squares of the eigenvalues of all AO's in a particular MO. The vertical singlet transition energies of the complexes were computed at the time-dependent density functional theory (TD-DFT) level

within G03 using the ground state optimized structures. Contribution of a specific electronic transition to an excitation of interest was calculated using the following equation:

$$\% \text{Conrtibution of Transition}(i) = \frac{C_{(i)}^2}{\sum C_{(all)}^2} \times 100$$

Where $C_{(i)}^2$ is the square of the configuration interaction coefficient calculated by G03 for a particular electronic transition and $\sum C_{(all)}^2$ is the sum of the squares of all of the configuration interaction coefficients for specific electronic transitions in a particular excitation.

5.8 Crystallographic Tables and Calculated Cartesian Coordinate Tables

Table 5.2. Crystallographic data and structural refinement parameters for $\text{Rh}_2^{11,11}(\text{tfepma})_2(\text{CNAd})_2\text{Cl}_4$ (5.6).

Identification code	11177	
Empirical formula	$\text{C}_{40}\text{H}_{52}\text{Cl}_4\text{F}_{24}\text{N}_4\text{O}_8\text{P}_4\text{Rh}_2$	
Formula weight	1644.36 g/mol	
Temperature	-173(2) °C	
Wavelength	0.70173 Å	
Crystal system	Triclinic	
Space group	$P-1$	
Unit cell dimensions	$a = 13.031(2)$ Å	$\alpha = 80.155(3)^\circ$
	$b = 14.865(2)$ Å	$\beta = 72.792(3)^\circ$
	$c = 17.600(3)$ Å	$\gamma = 66.233(2)^\circ$
Volume	$2975.3(9)$ Å ³	
Z	2	
Density (calculated)	1.835 Mg/m ³	
Absorption coefficient	0.968 mm ⁻¹	
F(000)	1636	
Crystal size	$0.20 \times 0.20 \times 0.20$ mm ³	
Θ range for data collection	1.21° to 25.68°	
Index ranges	$-15 \leq h \leq 15, -18 \leq k \leq 18, -21 \leq l \leq 21$	
Reflections collected	51850	
Independent reflections	11322 [$R_{\text{int}} = 0.0470$]	
Completeness to $\Theta = 28.28^\circ$	99.9%	
Absorption correction	Empirical SADABS	
Max. and min. transmission	0.8300 and 0.8300	
Refinement method	Full-matrix least-squared on F^2	
Data / restraints/ parameters	11322 / 0 / 818	
^a Goodness-of-fit on F^2	1.024	
^{b,c} Final R indices [$l > 2\sigma(l)$]	$R_1 = 0.0468, wR_2 = 0.1140$	
^{b,c} R indices (all data)	$R_1 = 0.0623, wR_2 = 0.1246$	
Largest diff. peak and hole	3.160 and -1.371 e/Å ⁻³	

^a $\text{GOF} = (\sum w(F_o^2 - F_c^2)^2 / (n - p))^{1/2}$ where n is the number of data and p is the number of parameters refined.

^b $R_1 = \sum ||F_o - |F_c|| / \sum |F_o|$

^c $wR_2 = \left(\frac{\sum (w(F_o^2 - F_c^2)^2)}{\sum (w(F_o^2)^2)} \right)^{1/2}$

Table 5.3. Crystallographic data and structural refinement parameters for $\text{Rh}_2^{\text{I,III}}(\text{tfepma})_2(\text{CNAd})_2\text{Cl}_4$ (**5.7**).

Identification code	Compound_1	
Empirical formula	$\text{C}_{40}\text{H}_{52}\text{Cl}_4\text{F}_{24}\text{N}_4\text{O}_8\text{P}_4\text{Rh}_2$	
Formula weight	1644.35 g/mol	
Temperature	-173(2) °C	
Wavelength	0.70173 Å	
Crystal system	Monoclinic	
Space group	$P2_1/n$	
Unit cell dimensions	$a = 12.7242(5)$ Å	$\alpha = 90.00^\circ$
	$b = 20.3878(8)$ Å	$\beta = 97.497(1)^\circ$
	$c = 23.2389(9)$ Å	$\gamma = 90.00^\circ$
Volume	5977.1(4) Å ³	
Z	4	
Density (calculated)	1.827 Mg/m ³	
Absorption coefficient	0.953 mm ⁻¹	
F(000)	2920	
Crystal size	0.40 × 0.40 × 0.20 mm ³	
θ range for data collection	1.33° to 30.03°	
Index ranges	$-17 \leq h \leq 17, -28 \leq k \leq 26, -32 \leq l \leq 32$	
Reflections collected	135954	
Independent reflections	17477 [$R_{\text{int}} = 0.0627$]	
Completeness to $\theta = 28.28^\circ$	99.9%	
Absorption correction	Empirical SADABS	
Max. and min. transmission	0.8322 and 0.7017	
Refinement method	Full-matrix least-squared on F^2	
Data / restraints/ parameters	17477 / 184 / 1024	
^a Goodness-of-fit on F^2	1.012	
^{b,c} Final R indices [$l > 2\sigma(l)$]	$R_1 = 0.0479, wR_2 = 0.1065$	
^{b,c} R indices (all data)	$R_1 = 0.0747, wR_2 = 0.1231$	
Largest diff. peak and hole	1.933 and -1.697 e/Å ⁻³	

^a GOF = $(\sum w(F_o^2 - F_c^2)^2 / (n - p))^{1/2}$ where n is the number of data and p is the number of parameters refined.

^b $R_1 = \sum ||F_o - |F_c|| / \sum |F_o|$

^c $wR_2 = \left(\frac{\sum (w(F_o^2 - F_c^2)^2)}{\sum (w(F_o^2)^2)} \right)^{1/2}$

Table 5.4. Crystallographic data and structural refinement parameters for $\text{Rh}_2^{\text{II}}(\text{tfepma})_2(\mu\text{-}p\text{-F-C}_6\text{H}_4\text{NC})\text{Cl}_2$ (**5.10**).

Identification code	Compound_6	
Empirical formula	$\text{C}_{25}\text{H}_{26}\text{Cl}_2\text{F}_{25}\text{N}_3\text{O}_8\text{P}_4\text{Rh}_2$	
Formula weight	1372.09g/mol	
Temperature	-173(2) °C	
Wavelength	0.70173 Å	
Crystal system	Triclinic	
Space group	$P\bar{1}$	
Unit cell dimensions	$a = 10.160(1)$ Å	$\alpha = 73.962(2)^\circ$
	$b = 10.386(1)$ Å	$\beta = 69.049(1)^\circ$
	$c = 12.028(2)$ Å	$\gamma = 71.477(2)^\circ$
Volume	$1104.7(2)$ Å ³	
Z	1	
Density (calculated)	2.062 Mg/m ³	
Absorption coefficient	1.166 mm ⁻¹	
F(000)	670	
Crystal size	0.20 × 0.10 × 0.10 mm ³	
θ range for data collection	1.84° to 30.55°	
Index ranges	$-14 \leq h \leq 14, -14 \leq k \leq 14, -17 \leq l \leq 17$	
Reflections collected	25891	
Independent reflections	12490 [$R_{\text{int}} = 0.0534$]	
Completeness to $\theta = 28.28^\circ$	98.3%	
Absorption correction	Empirical SADABS	
Max. and min. transmission	0.8923 and 0.8002	
Refinement method	Full-matrix least-squared on F^2	
Data / restraints/ parameters	12490 / 3 / 625	
^a Goodness-of-fit on F^2	1.033	
^{b,c} Final R indices [$I > 2\sigma(I)$]	$R_1 = 0.0367, wR_2 = 0.0806$	
^{b,c} R indices (all data)	$R_1 = 0.0439, wR_2 = 0.0849$	
Largest diff. peak and hole	2.221 and -0.801 e/Å ⁻³	

^a GOF = $(\sum w(F_o^2 - F_c^2)^2 / (n - p))^{1/2}$ where n is the number of data and p is the number of parameters refined.

^b $R_1 = \sum ||F_o - |F_c|| / \sum |F_o|$

$$^c wR_2 = \left(\frac{\sum (w(F_o^2 - F_c^2)^2)}{\sum (w(F_o^2)^2)} \right)^{1/2}$$

Table 5.5. Crystallographic data and structural refinement parameters for $\text{Rh}_2^{\text{II,III}}(\text{tfepma})_2(\mu\text{-}p\text{-F-C}_6\text{H}_4\text{NC})\text{Cl}_4$ (**5.12**).

Identification code	Compound_8	
Empirical formula	$\text{C}_{25}\text{H}_{26}\text{Cl}_4\text{F}_{25}\text{N}_3\text{O}_8\text{P}_4\text{Rh}_2$	
Formula weight	1442.99 g/mol	
Temperature	-173(2) °C	
Wavelength	0.70173 Å	
Crystal system	Monoclinic	
Space group	$P2_1/n$	
Unit cell dimensions	$a = 12.202(2)$ Å	$\alpha = 90.00^\circ$
	$b = 21.385(2)$ Å	$\beta = 98.351(2)^\circ$
	$c = 20.398(2)$ Å	$\gamma = 90.00^\circ$
Volume	5266.4(1) Å ³	
Z	4	
Density (calculated)	1.820 Mg/m ³	
Absorption coefficient	1.082 mm ⁻¹	
F(000)	2816	
Crystal size	0.10 × 0.10 × 0.10 mm ³	
θ range for data collection	1.39° to 26.37°	
Index ranges	$-15 \leq h \leq 15, 0 \leq k \leq 26, 0 \leq l \leq 25$	
Reflections collected	10766	
Independent reflections	10766 [$R_{\text{int}} = 0.0357$]	
Completeness to $\theta = 28.28^\circ$	99.8%	
Absorption correction	Empirical SADABS	
Max. and min. transmission	0.8995 and 0.8955	
Refinement method	Full-matrix least-squared on F^2	
Data / restraints/ parameters	10766 / 214 / 556	
^a Goodness-of-fit on F^2	1.054	
^{b,c} Final R indices [$I > 2\sigma(I)$]	$R_1 = 0.0745, wR_2 = 0.1924$	
^{b,c} R indices (all data)	$R_1 = 0.0915, wR_2 = 0.2042$	
Largest diff. peak and hole	2.734 and -2.431 e/Å ⁻³	

^a GOF = $(\sum w(F_o^2 - F_c^2)^2 / (n - p))^{1/2}$ where n is the number of data and p is the number of parameters refined.

^b $R_1 = \sum ||F_o - |F_c|| / \sum |F_o|$

$$^c wR_2 = \left(\frac{\sum (w(F_o^2 - F_c^2)^2)}{\sum (w(F_o^2)^2)} \right)^{1/2}$$

Table 5.6. Cartesian coordinates for the geometry optimized structure of $\text{Rh}_2^{\text{I,III}}(\text{dfpma})_2(\text{MeCN})_2\text{Cl}_4$ (**5.A**).

	<i>x</i>	<i>y</i>	<i>z</i>
Rh	-0.000234	-1.376129	0.000455
Rh	0.000186	1.423585	-0.000429
Cl	0.515702	1.438466	-2.373809
P	2.269383	1.444223	0.292403
Cl	-0.515296	1.440176	2.372967
Cl	-0.000594	-3.902444	0.001151
P	2.195054	-1.261829	-0.697643
Cl	0.000531	3.865951	-0.001215
P	-2.195495	-1.260762	0.698508
P	-2.268992	1.444632	-0.293353
N	3.109357	0.099980	-0.329792
N	-3.109377	0.101106	0.329850
C	0.624816	-1.418560	1.894690
N	-0.983400	-1.518804	-2.994239
N	0.983225	-1.516551	2.995171
C	-0.625263	-1.419673	-1.893778
C	-1.304353	-1.422426	-4.374652
H	-1.012408	-0.429620	-4.727578
H	-0.762666	-2.193372	-4.927437
H	-2.378368	-1.566941	-4.511453
C	1.304552	-1.417699	4.375334
H	1.012388	-0.424351	4.726553
H	0.763279	-2.187846	4.929632
H	2.378653	-1.561642	4.512062
F	-2.874935	1.553170	-1.760794
F	-3.110471	2.615592	0.352347
F	3.111163	2.614449	-0.354233
F	2.875433	1.553726	1.759733
F	3.147533	-2.392816	-0.112534
F	2.502817	-1.526995	-2.234081
F	-2.503317	-1.524902	2.235107
F	-3.148309	-2.391824	0.114086
C	-4.586160	0.099575	0.513152
H	-4.931394	1.131420	0.564110
H	-5.076051	-0.418518	-0.313562
H	-4.831066	-0.390349	1.457045
C	4.586140	0.097867	-0.513090
H	5.075855	-0.419959	0.313895
H	4.830889	-0.392628	-1.456728
H	4.931719	1.129569	-0.564585

Table 5.7. Cartesian coordinates for the geometry optimized structure of $\text{Rh}_2^{\text{II,II}}(\text{dfpma})_2(\text{MeCN})_2\text{Cl}_4$ (**5.B**).

	<i>x</i>	<i>y</i>	<i>z</i>
Rh	-0.037038	1.352321	0.336989
Rh	0.006134	-1.345156	-0.333088
Cl	0.062558	-3.788132	-0.820623
Cl	-0.716281	-0.844724	-2.611629
Cl	-0.055959	3.796562	0.814340
Cl	-0.731238	0.838159	2.620233
P	-2.294687	1.403909	-0.092036
P	-2.247599	-1.466166	0.096135
P	2.194546	1.190617	0.856094
P	2.231627	-1.138846	-0.859235
N	-3.152840	-0.043827	0.021304
N	3.097274	0.081632	-0.058298
N	0.645317	2.211308	-2.575874
N	0.714314	-2.182238	2.579792
C	-4.639778	-0.088208	-0.022476
H	-5.026769	0.881357	0.289523
H	-4.996400	-0.841791	0.681410
H	-4.984424	-0.324031	-1.030905
C	4.585922	0.078916	-0.056916
H	4.940052	1.086480	0.159030
H	4.942370	-0.207885	-1.047497
H	4.970257	-0.619699	0.688916
C	0.460445	-1.823638	1.503126
C	0.401192	1.842803	-1.500232
F	-3.189212	2.344461	0.808413
F	-2.751852	1.993668	-1.497913
F	-2.685991	-2.095033	1.491106
F	-3.120068	-2.408826	-0.821976
F	2.651606	0.875894	2.344299
F	3.084525	2.486930	0.642971
F	2.691809	-0.938062	-2.364652
F	3.161616	-2.381530	-0.527647
C	0.795310	2.432886	-3.971031
H	0.192853	3.294577	-4.267904
H	1.844716	2.630630	-4.201145
H	0.458208	1.536773	-4.499287
C	0.871472	-2.389277	3.976472
H	0.512112	-1.497691	4.497671
H	0.291459	-3.263684	4.280716
H	1.925841	-2.558408	4.206559

Table 5.8. Cartesian coordinates for the geometry optimized structure of $\text{Rh}_2(\text{dfpma})_2(\text{MeCN})\text{Cl}_4$ (**5.C**).

	<i>x</i>	<i>y</i>	<i>z</i>
Rh	-0.001059	-1.294827	-0.273732
Rh	0.002915	1.36477	0.009499
Cl	0.007963	1.503903	2.394641
P	-2.286203	1.516855	-0.006945
Cl	-0.007057	0.262467	-2.237931
Cl	-0.018787	-3.623845	-1.175048
P	-2.305492	-1.36036	-0.307739
Cl	-0.008427	3.792458	-0.356847
P	2.304202	-1.364425	-0.31279
P	2.294471	1.511853	-0.019062
N	-3.169969	0.071896	-0.152565
N	3.17053	0.073573	-0.253253
N	0.003479	-2.162635	2.691281
C	0.000822	-1.834	1.576039
C	0.003896	-2.412974	4.090115
H	0.012806	-1.457805	4.620954
H	-0.891936	-2.97853	4.357407
H	0.889905	-2.995107	4.353948
F	3.053032	2.141113	1.217372
F	2.943493	2.417508	-1.142932
F	-3.030852	2.208809	1.203756
F	-2.943234	2.366578	-1.168897
F	-3.000005	-2.013186	-1.568231
F	-2.97989	-2.281058	0.800979
F	2.993034	-2.089873	-1.536938
F	2.979976	-2.226377	0.842859
C	4.657212	0.090204	-0.352312
H	4.96543	1.009644	-0.850628
H	5.10521	0.034749	0.641715
H	4.982515	-0.755999	-0.957653
C	-4.650818	0.096949	-0.314947
H	-4.919354	0.224836	-1.365044
H	-5.068169	-0.835745	0.066275
H	-5.052312	0.920466	0.27639

5.9 References

- (1) Haynes, W. M. ed. *CRC Handbook of Chemistry and Physics*, 93rd Edition (Internet Version 2013), CRC Press/Taylor and Francis, Boca Raton FL.
- (2) Esswein, A. J.; Nocera, D. G. *Chem. Rev.* **2007**, *107*, 4022.
- (3) Abbott, D. *Proc. IEEE*, **2010**, *98*, 42.
- (4) Nocera, D.G. *Inorg. Chem.* **2009**, *48*, 10001.
- (5) Lewis, N. S.; Nocera, D. G. *Proc. Natl. Acad. Sci. U. S. A.* **2006**, *103*, 15729.
- (6) Nocera, D.G. *Daedalus* **2006**, *135*, 112.
- (7) Eisengerg, R.; Nocera, D.G. *Inorg. Chem.* **2005**, *44*, 6799.
- (8) Cook, T. R.; Dogutan, D.K.; Reece, S. Y.; Surendranath, Y.; Teets, T. S.; Nocera, D. G. *Chem. Rev.* **2010**, *110*, 6474.
- (9) Heyduk, A. F.; Nocera, D. G. *Science* **2001**, 1639.
- (10) Esswein, A. J.; Veige, A. S.; Nocera, D. G. *J. Am. Chem. Soc.* **2005**, *127*, 16641.
- (11) Heyduk, A. F.; Nocera, D. G. *Chem. Commun.* **1999**, 1519.
- (12) Gray, T. G.; Veige, A. S.; Nocera, D. G. *J. Am. Chem. Soc.* **2004**, *126*, 9760.
- (13) Cook, T. R.; Esswein, A. J.; Nocera, D. G. *Inorg. Chem.* **2007**, *129*, 10094.
- (14) Teets, T. S.; Lutterman, D. A.; Nocera, D. G. *Inorg. Chem.* **2010**, *49*, 3035.
- (15) Teets, T. S.; Nocera, D. G. *J. Am. Chem. Soc.* **2009**, *131*, 7411.
- (16) Recently, halogen photoelimination from a PtTe heterobimetallic has been disclosed: Lin, T.-P., Gabbai, F. P. *J. Am. Chem. Soc.* **2012**, *134*, 12230.
- (17) Cook, T. R.; Surendranath, Y.; Nocera, D. G. *J. Am. Chem. Soc.* **2009**, *131*, 28.
- (18) Odom, A. L.; Heyduk, A. F.; Nocera, D. G. *Inorg. Chim. Acta.* **2000**, *297*, 330.
- (19) Teets, T. S.; Cook, T. R.; McCarthy, B. D.; Nocera, D. G. *J. Am. Chem. Soc.* **2011**, *133*, 8114.
- (20) Teets, T. S.; Cook, T. R.; McCarthy, B. D.; Nocera, D. G. *Inorg. Chem.* **2011**, *50*, 5223.
- (21) Crociani, B.; Boschi, T.; Belluco, U. *Inorg. Chem.* **1970**, *9*, 2021.
- (22) Crociani, B.; Boschi, T.; Nicolini, M.; Belluco, U. *Inorg. Chem.* **1972**, *11*, 1292.
- (23) Calligaro, P. *J. Organomet. Chem.* **1977**, *142*, 105.
- (24) Crociani, B.; Boschi, T.; Nicolini, Richards, R. *Inorg. Chim. Acta.* **1975**, *12*, 53.
- (25) Frisch, M. J.; et al. *Gaussian 03*, revision B.05; Gaussian, Inc.: Wallingford, CT, 2004.

- (26) Lee, C.; Yang, W.; Parr, R. G. *Phys. Rev. B*, **1988**, *37*, 785.
- (27) Miehlisch, B.; Savin, A.; Stoll, H.; Preuss, H. *Chem. Phys. Lett.*, **1989**, *157*, 200.
- (28) A. J. Esswein, J. L. Dempsey, and D. G. Nocera, *Inorg. Chem.*, 2007, **46**, 2362.
- (29) Pangborn, A. B.; Giardello, M. A.; Grubbs, R. H.; Rosen, R. K.; Timmers, F. J. *Organometallics* **1996**, *15*, 1518–1520.
- (30) Teets, T. S.; Cook, T. R.; Nocera, D. G. *Inorg. Synth.* **2010**, *35*, 164.
- (31) Sasaki, T.; Nakanishi, A.; Ohno, M. *J. Org. Chem.* **1981**, *46*, 5445.
- (32) Montalti, M.; Credi, A.; Prodi, L.; Gandolfi, M. T. *Handbook of Photochemistry*, 3rd ed.; Taylor and Francis: Boca Raton, FL, 2006.
- (33) (a) Becke, A. D. *Phys. Rev. A* **1988**, *38*, 3098. (b) Becke, A. D. *J. Chem Phys.* **1993**, *98*, 1372. (c) Becke, A. D. *J. Chem. Phys.* **1993**, *98*, 5648.
- (34) (a) Wadt, W. R.; Hay, P.J. *J. Chem. Phys.* **1985**, *82*, 284. (b) Hay, P.J.; Wadt, W. R. *J. Chem. Phys.* **1985**, *82*, 299.
- (35) Hehre, W. J.; Random, L.; Schleyer, P. v. R.; Pople, J. A. *Ab Initio Molecular Orbital Theory*; John Wiley: New York, 1986.
- (36) Flükiger, P.; Lüthi, H.P.; Portmann, S.; Weber, J. *MOLEKEL*, 5.3; Swiss Center for Scientific Computing: Manno, Switzerland, 2000; www.cscs.ch/molekel.

Matt was born on April 19th, 1985 in Buffalo, New York, to David and Maureen Chambers. He grew up alongside 3 siblings, Alex, Danielle and Garrett, as the second oldest. Even though he was not the oldest (Alex) or the youngest (Garrett) or the only girl (Danielle), he actually was not continually overlooked, despite family lore. As close as he is to his parents and siblings, the author additionally grew up in a loving (and loud) extended family with a close knit group of grandparents, aunts, uncles and cousins where the importance of family as well as the ability to find his way in a large boisterous group was developed; a skill that would ultimately serve useful during graduate school. The author has a strong catholic educational background in attended St. Gregory the Great School between the ages of 5 and 14 years old and the proceeding to attend high school at St. Joseph's Collegiate Institute, graduating in 2003. It was during high school when a series of inspirational chemistry and biology classes convinced him to continue a path along the course of scientific studies in college. Matt proceeded to attend Cornell University where he initially began as a biology major with the intent of continuing to medical school. However, a life changing experience working in the laboratory of Professor Peter T. Wolczanski, where he worked for 2.5 years, instilled a passion for molecule making and substrate activation. With the support of Professor Wolczanski, Matt proceeded to graduate school at MIT where he joined the laboratory of Professor Daniel G. Nocera working on the synthesis of pseudotetrahedral metal-oxo complexes. The close knit, large and outgoing laboratory in which Matt worked, while being eerily reminiscent to his extended family of Buffalo in certain ways, exposed him to a plethora of interesting people from all over the world. Without a doubt, the most noteworthy of these people met continues to be Noémie Elgrishi. Despite meeting Matt in a hallway with coffee dripping all over his hands, a special connection was formed between them which continues to grow. After receiving his Ph.D., Matt plans on moving to Paris to join the laboratory of Professor Marc Fontecave at the Collège de France working the field of biomimetic carbon dioxide reduction.

My time at MIT and in the Nocera lab represents roughly 20% of my entire life. It is impossible to merely exist for that length of time without needing the assistance of a cornucopia of people. I was blessed with an incredible team of people who were with me along the way; from faculty to undergraduates. It would be extremely boring to any potential reader for me to attempt to acknowledge the impact of every single person, so I do not mention everybody extensively. I apologize for that. I'll do my best to touch upon everyone.

Any acknowledgements must begin with my advisor, Dan Nocera. Despite only having one real meeting with Dan prior to joining his group, for some reason Dan not only welcomed me into his lab but also gave me the freedom to pursue my own project ideas. While most of my ideas and project designs did not work out swimmingly, Dan had the patience to allow me to grow and learn through my failures. Where most advisors probably would have been outwardly frustrated, Dan continued to at least appear supportive and allow me to continue to try to find my way. Ultimately, I'd like to think that Dan's patience has paid off. I can't imagine going through grad school in any other group. In allowing me to fail I do firmly believe that Dan facilitated my growth and I am better prepared to succeed in the future. I'd also like to thank Dan for cultivating a truly unique lab atmosphere. The lab was perpetually a think-tank of scientific discussions and ideas and Dan was able to accept into his lab scores of exceptional people. It was almost impossible to avoid learning something new on a daily basis. It was a pleasure spending my graduate school years working for Dan.

I'll continue with acknowledging the Inorganic Chemistry faculty at MIT. When deciding where to attend graduate school, the MIT chemistry department was described to me as a *Mecca of Inorganic Chemistry* and it certainly did not disappoint. Throughout the duration of my time at MIT, the group of Professors Lippard, Schrock, Cummins, Dincă, Peters and Nocera were second to none. I am deeply appreciative for the time that all of these professors were able to give to me over the years, especially within the oral exam format and the classes they taught. I'd especially like to acknowledge the two faculty members who, along with Dan, formed my thesis committee: Professor Kit Cummins and Professor Mircea Dincă. My annual meetings with Kit were always insightful and helpful. To a fault, Kit made himself too available to me. Often he would complain that I didn't visit him enough in his office to chat about chemistry. Kit's blunt assessments of my progress in concert with specific suggestions of how to grow as a chemist were always appreciated. I met Mircea when he joined the Nocera group as a post-doc and somehow it seems fitting that ultimately he ended up as a member of my thesis committee. He was always extremely helpful as a senior member of Dan's lab and continues to be a great resource and someone I genuinely enjoy talking to about most topics; from science to the Buffalo Bills.

I'd also like to acknowledge Dilek Dođutan. She holds a unique position within the lab wherein she's part *advisor*, part *researcher*, part *grant coordinator*, and part *whatever the lab happens to need done*. Dilek has been instrumental in allowing Dan's lab to function and even though it is not always readily apparent, she facilitates pretty much all of the research executed within Dan's lab. Beyond all of this, Dilek has been a fantastic friend over the years. She constantly coordinates group events and has a fantastic habit of cooking way too much delicious Turkish food. I am truly grateful for all of the work she puts in to making research possible within Dan's lab and making the overall atmosphere enjoyable.

At this point, I'd like to specifically acknowledge those people who have directly contributed to work that reported within this thesis. Without the following people, this thesis would not have been possible.

Stas Groysman was without a doubt the person who most significantly influenced my time in graduate school. When I met Stas I had already been working for 2.5 years and had very little (or nothing) to show for my effort. Stas was a quintessential mentor and welcomed me into a project that he designed. Stas was the motivating force behind the usage of the ditox ligand. Together with Stas, we designed the synthesis of and characterized the reduced tris(alkoxide) compounds reported in Chapter 2. He initially synthesized $V(\text{ditox})_3\text{O}$ and $Cr(\text{ditox})_3\text{O}$ reported in Chapter 3 and pioneered many of the subsequent reactivity studies. Even after leaving the group and beginning his independent career at Wayne State University, Stas remains a key resource for all of the work on tris(alkoxide) metal complexes. I truly have no idea what would have become of my graduate school experience without Stas's assistance and I am eternally grateful for having the privilege of working with him. Not only was he a great mentor, but he was a great friend. I'll always cherish the times we worked side by side in the glovebox rocking out to rag time music and singing Thomas the Tank Engine songs (*They're 2, they're 4, they're 6, they're 8...*).

I'd also like to acknowledge Dino Villagrán for assistance in DFT reported throughout this dissertation. Dino was influential in directly training me in regards to executing DFT calculations on several metal tris(alkoxide) systems. He remained a great resource and was always willing to assist in any complications I came across while performing DFT calculations as well as any general technical issues. On a day to day level, I don't think I ever had a question that Dino either couldn't answer or wasn't willing to help me find the answer to. From synthetic techniques, to running DFT calculations, to electrochemistry, to writing papers, working with Dino was like working with a technical guide to chemical research. His breadth of expertise was something I always admired (and still do) and I honestly tried to pick up as many tips as I could from him. I have a feeling that I will continue to learning various things from Dino in the future, and in return I will continue to attempt to convert Dino into a fan of the Buffalo Bills.

I'd like to acknowledge Dave Powers as well. Dave was the driving force behind much photochemical work on halogen elimination reported in Chapter 5. The final chapter of my time in the Nocera lab was clearly dominated by Dave. It is unnerving to see most of the people whom you had spent your time with eventually graduate and leave you behind, but Dave came in as a post-doc and pretty much filled in for everyone. It's been a pleasure working with him on parts of the HX project and having long conversations about various topics of chemistry. Outside of lab he has opened my eyes to the wonder that is quality beer, and I will always be in debt to him for that.

Bryce Anderson needs to be acknowledged for acquiring the transient absorption data reported in Chapter 5. Additionally, although it was not reported within this dissertation, Bryce and I have spent significant effort working towards EPR studies of ^{17}O labeled d^1 metal oxos. Despite those studies clearly being a "work in progress" Bryce has been a fantastic person to collaborate with and has continually exercised extreme patience when being force to talk to me about spectroscopy. I wish him all the best as he finishes his dissertation and continues to fill in many of the technical voids within the groups. As a general rule, if you don't know how to do a spectroscopic experiment, Bryce is always willing and capable to help out...and he does it with an *unbridled enthusiasm* that could never be matched.

A very special acknowledgement needs to be given to Noémie Elgrishi. Noémie and I worked together on measuring hydrogen production reported in Chapter 5. She was the initial person who welcomed me into aspects of the HX splitting project. Working with Noémie was a life changing experience. Not only did she afford me the opportunity to learn new techniques and skills needed for the HX project but we unquestionably formed a very special bond throughout our time together in the Nocera Lab. I am very excited to continue to work with her and support her as I follow her lead and work in the lab of Marc Fontecave for my post-doctoral studies.

Despite not directly contributing to the work reported in this thesis, there are many other people that need to be acknowledged for impacting my experience in graduate school and shaping the person and scientist I am today.

Tim Cook was the ideal senior graduate student to work with. It's not always easy navigating through years of working in the Nocera lab, and I always admired Tim's approach to lab work and the lab in general. Inside of lab he was always willing to field questions and discuss minutia. Outside of lab we had plenty of memorable hockey games, group dinners at the Miracle, and barbeque chicken pizzas. His giving nature is highlighted by the fact that the very futon I'm sitting on while writing this was gifted to me by Tim. It isn't very comfortable, but it's the thought that counts.

Tom Teets wouldn't want me to acknowledge him for much. Much like his hustle on the softball diamond, he would likely deem it unnecessary. So I'll try to be brief. Tom and I entered Dan's lab at the same time. His incredible work ethic and productivity always made me jealous. At times I felt like a dog racing around a track chasing (but never catching) the mechanical rabbit that is Tom Teets's productivity. Working with Tom was great because you couldn't help but want to work harder just keep up with his *blue collar* approach to lab work. It was also great to discuss politics, eating habits, and Cleveland sports on a daily basis with Tom. I'd also like to acknowledge Tom for having great hair. Finally, despite that which is written all over the Nocera lab, Tom Teets doesn't actually smell.

Along with Tom, I joined the Nocera Lab with Arturo Pizano. In my mind, Arturo embodies the Nocera lab better than any other singular person. Arturo was the person I went through all aspects of grad school with (classes, oral exams, 4th year talks, karaoke). Without a doubt the most amusing person in any conversation is always Arturo. In my opinion, Arturo also has remarkable combination of spectroscopic skills, synthetic skills and chemical intuition. It has truly been a pleasure spending so much time with Arturo and, in many respects, watching him re-energize aspects of the PCET projects within Dan's lab.

Changhoon Lee is the best. I envy his meticulous attention to detail and his rigorous stretching routines. He definitely is *ok*. I don't think Changhoon would want any more words written about him.

Manos Roumpelakis and I sat next to each other for several years. Consequently I have more stupid inside jokes with him than anyone else. Manos was extremely influential in the maintenance of my sanity. I also thank him for allowing me to gaze over his shoulder when he was working up e-chem data so I could try to learn a little bit. His olive oil is delicious.

Yogi from MIT was an interesting person to work with for 4 years. I don't think there was ever a scientific conversation that he didn't not only get involved in, but also contribute greatly

to. I also admired his blunt assessments of things. You could always trust Yogi to be honest with you to a fault and that was extremely valuable. Most importantly, I will continue to cherish Yogi and my on-going quest to popularize Fantasy Spelling Bee competitions.

Honestly, there are too many people to go through everyone individually. I'll try to verbally talk to people at some point to thank and acknowledge people in more detail. But I do want to generally acknowledge the older graduate students who welcomed me into the Nocera lab. Liz Young, Emily Nytko, Becky Sommers, Emily McClaurin and Mike Marshak all were great people to look up to. Emily McClaurin is simply too nice. Not only did she push forward a project almost single handedly, she basically coordinated all the events for the group for years and made sure we were as much of a cohesive unit as we could be. Mike Marshak was influential in simply getting me to MIT, as I basically followed him to Dan's group from Cornell. I do value greatly working with Mike and living with Mike for several years. Many of my underlying scientific interests stem from conversations with Mike. His enthusiasm on certain topics can be infectious and definitely guided me towards that which I ultimately studied.

The classes below me in the Nocera lab are fantastic. Sadly, I can't mention details about everyone. Casandra Cox, Kwabena Bediako, Andrew Ullman, Chris Lemon, Lisa Olshansky, Dan Graham, Bon Jun Koo, Mike Hyuhn, Andrew Maher, Robert Halbach, and Dave Song all are great to work with and create a unique and interesting lab environment. I probably asked Kwabena more stupid e-chem questions than anyone else, and I thank him for not judging me too harshly. Ullman and Lemon are probably two of my favorite people to get coffee with and to talk to about any random topic. I wish Robert luck as his moves forward with some of the alkoxide chemistry I've left behind.

The Nocera Lab has also been populated by some incredible post-docs. I'd like to specifically acknowledge John Melnick, Alex Radosevich, Danny Lutterman, Yi Liu, Mark Symes, Tim Kucharski, Tom Kempa and Joel Rosenthal for being particularly helpful. It's great to work in a lab where there is a wealth of expertise all around you. You don't have to go far to find someone willing to help you in the Nocera lab and these post-docs certainly helped me. And yes, Joel wasn't actually a post-doc for Dan...but he was available enough that he might have been.

At this point I feel like I should finish up with the acknowledgements. I truly did enjoy working within the Nocera lab. The experience was fantastic and it was an honor meeting all of the people who have been affiliated with the Nocera lab. It's impossible to fully thank everyone to an appropriate extent in a few pages at the end of a thesis, so expect me to continue to express my gratitude in person throughout the years to come.